Transport coefficients of strongly interacting matter

Vom Fachbereich Physik
der Technischen Universität Darmstadt

zur Erlangung des Grades
eines Doktors der Naturwissenschaften
(Dr. rer. nat.)

genehmigte Dissertation von
Dipl.-Phys. Klaus Heckmann
aus Groß-Gerau

Darmstadt 2011
D17

Referent: Prof. Dr. Jochen Wambach

Koreferent: Priv. Doz. Dr. Michael Buballa

Tag der Einreichung: 05.04.2011

Tag der Prüfung: 04.05.2011

Abstract

In this thesis, we investigate the dissipative transport phenomena of strongly interacting matter. The special interest is in the shear viscosity and its value divided by entropy density. The performed calculations are based on effective models for Quantum Chromodynamics, mostly focused on the 2-flavor Nambu-Jona-Lasinio model. This allows us to study the hadronic sector as well as the quark sector within one single model. We expand the models up to next-to-leading order in inverse numbers of colors. We present different possibilities of calculating linear transport coefficients and give an overview over qualitative properties as well as over recent ideas concerning ideal fluids. As present methods are not able to calculate the quark two-point function in Minkowski space-time in the self-consistent approximation scheme of the Nambu-Jona-Lasinio model, a new method for this purpose is developed. This self-energy parametrization method is applied to the expansion scheme, yielding the quark spectral function with meson back-coupling effects. The usage of this spectral function in the transport calculation is only one result of this work. We also test the application of different transport approaches in the NJL model, and find an interesting behavior of the shear viscosity at the critical end point of the phase diagram. We also use the NJL model to calculate the viscosity of a pion gas in the dilute regime. After an analysis of other models for pions and their interaction, we find that the NJL-result leads to an important modification of transport properties in comparison with the calculations which purely rely on pion properties in the vacuum.

Zusammenfassung

In dieser Arbeit werden Transporteigenschaften von stark wechselwirkender Materie untersucht. Im Mittelpunkt steht hierbei der lineare Scherviskositäts-Koeffizient. Die Scherviskosität gilt nicht nur als dominierender Ursprung von Dissipation in heißer und dichter Materie, sondern kannn auch eine Aussage darüber machen, wie ideal ein Fluid ist. So ist auch ein Augenmerk dieser Arbeit darauf gerichtet, das Verhältnis von Scherviskosität und Entropiedichte auf eine mögliche universelle untere Grenze hin zu untersuchen. Dafür werden mikroskopische Berechnungen des Koeffizienten angestellt, die in erster Linie auf dem Nambu-Jona-Lasinio-Modell beruhen. Innerhalb dieses effektiven Modells für die Quantenchromodynamik kann sowohl die hadronische Phase bei kleinen Temperaturen wie auch die chiral restaurierte Quarkphase bei hohen Temperaturen untersucht werden und zusätzlich die Übergangsregion zwischen beiden. Um das Modell auf das Transportproblem anzuwenden, muss ein Entwicklungsschema über die Standard-Näherung des Modells hinaus angewendet werden. Es wird eine Übersicht über verschiedene Methoden der Transporttheorie, über qualitatives Verhalten von Transportkoeffizienten sowie über neue Konzepte und Vermutungen zur Universalität von stark gekoppelten Fluiden gegeben. Die notwendige Bestimmung der Quark-Zustandsdichte in einem selbstkonsistenten Näherungsschema ist mit bisherigen Berechnungsarten nicht möglich, und so wird die neue Methode der Selbstenergie-Parametrisierung entwickelt. Nach der Einführung dieses Konzepts und einiger möglicher Varianten wird die Quark-Spektralfunktion mit diesem Ansatz berechnet und in der Green-Kubo-Methode zur Bestimmung der Scherviskosität verwendet. Neben dieser Anwendung werden auch weitere Konzepte zur Berechnung der Scherviskosität im Nambu-Jona-Lasinio-Modell vorgestellt, welche unter anderem ein interessantes Verhalten der Viskosität am kritischen Endpunkt des Phasendiagrams implizieren. Außerdem beschäftigt sich diese Arbeit mit den Transporteigenschaften in einem Pionengas, wo auch andere Modelle für die Teilchenwechselwirkung angewendet werden. Dieser Ansatz kann mit einem Gas von wechselwirkenden Pionen, die mit Hilfe des Nambu-Jona-Lasinio-Modells berechnet werden, verglichen werden. Die im verwendeten Modell berücksichte zusammengesetzte Natur der Mesonen hat einen erheblichen Einfluss auf die Temperaturabhängigkeit der Scherviskosität hat.

Contents

List of Figures

List of Tables

Chapter 1

Introduction

The modern understanding of the fundamental physics of mesons and baryons began with the quark model [1, 2, 3]. Based on the existence of constituent particles of nucleons, quantum chromodynamics (QCD) was developed as a non-Abelian gauge theory, where quarks interact by exchange of gluons [4, 5]. An important property of this theory is the asymptotic freedom [6, 7, 8] of the theory at large momenta or small distances. The behavior at small momenta or large distances is more complicated, since single quarks are confined in hadrons and cannot be observed. The conditions of quarks at low distances with high momenta, as they are nessecary for the asymptotic freedom, can be realized in a system that is sufficiently compressed or heated up.

This idea of deconfined quarks at sufficiently high density or temperature solved the paradox of the hadron resonance gas [9, 10]. The idea of a phase diagram of strongly interacting matter was born, consisting of a hadronic phase at low temperatures and densities, a quark-gluon phase at high temperatures and densities [11], and possibly of more complex phases [12]. The term quark-gluon plasma was established [13] for the quark-gluon phase in analogy to a electromagnetic plasma where the atoms are split into electrons and ions.

More details about this new phase of matter, and the possible transitions to the hadron phase have been tried to be extracted from the underlying theory. Whereas perturbative and qualitative arguments only hold at asymptotically high temperatures or densities, the strong coupling of QCD leads to a failure of the usual perturbative methods of quantum field theory in the low-momentum sector. Nowadays, it is possible to study a discretized version of QCD with high computational effort, although these methods of lattice QCD are restricted to the region of low densities, i. e. small baryon chemical potentials [14, 15, 16]. The lack of an appropriate method to solve the exact theory in certain regimes gave rise to several effective models, which resemble real QCD to some extend. An important effective theory for quarks which has the same global symmetries as QCD is the Nambu-Jona-Lasinio model [17, 18]. With the nonperturbative quantum field theoretical methods and these models, several structures and phenomena of strongly interacting matter at finite temperature and density were proposed.

A selection of prominent phases is shown in the phase diagram in Fig. 1.1, where the phases take different positions in temperature T and chemical potential μ. The hadronic phase at low T and μ, and the quark-gluon plasma can be phases in a thermodynamical sense, and there can be a phase transition of first or second order, or a crossover between these two. The results from lattice QCD indicate that the transition is of crossover type for small μ [14, 15, 16]. Nevertheless, at higher baryon chemical potential a first-order transition may exist, which ends in a critical end point before reaching the temperature-axis. This is only one scenario at higher densities, more complicated shapes of a first-order transition line or inhomogeneous phases are other possibilities of the equilibrium state of strongly interacting matter at high densities and moderate temperatures. At very high densities, Cooper pairs of quarks may condense and a color superconductor [19, 20] is formed. A recent review of the phase structure of QCD is found in [21], and in [22] with a special emphasis on high densities.

While the considerations about the phase diagram of QCD presented so far were of theoretical nature, it is important to ask where such high energy densities exist in nature, that quarks and gluons are not confined in hadrons but real degrees of freedom. Shortly after the big bang, the

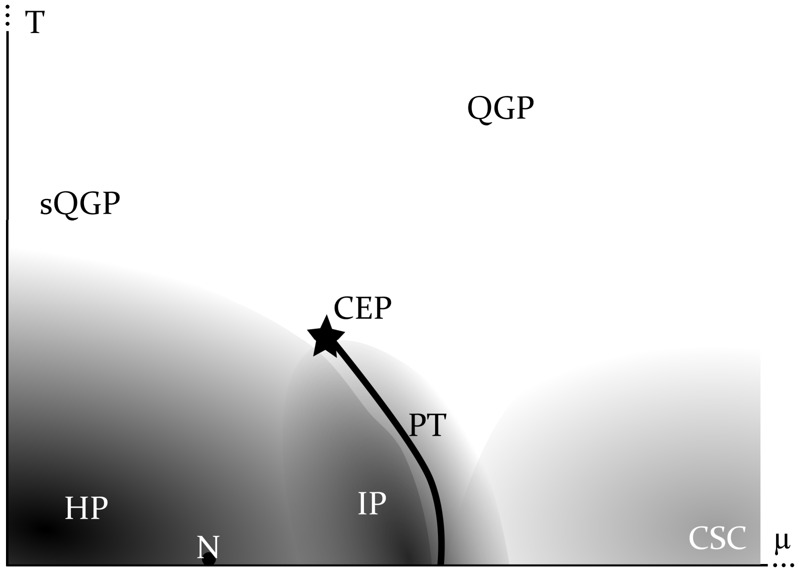

Figure 1.1: Possible phase diagram of Quantum Chromodynamics. The hadronic phase (HP) and the quark-gluon plasma (QGP) are possibly separated by a first-order phase transition (PT), which has a critical end point (CEP). Another transition scheme would involve inhomogeneous phases (IP). At high chemical potentials and low temperatures, color-superconducting phases (CSC) are expected. The position of nuclei (N) in this diagram is situated in the hadronic phase. There are indications that the matter in the vicinity of the crossover at low chemical potential forms a strongly coupled quark-gluon plasma (sQGP).

temperature and density of the early universe were very high, so the universe was first in a quark-gluon plasma phase, before undergoing a transition into hadrons. High densities at relatively low temperatures are found in the centers of compact stars, which are formed after the burning period of a star of a certain mass. Although there are astrophysical observations which are able to reveal some information about the early universe and compact stars, non of these possible realizations of deconfined quark matter is accessible in an experiment in laboratory.

The highest energy densities that are produced artificially in laboratory are formed in a collision of particles in an accelerator. For an investigation of thermodynamical phases, it is necessary to investigate a sufficiently large piece of strongly interacting matter. Thus, one can not hope to produce a quark-gluon plasma in a collision of two protons; heavier nuclei are the promising projectiles for such an experiment. The history of heavy-ion collision experiments was determined by the development of new accelerators that could attain higher collision energies than the predecessors. The possible formation of a quark-gluon plasma in a heavy-ion collision was an important perspective during the operation of the experiments at AGS (Brookhaven), SPS (Geneva), RHIC (Brookhaven), and the currently running investigations at LHC (Geneva). The results of the experiments at the first three accelerators have been discussed in literature, for examples in the review articles [23, 24]. While the beam energy at AGS was still too low, there are indications that a quark-gluon plasma was formed at SPS [25, 26]. The experiments at RHIC finished with the perspective that one measured signals of a deconfined matter, while some aspects remained unclear and will probably be understood after the run of the heavy-ion program at LHC. A complementary experiment that may reveal supplementary information about the phase diagram at higher chemical potentials is planned at FAIR.

For the interpretation of the detector signals of a heavy-ion collision, it is essential to understand the behavior of the formed fireball from a theoretical perspective (an early work to this topic was [27]). The formation of a quark-gluon plasma in the hot fireball of a nucleus-nucleus-collision requires not only a sufficiently high energy density. As the new state of matter is thought to form a thermodynamical phase, the strongly interacting matter in the fireball has to be spacious enough and attain thermal equilibrium. The spacial extend of the fireball is ensured by the usage

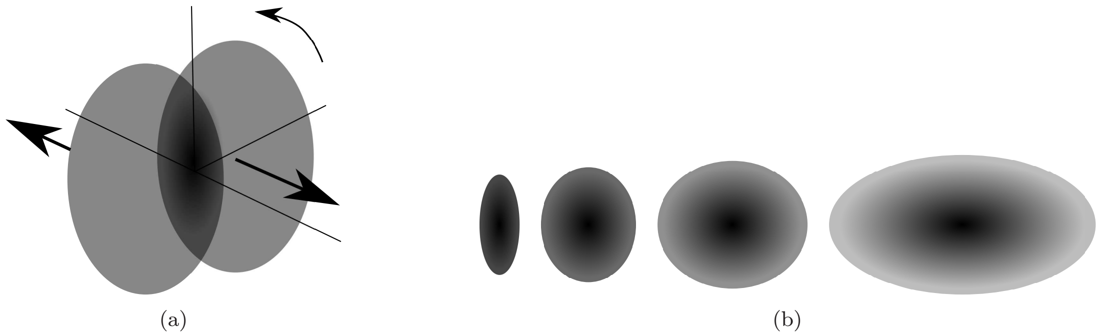

Figure 1.2: Evolution of a fireball after a non-central collision. (a) Non-central collision of two ultra-relativistic heavy nuclei, where the large arrows indicate the direction of movement along the beam axis. The azimuthal angle is indicated by a small arrow. (b) The fireball is shown for different times, the earliest one on the left directly after the collision, later times are shown on the right. The spacial anisotropy is transformed into a momentum anisotropy at later times.

of heavy nuclei instead of nucleons, while the question of thermalization is more difficult. It is believed that after an initial state after the collision, the matter is equilibrated to a thermalized quark-gluon plasma if the initial energy is high enough [23]. This thermalized matter expands and cools, until it is cold enough to hadronize when the hadronic transition temperature is reached. This hadronic matter continues its expansion, very unstable hadrons decay, and the detector, which is placed at macroscopic distances from the location of the collision, can measure the huge amount of particles that was produced in the collision or in secondary decays.

The difficult task is to identify signals that indicate the formation of a quark-gluon plasma, and several signatures of such a formation have been proposed (see [24] for a review). The statistics of the measured hadrons indicate that the matter at the chemical freeze-out, was equilibrated [28]. Another signal concerns medium modifications of charm quark bound states [29], which lead to suppression of certain states that are not bound in a dense medium due to screening. The different behavior of jets in heavy-ion collisions in contrast to proton-proton-collision is also an indication of the formation of an extended dense medium [30], since the propagation of the jets is affected by the matter. The summarized results at RHIC [31, 32, 33, 34] discuss these signals, and additionally the phenomenon that can be taken as the motivation of this work: The behavior of the so called elliptic flow and its implications is discussed in the next paragraphs, beginning with the underlying theoretical concept.

A non-central collision of two nuclei leads to a fireball of irregular shape. Such a collision is shown in Fig. 1.2(a). In the overlapping region of the two nuclei the initial fireball forms with a very high energy density. Such a state of matter has anisotropic pressure gradients, and this will affect its evolution. A sketch of an expansion of such a fireball is shown in Fig. (1.2(b)). The different pressure gradients lead to a larger velocity of the fluid in one direction, thus the shape of the fireball changes with times, and the spatial anisotropy is transformed into a velocity anisotropy in the end. For a systematic study of this anisotropy, it is helpful to analyze the Fourier components with respect to the azimuthal angle of the momentum distributions [35, 36, 37, 38]. The second Fourier component v_2 is called the elliptic flow.

In order to understand the experimental value of v_2 for different particle species measured in the detectors (see [39] for one of the first results at RHIC), one has to understand the processes leading to this collective property of the collision products. The description of the matter in a fireball of a heavy-ion collision requires a knowledge of the initial conditions after the collision (or after thermalization), and of the physical processes governing the further evolution. A general treatment of the matter is a hydrodynamical description of the matter in a certain space-time region [40, 41]. Such a hydrodynamical model requires relatively few assumptions, for example the description of the matter as a continuous fluid. The hydrodynamical parameters that indicate the importance of dissipative processes can be taken as free parameters.

Surprisingly, the predictions from ideal hydrodynamics [42, 43], which neglects completely dis-

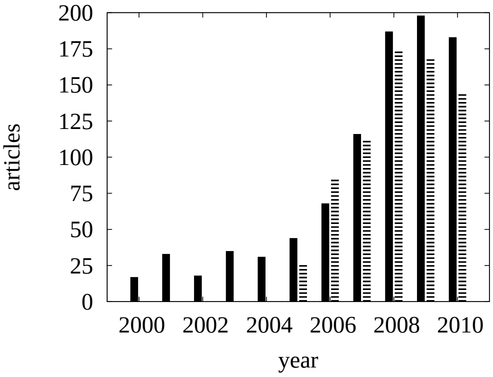

Figure 1.3: Scientific work dedicated to viscous phenomena. The bars indicate the number of articles published in one specific year. The solid bars correspond to articles with the keyword “viscosity”, the dashed bars to articles citing [50]. The numbers are taken from the High-Energy Physics Literature Database, http://www.slac.stanford.edu/spires.

sipative phenomena, show a reasonable agreement with the data from the different detectors at the RHIC experiment [44, 45]. This observation even motivated improvements in hydrodynamic descriptions with included viscous effects [46], which allowed a more accurate study of the fireball-fluid. Indeed, it seems that the dissipative effects, dominated by the shear viscosity coefficient η, correspond to a small but apparently nonvanishing value of η [47, 48, 49]. These developments were also pushed by a conjecture that the shear viscosity, more precisely the ratio of the shear viscosity η over the entropy density s of a fluid, can not be arbitrarily small, but has a lower limit [50]. Especially this conjecture, which has its origin in string theory, motivated many works to study the shear viscosity and other transport coefficients of strongly interacting matter. An illustration of this development is shown in Fig. 1.3, it expresses the influence of the possible discovery of the most ideal fluid in nature at RHIC.

Although the shear viscosity of a fluid is a parameter that can be calculated starting from the microscopic description of the matter, the understanding of the small viscosity in fireball matter is difficult. This is closely related to the fact that η/s in this matter is thought to be small, because a small viscosity requires a strong coupling between the underlying particles. This counterintuitive relation between coupling and fluidity implies that the quark-gluon plasma, at least for temperatures close to the crossover region, is not quasi-free as one could naively expect from the concept of asymptotic freedom, but is still strongly interacting. Therefore, this region is often called strongly coupled quark-gluon plasma (see Fig. 1.1). The strong coupling complicates the calculation of microscopic properties from the underlying quantum field theory enormously, since it implies the failure of perturbative techniques that are valid for small couplings. Additionally, the high density leads to complications in the calculation of transport properties, which are obtained the easiest in a dilute gas.

Historically, the first microscopic calculations of transport phenomena in fluids were performed in the end of the nineteenth century, in the approximative treatment of the kinetic theory of gases. These classical transport theories assume that fluids are dilute and behave almost like noninteracting systems of free particles. Later, these methods became more accurate and were adapted to relativistic and quantum-mechanical systems. In the 1950s, the first exact formulas for transport coefficients were formulated without assuming that the particles in the fluid are sufficiently rarefied. However, the information that is needed in these Green-Kubo formulas is much more difficult to obtain than the building blocks of the kinetic theory of gases before. In a quantum field theoretical approach, the dressed two-particle Green’s functions in Minkowski space-times are needed, which are not accessible in the different non-perturbative methods: Lattice QCD, as well as the Dyson-Schwinger approach, is restricted to Euclidean space-time, and dynamical properties stay obscure.

So, the transport properties of the quark-gluon plasma can only be calculated from QCD for very high temperatures [51], where asymptotic freedom leads to a decrease of the effective coupling.

In the interesting region, where the strongly coupled quark-gluon plasma is expected, these approaches fail. In the same way as in the case of the QCD phase diagram, one can try to investigate this region, where the direct approach from QCD is impossible, in QCD-like models. One the one hand, this simplifies certainly the quantum-field theoretical calculus, but on the other hand, it does not avoid the necessity of the use of the Green-Kubo method for the transport coefficient calculation. Even in these simpler models, the efforts that are necessary to obtain a result for the shear viscosity in a dense and strongly interacting system are huge, especially concerning the calculation of Green's functions in Minkowski space-time. Thus, a suitable method for the calculation of dynamical Green's functions has to be developed.

Due to these inadequacies of the microscopic calculation of shear viscosity and other transport coefficients in nearly-ideal fluids, one may learn more about transport phenomena in strongly coupled systems from fundamentally different experiments. Cold atoms in optical traps are objects that are intensively studied, and behaviors similar to the elliptic flow of particles in heavy-ion collisions have been observed [52]. Furthermore, the interaction of the cold fermionic gases can be controlled using Feshbach resonances, thus a system at very strong coupling can be produced and observed in laboratory. In that unitary limit, the experimental results of collective properties [53, 54, 55] led to several studies about viscosity and hydrodynamics [56, 57, 58]. It was argued that the ratio of shear viscosity over entropy density takes a very small value in these systems, smaller than in all other materials that have been measured [59].

One can conclude that the question of transport coefficients of strongly interacting matter is an exciting topic today. Especially the shear viscosity of a quark-gluon plasma close to the crossover to the hadronic phase is interesting. The calculation makes use of transport theory mostly used for physical chemistry and solid state physics, and involves QCD and QCD-inspired models with field-theoretical methods. It may lead to the confirmation of a universal lower bound for dissipation processes that was constructed from string theory, and can possibly underline the discovery of the most ideal fluid in nature at RHIC. Furthermore, the result obtained a systems of hadrons and quarks can be compared to the behavior of ultra-cold atoms. Thus, our goal is the calculation of transport coefficients of hot and dense QCD-matter, where the focus is on shear viscosity.

After this introduction, chapter 2 will introduce the Nambu-Jona-Lasinio model in its version for two quark flavors. The advantage of this model is that there is a hadronic phase at low temperatures and chemical potentials, dominated by pions, and a quark phase at high temperatures and chemical potentials. This model is able to describe the two phases as well as the crossover region. The model will be discussed in the usual approximation scheme in a detailedness that is necessary for the further investigations of transport properties. More emphasis is spent on the extensions beyond this approximations, which are necessary for the Green-Kubo formalism.

Chapter 3 is dedicated to transport phenomena. Because transport processes are not so common in high-energy physics as in other fields, and as textbooks that deal with transport theory are not adapted to the context of heavy-ion collisions, some more space is spent on this topic. We begin with a review of the concept of hydrodynamics and show the different methods to calculate transport coefficients, where we proceed in an order that is inverse to the historical one: We begin with the exact formulation in terms of time-correlation functions and show the Green-Kubo formulas, we continue with the relativistic kinetic theory which is accurate in dilute gases, and end up with the simple estimate that were derived the earliest. In the end of the chapter, one finds a general perspective on transport and a review of the different concepts of (ideal) fluidity.

After that, we investigate spectral functions in chapter 4, which are essential in the Kubo formula for shear viscosity. After a short overview over general properties, a review about different methods is given which are used to calculate spectral functions in practice. We demonstrate that none of these methods is suitable for the application in the field theory and the approximation scheme we are interested in, and develop a new method. After some examples for a possible realization of the self-energy parametrization method, we apply the new method to the Nambu-Jona-Lasinio model and calculate the quark spectral function.

The theoretical concept of transport phenomena, together with the microscopic description from the Nambu-Jona-Lasinio model, allows the calculation of the shear viscosity. The different approaches that are used are explained in chapter 5. We begin with a kinetic theory of quarks, which is not the most reliable, but the most direct transport phenomenon that can be studied

within the model. After that, we perform calculations of transport in pion gases, where we use the Nambu-Jona-Lasinio model as well as other theoretical descriptions of pions. We then leave the kinetic derivation of shear viscosity and switch to the Green-Kubo method. We first use a diagrammatic expansion scheme that leads to some viscosity contributions of mesons, which are essential at the critical end point of the phase diagram. In the end, using another expansion, we make use of the spectral function calculated with the self-energy parametrization method and calculate the shear viscosity in the quark phase.
A summary and an overview over the conclusions is given in chapter 6.

Chapter 2

Nambu-Jona-Lasinio model

The original work of Nambu and Jona-Lasinio [17, 18] was written in the pre-QCD era, where a field-theoretical description of nucleons was introduced inspired by the theory of superconductivity [60]. Later, the fermionic fields in the Lagrangian were used to describe quarks, leading to a low-energy effective theory for strongly interacting fermions, incorporating additional quantum numbers, i.e. color degrees of freedom. This model has the same global symmetries as Quantum Chromodynamics, but no gluons and no confinement.

2.1 Basics

The original work inspired people to extend the model to different Nambu-Jona-Lasinio (NJL)-type models [61, 62, 63]. In the whole work, the version for quarks with two flavors ($N_f = 2$) and three colors ($N_c = 3$) is investigated.

2.1.1 The model

The Nambu-Jona-Lasinio model is defined by the Lagrangian[1]

$$\mathscr{L} = \bar{q}\left(i\partial\!\!\!/ - m_0\right)q + g\left[\left(\bar{q}q\right)^2 + \left(\bar{q}i\gamma_5\vec{\tau}q\right)^2\right]. \tag{2.1}$$

The quark field operator q carries Dirac-, color- and flavor indices, and thus has $4 \times 3 \times 2 = 24$ components. The symbol $\vec{\tau}$ is the vector of Pauli matrices in isospin space. Quarks and antiquarks interact by a point interaction, proportional to the coupling constant g. The mass m_0 denotes the bare quark mass, u and d quarks are degenerate[2].

The model has the same global symmetries as QCD. The Lagrangian is invariant under the transformation

$$q \rightarrow \exp(-i\alpha)q, \qquad \alpha \in \mathbb{R}. \tag{2.2}$$

This symmetry is associated with conservation of baryon number. $\mathscr{L}$ is invariant under the $SU_V(2)$ transformation

$$q \rightarrow \exp(-i\vec{\tau}\vec{\theta}_V/2)q, \qquad \vec{\theta}_V \in \mathbb{R}^2, \tag{2.3}$$

too. In the special case of $m_0 = 0$, it is also invariant under the $SU_A(2)$ rotation

$$q \rightarrow \exp(-i\gamma_5\vec{\tau}\vec{\theta}_A/2)q, \qquad \vec{\theta}_A \in \mathbb{R}^2. \tag{2.4}$$

In this case the Lagrangian possesses chiral symmetry, the symmetry under

$$SU_V(2) \otimes SU_A(2) \cong SU_L(2) \otimes SU_R(2) \tag{2.5}$$

transformations. For this reason, the case of vanishing bare quark mass is called *chiral limit*.

---

[1] The conventions that are used in the whole work are listed in Appendix A, notably $\hbar = c = 1$.

[2] The degeneracy of u and d is equivalent to the isospin limit.

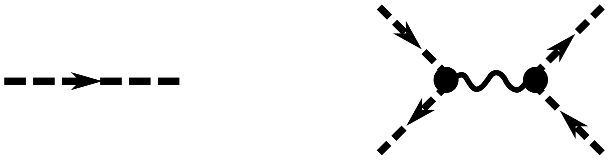

(a) (b)

Figure 2.1: Diagrammatic representation of elements of the Nambu-Jona-Lasinio model. The dashed line of diagram 2.1(a) symbolizes the bare quark propagator S_0, figure 2.1(b) denotes the bare quark vertex $\varGamma_M$, with $M \in \{\sigma, \pi^a\}$.

2.1.2 Diagrammatic techniques

The Lagrangian $\mathscr{L}$ from Eq. (2.1) consists of the free Dirac part

$$\mathscr{L}_{free} = \bar{q}\left(i\not{\partial} - m_0\right) q \tag{2.6}$$

and the interaction part

$$\mathscr{L}_{int} = g\left[\left(\bar{q}q\right)^2 + \left(\bar{q}i\gamma_5\vec{\tau}q\right)^2\right]. \tag{2.7}$$

There is one scalar interaction channel

$$(\bar{q}\varGamma_\sigma q)g(\bar{q}\varGamma_\sigma q) \tag{2.8}$$

with

$$\varGamma_\sigma = \mathbb{1}_{\text{Dirac}} \otimes \mathbb{1}_{\text{color}} \otimes \mathbb{1}_{\text{flavor}}, \tag{2.9}$$

and three pseudoscalar channels

$$(\bar{q}\varGamma_{\pi^a} q)g(\bar{q}\varGamma_{\pi^a} q) \tag{2.10}$$

with

$$\varGamma_{\pi^a} = \gamma_5 \otimes \mathbb{1}_{\text{color}} \otimes \tau^a. \tag{2.11}$$

In terms of Feynman diagrams, we draw the building blocks of the model according to the nomenclature shown in figure 2.1. The bare Matsubara propagator S_0 at temperature T in momentum space is given by

$$S_0(i\omega_p, \mathbf{p}) = \frac{1}{\gamma_0 i\omega_p - \boldsymbol{\gamma}\cdot\mathbf{p} - m_0} \tag{2.12}$$

where $i\omega_p \in \{(2n+1)i\pi T,\, n \in \mathbb{Z}\}$ is a fermionic Matsubara frequency. The retarded and advanced free propagators S_0^R and S_0^A in momentum space are

$$S_0^{\overset{R}{A}}(p_0, \mathbf{p}) = \frac{1}{\not{p} - m_0 \pm i\,\mathrm{sgn}(p_0)\epsilon}. \tag{2.13}$$

This model is designed to study the strong coupling regime: large values for the NJL coupling constant g are interesting. Perturbative techniques will fail far from the free theory, which gives rise to the methods discussed in the following sections.
Since this interaction corresponds to a nonrenormalizable theory (see e.g. [64]), the coupling is dimensionful and appearing integrals will be divergent. Therefore, a regularization scheme is needed.

2.2 Quarks in Hartree approximation

2.2.1 Approximation scheme

The most common approximation scheme in the two-flavor NJL model is mean field theory, which, as we will show, correspond to Hartree approximation. There exists an illustrative way of deriving the appropriate equations, which is presented first. A more systematic explanation is given, too, which is useful for further investigations in this chapter.

Mean field approximation

For the mean field expansion, we write the operator products in the Lagrangian (2.1) as its mean value plus a correction,

$$\bar{q}\Gamma_M q = \langle \bar{q}\Gamma_M q \rangle + \delta_M. \tag{2.14}$$

The scalar average $\langle \bar{q}\Gamma_\sigma q\rangle$ is called the *quark condensate*. With help of this decomposition, the quartic interaction terms become

$$(\bar{q}\Gamma_M q)^2 = -\langle \bar{q}\Gamma_M q\rangle^2 + 2\langle \bar{q}\Gamma_M q\rangle \bar{q}\Gamma_M q + \delta_M^2, \tag{2.15}$$

which leads to a Lagrangian in terms of quark condensates,

$$\mathscr{L} = \bar{q}\left(i\partial\!\!\!/ - m_0 + \sum_M 2g\langle \bar{q}\Gamma_M q\rangle \right) q + \sum_M \left(g\langle \bar{q}\Gamma_M q\rangle^2 + \delta_M^2 \right). \tag{2.16}$$

The pseudoscalar quark condensates $\langle \bar{q}i\gamma_5\tau^a q\rangle$ is only present if parity is spontaneously broken, which is not the case for all investigations in this work. Thus, only the scalar quark condensate can exhibit a nonzero value. The mean field approximation is taken if one neglects terms of order δ_M^2. Making use of these circumstances, we obtain finally the mean field Lagrangian of the Nambu-Jona-Lasinio model.

$$\mathscr{L}_{\mathrm{mf}} = \bar{q}\left(i\partial\!\!\!/ - m_0 + 2g\langle \bar{q}q\rangle \right) q + g\langle \bar{q}q\rangle^2 \tag{2.17}$$

It is the Lagrangian of a free quark system without interaction, each quark carrying the mass

$$m_H = m_0 - 2g\langle \bar{q}q\rangle, \tag{2.18}$$

where m_H is called the *Hartree mass*. So, the NJL model in mean field replaces the free bare quarks by effective quarks with a real, scalar, constant self-energy $-2g\langle \bar{q}q\rangle$ which is exactly the same as speaking of an effective mass. The effective degrees of freedom can be seen as constituent quarks.

Leading order $1/N_c$ expansion

The more systematic way of motivating NJL Hartree approximation is the expansion in the inverse number of colors $1/N_c$. Of course, in nature and for any practical calculation, the number of colors is three and therefore fixed. However, one can imagine to take $1/3$ as small number and expand in powers of it. This idea, closely related to the $1/N$ expansion in the $O(N)$-model, gives rise to the derivation of the Hartree gap equation.

First ingredient of this construction is the functional Φ, which is the reason to call the method Φ-derivable theory [65, 66]. The functional contains all closed two-particle-irreducible diagrams of the NJL Lagrangian [67]. All appearing propagator lines are understood to be the dressed ones. The thermodynamic potential per volume Ω is related to the functional Φ by

$$\Omega = i\mathcal{Tr}\ln\left(iS^{-1}\right) + \mathcal{Tr}\left(\Sigma iS\right) + \Phi(S), \tag{2.19}$$

where Σ is the self-energy: $S^{-1} = S_0^{-1} - \Sigma$. The trace $\mathcal{Tr}$ denotes a trace over all internal degrees of freedom, including momentum or coordinate space integrals. The self-energy Σ and the dressed Green's function S can be derived by the minimization of Ω. From the functional stationarity condition $\delta\Omega/\delta(iS) = 0$, one finds

$$\Sigma = -\frac{\delta\Phi}{\delta(iS)}. \tag{2.20}$$

This derivative can be associated with cutting quark lines at all possible places. Starting from the Φ-derivable method, an approximation scheme is obtained by restricting Φ to a finite set of diagrams. This can be done by ordering in powers of $1/N_c$. One can derive the order in $1/N_c$ of a given diagram using the following rules.

The bare propagator iS_0 is defined to be of order $(1/N_c)^0$. The NJL four-point interaction is of order $(1/N_c)^1$. For each closed quark loop in the diagram, a factor proportional to the number of color arises, so a factor of $(1/N_c)^{-1}$ has to be multiplied.

Making use of these factors, the leading order diagram, proportional to $(1/N_c)^{-1}$, is the "glasses"-diagram shown in Fig. 2.2(a). By cutting the dressed quark lines, one obtains the self-energy shown in Fig. 2.2(b).

(a) (b)

Figure 2.2: Diagram 2.2(a) contributes to the Φ-functional of order $(1/N_c)^{-1}$. By cutting one fermion line, one obtains figure 2.2(b), the self-energy contribution of the quarks.

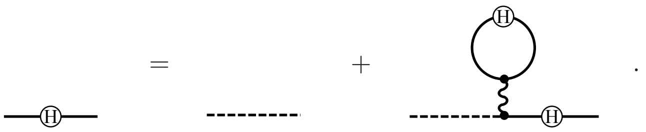

Figure 2.3: Gap equation in Hartree approximation. The dashed line correspond to the bare propagator S_0, the solid line indicated with 'H' correspond to the Hartree propagator S_H.

2.2.2 Gap equation

The thermodynamic potential per volume for the Φ-functional containing the glasses diagram can be calculated using expression (2.19). We now already from Eq. (2.17) and (2.18) that the Hartree quark propagator S_H is the propagator of a free particle with mass m_H. This leads to the equation

$$\begin{aligned} \Omega_H = & - T \sum_{i\omega_k} \int \frac{\mathrm{d}^3 k}{(2\pi)^3} \ln\det S_H^{-1}(i\omega_k + \mu, \mathbf{k}) - T \sum_{i\omega_k} \int \frac{\mathrm{d}^3 k}{(2\pi)^3} \mathrm{Tr}\big[\Sigma_H S_H(i\omega_k + \mu, \mathbf{k})\big] \\ & - \frac{1}{2} \sum_M 2g \left\{ T \sum_{i\omega_k} \int \frac{\mathrm{d}^3 k}{(2\pi)^3} \mathrm{Tr}\big[\Gamma_M S_H(i\omega_k + \mu, \mathbf{k})\big] \right\}^2 . \end{aligned} \tag{2.21}$$

The analytic steps which leads to a simplification of the equation are shown in Appendix B.5. The resulting thermodynamic potential per volume Ω_H reads

$$\begin{aligned} \Omega_H = \frac{(m_H - m_0)^2}{4g} - 2N_c N_f \int \frac{\mathrm{d}^3 k}{(2\pi)^3} \Big\{ & E_k + T \ln\left(1 + \exp\left(-\frac{E_k - \mu}{T}\right)\right) \\ & + T \ln\left(1 + \exp\left(-\frac{E_k + \mu}{T}\right)\right)\Big\} , \end{aligned} \tag{2.22}$$

which is the potential of a free gas of $N_c \times N_f$ fermions plus a mass-dependent shift. The energy E_k is the energy of a Hartree quark with momentum $\mathbf{k}$, $E_k^2 = m_H^2 + \mathbf{k}^2$. The self-energy can be expressed using cutting rules, ending up with the equation

$$-S_H^{-1} = -S_0^{-1} + \Sigma_H . \tag{2.23}$$

Equivalently, just by multiplying S_0 from the left and S_H from the right, the diagrammatic equation can take the form Fig. 2.3. The Hartree self-energy Σ_H can be calculated from its diagram in Fig. (2.3).

$$\Sigma_H = T \sum_{i\omega_k} \int \frac{\mathrm{d}^3 k}{(2\pi)^3} \mathrm{Tr}\left[2g\Gamma_\sigma S_H(i\omega_k, \vec{k})\right] \tag{2.24}$$

The same result can be obtained from the explicit expression of the thermodynamic potential by deriving with respect to m_H and imposing the stationarity condition. The functional derivative

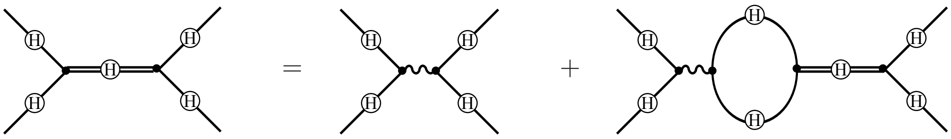

Figure 2.4: Bethe-Salpeter equation for quark-antiquark scattering. The solution of the Hartree gap equation S_H enters in the calculation.

of the thermodynamic potential per volume with respect to the dressed propagator can be written as derivative with respect to the mass parameter, and the stationarity condition reads

$$\frac{\mathrm{d}}{\mathrm{d}m_H}\Omega_H = 0. \tag{2.25}$$

The algebraic version of the diagrammatic gap equation can be expressed in terms of an elementary integral,

$$m_H = m_0 + 8N_cN_f g m_H iI_1, \tag{2.26}$$

where the constant iI_1 is the quark loop integral appearing in the Hartree self energy Σ_H,

$$iI_1 = T\sum_{i\omega_k}\int \frac{\mathrm{d}^3k}{(2\pi)^3}\frac{1}{(i\omega_k+\mu)^2-\mathbf{k}^2-m_H^2}. \tag{2.27}$$

It is shown in Appendix B.2 how to simplify the expression in the case of a Hartree propagator in the loop, leading to

$$iI_1 = \frac{4\pi}{(2\pi)^3}\int_0^\infty \mathrm{d}|\mathbf{k}|\frac{1}{2E_k}\left(1-n_F(E_k-\mu)-n_F(E_k+\mu)\right). \tag{2.28}$$

This 1-dimensional integral contains the Fermi distribution function n_F, and the energy E_k, where $E_k^2 = m_H^2 + \mathbf{k}^2$. The discussion of solutions of the gap equation (2.26) is postponed, since all parameters of $\mathscr{L}$ are not fixed yet.

2.3 Mesons in Random Phase approximation

The description of meson properties is one of the striking features of the Nambu-Jona-Lasinio model. As the only fundamental degrees of freedom in the Lagrangian are the quark fields, mesons will appear as fermion-antifermion correlations.

2.3.1 Bethe-Salpeter equation

The starting point for the description of mesons is the Bethe-Salpeter equation for quark-antiquark scattering shown in Fig. 2.4. The meson propagator can be extracted from the quark-antiquark scattering matrix

$$\hat{T}_M = \hat{K}_M + \hat{K}_M\left(\hat{\Pi}_M\right)\hat{T}_M, \tag{2.29}$$

with the bare scattering kernel

$$\hat{K}_M = \Gamma_M 2g\Gamma_M. \tag{2.30}$$

and the polarization loop $\hat{\Pi}_M$. Because of isospin, the different channels M do not mix. We separate the polarization loop Π_M from its external structure,

$$\Pi_M = \Gamma_M\hat{\Pi}_M\Gamma_M, \tag{2.31}$$

and define a new the scattering matrix in terms of a new scalar function D_M,

$$\hat{T} = -\Gamma_M D_M\Gamma_M. \tag{2.32}$$

We can now substitute the iteration of the scattering scattering kernel by the scalar equation

$$D_M(i\omega_q, \mathbf{q}) = \frac{-2g}{1 - 2g\mathit{\Pi}_M(i\omega_q, \mathbf{q})}. \tag{2.33}$$

$\mathit{\Pi}_M$ is the truncated quark loop with external vertices $\mathit{\Gamma}_M$,

$$\mathit{\Pi}_M(i\omega_q, \mathbf{q}) = -T\sum_{i\omega_k}\int\frac{\mathrm{d}^3k}{(2\pi)^3}\mathrm{Tr}\left[S(i\omega_q + i\omega_k, \mathbf{q}+\mathbf{k})\mathit{\Gamma}_M S(i\omega_k, \mathbf{k})\mathit{\Gamma}_M\right]. \tag{2.34}$$

It is shown in Appendix B.3 how to decompose $\mathit{\Pi}_M$ in terms of elementary integrals,

$$\mathit{\Pi}_{\pi^i} = 4N_cN_f iI_1 - 2N_cN_f(i\omega_q^2 - \mathbf{q}^2)iI(i\omega_q, \mathbf{q}) \tag{2.35}$$

$$\mathit{\Pi}_{\sigma} = 4N_cN_f iI_1 - 2N_cN_f(i\omega_q^2 - \mathbf{q}^2 - 4m_H^2)iI(i\omega_q, \mathbf{q}). \tag{2.36}$$

The new function $iI(q)$ is the elementary integral

$$iI(i\omega_q, \mathbf{q}) = -\int\frac{\mathrm{d}^3k}{(2\pi)^3}T\sum_{i\omega_k}\frac{1}{[(i\omega_k+\mu) - \mathbf{k}^2 - m_H^2][(i\omega_k + i\omega_q + \mu) - (\mathbf{k}+\mathbf{q})^2 - m_H^2]}. \tag{2.37}$$

In a diagrammatic interpretation of Eq. (2.33), the new quantity D_M is a meson that is coupled to quarks on both sides,

$$D_M = g_{Mqq}\mathcal{D}_M g_{Mqq}. \tag{2.38}$$

However, we call D_M the meson propagator of meson M and not the quantity $\mathcal{D}_M$. The reason is that the decomposition in Eq. (2.38) is artificial, guided by the interpretation of the quark scattering matrix. In all diagrammatic evaluations, only D_M enters. From the quantum number of $\mathit{\Gamma}_M$, one can see that $M = \sigma$ is a scalar meson and $M = \pi^i$ forms a pseudoscalar degenerate triplet. So we call D_σ the propagator of the σ-meson and D_π the propagator of the pions.

2.3.2 Meson mass

The mass of the meson can be extracted from the retarded meson propagator $D_M^R(q_0, \mathbf{q})$. The retarded propagator is obtained by analytic continuation of the Matsubara propagator calculated in the previous section,

$$D_M^R(q_0, \mathbf{q}) = D_M(i\omega_q \to q_0 + i\epsilon, \mathbf{q}). \tag{2.39}$$

The advanced propagator is obtained similarly, but by the continuation $i\omega_q \to q_0 - i\epsilon$, so with the complex conjugated argument. These propagators are obtained from the retarded and advanced polarization, which can be calculated from Eqs. (2.35) and (2.36). The corresponding elementary integral iI for real external 0-momenta reads

$$\begin{aligned} iI(q_0 \pm i\epsilon, \mathbf{q}) = \int\frac{\mathrm{d}^3k}{(2\pi)^3}\Bigg\{&\left(\frac{1}{E_k} - \frac{n_F(E_k-\mu) + n_F(E_k+\mu)}{2E_kE_{kq}}s_E\right)\frac{1}{(q_0 \pm i\epsilon)^2 - s_E^2} \\ &- \frac{n_F(E_k-\mu) + n_F(E_k+\mu)}{2E_kE_{kq}}d_E\frac{1}{(q_0 \pm i\epsilon)^2 - d_E^2}\Bigg\}, \end{aligned} \tag{2.40}$$

the details of the calculation is found in appendix B.4. The quantities s_E and d_E are the sum and the difference of the energies E_{kq} and E_k, respectively.

As the retarded propagator of a free boson has a singularity at its mass, we can try to approximate D_M by a free boson propagator times the coupling constant squared,

$$D_M^R(q_0, \mathbf{q}) \approx \frac{\left(g_{Mqq}\right)^2}{q_0^2 - \mathbf{q}^2 - m_M^2}. \tag{2.41}$$

We suppressed the infinitesimal imaginary part in the expression of the retarded propagator on the right hand side for simplicity. This condition is sufficient to determine the *meson mass* m_M and the *meson-quark-quark coupling constant* g_{Mqq} if the propagator D_M^R has one first-order pole in q^2 on the real axis. Equivalently, one can say that the inverse propagator has a zero at the mass. This will not be the case for all possible situations we are investigating. A generalized version of the above condition can be formulated concentrating on the real part of the inverse propagator,

$$1 - 2g\mathrm{Re}\mathit{\Pi}_M(q_0 = \pm\sqrt{m_M^2 + \mathbf{q}^2}, \mathbf{q}) = 0. \tag{2.42}$$

The mass m_M can depend on temperature T, quark chemical potential μ and 3-momentum $\mathbf{q}$ [3]. The on-shell coupling constant g_{Mqq} is determined by the residue of the pole,

$$g_{Mqq} = \left(\frac{\mathrm{dRe}\mathit{\Pi}_M}{\mathrm{d}(q_0^2)}\right)^{-\frac{1}{2}}\Bigg|_{q_0^2 = m_M^2 + \mathbf{q}^2}. \tag{2.43}$$

The replacement of the propagator by the form of Eq. (2.41) is called the *pole approximation.* It is possible to make the relation of Eq. (2.41) an exact statement allowing g_{Mqq} to be momentum dependent,

$$D_M^R(q_0, \mathbf{q}) = \frac{g_{Mqq}(q_0, \mathbf{q})^2}{q_0^2 - \mathbf{q}^2 - m_M^2}. \tag{2.44}$$

Another possible extension of the pole approximation is the *resonance approximation.* In this generalization, the propagator has also a finite imaginary part $\mathit{\Upsilon}_M$,

$$D_M^R(q_0, \mathbf{q}) \approx \frac{g_{Mqq}^2}{q_0^2 - \mathbf{q}^2 - m_M^2 + i\mathrm{sgn}(q_0)\mathit{\Upsilon}_M}, \tag{2.45}$$

where the new parameter $\mathit{\Upsilon}_M$ is related to the on-shell width of the propagator. It can be calculated using the relation

$$\mathit{\Upsilon}_M = g_{Mqq}^2 \mathrm{Im}\mathit{\Pi}_M\left(q_0 = +\sqrt{\mathbf{q}^2 + m_M^2}, \mathbf{q}\right). \tag{2.46}$$

This width and the mass m_M can be related to the usual width of a Breit-Wigner parametrization

$$D_M^{\text{Breit-Wigner}\,R}(q_0, \mathbf{q}) = \frac{1}{q_0^2 - \mathbf{q}^2 - (M_M^{\text{Breit-Wigner}} - i\mathrm{sgn}(q_0)\mathit{\Gamma}_M^{\text{Breit-Wigner}})^2}. \tag{2.47}$$

The translation prescription reads

$$m_M^2 = M_M^{\text{Breit-Wigner}2} - \mathit{\Gamma}_M^{\text{Breit-Wigner}2}, \quad \mathit{\Upsilon}_M = 2M_M^{\text{Breit-Wigner}}\mathit{\Gamma}_M^{\text{Breit-Wigner}}. \tag{2.48}$$

The presented approximations for meson propagators are not only justifiable approximation methods for the full random phase approximation. They also represent possibilities to characterize quark-antiquark scattering just by the two (three if a width $\mathit{\Upsilon}_M$ is present) variables of the meson propagator parametrization.

2.4 Regularization in standard approximation

The integrals appearing in the evaluation of the NJL model in standard approximation (Hartree and RPA) are ultraviolet divergent. Due to the pointlike interaction in the NJL Lagrangian, the model is not renormalizable. Thus it will be necessary to construct a regularization scheme that allows the calculation of thermodynamic potential per volume $\mathit{\Omega}_H$, Hartree self-energy $\mathit{\Sigma}_H$ and polarization loop $\mathit{\Pi}_M$.

Concentrating on the finite-temperature versions of Hartree- and RPA integrals iI_1 and iI, it is useful to analyze these two cases more in detail. The formulations of these integrals in Eqs. (2.28) and (2.40) show the thermal distribution function n_F, which is exponentially decreasing for high energies. These contributions are finite, and they do not need a regularization. We use this observation to separate the integrals in a vacuum part and a medium part,

$$\int \frac{\mathrm{d}^3k}{(2\pi)^3} f(k) = \int \frac{\mathrm{d}^3k}{(2\pi)^3} f_{\mathrm{vac}}(k) + \int \frac{\mathrm{d}^3k}{(2\pi)^3} f_{\mathrm{med}}. \tag{2.49}$$

---

[3] In vacuum, J_M can only depend on q^2, so m_M is independent of $\mathbf{q}$.

We define the part that does not depend on T and μ explicitly as the vacuum part, it can be constructed by

$$\lim_{T\to 0}\lim_{\mu\to 0} f(k) = f_{\text{vac}}(k), \tag{2.50}$$

whereas the remaining terms are defined to be the medium parts. One observes that only the vacuum contribution is divergent. So, whenever it is possible to decompose the integral in a thermal and a vacuum term, one has the possibility to apply the regularization procedure only to the divergent vacuum part. Another observation in the Minkowski formulation of the integrals is the different role of real and imaginary part of the integrand[4],

$$\int \frac{\mathrm{d}^3k}{(2\pi)^3} f(k) = \int \frac{\mathrm{d}^3k}{(2\pi)^3} \mathrm{Re}f(k) + i\int \frac{\mathrm{d}^3k}{(2\pi)^3} \mathrm{Im}f. \tag{2.51}$$

The integral over the imaginary part of $f(k)$ is well defined, only the real part of the integrand diverges. A way of regularizing the integrals can be constructed by only apply the chosen scheme to the real part.

There are different ways to treat the divergent integrals in the Nambu-Jona-Lasinio model. Each regularization scheme has certain advantages and disadvantages. In the following paragraphs the two methods used in this work are explained.

2.4.1 3-dimensional cut-off

In standard approximation, the evaluation of finite-temperature elementary integrals iI_1 and iI involves a Matsubara sum over complex frequencies and an integral over 3-momentum. The discrete sum can be performed analytically in the case of free propagators, as shown in Appendix B. This first summation avoids regularization problems, they are postponed in the remaining integral over 3-momentum. The divergence of the integrals arises from the asymptotic behavior at high 3-momentum. If the integration is cut at a finite value of absolute momentum,

$$\int \frac{\mathrm{d}^3k}{(2\pi)^3} f(k) = \int \mathrm{d}\Omega \int_0^\infty \mathrm{d}k f(k) \to \int \mathrm{d}\Omega \int_0^{\Lambda_q} \mathrm{d}k f(k), \tag{2.52}$$

the result is also finite.

A main disadvantage of this procedure is the loss of boost invariance, i.e. Lorentz covariance. This problem becomes manifest especially in the case of iI, thus in the calculation of the meson propagator. Even in vacuum, the meson propagator $D_M(q_0, \mathbf{q})$ will not depend on q^2, but on q_0 and $|\mathbf{q}|$ separately. This leads to a considerable and unphysical dependency of the meson mass m_M on the momentum $|\mathbf{q}|$. Sometimes, this problem is avoided by only calculating mesons at rest, but this limits the possible applications dramatically.

2.4.2 Pauli-Villars regularization

An alternative scheme is the Paul-Villars regularization. To introduce this scheme not in the historical context [68] but as a mathematical tool for our purposes, we first revisit the 3-momentum cut-off method. The sharp cut-off of the integral as it was introduced in Eq. (2.52) can also be written as

$$\int \mathrm{d}\Omega \int_0^{\Lambda_q} \mathrm{d}k f(k) = \int \mathrm{d}\Omega \int_0^\infty \mathrm{d}k \left\{ f(k) - \theta(k-\Lambda_q) f(k) \right\}. \tag{2.53}$$

So in principle the 3-momentum cut-off subtracts a function with the same values as $f(k)$ at high momentum, regularizing the integral and keeping the low-momentum behavior. It is not necessary to subtract the function $f(k)$ completely at high energy - a function is sufficient with the same asymptotic behavior as $f(k)$ chosen such that the difference is integrable. For example, instead of $\theta(k-\Lambda_q)$ one could replace the step function by a smooth function and obtain a smooth 3-momentum cut-off.

It was discussed in the previous subsection that the disadvantage of the sharp 3-momentum cut-off is the breaking of Lorentz covariance. In equation (2.53), we see that the violation of boost

---

[4] Of course, only iI can exhibit a finite imaginary part, whereas iI_1 is always real.

invariance is due to the factor $\theta(k-\Lambda_q)$ in front of the regulator term. If one could find another regulating subtraction term $\tilde{f}(k)$,

$$\int \mathrm{d}\Omega \int_0^\infty \mathrm{d}k f(k) \rightarrow \int \mathrm{d}\Omega \int_0^\infty \mathrm{d}k \left\{ f(k) - \tilde{f}(k) \right\}, \tag{2.54}$$

that has the same invariance as $f(k)$, one could avoid this problem.
The remaining task is the construction of the function $\tilde{f}(k)$. The Pauli-Villars scheme used here is based on the replacement of the mass[5] m. As the integrand $f(k)$ in iI_1 and iI depends on the mass parameter, a suitable substitution lead to an appropriate compensation term. The regularization procedure can then be written as

$$\int \frac{\mathrm{d}^3k}{(2\pi)^3} f_m(k) \rightarrow \int \frac{\mathrm{d}^3k}{(2\pi)^3} \sum_{j=0}^{N_{PV}} c_j f_{m_j}(k). \tag{2.55}$$

For our case of NJL standard approximation, the elementary integrals iI_1 and iI are sufficiently regularized with two additional regulators $N_{PV}=2$. The scheme used in this work is characterized by the following choice of c_j and m_j,

$$c_0 = +1, \quad c_1 = -2, \quad c_2 = +1, \qquad m_j^2 = m^2 + j\Lambda_{PV}^2. \tag{2.56}$$

The Pauli-Villars method is an appropriate scheme to study mesons with finite 3-momentum, whereas a sharp cut-off produced regularization artifacts. However, also the subtraction of asymptotically similar terms has its limitations. It is known that the positivity of meson spectra is violated if Π_M is regulated within a Pauli-Villars scheme. A more severe limitation arises beyond NJL standard approximation. As soon as the dressed Green's functions are no longer free propagators with a mass m, the construction procedure of regulator terms breaks down.

2.5 Properties in mean field

The Nambu-Jona-Lasinio model has the same global symmetries as QCD, which result in the fact that theorems that rely on these symmetries of a quantum field theory are valid for both. In the following three theorems based on chiral symmetry are summarized.

2.5.1 Chiral theorems

Goldstone theorem

The global chiral symmetry of the Nambu-Jona-Lasinio Lagrangian in the chiral limit ($m_0 = 0$) is spontaneously broken in vacuum. This implies the existence of a gapless Nambu-Goldstone boson. For mean-field, it turns out that this is the RPA pion. The fact that the pion is massless can be written according to the mass definition of RPA mesons in Eq. (2.42),

$$1 - 2gJ_\pi(q^2=0) = 0. \tag{2.57}$$

This theorem is satisfied because of the chiral Ward identities. They are fulfilled for the pion quark scattering because the scattering kernel in the definition of the RPA meson propagators was constructed from the Φ-functional.

Goldberger-Treiman relation

In the chiral limit the pion decay constant f_π obeys the Goldberger-Treiman relation

$$f_\pi g_{\pi qq} = m_H. \tag{2.58}$$

The on-shell pion-quark coupling $g_{\pi qq}$ is defined in Eq. (2.43). The decay constant describes the weak pion decay [64]. Empirically, the pion decay constant is found to be $f_\pi = 93\,\mathrm{MeV}$.

---

[5] As this method relies primarily on the existence of a mass m and not on the concrete solution of the Hartree gap equation m_H, we formulate these lines in the more general way, though for NJL in standard approximation m_H is used.

set	Λ_q[MeV]	$g\Lambda_q^2$	m_0[MeV]	m_H^{vac}[MeV]
1	664.3	2.06	5.0	300
2	587.9	2.44	5.6	400
3	569.3	2.81	5.5	500
4	568.6	3.17	5.1	600

Table 2.1: Parameters for 3-momentum cut-off regularization scheme. The fitting is done to reproduce $m_\pi = 135.0$MeV and $f_\pi = 92.4$MeV in standard approximation. This parameter table is taken from Ref. [63].

set	Λ_{PV} [MeV]	$g\Lambda_{PV}^2$	m_0 [MeV]	m_H^{vac} [MeV]	f_π [MeV]
1	800.0	2.90	6.13	260	93.6
2	800.0	3.07	6.40	304	100.6
3	800.0	3.49	6.77	396	111.1
4	820.0	3.70	6.70	446	117.0
5	852.0	4.16	6.54	550	126.0

Table 2.2: Parameters for Pauli-Villars regularization scheme. The fitting is done to reproduce m_π and f_π in an extended approximation scheme. The RPA pion mass for all parameter sets is $m_\pi = 140.0$MeV, and the the resulting value of f_π in standard approximation is listed in the table. This parameter table is taken from [69].

Gell-Mann-Oakes-Renner relation

If a mass term in $\mathscr{L}$ breaks chiral symmetry explicitly, the dependency of m_π on the quark condensate obeys the equation

$$m_\pi^2 f_\pi^2 = -m_0 \langle \bar{q}q \rangle + O(m_0^2). \tag{2.59}$$

The mass m_π is the pole mass deduced from the RPA meson propagator as defined in Eq. (2.42), and f_π again is the pion decay constant.

2.5.2 Parameters

The free parameters of the Lagrangian m_0 and g, together with the additional regularization parameter Λ_q or Λ_{PV}, are usually determined by fitting observables in vacuum. The pion mass and the pion decay constant are often taken as a reference. The third condition is a reasonable value for the quark condensate.

The focus here will not be on parameter fits. We use parameter sets from literature, one table for sharp 3-momentum cut-off parametrization (Tab. 2.1, from [63]), and another one for Pauli-Villars regularization (Tab. 2.2, from [69]). In the latter, only the first parameter set is fitted to the given values in standard approximation, while the other four sets are fitted in a different scheme. All nine parameter sets that are presented in the table can either be used with the same treatment of vacuum and medium part, or with the procedure that is only applied to the vacuum contribution of the integrands. Additionally, it is possible to study all parameter sets in chiral limit, i.e. $m_0 = 0$.

2.5.3 NJL matter in medium

Properties of quarks and mesons in medium

The thermodynamic potential per volume Ω is minimized with respect to the constituent quark mass m_H for different values of T and μ. The chiral symmetry is spontaneously broken in vacuum, thus m_H is large compared to m_0 at low temperature and chemical potential. At higher values of T and μ, the symmetry is restored. This can be a phase transition of first or second order in the

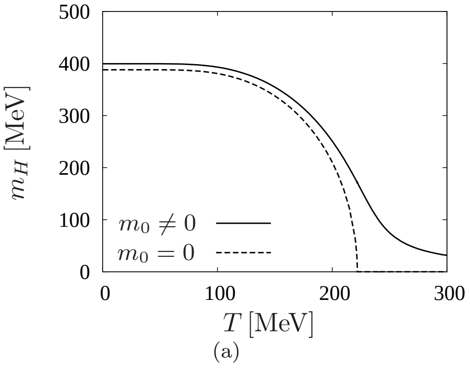

(a) (b)

Figure 2.5: Hartree quark mass as a function of temperature T for $\mu = 0$ (left), and as a function of chemical potential at $T = 0$ (right). Parameters from Tab. 2.1 No 2. are shown in solid lines, same parameters in the chiral limit are plotted with dashed lines.

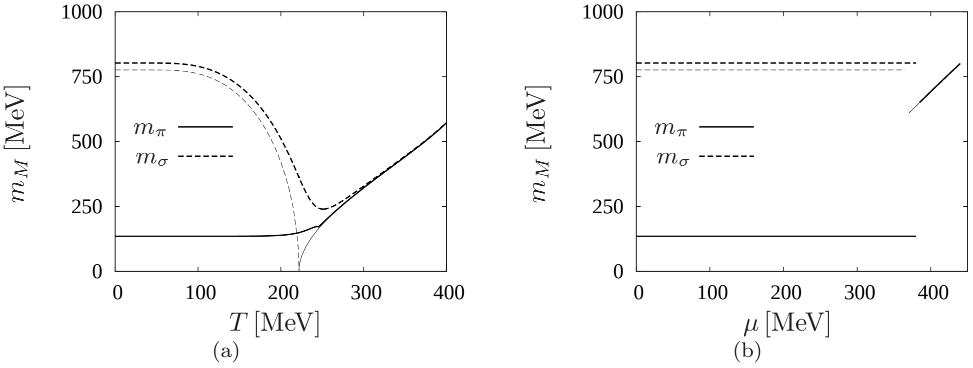

(a) (b)

Figure 2.6: Medium dependent meson masses: Solid lines correspond to m_π, dashed lines correspond to m_σ. Bold lines represent results at finite m_0 whereas thin lines show calculations in the chiral limit. Parameters from Tab. 2.1 No 2.

chiral limit ($m_0 = 0$), or a crossover for finite bare quark masses. This different behavior of Ω and the resulting phase transitions are extensively discussed in literature (see for example [63]), thus we limit our discussion of chiral symmetry restoration in the NJL model to the properties that are essential for the understanding of the result of this work.

In Fig. 2.5(a) the mass m_H is shown as a function of temperature in the chirally symmetric case and in the explicitly broken case. In both cases, the constituent quark mass is rather large compared to the bare quark mass in vacuum. At higher temperatures, the mass falls continuously to smaller values. In the chiral limit, the second-order phase transition happens at the point where m_H reaches the zero axis. For varying chemical potential (Fig. 2.5(b)), the mass stays at its vacuum value[6] until the first-order phase transition happens. In the restored phase, the mass is small if $m_0 > 0$ and zero if $m_0 = 0$.

The meson masses at finite temperature and chemical potential shown in Fig. 2.6 have a different behavior. We first analyze the chiral limit. The pion is the Nambu-Goldstone boson of the spontaneously broken chiral symmetry and has zero mass m_π in vacuum. Its chiral partner, the σ-meson, has a mass m_σ different from m_π due to the broken symmetry: the mass of the scalar meson is exactly two times the Hartree quark mass m_H. At finite temperature, this situation changes when the second-order phase transition occurs at T_C. At T_C, the masses m_H, m_π and

---

[6] For $\mu < m_H$, m_H either has to be constant or has to jump. This can be seen from Eq. (2.22) in the case $T = 0$.

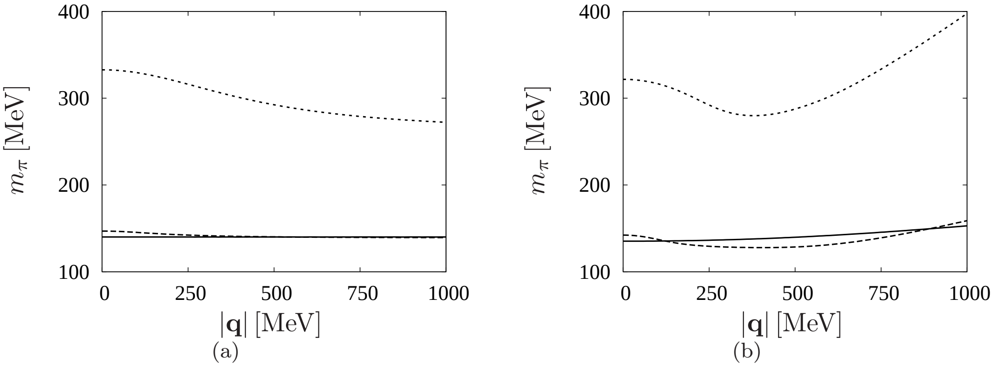

Figure 2.7: Pion mass m_π as a function of 3-momentum as defined in Eq. (2.42). The different lines correspond to different temperatures at zero chemical potential. (a) is calculated Pauli-Villars regularized with parameters from Tab. 2.2 No 2 at temperature $T = 0$ (solid), $T = 150\,\mathrm{MeV}$ (dashed), $T = 250\,\mathrm{MeV}$ (dotted). (b) is calculated with sharp 3-momentum cut-off with parameters from Tab. 2.1 No 2 at temperature $T = 0$ (solid), $T = 210\,\mathrm{MeV}$ (dashed), $T = 300\,\mathrm{MeV}$ (dotted).

m_σ are all zero. At higher temperatures, m_H is zero while m_π and m_σ are degenerate[7] and chiral symmetry is restored.

If a small bare quark mass m_0 is switched on, a few changes appear. m_π does not vanish in vacuum, but takes a small value compared to m_H. The mass of the scalar meson m_σ turns out to be slightly above the threshold $2m_H$. At finite μ and zero temperature, a similar behavior is observed, but with the first-order transition.

The meson mass in general is also a function of relative momentum between the particle and the thermal medium. This dependency of the pion mass is shown in Fig. 2.7. In vacuum, due to Lorentz covariance, the mass should be independent of $\mathbf{q}$ and only at finite temperature an effect may appear. But as the regularization scheme using a sharp 3-momentum cut-off (Fig. 2.7(b)) violates this symmetry, even in vacuum a momentum dependency arises as an artifact. This is not the case for the Lorentz covariant Pauli-Villars prescription (Fig. 2.7(a)). At finite temperature the meson mass has a momentum dependency as a medium effect: The pion mass drops at large momentum in the Pauli-Villars calculation. For small momenta, this behavior is also present in calculations using a sharp 3-momentum cut-off, but for higher values of $\mathbf{q}$ again the cut-off artifact is visible.

There are two important temperatures[8] in the meson mass function. The first is the dissociation temperature T_{diss} . For $T < T_{\mathrm{diss}}$, it is energetically possible that σ decays into two pions. At T_{diss}, this process is at the threshold $m_\sigma = 2m_\pi$. The other important temperature is the Mott temperature T_{Mott} . For temperatures higher than T_{Mott}, the pion is heavier than two constituent quarks. Because there is no confinement in Nambu-Jona-Lasinio model, the pion becomes unstable due to decays into two quarks in this region. The Mott temperature is defined by the relation $m_\pi = 2m_H$. Because in medium the mass depends on the relative momentum between the particle and the background medium, these two transitions are not single points, but regions in which the transition for a given momentum takes place.

The temperature dependency of the quark-meson coupling constants g_{Mqq} is shown in Fig. 2.8(a). The quark-pion coupling is larger than the coupling for the sigma meson in vacuum. If temperature T increases, the sigma coupling grows and the pion coupling decreases, leading to a crossing at temperatures slightly below the Mott transition. The asymptotic degeneracy of π and σ is achieved after the transition. The meson widths as functions of temperature are shown in the second figure, 2.8(b). The pion is stable in vacuum, hence the width Υ_π is zero. The σ, in contrast, has a finite width. The width of π stays zero up to the Mott transition, that is defined as the point where the pion becomes unstable. The width of σ increases slowly in the chirally

---

[7] This can be seen from Eq. (2.35) and (2.36).

[8] More precisely, there are two important lines in the $T-\mu$-plane separating two regions.

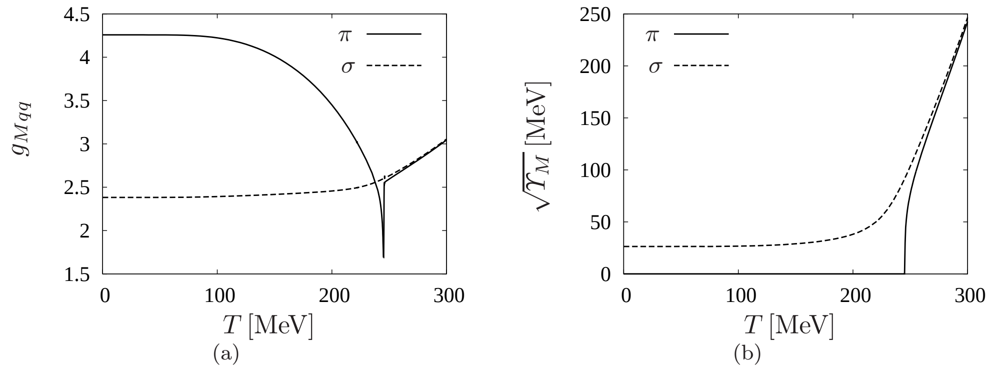

(a) (b)

Figure 2.8: Properties of π-meson (solid lines) and σ-meson (dashed line) at finite temperature and $\mu = 0$. The left figure shows the quark-meson coupling constant g_{Mqq}, the right figure the square-root of the propagator width Υ_M. Parameters from Tab. 2.1 No 2.

broken phase. In the restored phase, the width of both mesons increase quickly since the quark mass is very low and the meson masses are growing — the peaks are deeply in the continuum.

Thermodynamic quantities

The aim of this work is the description of strong interacting matter at high temperature and high densities. Such a material is characterized by its equilibrium properties and nonequilibrium properties. This section is dedicated to the equilibrium thermodynamic quantities of mean-field NJL. This topic is for example discussed in [63].
The pressure p in a uniform system is related to the grand canonical potential $\boldsymbol{\Omega}$ by the equation

$$\boldsymbol{\Omega}(T,\mu,V) = \Omega(T,\mu)V = -pV. \tag{2.60}$$

This means that the pressure p is simply the negative thermodynamic potential per volume, calculated from the Φ-functional in Sec. 2.2. The equilibrium state is the phase with maximal pressure p. As Ω is only defined up to a constant, one usually normalizes Ω (and p) in such a way that the pressure of the vacuum vanishes,

$$p(T=0,\mu=0) = 0. \tag{2.61}$$

Other important quantities are the entropy S and the entropy density s. They can be obtained from the thermodynamic potential Ω,

$$S = -\frac{\partial \boldsymbol{\Omega}}{\partial T}, \qquad s = -\frac{\partial \Omega}{\partial T} = \frac{\partial p}{\partial T}. \tag{2.62}$$

Similarly, the particle number N and its density n are calculated using the derivative with respect to the chemical potential μ,

$$N = -\frac{\partial \boldsymbol{\Omega}}{\partial \mu}, \qquad n = -\frac{\partial \Omega}{\partial \mu} = \frac{\partial p}{\partial \mu}. \tag{2.63}$$

With these terms, we calculate the internal energy E and the energy density ε,

$$E = \boldsymbol{\Omega} + TS + \mu N, \qquad \varepsilon = -p + Ts + \mu n. \tag{2.64}$$

Energy density plays an important role in nuclear astrophysics because the dependency of pressure, particle density and energy density defines the equation of state. For the question of transport and fluidity, entropy density is essential. Another thermodynamic quantity used in context of fluidity is the enthalpy density h. It is related to the functions above by the equation

$$H = E + pV = TS + \mu N, \qquad h = \varepsilon + p = Ts + \mu n. \tag{2.65}$$

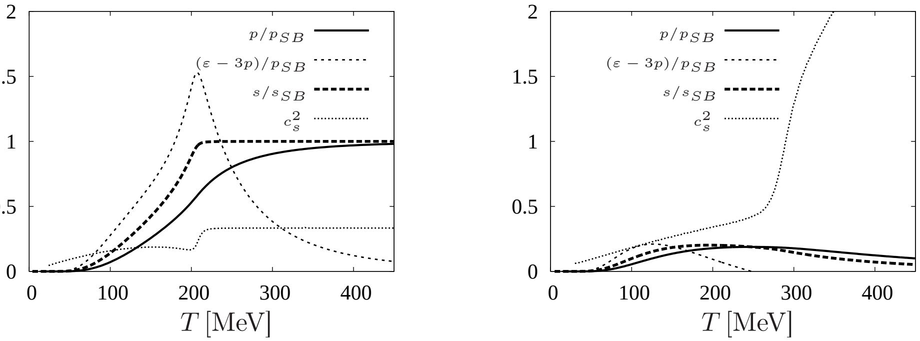

(a) (b)

Figure 2.9: Different thermodynamic quantities of mean field NJL as a function of temperature T for chemical potential $\mu = 0$. Parameters from Tab. 2.1 No 3: (a) only the vacuum terms are regularized, (b) vacuum and medium parts are regularized.

A quantity related to the equation of state is c_s, the speed of sound. This velocity can be deduced from the equation of state.

$$c_s^2 = \frac{\partial p}{\partial \epsilon} \tag{2.66}$$

An important system of reference is the ultra-relativistic fermion gas with $4 \times N_c \times N_f$ degrees of freedom. This Stefan-Boltzmann limit at $\mu = 0$ takes the exact values

$$p_{SB} = 4N_c N_f \frac{7\pi^2}{720} T^4, \tag{2.67}$$

$$s_{SB} = 4N_c N_f \frac{7\pi^2}{180} T^3, \tag{2.68}$$

$$n_{SB} = 0, \tag{2.69}$$

$$\varepsilon_{SB} = 3p_{SB}, \tag{2.70}$$

$$h_{SB} = 4p_{SB}, \tag{2.71}$$

$$c_{s,\,SB} = \frac{1}{\sqrt{3}}. \tag{2.72}$$

All quantities shown here should behave like such a conformal system at high temperatures. However, this Stefan-Boltzmann limit of thermodynamic quantities is only obtained if the medium part of the thermodynamic potential Ω is not affected by the regularization procedure (see Sec. 2.4 and Eq. (2.49)).

The temperature dependency of some of the presented quantities is shown in Fig. 2.9. Beside pressure p and entropy density s, also the difference $\epsilon - 3p$ is shown as a measure of deviation from the conformal limit. All quantities are normalized with the Stefan-Boltzmann values. Additionally, the square of speed of sound c_s is shown in the same plot. The lines in Fig. 2.9(a) are calculated using a regularization scheme which is only applied to the vacuum part. Entropy density s reaches its Stefan-Boltzmann-value shortly after the crossover, the pressure p approaches this limit also for large temperatures T. The normalized measure $\epsilon - 3p$ has a maximal value at the crossover and vanishes for high temperatures, as it should do. The speed of sound is low in the broken phase, has a kink at the crossover and attains the conformal value $c_s^2 = 1/3$ in the chirally restored phase. The same parameters in the same temperature range are shown in Fig. 2.9(b), but with regularized temperature dependent integrand part. The change in the behavior in this synopsis is obvious. Pressure and entropy density stay well below the conformal limit and are decreasing at high temperatures. This can be understood because the constant momentum cut-off erases more contributions the higher the temperature T becomes since the distribution functions n_F has more important ultraviolet parts for high temperatures than for lower ones. The

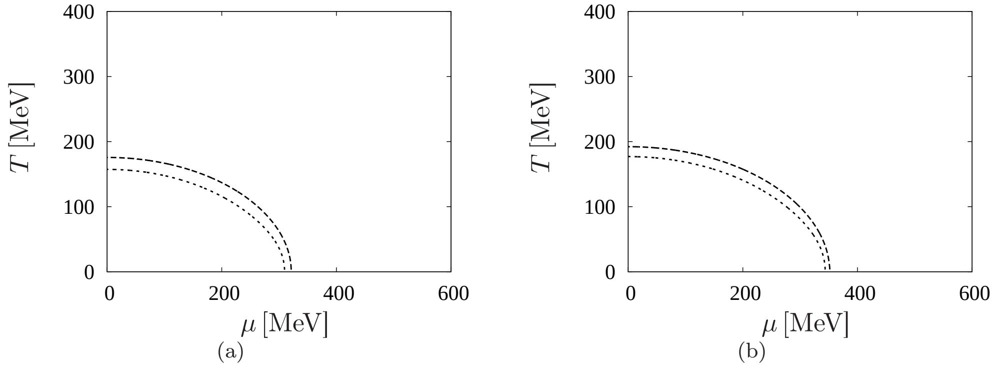

Figure 2.10: Phase diagrams in mean field NJL model for different parameter sets. The σ-dissociation line (at $\mathbf{q} = 0$) is shown as dotted line, the Mott transition line (at $\mathbf{q} = 0$) is shown as dashed line. The parameter sets are those from Tab. 2.2, with (a) No 1, and (b) No 2. The phase diagrams obtained from these parameters do not have a first-order phase transition.

difference $\epsilon - 3p$ is much smaller than in the previous case, and gets negative for intermediate values of T. The speed of sound c_s is strongly effected by these changes in the equation of state, the conformal value of $1/\sqrt{3}$ is overshot and the speed of sound becomes larger than the speed of light in the restored phase.

2.5.4 Mean-field phase diagram

Plotting the known phase transition lines in a T-μ diagram, one obtains a phase diagram. Such type of diagrams are shown in Figs. 2.10 and 2.11 for parameters from Tab. 2.2, and in Figs. 2.12 for all parameters from Tab. 2.1, respectively. In the chiral limit, the transition is either of 1st or of second order. For finite m_0, a first-order transition can occur, and if the first-order line ends in the diagram, it is not continued by a second-order transition as in chiral limit, but stops completely in a critical end point. The remaining part is only separated by a crossover transition. The line of Mott transition and σ-dissociation can be seen as indication for this crossover, since there is not a strict measure for this transition.

The phase diagrams corresponding to different parameter sets differ quantitatively and qualitatively. There are parameters that do not show a first order phase transition at all (Fig. 2.10(a), 2.10(b), and 2.12(a)) and there are parameters that have such a transition for high values of chemical potential μ (Fig. 2.11(a)–2.10(a), and 2.12(b)–2.12(d)). For all parameter sets, the transition in the chiral limit is the closest one to vacuum, followed by the σ-dissociation and the Mott transition. The first-order line is longer in the chiral limit than for a finite bare quark mass, and longer for larger values of m_H in vacuum. The meson transition lines coincide with the first-order transition line at low temperatures, but deviate from it close to the critical end point. First the Mott transition bends to higher temperatures, later the dissociation line, none of them hits the critical end point. Thus the two transition lines are a reasonable measure for the crossover for a large range of chemical potentials μ, but not in the vicinity of the critical end point.

We see that the effective 2-flavor model in mean field approximation allows the calculation of the full phase diagram for all values of T and μ. Real QCD can not be solved in this range, however it is useful to compare the model results to the insights obtained from lattice QCD calculations. Nowadays it is believed that the nature of the transition at $\mu = 0$ is a crossover [14]. Thus there is no exact value for a crossover temperature at zero chemical potential from general reasons, the extraction of a value depends solely on the observables. Beside this ambiguity, the exact value of the crossover temperature is still matter of discussion between different groups [15, 16]. Recent values for the transition region are 180–200 MeV [70] or 150–170 MeV [71, 72].

It is not possible to do such a type of calculation at finite baryon chemical potential due to the fermion sign problem. Hence it is unknown if there exists a region where the transition is of

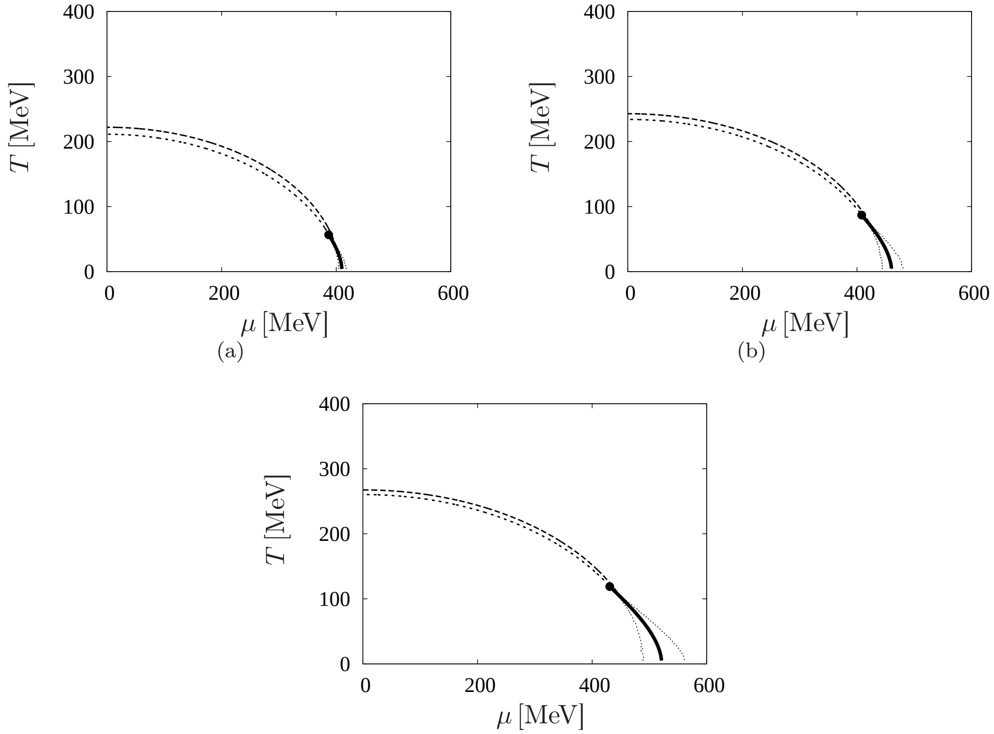

(a) (b) (c)

Figure 2.11: Phase diagrams in mean field Nambu-Jona-Lasinio model for different parameter sets. The bold solid line denotes a first-order phase transition, the filled circle marks the critical end point. The σ-dissociation line (at $\mathbf{q} = 0$) is shown as dotted line, the Mott transition line (at $\mathbf{q} = 0$) is shown as dashed line. The region surrounded by tiny dotted lines is the spinodal region where three minima of thermodynamic potential exist. The parameter sets are those from Tab. 2.2, with (a) No 3, (b) No 4, and (c) No 5.

first order, which implies an existence of a critical end point. Different extrapolation methods indicated such a point in the QCD phase diagram [73], but advanced methods yield contrary results [74]. Recent investigations show that extrapolations to larger values of μ have to be done with care [75].

In comparison to the mean field phase diagrams of $N_f = 2$ Nambu-Jona-Lasinio model, in lattice QCD the chiral transition occurs at lower temperature than in almost all parameters visualized in Fig. 2.10, 2.11, and in Fig. 2.12. If one takes the lines of Mott-transition and σ-dissociation as an indication for chiral phase transition, most of the parameters attain a T_C at $\mu = 0$ of more than 200 MeV. On the other hand, all phase-transitions at zero chemical potential are of crossover-type, as it is expected from lattice QCD calculation. Furthermore, with the appropriate parameter set one is able to describe strong interacting matter with critical endpoint, and without critical endpoint at finite μ.

The lack of gluons in the calculation and the deconfinement phase transition is clearly one origin of deviations of the NJL calculation in mean field from real QCD. There have been tries to include a gluonic background-field in NJL-type models [76, 77, 78, 79] which lead to the PNJL model. The effects of such an extension on the transition temperature is not automatically a lowering of the crossover temperature, and we will not incorporate these modifications in the calculation. In summary, we can expect that quantitatively the transition temperatures will be overestimated in the NJL calculations.

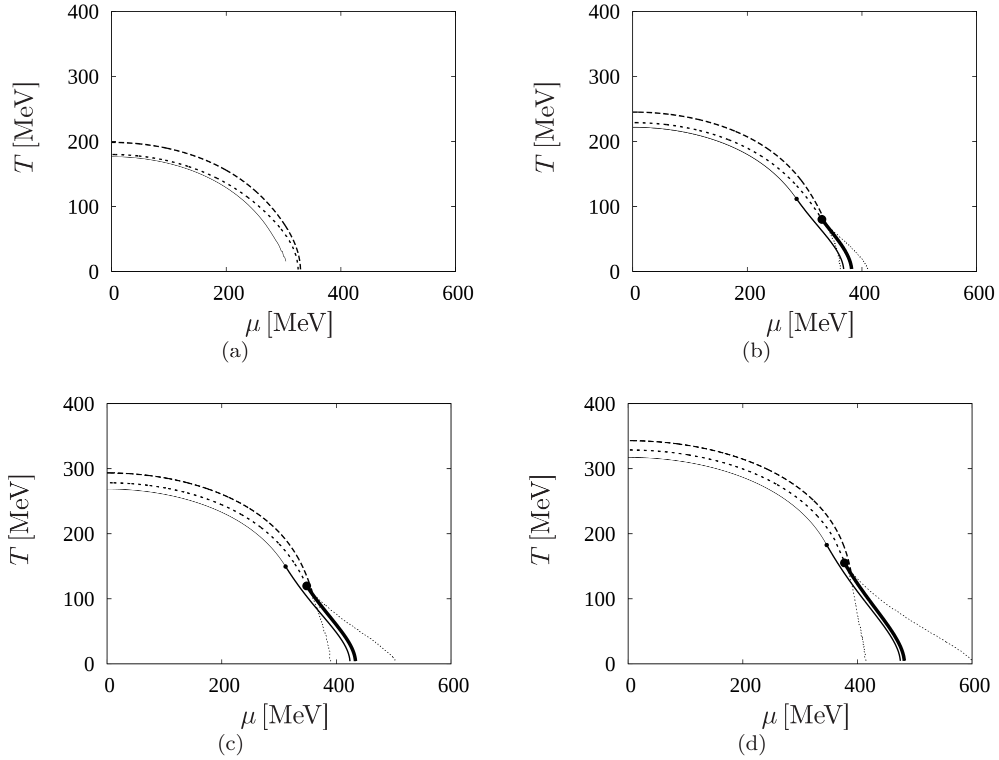

(a) (b) (c) (d)

Figure 2.12: Phase diagrams in mean field Nambu-Jona-Lasinio model for different parameter sets. The bold solid line denotes a first-order phase transition, the filled circle marks the critical end point. The σ-dissociation at $\mathbf{q} = 0$ is marked with a dotted line, the Mott transition at $\mathbf{q} = 0$ is indicated with a dashed line. The region surrounded by tiny dotted lines is the spinodal region. The same parameter set in the chiral limit is shown in smaller lines, the thin solid line correspond to the second-order phase transition. The parameter sets are those from Tab. 2.1, with (a) No 1, (b) No 2, (c) No 3, and (d) No 4.

2.6 Beyond mean-field approximation

There are different ways of extending the standard approximation of the NJL model. We only use a scheme that was already prepared in the derivation of Hartree approximation in Sec. 2.2.1, an overview over other possibilities is given in [69].

2.6.1 Approximation scheme

In Sec. 2.2 the glasses-diagram in the Φ-functional of the effective action was selected because of its power of inverse number of colors. A natural extension of this approximation is the investigations of the next-to-leading order diagrams in $1/N_c$ [80, 81, 82].

For a systematic generalization of the set of two-particle irreducible diagrams, we revisit the counting scheme first presented in Sec. 2.2.1. The order of the dressed propagator is obtained by the consideration of the self-energy. The leading-order self-energy that is obtained from the glasses-diagram is of order $(1/N)^0$, and as all further contributions are sub-leading, we have a dressed quark propagator that is of order $(1/N_c)^0$. The bare coupling and the effect of closed fermion loops stay the same as before, the new diagrammatic building block is the RPA meson propagator D_M. From the analysis of the Bethe-Salpeter equation, we find that D_M has the order $(1/N_c)^1$. We summarize these conclusions in Tab. 2.3.

The Φ-functional was truncated in the Hartree version to the glasses-diagram, which is of order $(1/N_c)^{-1}$: we have two closed quark loops, and one coupling. The diagrams of order $(1/N_c)^0$ have as many closed fermion loops as bare couplings. The diagrams that can be constructed

name	algebraic symbol	diagrammatic symbol	order
dressed propagator	S	—	$(1/N_c)^0$
coupling constant	g	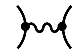	$(1/N_c)^1$
closed fermion loop	$\mathrm{Tr}\big[\ldots\big]$	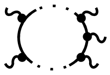	$(1/N_c)^{-1}$
Meson propagator	D_M	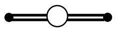	$(1/N_c)^1$

Table 2.3: Counting rules in inverse numbers of colors $1/N_c$. The different elements of the diagrammatic formulation of the Nambu-Jona-Lasinio model are shown with their order.

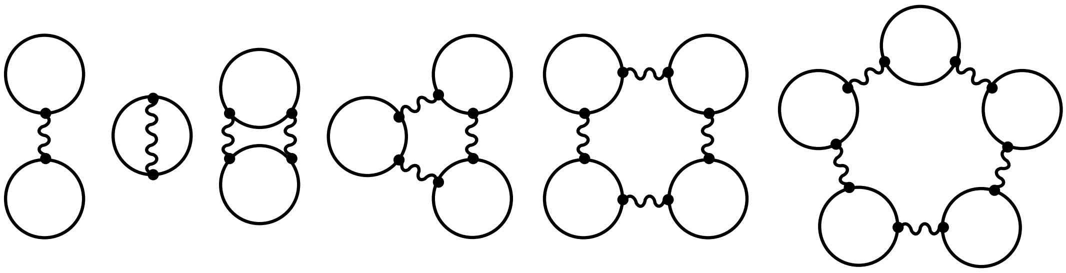
(a) (b) (c) (d) (e) (f)

Figure 2.13: Mean field diagram and ring sum contributions for self-consistent $1/N_c$ expansion in next-to-leading order. The glasses-diagram 2.13(a) is the leading-order term, the diagrams (b) to (f) are examples for the next-to-leading order contributions. The propagator lines correspond to the full quark propagator to that order.

under this condition are closed rings with different total numbers of loops and couplings. In the Φ-functional, all these contributions are summed, and hence this extension of the thermodynamic potential per volume is called *ring sum*. A selection of typical diagrams in the ring sum is shown in Fig. 2.13.

The thermodynamic potential per volume Ω depends on the dressed quark propagator S,

$$\Omega_1[S] = i\mathcal{T}r\ln(iS^{-1}) + \mathcal{T}r(\Sigma iS) + \Phi_1[S], \tag{2.73}$$

it has not only a contribution from the glasses diagram, but also contains the ring sum. One can see that the contributions to the thermodynamic potential per volume from the functional Φ can be written as

$$\Phi_1[S] = \Phi_{glasses}[S] + \sum_M \Phi_M[S], \tag{2.74}$$

so each interaction channel M has a separate term.

2.6.2 Self-consistent and perturbative extension

The NJL model in next-to-leading order in $1/N_c$ was derived as a self-consistent scheme, that means that the quark propagator in this approximation is the solution of the equation

$$\left.\frac{\delta\Omega}{\delta S}\right|_{S=S_1} = 0. \tag{2.75}$$

This can be taken as the definition of S_1, the dressed quark propagator in next-to-leading order in $1/N_c$. The minimization of Ω_1 will lead to a significant difference between the thermodynamic quantities in mean-field approximation and the ones beyond mean-field.

We investigate Eq. (2.73) more in detail. The relation can be seen as an equation for the pressure p,

$$p = p_{LO} + p_{NLO}, \tag{2.76}$$

where $p_{LO} = -\Omega_H$ contains the terms of leading-order, and $p_{NLO} = -\sum_M \Omega_M$ the terms of next-to-leading order in $1/N_c$. This equation can be read as the representation of the pressure p as the sum of different partial pressures. We calculated the pressure in mean-field in the previous section, which was identified as the partial pressure of constituent quarks. If we want to use this observation as a starting point and take p_{NLO} as a correction to that pressure, we can not use the self-consistent scheme and S_1, because p_{LO} will be affected by the new dressing of the quark propagator. What we can do is to keep p_{LO} at its mean-field value and to add the partial pressure p_{NLO} without an additional minimization. The correction to Ω from the next-to-leading order terms is then calculated with help of the Green's functions in Hartree-approximation. Because the next-to-leading order contributions to the thermodynamic potential are added perturbatively, we call this approximation *perturbative* $1/N_c$*-expansion*, whereas the original framework is denoted as *self-consistent* $1/N_c$*-expansion*. We first investigate the perturbative expansion

$$\frac{\delta \Omega_H}{\delta S}[S_H] = 0, \qquad p = -\Omega_H(S_H) - \sum_M \Omega_M(S_H) \tag{2.77}$$

in Sec. 2.7 because the relations to the mean-field results are closer and the derivation requires less technical effort. The self-consistent $1/N_c$-expansion

$$\frac{\delta \Omega_1}{\delta S}[S_1] = 0, \qquad p = -\Omega_H(S_1) - \sum_M \Omega_M(S_1) \tag{2.78}$$

is discussed afterward in Sec. 2.8.

2.7 Perturbative $1/N_c$ expansion

In this section, we investigate the NJL model in the perturbative $1/N_c$ expansion in next-to-leading order. This approximation scheme has been discussed in literature (see Ref. [81, 69, 83]).

2.7.1 Introduction

We will see that this framework will include RPA mesons in the calculation of the thermodynamic potential Ω,

$$\Omega_P(S_H) = \Omega_H(S_H) + \sum_M \Omega_M(S_H). \tag{2.79}$$

The meson contributions Ω_M are obtained by including higher-order diagrams perturbatively in the action functional Φ, thus they are not regarded in the minimization of the thermodynamic potential Ω. The fermion Green's functions S_H entering in the calculation are those obtained in mean field.

The leading order $1/N_c$ diagram, the glasses, is the same as in Sec. 2.2.1. Examples of two-particle-irreducible diagrams of the higher order, are shown in Fig. 2.14, where some representative examples of the ring sum are figured.

The evaluation of the perturbative meson potential Ω_M from these diagrams leads to

$$\Omega_M = \frac{1}{2} T \sum_{i\omega_q} \int \frac{\mathrm{d}^3 q}{(2\pi)^3} \ln\left[1 - 2g\Pi_M(i\omega_q, \mathbf{q})\right], \tag{2.80}$$

where Π_M is the polarization loop from Eq. (2.34). As this is a contribution to the thermodynamic potential Ω, also pressure p, entropy density s and other thermodynamic quantities will be modified by the mesonic correction. A complication arises due to the perturbative treatment of Ω_M when dealing with derivatives, since Ω is not stationary any more at the equilibrium point m_H.

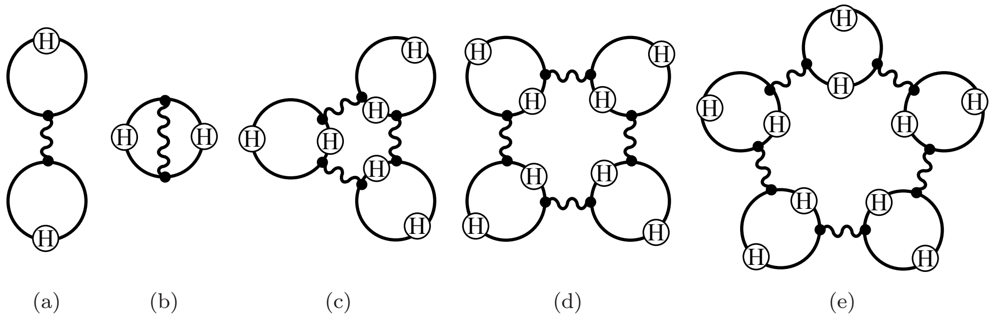

Figure 2.14: Leading-order term (a) and examples of perturbative ring sum contributions to the thermodynamic potential. Note that all fermion lines in the diagrams are Hartree-dressed propagators. The summation of these diagrams leads to the mesonic contribution of the thermodynamic potential $\Omega_M[S_H]$.

Parameter No	1	2	3	4	5
Λ_M [MeV]	0	300	500	600	700

Table 2.4: Mesonic cut-off Λ_M for the next-to-leading order $1/N_c$-expansion. This parameter table is taken from [69], where more details about the fitting are found.

2.7.2 Regularization

The meson thermodynamic potential shown in Eq. (2.80) involves integrations over all meson or polarization loop 4-momenta $(i\omega_q, \mathbf{q})$. In the Sec. 2.2 and Fig. 2.7 it was discussed that the meson propagator $D_M(i\omega_q, \mathbf{q})$ for finite 3-momentum is sensitive to the regularization procedure used in the quark loop. It is favorable to use a Lorentz covariant regularization scheme in order to avoid unphysical artifacts like the mass variation shown in Fig. 2.7.
As the Nambu-Jona-Lasinio model is not renormalizable, the integral over the meson momentum q is divergent again, and an additional cut-off prescription like the ones discussed in Sec. 2.4 is necessary. This work follows Ref. [69] and uses a sharp 3-momentum cut-off Λ_M for the integral in Eq. (2.80). The cut-off momentum does not depend on the regularization parameter of the standard approximation Λ_q or Λ_{PV}. For a unique parameter fixing, it is necessary to fit a given observable in the extended scheme. We use the Pauli-Villars parameter sets from [69], where the mesonic cut-off Λ_M was fitted to the values listed in Tab. 2.4.

2.7.3 Scattering phases

With appropriate techniques, the expression for Ω_M in Eq. (2.80) can be simplified in order to identify different kinds of contributions. It is shown in appendix C.1 how to perform the analytic continuation to real frequencies that end up with the expression

$$\Omega_M = \int \frac{\mathrm{d}^3 q}{(2\pi)^3} \int_0^{+\infty} \frac{\mathrm{d}q_0}{2\pi i} \left(n_B(q_0) + \frac{1}{2} \right) \ln \frac{1 - 2g\Pi_M(q_0 + i\epsilon)}{1 - 2g\Pi_M(q_0 - i\epsilon)}. \tag{2.81}$$

The argument of the logarithm can also be identified as D_M^R / D_M^A, the fraction of retarded over advanced meson propagator. The method used next is also used by Ref. [83]. We write the retarded meson propagator as its absolute value and a phase,

$$D_M^R(q_0, \mathbf{q}) = |D_M^R(q_0, \mathbf{q})| e^{-i\phi_M(q_0, \mathbf{q})}. \tag{2.82}$$

This phase ϕ_M can be identified with the scattering phase of quark-antiquark scattering from the Dyson-Lehmann-Jost representation. The integrand in Eq. (2.81) simplifies with help of the scattering phase ϕ_M.

$$\Omega_M = \int \frac{\mathrm{d}^3 q}{(2\pi)^3} \int_0^{+\infty} \frac{\mathrm{d}q_0}{\pi} \left(n_B(q_0) + \frac{1}{2} \right) \phi_M \tag{2.83}$$

The phase ϕ_M [9] is only defined up to an additive constant,

$$\phi_M \to \phi_M + 2\pi n, \quad n \in \mathbb{Z}. \tag{2.84}$$

The choice of the constant does not change any observables since a thermodynamic potential can also be shifted by a constant value. A convention for this constant also used in scattering theory is the condition

$$\lim_{q_0 \to \infty} \phi_M = 0. \tag{2.85}$$

If the constant is fixed in order to fulfill this condition, the scattering phase yields the Levinson theorem

$$\phi_M(0) = \big(\text{number of bound states}\big) \times \pi. \tag{2.86}$$

However, with this convention the integrand is infrared divergent due to the Bose distribution function n_B. Hence it is convenient to use a phase convention that obeys the condition

$$\lim_{q_0 \to 0} \phi_M(q_0, \mathbf{q}) = 0. \tag{2.87}$$

One should note that the scattering phase is not a continuous function of q_0 and $\mathbf{q}$. For example, if D_M^R or $1/D_M^R$ is real and changes its sign at some point, the complex phase will change its value from 0 to $\pm\pi$ at this point. Exactly this happens at the pion mass pole, and it is essential for the following subsection.

2.7.4 Meson gas

The aim of this part is the decomposition of the meson thermodynamic potential. It is first shown how it can be understood as the partial pressure of the mesons in the quark medium. Then the origin of the different contributions will be shown.

Pole approximation

For a free meson [10] with a retarded propagator

$$D_M^R(q_0, \mathbf{q}) = \frac{g_{Mqq}^2}{(q_0 + i\epsilon)^2 - \mathbf{q}^2 - m_M^2}, \tag{2.88}$$

the scattering phase ϕ_M^{pole} is simply

$$\phi_M^{pole} = \mathrm{sgn}(q_0)\pi\theta\left(-(q_0^2 - \mathbf{q}^2 - m_M^2)\right) \tag{2.89}$$

The same behavior is found if the propagator D_M has a real mass pole for a specific range of momentum. If $m_M < 2m_H$, Eq. (2.89) is also true for an RPA meson with momentum $\mathbf{q}^2 < q_0^2 < 4m_H^2 + \mathbf{q}^2$. If one decomposes the scattering length into a free part and the corrections

$$\phi_M = \phi_M^{pole} + \phi_M^{corr}, \tag{2.90}$$

one obtains directly the corresponding decomposition of Ω_M due to the linearity of Eq. (2.83).

$$\Omega_M = \Omega_M^{pole} + \Omega_M^{corr} \tag{2.91}$$

In the pole part the integrand reduces to $1/2 + n_B(q_0)$, allowing to perform the integration over q_0 analytically. The result,

$$\Omega_M^{pole} = \theta(2m_H - m_M) \int \frac{\mathrm{d}^3 q}{(2\pi)^3} \left\{ \frac{1}{2} E_{M\mathbf{q}} + T \ln\left[1 - \exp\left(-\frac{E_{M\mathbf{q}}}{T}\right)\right]\right\}, \tag{2.92}$$

is the expression for an ideal Bose gas[11], where $E_{M\mathbf{q}} = (m_M^2 + \mathbf{q}^2)^{1/2}$.
The second term Ω_M^{corr} can be understood as a contribution additional to the free particle part. All momenta enter where $\phi \notin \mathbb{Z}\pi$, i. e. all momenta where D_M^R has a finite imaginary part. With these considerations, we see that Ω_M^{corr} is the pressure contribution from scattering processes ($q_0^2 - \mathbf{q}^2 < 0$) and the continuum ($q_0^2 - \mathbf{q}^2 > 2m_H$).

---

[9] This is a general statement for all complex phases, of course.

[10] This can be thought to be an RPA meson in pole approximation, see (2.41).

[11] As already discussed, in general the meson mass m_M can depend on the 3-momentum $\mathbf{q}$.

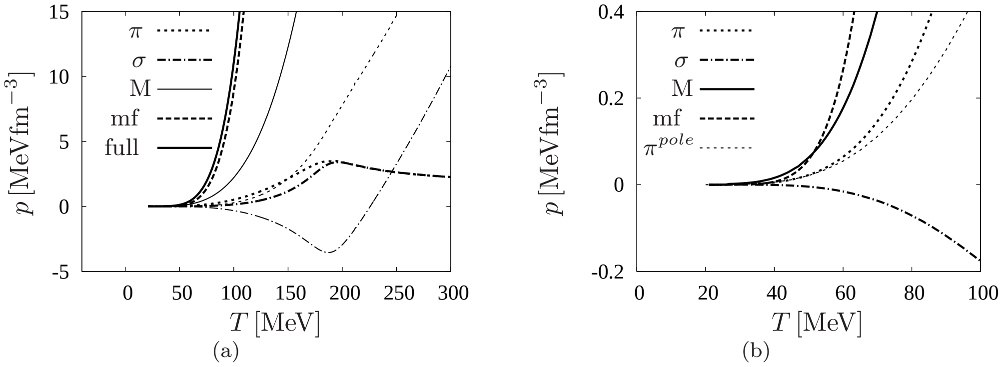

(a) (b)

Figure 2.15: Pressure p as a function of temperature T at $\mu = 0$. The values for the pions and σ-mesons are those for one single meson species, i.e. the partial pressure of all mesons is $3\pi + \sigma$. (a) Comparison of mean-field pressure (mf), pions and sigma (π and σ, bold line correspond to $p_{M,NSR}$, thin line to $p_{M,qfl}$), summed mesonic contribution (M) and the total pressure (full). (b) The focus is on the low-temperature region. The mean field pressure (mf) is shown as well as the mesonic pressure (π and σ) and the total pressure (full). The π^{pole}-curve denotes the π-contribution in pole approximation.

Nozière-Schmitt-Rink contribution and quantum fluctuations

Another way of decomposing Ω_M is closely related to the considerations in Sec. 2.4. A complementary approach leading to the same results was discussed in the context of BEC-BSC crossover [83], where the notation is taken from.

The integrand of Eq. (2.83) is a sum of a term proportional to the Bose distribution function n_B and a term proportional to the constant 1/2. In elementary NJL integrals, terms proportional to (Fermi-) distribution functions and constant terms, respectively, arise, too. As we did for this case, we can call them a medium part and a vacuum part, respectively. In this context, it is more usual to call them Nozière-Schmitt-Rink contribution and quantum fluctuations.

The Nozière-Schmitt-Rink contribution (first derived for non-relativistic system in Ref. [84]) to the thermodynamic potential reads

$$\Omega_M^{NSR} = \int \frac{\mathrm{d}^3 q}{(2\pi)^3} \int_0^\infty \frac{\mathrm{d}q_0}{\pi} n_B(q_0)\phi_M. \tag{2.93}$$

The quantum fluctuation part of Ω_M reads

$$\Omega_M^{qfl} = \int \frac{\mathrm{d}^3 q}{(2\pi)^3} \int_0^\infty \frac{\mathrm{d}q_0}{2\pi} \phi_M. \tag{2.94}$$

Quantum fluctuations are ignored in the non-relativistic Nozière-Schmitt-Rink theory which describes thermal fluctuations.

2.7.5 Numerical results

The calculation of Ω_M is done in the Minkowski formulation, thus starting from Eq. (2.83), for the Pauli-Villars parameter set No 2 from Tab. 2.2. The meson cut-off parameter is chosen to be $\Lambda_M = 300\,\mathrm{MeV}$, according to Tab. 2.4. We restrict the investigations to the $\mu = 0$-axis of the phase diagram.

The result for the pressure p is shown in Fig. 2.15. The formulation in terms of scattering phases allows the distinction between the Noziére-Schmitt-Rink contribution and quantum fluctuations for the mesonic pressures p_M. The pressure components all are normalized $p(T = 0, \mu = 0) = 0$[12].

---

[12] For technical reasons, the pressure components are normalized to $p = 0$ at $T = 20\,\mathrm{MeV}$, except the partial pressure of pions, which is set to the free-pion gas value at $T = 20$ MeV.

In the left plot, the lines for Hartree-quark pressure, pion pressure $p_{\pi,\,NSR}$ and $p_{\pi,\,qfl}$, and σ-pressure $p_{\sigma,\,NSR}$ and $p_{\sigma,\,qfl}$ are shown as well as the sum of all mesonic contributions

$$p_{\text{mesonic}} = \sum_M p_M = \sum_M (p_{M,\,NSR} + p_{M,\,qfl}) = 3(p_{\pi,\,NSR} + p_{\pi,\,qfl}) + p_{\sigma,\,NSR} + p_{\sigma,\,qfl}, \tag{2.95}$$

and the resulting total pressure. First, one sees that the quark contribution rapidly becomes the dominant partial pressure of the system, while the mesonic partial pressure p_{mesonic} is significantly smaller. The pressure components of the single mesons π and σ show a very different behavior. At high temperatures one can clearly see the asymptotic degeneracy of σ and π due to restoration of chiral symmetry[13]. The Noziére-Schmitt-Rink pressure of the mesons is growing for low temperatures, attains a maximum and decreases for higher temperatures. As one can see from the degeneracy of the curves, the kink in $p_{M,\,NSR}$ coincides with the restoration of chiral symmetry. The quantum fluctuation part of the σ-meson leads to a negative contribution to the total pressure because the mass of the scalar meson is decreasing with temperature in the broken phase. At the transition temperature this decrease stops, and the pressure of σ becomes positive at higher T. However, the total pressure of all mesons p_{mesonic} is always positive, as one would expect from a partial pressure of additional particles included in the system.

In the right hand figure, Fig. 2.15(b), the region for small temperatures is magnified. The total meson pressures $p_{M,\,NSR} + p_{M,\,qfl}$ are compared to the mean-field pressure of Hartree quarks as well as to the π-contribution in pole approximation. The mesonic contribution p_{mesonic} is dominant for temperatures below 50 MeV, for higher temperatures the quarks have an important partial pressure. The meson pressure itself is dominated by the pions, and the pions are well described by the pole approximation,

$$p_{\text{mesonic}} \approx 3p_\pi \approx 3p_\pi^{pole}. \tag{2.96}$$

Visible deviations between the exact π-part and the pole approximations appear for temperatures higher than about 60 MeV. The total σ-contribution is negative but less important than the pions due to the higher mass of the scalar excitation and the 3-fold degeneracy of the pions.

Another interesting thermodynamic quantity is the entropy density, it can be calculated by numerical derivation of p with respect to T,

$$s_{M,\,NSR,\,qfl} = \frac{\partial}{\partial T} p_{M,\,NSR,\,qfl}. \tag{2.97}$$

This defines a scheme to deal with the thermodynamical inconsistency of the thermodynamic potential per volume $\mathit{\Omega}_P$. The results obtained from the pressure data are shown in Fig. 2.16.

In Fig. 2.16(a) the different contributions to the entropy density are shown similar to the plot of the pressure (see Fig. 2.15(a)). One can see that the mean-field result becomes dominant even for intermediate temperatures, the mesonic entropy density s_{mesonic} grows slower with temperature. The different meson contributions all behave differently in the broken phase. The quantum fluctuation part of the scalar meson is negative again, because its pressure is not only negative but also decreases in that temperature range. All other parts are positive for low temperatures, resulting in a positive total mesonic entropy density s_{mesonic}. At the crossover, the Noziére-Schmitt-Rink parts of π and σ have a maximum and change their sign, leading to small but negative entropy contributions in the chirally restored phase. In contrast the quantum fluctuations of both mesons are positive in the high temperature region. It is clearly visible that σ and π are degenerate asymptotically[14]. The total mesonic entropy density grows slowly at high temperature — a behavior that is directly related to the almost linear shape of p_{mesonic} for $T > 200\,\text{MeV}$.

The behavior for small temperatures is investigated in detail in Fig. 2.16(b). One can see that the total entropy density in that range is dominated by the pion contribution, that is close to the

---

[13] The quantum fluctuation parts of meson thermodynamic potentials become not degenerate by its absolute value, but have the same slope. This is due to the normalization procedure $p(T = 0) = 0$ chosen for all pressures: The thermodynamic potential for π and σ in an other normalization would have different values in vacuum and would be degenerate in the restored phase.

[14] This is an advantage of the plot of the entropy density: While the thermodynamic potential per volume and hence the pressure requires a fixing of a constant, the entropy density has a finite value from the beginning. So the chiral restoration effect on the mesons is clearly visible.

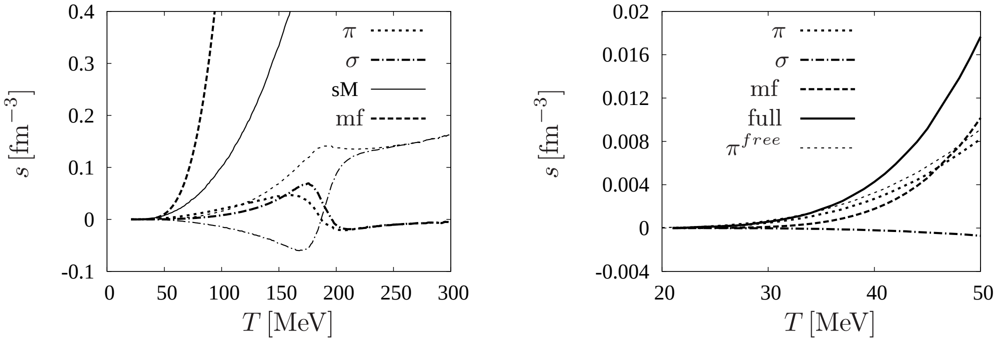

(a)

(b)

Figure 2.16: Entropy density s as a function of temperature T at $\mu = 0$. (a) Comparison of mean-field (mf), pions and sigma (π and σ, bold line correspond to $s_{M,\,NSR}$, thin line to $s_{M,\,qfl}$), and the summed mesonic contribution (M). (b) Low-temperature behavior of entropy density. The mean field entropy density (mf) is shown as well as the mesonic pressure (π and σ, NSR- and qfl contribution are summed and multiplied with the degeneracy factor) and the total pressure (full). The π^{free}-curve denotes the entropy density of a free pion gas.

behavior of a free pion gas. The quarks in mean field approximation attain the entropy density of the pions when temperature is sufficiently increased. The scalar meson has only a very small contribution.

We conclude that the perturbative ring sum scheme leads to the thermodynamic behavior of a system that can be interpreted as a gas of quarks and mesons. At low temperatures the importance ordering of the different excitations takes place according to the particle mass, i. e. a pion gas is found close to vacuum.

2.8 Self-consistent $1/N_c$ expansion

In the previous section, the NJL standard approximation Hartree+RPA was extended using higher order terms in the $1/N_c$ counting scheme which lead to additional 2-particle irreducible diagrams in the Φ-functional. In the perturbative treatment in Sec. 2.7 these additional terms were added simply to the Hartree-solution, hence the described state does not lie on a stationary point of the thermodynamic potential and is not self-consistent. In this section a self-consistent formulation of the $1/N_c$ expansion will be discussed.

This generalization is much more complicated than the approximation schemes above, and some observables are not affected much by the effects of fluctuations. The authors of an article dealing with a similar treatment in a non-relativistic model with a four fermion interaction (Ref. [85]) wrote: “In the end, we are not convinced from the solutions of the new gap and number equations that the self-consistent theory is worth the effort.” But as this approach will be important for the calculation of transport properties in the Nambu-Jona-Lasinio model, it is inevitable to deal with these obstacles.

2.8.1 Φ-functional and gap equation

The starting point for the self-consistent $1/N_c$ expansion is again the functional Φ containing 2-particle irreducible diagrams. These diagrams (shown in Fig. 2.13) are the same types of diagrams as in the perturbative extension of the thermodynamic potential (shown in Fig. 2.14). But here the physical equilibrium state is the one that minimizes the corresponding thermodynamic potential per volume

$$\mathit{\Omega}_1 = i\mathcal{T}r\ln(iS^{-1}) + \mathcal{T}r(\mathit{\Sigma} iS) + \mathit{\Phi}_1[S]. \tag{2.98}$$

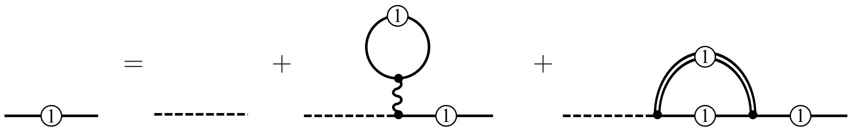

Figure 2.17: Gap equation for the quark propagator in next-to-leading order in $1/N_c$.

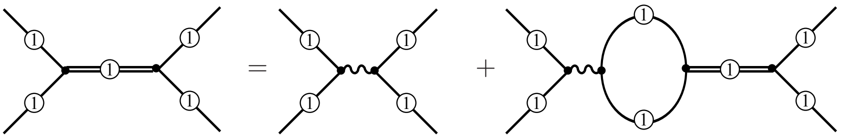

Figure 2.18: Bethe-Salpeter equation for mesons. The internal quark lines are dressed according to Fig. 2.17.

The stationarity condition

$$\left.\frac{\delta\Omega_1[S]}{\delta S}\right|_{S=S_1} = 0 \tag{2.99}$$

is the definition of the quark propagator S_1 in self-consistent next-to-leading order $1/N_c$ expansion.
Using cutting rules as in case of Hartree approximation in Sec. 2.2 makes it possible to derive the Dyson equation for the quark propagator. This equation is shown in Fig. 2.17. The double line with index 1 is the RPA meson propagator containing the $1/N_c$ dressed quark propagator. The Bethe-Salpeter equation for this propagator is shown in Fig. 2.18. The glasses-diagram, the Hartree self-energy and the RPA mesons seem to be familiar. But as they contain the dressed propagator S_1 and not the Hartree propagator[15] the evaluation of these quantities will differ from the mean-field results.

2.8.2 Algebraical formulation of the approximation

For the discussion of the terms involving S_1 it is useful to introduce the decomposition of the propagator [16]

$$S_1(p_0, \mathbf{p}) = S_0(p_0, \mathbf{p})\gamma^0 + S_3(p_0, \mathbf{p})\mathbf{p}\cdot\boldsymbol{\gamma} + S_s(p_0, \mathbf{p}) \tag{2.100}$$

for $p_0 \in \mathbb{C}$. This decomposition in the vector part and the scalar part can also be done for the inverse propagator[17]. The components of the inverse propagator

$$S_1^{-1}(p_0, \mathbf{p}) = a_0(p_0, \mathbf{p})\gamma^0 + a_3(p_0, \mathbf{p})\mathbf{p}\cdot\boldsymbol{\gamma} + a_s(p_0, \mathbf{p}) \tag{2.101}$$

are usually called dressing functions. These different components arise naturally in the explicit expressions for the $1/N_c$ terms presented in the following.

---

[15] The mean-field propagator S_H is simply the propagator of a free fermion with an effective mass m_H, whereas the quark two-point function S_1 has a much richer structure in general.

[16] This decomposition can be done for Matsubara, retarded, and other 2-point functions, so not specification is made here. For concrete calculations, the superscript ^{R} for retarded and ^{A} for advanced will be added to S and other quantities if necessary.

[17] A convention often used in context of Dyson-Schwinger equation uses the symbols $S^{-1}(p) = A(p)\not{p} + B(p)$ in vacuum, and $S^{-1}(p) = A(p)p_0\gamma^0 + C(p)\mathbf{p}\cdot\boldsymbol{\gamma} + B(p)$ in medium, respectively. The convention used here (and similar in Ref. [86]) is preferred because the focus is not on the calculation of fermion Greens functions — the symbols A, B and C are used for various quantities in the work. Additionally, the use of the subscript indices 0, 3 and s reminds the reader of the origin of the components (0-component of Lorentz-vector, 3 spacelike components of Lorentz-vector, and scalar part, respectively).

Thermodynamic potential

The evaluation of the thermodynamic potential per volume Ω_1 defined in Eq. (2.98) yields

$$\Omega_1[S_1] = i\mathcal{Tr}\ln(iS_1^{-1}) + \mathcal{Tr}(\Sigma_1 iS_1) + \Omega_H(S_1) + \sum_M \Omega_M(S_1) \tag{2.102}$$

The four parts of the potential are

$$i\mathcal{Tr}\ln(iS_1^{-1}) = -T\sum_{i\omega_p}\int\frac{\mathrm{d}^3p}{(2\pi)^3}\ln\det S_1^{-1}(i\omega_p+\mu,\mathbf{p}), \tag{2.103}$$

$$\mathcal{Tr}(\Sigma iS_1) = -T\sum_{i\omega_p}\int\frac{\mathrm{d}^3p}{(2\pi)^3}\mathrm{Tr}(\Sigma_1(i\omega_p+\mu,\mathbf{p})iS_1(i\omega_p+\mu,\mathbf{p})), \tag{2.104}$$

$$\Omega_H = -\frac{1}{2}\sum_M 2g\left\{-T\sum_{i\omega_p}\int\frac{\mathrm{d}^3p}{(2\pi)^3}\mathrm{Tr}[\Gamma_M iS_1(i\omega_p+\mu,\mathbf{p})]\right\}^2, \tag{2.105}$$

and

$$\Omega_M = \frac{i}{2}T\sum_{i\omega_q}\int\frac{\mathrm{d}^3q}{(2\pi)^3}\ln\left[1-2g\Pi_M(i\omega_q,\mathbf{q})\right]. \tag{2.106}$$

The last part Ω_M contains the quark polarization loop with the dressed quark propagator S_1.

$$\Pi_M(i\omega_q,\mathbf{q}) = -T\sum_{i\omega_p}\int\frac{\mathrm{d}^3p}{(2\pi)^3}\mathrm{Tr}\left[S_1(i\omega_p+\mu,\mathbf{p})\Gamma_M S_1(i\omega_p+i\omega_q+\mu,\mathbf{p}+\mathbf{q})\Gamma_M\right] \tag{2.107}$$

After the evaluation of the trace Tr() in Dirac-, color-, and flavor-space, the thermodynamic potential per volume in next-to-leading order in $1/N_c$ can be written as

$$\begin{aligned}\Omega_1[S_1] \;=\; & 2N_cN_fT\sum_{i\omega_p}\int\frac{\mathrm{d}^3p}{(2\pi)^3}\ln\left[a_0^2(p)-a_3^2(p)\mathbf{p}^2-a_s^2(p)\right]\\ & -4N_cN_fT\sum_{i\omega_p}\int\frac{\mathrm{d}^3p}{(2\pi)^3}\left[S_0(p)\Sigma_0(p)-S_3(p)\Sigma_3(p)\mathbf{p}^2+S_s(p)\Sigma_s(p)\right]\\ & -g\left\{4N_cN_fT\sum_{i\omega_p}\int\frac{\mathrm{d}^3p}{(2\pi)^3}S_s(p)\right\}^2\\ & +\frac{1}{2}T\sum_{i\omega_q}\int\frac{\mathrm{d}^3q}{(2\pi)^3}\ln\left[1-2g\Pi_M(i\omega_q,\mathbf{q})\right].\end{aligned} \tag{2.108}$$

The quark polarization loop Π_M simplifies to

$$\Pi_M(i\omega_q,\mathbf{q}) = 4N_cN_fT\sum_{i\omega_p}\int\frac{\mathrm{d}^3p}{(2\pi)^3}\left[S_0(p+q)S_0(p)+S_3(p+q)S_3(p)\pm S_s(p+q)S_s(p)\right], \tag{2.109}$$

where the upper sign corresponds to $M=\sigma$ and the lower one to $M=\pi$, respectively.

Gap equation and self-energies

The self-consistent $1/N_c$ gap equation in Fig. 2.17 has the algebraic form

$$S_1(i\omega_p,\mathbf{p}) = S_0(i\omega_p,\mathbf{p}) + S_0(i\omega_p,\mathbf{p})\Sigma_H(i\omega_p,\mathbf{p})S_1(i\omega_p,\mathbf{p}) + \sum_M S_0(i\omega_p,\mathbf{p})\Sigma_M(i\omega_p,\mathbf{p})S_1(i\omega_p,\mathbf{p}). \tag{2.110}$$

We can also write

$$S_1^{-1}(i\omega_p,\mathbf{p}) = S_0^{-1}(i\omega_p,\mathbf{p}) - \varSigma_H[S_1](i\omega_p,\mathbf{p}) - \sum_M \varSigma_M[S_1](i\omega_p,\mathbf{p}). \tag{2.111}$$

The self-energy $\varSigma_H$ can be written

$$\varSigma_H = 2gT\sum_{i\omega_k}\int\frac{\mathrm{d}^3k}{(2\pi)^3}\mathrm{Tr}\,[S_1(k)] = 8N_cN_fgT\sum_{i\omega_k}\int\frac{\mathrm{d}^3k}{(2\pi)^3}S_s(k). \tag{2.112}$$

We note that the Hartree self-energy, even for a dressed propagator, is constant and has only a scalar component. For reasons of analyticity[18], it is immediately clear that $\varSigma_H$ is just a real number. Thus also in the self-consistent next-to-leading order $1/N_c$-expansion the Hartree self-energy only shifts the effective mass and does not give rise to a richer spectral structure.
The meson-exchange self-energies $\varSigma_M$ take the form

$$\varSigma_M(i\omega_p,\mathbf{p}) = -T\sum_{i\omega_q}\int\frac{\mathrm{d}^3q}{(2\pi)^3}D_M(i\omega_q,\mathbf{q})\varGamma_M S_1(i\omega_q+i\omega_p+\mu,\mathbf{q}+\mathbf{p})\varGamma_M, \tag{2.113}$$

where D_M is the meson propagator defined in Fig. 2.18. Like in standard approximation (see Eq. (2.33)), the meson propagator reads

$$D_M(i\omega_q,\mathbf{q}) = \frac{-2g}{1-2g\varPi_M(i\omega_q,\mathbf{q})}. \tag{2.114}$$

where $\varPi_M$ is the polarization loop introduced in Eq. (2.107).
Since S_1 has one scalar and two vector components, $\varSigma_M$ has three independent Dirac-structures, too. Furthermore, $\varSigma_M$ depends non-trivially on the external momentum p.

2.8.3 Solution in Euclidean space-time

Regularization

For the practical evaluation of the expression derived in the previous part, the results have to be brought to a finite value. The divergences of potentials and self energies have two different origins. The first origin is the fact that one has to subtract the infinite but constant vacuum contribution from the thermodynamic potential $\varOmega_1$. The second source of divergences is the nonrenormalizability of the Nambu-Jona-Lasinio model: One has to introduce cut-off schemes.
The infinite constant energy shift in $\varOmega_1$ is completely caused by the first term $-i\mathcal{Tr}\ln iS_1^{-1}$. The constant can be chosen to be a similar term generated by a free Fermi gas. In standard approximation, the vacuum contribution (the free Fermi gas with effective mass m_H^{vac}) was subtracted. This is a nice calibration because this sets the thermodynamic potential per volume as well as the pressure to zero in vacuum. In the self-consistent $1/N_c$ extended scheme, as the quark propagator even in vacuum is not the free particle Greens function and much more difficult to obtain, an other subtraction seems to be favorable. A simple choice is the subtraction of the bare quark contribution $i\mathcal{Tr}\ln iS_0^{-1}$. In practice, this modifies the formulas (2.103) and (2.108) via the substitution prescription

$$i\mathcal{Tr}\ln iS_1^{-1} \to 2N_cN_fT\sum_{i\omega_p}\int\frac{\mathrm{d}^3p}{(2\pi)^3}\ln\left[\frac{a_0^2(p)-a_3^2(p)\mathbf{p}^2-a_s^2(p)}{(i\omega_p+\mu)^2-\mathbf{p}^2-m_0^2}\right]. \tag{2.115}$$

The regularization of divergent integrals is a task that already arose in the sections dealing with the simpler approximation schemes. As in the perturbative ring sum calculation (see Sec. 2.7) there are two independent regularizations needed for fermion loops and for meson integrals. Here, the methods discussed in standard approximation encounter several problems. On the one hand, the 3-dimensional sharp cut-off seems to be disadvantageous because the regularization

---

[18] These arguments coming from the analysis of the structure of Green's functions in the complex plane are discussed in detail in Chap. 4

artifacts of mesons with finite 3-momentum entering in Ω_M and Σ_M should be avoided[19]. On the other hand, the Pauli-Villars prescription makes use of the mass parameter of S in order to construct a Lorentz-covariant regularization scheme. But as it is clear from Eq. (2.113), the self-consistent quark two-point function S_1 has no well defined mass because the quark self-energy is a momentum dependent quantity[20]. The way out of this dilemma is to use the sharp 3-momentum cut-off scheme regardless of artifacts due to the explicitly broken Lorentz covariance. It is also not possible to distinguish between (infinite) vacuum and (finite) medium parts in the Matsubara formulation of the gap equation. This problem is a feature of the Matsubara formulation in general, and is also present in the NJL approximations in lower order.

Computation

In principle, the gap equation (2.111) can be iterated yielding the solution of the minimizing problem Eq. (2.99) and hence the full quark propagator in next-to-leading order $1/N_c$ S_1. All expressions are formulated in the Euclidean space-time containing Matsubara sums over imaginary frequencies, and also the result is the Euclidean propagator $S_1(i\omega_p, \mathbf{p})$.

This type of integral equations is very similar to that in the context of Dyson-Schwinger equations (see e.g. [87, 88, 89]). Thus, it is possible to adopt the highly developed techniques in this field. The straight forward method is the discretization of the Euclidean quark propagator $S(i\omega_p, \mathbf{p})$. Because of isotropy the three Dirac components of the quark propagator in medium all depend on two variables:

$$S_{0,3,s}(i\omega_p, \mathbf{p}) = S_{0,3,s}(p_4, |\mathbf{p}|). \tag{2.116}$$

Each component $S_{0,3,s}$ can be set on a finite $N_4 \times N_3$ grid of values

$$(p_4^i, |\mathbf{p}|^j), \quad (i,j) \in \{0, \ldots, N_4\} \times \{0, \ldots, N_3\}, \tag{2.117}$$

the other values are obtained either by interpolation between the grid points or by extrapolation. The value of S at each grid point can be calculated from the Dyson equation (2.111): The external momentum $(p_4, \mathbf{p})$ can be chosen to be one momentum-grid point $(p_4^i, |\mathbf{p}|^j)$. If one starts with a certain $S^{[0]}$, one can calculate the self-energies from the Dyson equation for every grid point and obtains a new propagator $S^{[1]}$. By repeating this process, an iteration process is defined with the solution of the gap equation S_1 as a fixed point.

With this grid method the remaining task is the numerical implementation of the multiple integrals and Matsubara frequency sums. This iteration process has been performed in the 2-flavor NJL model [90, 91].

2.8.4 Formulation in Minkowski space

In the previous section, we saw that the solution process of the $1/N_c$-extended NJL model in Euclidean space-time has certain disadvantages. The first point is the missing splitting in vacuum part and medium contribution. This decomposition allows an interpretation of different terms entering in the calculation of two-point functions, but also affects the regularization procedure. The restriction to the vacuum part avoids cut-off artifacts, i.e. a more physical behavior at high temperatures. The second point concerns the resulting Green's function itself — since the iteration in Sec. 2.8.3 yields the Matsubara quark propagator $S_1(i\omega_p, \mathbf{p})$, spectral properties stay obscure. Therefore, dynamical properties, such as transport coefficients, which need the knowledge of the time-like sector, can not be calculated with the solutions in Euclidean space-time.

---

[19] This is exactly the same argument already used in the discussion of the regularization of the perturbative ring sum in Sec. 2.7.2

[20] In fact, one could imagine a generalized Pauli-Villars regularization scheme, based on the observation that the main ingredient of this prescription is the subtraction of functions with equal asymptotic behavior like the integrand. As the asymptotic behavior of a propagator is similar to the free propagator, it seems possible to construct a generalized Pauli-Villars regularization scheme by a propagator replacement prescription. However, the prescription has to be adapted to each divergent integral. Additionally, it is known that in the standard approximation, a naive mass substitution in the diagrams does not lead to the correct physical observables in the case of RPA mesons, whereas a substitution in the elementary integrals yield the correct result. It is not clear how to identify the correct integrals for a Pauli-Villars scheme in next-to-leading order in $1/N_c$.

In the following the different quantities in Minkowski formulation are presented. As the Matsubara propagator was decomposed in Sec. 2.8.2, the same can be done with the spectral function $\rho_1 = i[S_1^R - S_1^A]$,

$$\rho_1(p_0,\mathbf{p}) = \rho_0(p_0,\mathbf{p})\gamma^0 + \rho_3(p_0,\mathbf{p})\mathbf{p}\cdot\boldsymbol{\gamma} + \rho_s(p_0,\mathbf{p}). \tag{2.118}$$

The superscripts R and A denote the retarded and advanced quantities, respectively[21].

Thermodynamic potential

It is described in appendix C.4 how to write the Matsubara sums in Eq. (2.108) as integrals over real momenta. The four parts of the potential are listed in the following.
The first term of the thermodynamic potential per volume

$$\begin{aligned}-i\mathcal{T}r\ln(iS_1^{-1}) \;&=\; -2N_cN_f\int\frac{\mathrm{d}^3p}{(2\pi)^3}\int_0^\infty\frac{\mathrm{d}p_0}{\pi}\Bigg\{[1+n_F(p_0-\mu)+n_F(p_0+\mu)]\times\\ &\qquad\times\arg\left\{a_0^R(p)^2-a_3^R(p)^2-a_s^R(p)^2\right\}\Bigg\}\end{aligned} \tag{2.119}$$

contains the complex angle of inverse retarded propagator components in the integrand. The second term of $\varOmega_1$ is

$$\mathcal{T}r(\varSigma iS_1) = 4N_cN_f\int\frac{\mathrm{d}^3p}{(2\pi)^3}\int_0^\infty\frac{\mathrm{d}p_0}{2\pi i}\Bigg\{P^{vac}+P^q+P^{\bar{q}}\Bigg\} \tag{2.120}$$

where the integrand P^{vac} is the divergent vacuum contribution,

$$P^{vac} = \left[\varSigma_0^RS_0^R-\varSigma_0^AS_0^A-(\varSigma_3^RS_3^R-\varSigma_3^AS_3^A)\mathbf{p}^2+\varSigma_s^RS_s^R-\varSigma_s^AS_s^A\right]_{p=(-p_0,\mathbf{p})}. \tag{2.121}$$

The other two terms can be interpreted as pressure of quarks,

$$P^q = n_F(p_0-\mu)\left[\varSigma_0^AS_0^A-\varSigma_0^RS_0^R-(\varSigma_3^AS_3^A-\varSigma_3^RS_3^R)\mathbf{p}^2+\varSigma_s^AS_s^A-\varSigma_s^RS_s^R\right]_{p=(p_0,\mathbf{p})}, \tag{2.122}$$

and antiquarks,

$$P^{\bar{q}} = n_F(p_0+\mu)\left[\varSigma_0^RS_0^R-\varSigma_0^AS_0^A-(\varSigma_3^RS_3^R-\varSigma_3^AS_3^A)\mathbf{p}^2+\varSigma_s^RS_s^R-\varSigma_s^AS_s^A\right]_{p=(-p_0,\mathbf{p})}, \tag{2.123}$$

respectively. The latter two are finite and need no regularization procedure. The contribution from the leading-order glasses diagram in Minkowski space can be rewritten as

$$\varOmega_H = -g\left(\int\frac{\mathrm{d}^3p}{(2\pi)^3}\int_0^\infty\frac{\mathrm{d}p_0}{\pi}\left\{[1-n_F(p_0-\mu)-n_F(p_0+\mu)]\,\rho_s(p_0,\mathbf{p})\right\}\right)^2 \tag{2.124}$$

because just the Hartree self-energy enters that is calculated in Appendix C.2. The last term, the self-consistent ring sum contribution, takes the same form as in the perturbative case in Sec. 2.7[22].

$$\varOmega_M = \int\frac{\mathrm{d}^3q}{(2\pi)^3}\int_0^\infty\frac{q_0}{\pi}\left\{\left(\frac{1}{2}+n_B(q_0)\right)\arg D_M^R(q_0,\mathbf{q})\right\} \tag{2.125}$$

Only the retarded meson propagator D_M^R itself has to be calculated for general dressed quark propagators, which is done in Appendix C.3. The polarization loop obtained this way yields

$$\begin{aligned}\varPi_M^R(q_0,\mathbf{q}) = -\int\frac{\mathrm{d}^3p}{(2\pi)^3}\int_0^\infty\frac{\mathrm{d}p_0}{2\pi}\Bigg\{&\\ &\mathrm{Tr}\left[\varGamma_M\rho_1(-p_0,\mathbf{p})\varGamma_M\left(S_1^R(-p_0+q_0)+S_1^A(-p_0-q_0)\right)\right]\\ &+n_F(p_0-\mu)\mathrm{Tr}\left[\varGamma_M\rho_1(p_0,\mathbf{p})\varGamma_M\left(S_1^R(p_0+q_0)+S_1^A(p_0-q_0)\right)\right]\\ &-n_F(p_0+\mu)\mathrm{Tr}\left[\varGamma_M\rho_1(-p_0,\mathbf{p})\varGamma_M\left(S_1^R(-p_0+q_0)+S_1^A(-p_0-q_0)\right)\right]\Bigg\}\end{aligned} \tag{2.126}$$

---

[21] An intense discussion of real momentum Green's function and spectral densities is in Chap. 4. Here, they are just used as abbreviations for the quantities arising naturally in the Minkowski expressions.

[22] This is not surprising since even in the perturbative case the analytical structure of the meson propagator in the complex plane was allowed to have the most general form.

It is an important point to notice that there is no loss or gain of information by formulating the thermodynamic potential per volume in terms of Matsubara sums or in terms of integrals over real frequencies. The only difference is that in one formulation the Matsubara quark propagator enters while in the other the retarded and advanced Green's functions arise. The situation is different for the gap equation, which is discussed in the next paragraphs.

Gap equation

The external momentum in the gap equation (2.111) can be moved to real frequencies by analytical continuation. The gap equation for the retarded propagator S_1^R is obtained by the rule $i\omega_p \rightarrow p_0 + i\epsilon$[23] and simply leads to

$$(S_1^R)^{-1}(p_0, \mathbf{p}) = (S_0^R)^{-1}(p_0, \mathbf{p}) - \Sigma_H^R[S_1](p_0, \mathbf{p}) - \sum_M \Sigma_M^R[S_1](p_0, \mathbf{p}). \tag{2.127}$$

The retarded self-energies Σ_H^R and Σ_M^R are calculated in appendix C.2 and C.5, respectively. The result is

$$\Sigma_H^R = 2g \int \frac{\mathrm{d}^3 p}{(2\pi)^3} \int_0^\infty \frac{\mathrm{d}p_0}{\pi} \left[1 - n_F(p_0 - \mu) - n_F(p_0 + \mu)\right] \rho_s(p_0, \mathbf{p}) \tag{2.128}$$

and

$$\begin{aligned}
\Sigma_M^R(p_0, \mathbf{p}) = - \int \frac{\mathrm{d}^3 q}{(2\pi)^3} \int_0^\infty \frac{\mathrm{d}q_0}{\pi} \Bigg\{ & \rho_M(q_0, \mathbf{q}) \Gamma_M S_1^R(-q_0 + p_0 + \mu, \mathbf{p} + \mathbf{q}) \Gamma_M \\
& + \frac{1}{2} D_M^A(-q_0 - p_0 - \mu, \mathbf{q}) \Gamma_M \rho_1(-q_0) \Gamma_M \\
& + n_B(q_0) \rho_M(q_0, \mathbf{q}) \Gamma_M \left(S_1^R(-q_0 + p_0 + \mu, \mathbf{p} + \mathbf{q}) - S_1^R(q_0 + p_0 + \mu, \mathbf{p} + \mathbf{q}) \right) \Gamma_M \\
& + \frac{1}{2} n_F(q_0 - \mu) D_M^A(q_0 - p_0 - \mu) \Gamma_M \rho_1(q_0) \Gamma_M \\
& + \frac{1}{2} n_F(q_0 + \mu) D_M^A(-q_0 - p_0 - \mu) \Gamma_M \rho_1(-q_0) \Gamma_M \Bigg\}
\end{aligned} \tag{2.129}$$

We see again that every contribution can be decomposed into a vacuum and a medium part.
The retarded Hartree self-energy Σ_H^R even with an arbitrary fermion propagator inside is constant and real, because the integrand is just the scalar part of the quark spectral function times a prefactor. All imaginary parts entering in the propagator come from the meson contributions Σ_M.

Solution of the Minkowski formulation

In principle, the solution of the Dyson equation (2.127) can be found in a way similar to the Euclidean version in Sec. 2.8.3. The components $S_{0,3,s}^R$ of the retarded quark propagator depend on the real momentum p_0 and the absolute value of the 3-momentum,

$$S_{0,3,s}^R(p_0, \mathbf{p}) = S_{0,3,s}^R(p_0, |\mathbf{p}|). \tag{2.130}$$

Again each component $S_{0,3,s}^R$ can be set on a finite $N_0 \times N_3$ complex grid of values

$$(p_0^i, |\mathbf{p}|^j), \quad (i,j) \in \{0, \dots, N_0\} \times \{0, \dots, N_3\}, \tag{2.131}$$

which can be interpolated and extrapolated in order to obtain the propagator for an arbitrary momentum $(p_0, \mathbf{p})$. It is sufficient to solve the equation for the retarded propagator since it is connected to the advanced one by an analytic relation (see Sec. 4 for details).
Despite all tries to iterate Eq. (2.127), no one ever[24] solved the $1/N_c$ gap equation in Minkowski space. This task is so difficult because the integral kernels of the integral equation are not only high dimensional but are also singular at many points. This prevents the simple use of extensive

---

[23] The advanced propagator S^A would be obtained by the procedure $i\omega_p \rightarrow p_0 - i\epsilon$.

[24] At least till January 2011, nobody solved the equation for real momenta.

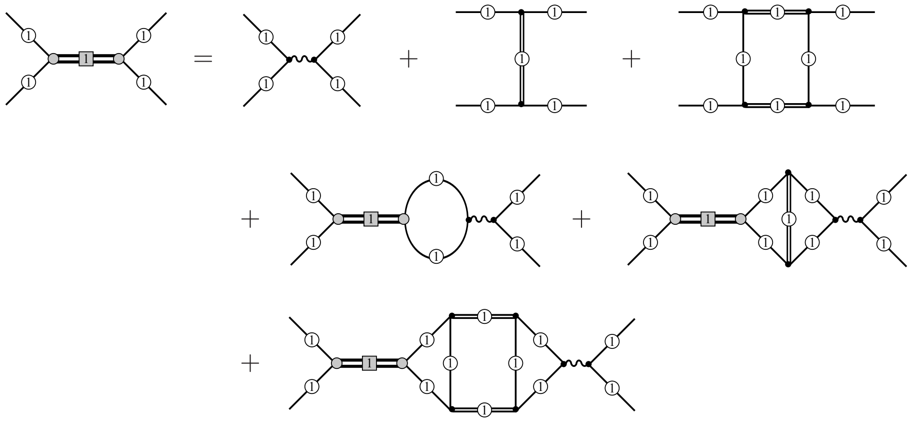

Figure 2.19: Bethe-Salpeter equation for the mesons in next-to-leading order in $1/N_c$. The $1/N_c$-corrected meson propagator (left-hand side of the equation) is defined in terms of $1/N_c$-corrected quarks propagators and RPA mesons which include the $1/N_c$-dressed quark propagators.

computational power as it is for example done for Dyson-Schwinger equations and lattice field theory — both dealing only with Euclidean quantities — because the expressions are numerically unstable. The introduction of a new method leading to Minkowski Green's functions is matter of Sec. 4.3, and it is applied to the $1/N_c$ problem thereafter.

2.8.5 Mesons

The quark-antiquark scattering can be derived from the Φ-functional by cutting quark lines. The scattering diagrams contributing to the matrix to the given order have been derived in [92]. They can be used to construct new Bethe-Salpeter equations leading to the NLO meson propagators shown in Fig. 2.19. Two diagrams on the right hand side of the equation were also present in the RPA mesons: the bare NJL coupling and the summation of the polarization loop. The other diagrams are new and involve RPA propagators with fully dressed quarks inside. There are two non-local kernels involving one and two RPA mesons, and two which arise when the kernels are resummed. These diagrams can be interpreted as scattering processes of the mesons themselves contributing to the amplitude.

It can be shown (see e.g. [69]) that the resulting meson propagators obey the Goldstone theorem, so the pseudoscalar channel will have a massless excitation in case of spontaneously broken chiral symmetry. This is only the case for this dressed meson propagator — the RPA pions, even with the self-consistent quark propagator, are no longer massless. As RPA propagators arise only at intermediate states in the NLO approach, they are not restricted by chiral Ward identities. This subject is summarized in [90].

Chapter 3

Transport phenomena

3.1 Relativistic hydrodynamics

3.1.1 General concept

Relativistic hydrodynamics is the relativistic theory of fluids [93]. It describes the macroscopic behavior of continuous media, such as gases or liquids. The importance of a relativistic description may arise due to the relativistic speed of the macroscopic motion or due to the relativistic velocities of the microscopic motion of the fluid particles.

The fundamental quantity in the mathematical description of fluids is the fluid 4-velocity $U^{\mu}(x)$. As it is a relativistic 4-velocity, it obeys the condition

$$U_{\mu}(x)U^{\mu}(x) = 1. \tag{3.1}$$

By a Lorenz transformation, one can perform locally a boost in the rest frame of the fluid, which has the property

$$U = (1, \mathbf{0}). \tag{3.2}$$

The fluid is characterized by its energy-momentum tensor $T^{\mu\nu}$ as a function of space time. Relativistic hydrodynamics expands the energy-momentum tensor in terms of fluid 4-velocity gradients. That means that the static, homogeneous fluid is taken as a starting point, with derivatives taken as small corrections. For our purpose, the leading order (without gradients) and the next-to-leading order[1] (linear in velocity gradients) of this expansion are necessary.

For a practical hydrodynamic description, one has to remember the elementary condition, that the mean free path of the microscopic constituents of the fluid is much smaller than the system. So, by increasing the distances a particle can propagate, one has to scale the system in the correct way in order not to violate the requirements of relativistic hydrodynamics.

3.1.2 Ideal hydrodynamics

In *ideal hydrodynamic*, the energy-momentum tensor reads

$$T^{\mu\nu} = (\epsilon(x) + p(x))\, U^{\mu}U^{\nu} - p(x)g^{\mu\nu}, \tag{3.3}$$

where ϵ and p are energy density and pressure, respectively. In the local rest frame[2], the tensor $T^{\mu\nu}$ becomes

$$T^{\mu\nu} = \begin{pmatrix} \epsilon & 0 & 0 & 0 \\ 0 & p & 0 & 0 \\ 0 & 0 & p & 0 \\ 0 & 0 & 0 & p \end{pmatrix}.$$

The particle current J^{μ} is

$$J^{\mu}(x) = n(x)U^{\mu}(x), \tag{3.4}$$

---

[1] Note that sometimes these orders are referred as zeroth and first order.

[2] This expression is especially true in the case of hydrostatics, $\mathbf{U} \equiv 0$

where $n(x)$ is the local particle density.
Thus, there are seven input parameters of the ideal hydrodynamical description: pressure, energy density, particle density and the components of the 4-velocity. Energy momentum conservation

$$\partial_\mu T^{\mu\nu} = 0 \tag{3.5}$$

and the equation of continuity for the flux

$$\partial_\mu J^\mu = 0, \tag{3.6}$$

together with the normalization of relativistic 4-velocity (3.1) lead to six constraints of the equation. In order to obtain the last required condition, one assumes that the system is in local thermal equilibrium. This connects pressure, density and energy density by the equation of state,

$$p(x) = p\left(\epsilon(x), n(x)\right). \tag{3.7}$$

Under this assumption, ideal relativistic hydrodynamics is a complete description of a fluid with sufficiently small velocity gradients. Fluids that obey the ideal hydrodynamic equations are usually called *ideal fluids*.

Entropy

An important issue is the evolution of entropy in a fluid. It will not only characterize the different stages of hydrodynamic descriptions but will also give rise to an understanding of transport in fluids. The thermodynamic relation for entropy is

$$TS = E - pV \tag{3.8}$$

where we set $\mu = 0$ for these considerations. Therefore, the entropy density is given by

$$s(x) = \frac{1}{T}\left(p(x) + \epsilon(x)\right), \tag{3.9}$$

which of course depends on the space-time coordinate x. In analogy to the relation (3.4) for the particle number 4-flow, one can write the entropy 4-flow as

$$s^\mu(x) = \frac{1}{T}\left(p(x) + \epsilon(x)\right) U^\mu. \tag{3.10}$$

In order to derive the evolution of the entropy density in an ideal fluid, we start from energy-momentum conservation (3.5) and take the derivative with respect to the 4-velocity U^μ,

$$\frac{\partial}{\partial U^\nu}\partial_\mu T^{\mu\nu} = 0. \tag{3.11}$$

Applied to the energy-momentum tensor $T^{\mu\nu}$ in ideal hydrodynamics (3.3), one obtains

$$\partial_\mu(\epsilon(x) + p(x))U^\mu = 0, \tag{3.12}$$

which implies, in comparison with equation (3.10), that the entropy density is locally conserved,

$$\partial_\mu s^\mu = 0. \tag{3.13}$$

So no entropy production and no dissipative processes are described in ideal hydrodynamics. In order to take those effects into account, a further extension of relativistic hydrodynamics becomes necessary.

3.1.3 Viscous hydrodynamics

In the previous section, the concept of a systematic expansion of the energy-momentum tensor in powers of 4-velocity gradients was summarized. The truncation after the leading order gave rise to ideal hydrodynamics. The equations of ideal hydrodynamics (3.3) and (3.4) do not contain 4-velocity gradients, whereas the second order can also involve terms that are linear in 4-velocity gradients. These terms give a correction to the ideal hydrodynamic equations,

$$\begin{aligned} T^{\mu\nu} &= (\epsilon(x)+p(x))\,U^\mu U^\nu - p(x)g^{\mu\nu} + T^{(1)\mu\nu} && (3.14)\\ J^\mu &= n(x)U^\mu + J^{(1)\mu}. && (3.15)\end{aligned}$$

The correction terms $T^{(1)\mu\nu}$ and $J^{(1)\mu}$ read

$$\begin{aligned} T^{(1)\mu\nu} &= \eta\left[\partial^\mu U^\nu + \partial^\nu U^\mu + U^\nu U^\lambda \partial_\lambda U^\mu + U^\mu U^\lambda \partial_\lambda U^\nu\right] \\ &\quad + \left(\zeta - \frac{2}{3}\eta\right)\left[g^{\mu\nu} - U^\mu U^\nu\right]\partial_\lambda U^\lambda && (3.16)\\ J^{(1)\mu} &= \kappa\left(\frac{nT}{\epsilon+p}\right)\left[\partial^\mu - U^\mu U^\lambda \partial_\lambda\right]\frac{\mu}{T} && (3.17)\end{aligned}$$

The coefficients presented here are the *shear viscosity* η, the *bulk viscosity* ζ and the *thermal conductivity* κ. They are called *transport coefficients*. As the equation of state that was already required in ideal hydrodynamics, they are a microscopic input to the hydrodynamical description. The part of the hydrodynamic energy-momentum tensor proportional to η, i.e. off-diagonal spatial elements of $T^{(1)\mu\nu}$, is the shear component. The thermal conductivity κ is only present if there is a conserved 4-current in the system, associated with the charge density n and a chemical potential μ.

In contrast to ideal hydrodynamics, entropy is not conserved in viscous hydrodynamics. This is subject of the H-theorem: entropy increases in the system due to irreversible processes. We do not investigate this property of viscous hydrodynamics in detail, for reference see [94]. However, it is important to notice that the correction terms $T^{(1)\mu\nu}$ and $J^{(1)\mu}$ in the hydrodynamical energy-momentum tensor $T^{\mu\nu}$ that are responsible for entropy production are proportional to the transport coefficients η, ζ, and κ.

3.1.4 Beyond viscous hydrodynamics

Although transport phenomena can be described in the first-order relativistic hydrodynamic formulation presented in the preceding paragraphs, the physical properties of the fluids described by the equations (3.16) and (3.17) are not completely satisfying. By a detailed analysis one can see that the differential equation for heat flow is parabolic, leading to a instantaneous propagation of heat (see e.g. [93]).

The acausal behavior of viscous hydrodynamics is a shortcoming of the first-order gradient expansion. It was shown that the extension to second-order gradients of hydrodynamical 4-velocity lead to hyperbolic equations for heat propagation, and a causal viscous hydrodynamic can be formulated [95]. These extensions of the first-order methods have been rediscussed in the last years, especially in the context of hydrodynamic description of fireballs in heavy-ion collisions [46, 96, 97, 98].

3.2 Green-Kubo Formalism

Transport coefficients can be calculated from time correlation functions. The advantage of this procedure is that it is an exact formulation of the hydrodynamic quantities. However, it is known that the practical application involves a lot of problems. For example, Zwanzig [99] wrote "The calculation may be hard, but we know where to start.". Jeon and Yaffe [100] wrote "The diagrammatic evaluation of transport coefficients is a remarkably inefficient approach".

3.2.1 Formalism and Kubo transformation

The foundation of the theory of transport coefficients was given by works concerning friction of Brownian motion and line-widths of nuclear magnetic resonances. In these articles, the quantity related to dissipation processes was expressed as a time correlation function, as it is the case in the general fluctuation-dissipation theorem. Later, it was possible to express electrical conductivity, viscosity, and thermal conductivity in terms of time-correlation functions. The name on this method varies, referring to the important works of Green [101, 102], Mori [103], and Kubo [104]. The names Green-Kubo-method, Kubo-Mori formula, or Kubo formula will be used equivalently in this thesis, although the term Kubo formula is better used solely for the expression of electrical conductivity and the term time-correlation function method is maybe the most appropriate one. A useful introduction to a non-relativistic version of these formulas is given by [99], where an overview over the different derivations is given. A synopsis of transport coefficient calculus in relativistic quantum field theory was given later [105].
All Green-Kubo relations have a similar structure, involving a Fourier transformed time correlation function

$$\rho_A(p_0, \mathbf{p}) = \int \mathrm{d}^4x \; e^{ip_\mu x^\mu} \langle [A(x), A(0)] \rangle . \tag{3.18}$$

Such a type of Fourier transform is called *Kubo transform*. The thermal average $\langle \ldots \rangle$ in the integrand involves the retarded Green's function. As we will see, each transport coefficient will be expressed as such a correlator.

3.2.2 Green-Kubo formulas for different transport coefficients

Electrical conductivity

We start with the electrical conductivity, which was the material coefficient that was calculated in the original work of Kubo [104] and is investigated in many textbooks of many-particle physics and solid state physics [106], mainly in its non-relativistic version. We use the relativistic formulation of [107] in this section. The ac conductivity is given by

$$\sigma_{el}(p_0) = -\frac{1}{6} \lim_{\mathbf{p}\to 0} \frac{1}{p_0} \int \mathrm{d}^4x e^{ipx} \langle \left[J^i_{el}(x), J^i_{el}(0) \right] \rangle \tag{3.19}$$

where J_{el} is the electric charge current, where the frequency is p_0 in natural units. The dc conductivity reads

$$\sigma_{el} = -\frac{1}{6} \lim_{p_0 \to 0+i\epsilon} \lim_{\mathbf{p}\to 0} \frac{1}{p_0} \int \mathrm{d}^4x e^{ipx} \langle \left[J^i_{el}(x), J^i_{el}(0) \right] \rangle . \tag{3.20}$$

Thus, for electrical conductivity the retarded current-current correlation function

$$\rho_J(p_0, \mathbf{p}) = \int \mathrm{d}^4x e^{ip_\mu x^\mu} \langle \left[J^i_{el}(x), J^i_{el}(0) \right] \rangle \tag{3.21}$$

has to be evaluated. Electrical conductivity is a phenomenon that is related to the linear response of matter under the influence of an external field: An electric field $\mathbf{E}$ is applied to a piece of metal, and as its consequence, an electric current $\mathbf{J}_{el}$ is observed, obeying the relation

$$\mathbf{J}_{el} = \sigma_{el}(\omega)\mathbf{E}. \tag{3.22}$$

The calculation of such a type of linear response is nicely done with the derivation of Kubo, however, there are dissipation processes that are not induced by external fields but by internal, thermal currents. One example for such a type of coefficient is shear viscosity η.

Shear viscosity

In contrast to electrical conductivity, shear viscosity cannot be calculated as a response to an external field, since the correlations of internal thermal currents are not induced by an external source, but by internal inhomogeneities. There are several methods to deal with this difficulty

[108, 99], which is primarily a problem in deriving a Green-Kubo type relation for thermal currents rather than a main difference in the further application.
We follow the works of [109, 107] in this section. The time-correlation function expression for the frequency-dependent shear viscosity coefficient is

$$\eta(p_0) = \frac{1}{20} \lim_{\mathbf{p}\to 0} \frac{1}{p_0} \int \mathrm{d}^4 x e^{ip^\mu x_\mu} \langle \left[T^{ij}_{\text{traceless}}(x), T^{ij}_{\text{traceless}}(0) \right] \rangle, \tag{3.23}$$

the static shear viscosity is obtained from the expression at zero frequency,

$$\eta = \frac{1}{20} \lim_{p_0 \to 0+i\epsilon} \lim_{\mathbf{p}\to 0} \frac{1}{p_0} \int \mathrm{d}^4 x e^{ip^\mu x_\mu} \langle \left[T^{ij}_{\text{traceless}}(x), T^{ij}_{\text{traceless}}(0) \right] \rangle. \tag{3.24}$$

Here, $T_{\text{traceless}}$ is the traceless part of the energy-momentum tensor,

$$T^{ij}_{\text{traceless}} = T^{ij} - \frac{1}{3}\delta^{ij} T^k_k. \tag{3.25}$$

In comparison to Eq. (3.18) it becomes clear that the correlator for the shear viscosity involves this part of the energy-momentum tensor,

$$\rho_{\text{shear}} = \langle \left[T^{ij}_{\text{traceless}}(x), T^{ij}_{\text{traceless}}(0) \right] \rangle, \tag{3.26}$$

insead of the electric current J^i.

Thermal conductivity

The thermal conductivity κ is present in the correction term $J^{(1)\mu\nu}$ in viscous hydrodynamics. Like shear viscosity, it is not a coefficient of a linear response to an external field, but a measure of reaction to internal inhomogeneities. The time-correlation function expression for κ reads [105, 107]

$$\kappa = \frac{1}{6T} \lim_{p_0 \to 0} \lim_{\mathbf{p}\to 0} \frac{1}{p_0} \int \mathrm{d}^4 x e^{ip_\mu x^\mu} \langle \left[I^i(x), I^i(0) \right] \rangle \tag{3.27}$$

where the current that enters in the correlator is

$$I^i(x) = T^{0i} - \frac{h}{n} J^i. \tag{3.28}$$

Here, h is the enthalpy density and n the particle number density, thus h/n is the enthalpy per particle. The existence of a conserved current J^μ is essential for the thermal conductivity — it can be seen from the definition of κ in Eq. (3.17) and will be discussed again in Sec. 3.4. The correlator of the general Green-Kubo expression is

$$\rho_{\text{heat}} = \langle \left[I^i(x), I^i(0) \right] \rangle, \tag{3.29}$$

according to Eq. (3.18).

Bulk viscosity

The static bulk-viscosity ζ can be written as

$$\zeta = \frac{1}{2} \lim_{p_0 \to 0} \lim_{\mathbf{p}\to 0} \frac{1}{p_0} \int \mathrm{d}^4 x e^{ip_\mu x^\mu} \langle \left[\frac{1}{3} T^i_i(x), \frac{1}{3} T^j_j(0) \right] \rangle, \tag{3.30}$$

according to [107]. The diagonal elements T^i_i of the energy-momentum tensor enter in the Green-Kubo expression for bulk viscosity, whereas the off-diagonal elements contribute to the shear viscosity formula. The correlator reads

$$\rho_{T^i_i} = \int \mathrm{d}^4 x e^{ip_\mu x^\mu} \langle \left[\frac{1}{3} T^i_i(x), \frac{1}{3} T^j_j(0) \right] \rangle, \tag{3.31}$$

where we limit the discussion, although there are modifications of this formula depending on the situation [105, 110, 107].

Other Green-Kubo relations

There are other types of relations similar to the Green-Kubo formulas for electrical conductivity, and hydrodynamic transport coefficients shear viscosity, thermal conductivity, and bulk viscosity. One important example from a historical point of view is the early work concerning friction of Brownian motion. Another application in solid state physics is the calculation of the paramagnetic susceptibility. We stop here with the presentation of the time-correlation functions belonging to different transport coefficient and discuss the practical application of the method more in detail.

3.2.3 Analysis of the Kubo transforms

In the preceding paragraphs, we saw that the transport coefficients can be expressed in terms of Kubo transforms, which are quite abstract correlation functions. An analysis and interpretation of these time-correlators and its properties is given in [111]. We want to focus on the practical calculation of these correlators in certain theories and on the shear viscosity coefficient η, although the treatment of the other coefficients is very similar.

Energy-momentum tensor

We want to investigate the expression in Eq. (3.26) a bit more in detail for a microscopic calculation in a quantum-field theoretical model. In general, the energy-momentum tensor for a Lagrangian $\mathscr{L}$ depending on N fields $(\phi_1, \ldots, \phi_N)$ is given by

$$T^{\mu\nu} = \sum_a \frac{\partial \mathscr{L}}{\partial(\partial_\mu \phi_a)} \partial^\nu \phi_a - g^{\mu\nu} \mathscr{L}. \tag{3.32}$$

The off-diagonal part $i \neq j$ can be written in a single form for a huge class of theories. Assuming a multicomponent scalar field with an interaction that does not depend on field derivatives, i.e.

$$\mathscr{L}_{\text{scalar}} = \frac{1}{2} \sum_a \left[\partial_\mu \phi_a \partial^\mu \phi_a - m_a^2 \phi_a^2\right] + \mathscr{L}_{\text{int}}[\phi_1, \ldots, \phi_N], \tag{3.33}$$

the off-diagonal-part $i \neq j$ is

$$T^{ij}_{\text{scalar}} = \sum_a \partial^i \phi_a \partial^j \phi_a \quad \text{for} \quad i \neq j. \tag{3.34}$$

For a fermion Lagrangian without derivatives in the interaction part,

$$\mathscr{L}_{\text{fermion}} = \sum_a \bar{\psi}_a (i\partial\!\!\!/ - m_a) \psi_a + \mathscr{L}_{\text{int}}[\psi_1, \ldots, \psi_N], \tag{3.35}$$

the traceless part becomes

$$T^{ij}_{\text{fermion}} = \sum_a i\bar{\psi}_a \gamma^i \partial^j \psi_a \quad \text{for} \quad i \neq j. \tag{3.36}$$

This expression for the fermionic energy-momentum tensor is not symmetric in its indices as it was for the multi-component scalar field. It is possible to bring it into a symmetric form by adding a divergence-free term.

Evaluation of the correlator

The diagrammatic representation of the correlator of the shear viscosity coefficient is shown in Fig. 3.1. This form is general for the classes of models that were discussed before, it is an effective one-loop diagram in case of the Nambu-Jona-Lasinio model and for the $O(N)$ model if the correct propagators are taken, respectively. The solid lines correspond to the fully dressed fermion- or boson propagator, the filled circle correspond to the fully dressed vertex. The external dotted lines indicate the external 4-momentum, there is no external physical particle that is coupled to the diagram in Fig. 3.1. The evaluation of the correlators of the other transport coefficients involve similar diagrams, with different kinds of external vertices.

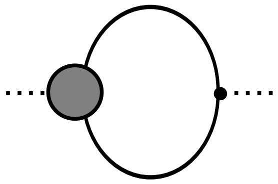

Figure 3.1: Diagrammatic representation of the Kubo-transformed correlation function. Bold lines denote the fully dressed propagator, the filled circle denotes the fully dressed vertex.

The diagram in Fig. 3.1 is called $\mathit{\Pi}$, and we can express the frequency-dependent viscosity in terms of the retarded expression $\mathit{\Pi}^R$ according to [112, 113],

$$\eta(p_0) = \frac{i}{p_0}\left[\mathit{\Pi}^R(p_0,0) - \mathit{\Pi}^R(0,0)\right], \tag{3.37}$$

where the frequency is equal to p_0 in natural units. For the static viscosity, the limit $p_0 \to 0$ is taken, which leads to the derivative of the imaginary part of $\mathit{\Pi}^R$ at zero external momentum,

$$\eta = -\lim_{p_0\to 0}\lim_{\mathbf{p}\to 0}\frac{\mathrm{d}}{\mathrm{d}p_0}\mathrm{Im}\mathit{\Pi}^R(p_0,\mathbf{p}). \tag{3.38}$$

We now evaluate the expression $\mathit{\Pi}$ for a specific Lagrangian. For the Nambu-Jona Lasinio model, the bare vertex related to the energy-momentum tensor is $p^i\gamma^j$. After setting the external 3-momentum to zero[3], the resulting equation involving the full quark vertex $\mathit{\Gamma}^{ij}_{full}$ and the full quark propagator S_{full} reads

$$\mathit{\Pi}_\eta(i\omega_p,0) = T\sum_{i\omega_k}\int\frac{\mathrm{d}^3k}{(2\pi)^3}\mathrm{Tr}\left[\mathit{\Gamma}^{ij}_{full}(p+k;k)S_{full}(k)k^i\gamma^j S_{full}(k+p)\right] \tag{3.39}$$

where $k = (i\omega_k + \mu, \mathbf{k})$ and $k + p = (i\omega_p + i\omega_k + \mu, \mathbf{k})$ [112, 114, 113]. For transport calculation this Matsubara correlator has to be transformed to obtain the retarded correlation function. This step is explained in detail in appendix D.1. The resulting retarded polarization function for the case of the bare vertex reads

$$\begin{aligned}\mathit{\Pi}^R_\eta(p_0,0) = \int\frac{\mathrm{d}^3k}{(2\pi)^3}\int_{-\infty}^{+\infty}\frac{\mathrm{d}k_0}{2\pi}\Bigg\{& n_F(k_0)\times\\ &\times\mathrm{Tr}\left[k^i\gamma^j(p_0+k_0+\mu;k_0)\rho_{full}(k_0)k^i\gamma^j(S^R_{full}(k_0+p_0)+S^A_{full}(k_0-p_0))\right]\Bigg\},\end{aligned} \tag{3.40}$$

where S_{full} is the dressed propagator, and ρ_{full} is the spectral function of S_{full}. In the Kubo formula of the static shear viscosity (3.38), the derivative of the imaginary part of this expression at vanishing external momentum is needed. It is shown in appendix D.1 that this derivative can be written as

$$\frac{\mathrm{d}}{\mathrm{d}p_0}\mathrm{Im}\mathit{\Pi}^R_\eta(p_0,0)\Big|_{p_0=0} = \frac{1}{2}\int\frac{\mathrm{d}^3k}{(2\pi)^3}\int_{-\infty}^{+\infty}\frac{\mathrm{d}k_0}{2\pi}\left\{n_F'(k_0-\mu)\mathrm{Tr}\left[k^i\gamma^j\rho_{full}(k_0)k^i\gamma^j\rho_{full}(k_0)\right]\right\}. \tag{3.41}$$

Starting from this equation, one can identify the processes that are responsible for the dissipative transport phenomena in a fermionic system. If one specifies the situation to a Fermi gas at relatively low temperature, one can see that the contributions to integral in Eq. (3.41) are

---

[3] It is useful to make this limit already here since the 3-momentum at the external couplings enters in the bare vertex $p^i\gamma^j$

dominated by the density of states (which is ρ_{full}) in the vicinity of the Fermi surface (where n'_F has the most contributions). The particles at energies much lower that μ do not contribute to tranport processes because of Pauli blocking.

In the present approxmation of a bare vertex, the fully dressed quark spectral function ρ_{full} enters the expression for the static viscosity. Eq. (3.41) is nice to explain the problem of propagator dressings in Green-Kubo formalism. Consider a free particle Green's function as it would be taken in perturbation theory. The spectrum of such a function is δ-like with a pole at $\sqrt{m^2+\mathbf{k}^2}$. If one takes the imaginary part of the expressions in Eq. (3.40), one obtains a product of Dirac-functions with arguments that are shifted by q_0, thus the product vanishes and the shear viscosity is zero for all frequencies. We conclude hat simple perturbative or mean-field dressings that lead to δ-like spectra for the 2-point functions are not suitable for the Green-Kubo correlator. The reason is that the retarded propagators in such an approximation are those of free particles, eventually with a modified effective mass. The question of linear response of a system that does not react on a field is nonsensical.

Remarkably, the shear viscosity calculated with nontrivial dressing, but in the limit of free propagators shows the contrary behavior. This is understood mathematically from the Kubo formula in its form in Eq. (3.41). The shear viscosity coefficient η is proportional to the square of the spectral function ρ_{full}, which has some normalization. If the contributions to the integral over ρ_{full} is dominated by a smaller and smaller region, as it is the case in the limit of a free δ-like spectrum, the integral over the square of the normalized function increases.

Explicit versions of this dependency of η on the propagator dressing were derived in several approximative calculations of the shear viscosity [112, 107], where this relation between spectral width and transport coefficients is manifest. Interpretations for this behavior for different coefficients are discussed in literature, see e. g. [106] for electrical conductivity, and [115] for shear viscosity.

3.3 Relativistic Kinetic Theory

Under certain circumstances, a system can be described as an ensemble of almost free particles. The treatment as quasi-free particles is valid, if the particles do not interact most of the time. Kinetic theory is the description of such dilute gases in terms of distribution functions. Additional to the assumption of approximately free particles, particle correlations before a collision are neglected ("hypothesis of molecular chaos" or "Stoßzahlansatz"). It is also required that the particle distribution functions vary only slowly in space and time. Although it is not a general restriction of kinetic theory, we take only two-particle interactions into account in this particular work.

Kinetic theory and the calculation of nonequilibrium properties in this framework has a relatively long history [116, 117] and thus are older than the Green-Kubo formalism. The kinetic description is possible for constituents obeying either classical or quantum statistics, and for either non-relativistic or relativistic systems. Each of the four[4] possible combinations of statistics and relativity can be explored. All these potential kinetic descriptions have been investigated and are discussed in the literature, however, the detailedness of discussions of the various combinations varies. The classical, non-relativistic version of kinetic theory is not only subject to many textbooks (see e.g. Ref. [118, 119]) but also to works concerning the mathematical foundation (see e.g. Ref. [120]). For the classical relativistic version or the non-relativistic quantum case, there are still some textbooks dealing with the general framework (see Ref. [94] for the classical relativistic and Ref. [121] for the latter). For the relativistic quantum description, there is few literature deriving general properties, but more works concentrated on special situations [122, 123, 124, 125]. Therefore, some more space is spend for a systematic overview of quantum relativistic kinetic theory.

In this section, we start with the practical calculation of transport coefficients in relativistic kinetic theory and discuss the result and its validity in the end.

---

[4] Additionally, one has to take into account how the particle interactions were calculated. Notably for kinetic theory of gases it is usual to take classical molecules with an interaction calculated from quantum mechanics.

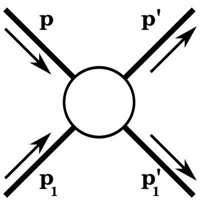

Figure 3.2: Two particle scattering with momentum labels according to Uehling and Uhlenbeck.

3.3.1 Uehling-Uhlenbeck equation

Assume that there are N_p particle species in the system. Each particle species a,

$$a \in \{P_1, P_2, \ldots, P_{N_p}\} =: \mathcal{P} \tag{3.42}$$

has a degeneracy factor g_a. The main ingredients of kinetic description are the distribution functions f_a.
If we only consider elastic two-particle interactions, the evolution of the distribution function f_a[5] is governed by the *(Boltzmann-)Uehling-Uhlenbeck equation*

$$\frac{\mathrm{d}}{\mathrm{d}t} f_a(\mathbf{x}, \mathbf{p}, t) = \sum_{b \in \mathcal{P}} C[f_a, f_b], \tag{3.43}$$

where the left hand side is called *advective term* and the right hand side is called *collision term*. The scattering process is sketched in figure 3.2. The same figure explains the usual momentum labeling according to Uehling and Uhlenbeck,

$$p + p_1 \longrightarrow p' + p_1'. \tag{3.44}$$

All functions of these momenta are written shortly with the same suffix, i.e. $f_a(p') = f_a'$, $E_b(p_1') = E_{1b}'$. Rewriting the spatial gradient in the advective term, one obtains

$$\frac{p^\mu}{p_0} \partial_\mu f_a = \frac{p_\mu}{p_0} U^\mu \underbrace{U^\nu \partial_\nu}_{\mathcal{D}} f_a + \frac{p_\mu}{p_0} \underbrace{(g^{\mu\nu} - U^\mu U^\nu) \partial_\nu}_{\nabla^\mu} f_a. \tag{3.45}$$

In this last step, the splitting in convective derivative $\mathcal{D}$ and purely spatial derivative ∇^μ in the local rest frame was performed. The collision term $C[f_a, f_b]$ can be expressed as

$$\begin{aligned} C[f_a, f_b] = \frac{1}{1+\delta_{ab}} \frac{g_b}{2E_p} \int \frac{\mathrm{d}^3 p_1}{(2\pi)^3} \int \frac{\mathrm{d}^3 p'}{(2\pi)^3} \int \frac{\mathrm{d}^3 p_1'}{(2\pi)^3} \Big\{ (2\pi)^4 \delta^{(4)}(p + p_1 - p' - p_1') \left|\mathcal{M}_{ab}\right|^2 \times \\ \times \left[f_a' f_{1b}' (1 + \theta_a f_a)(1 + \theta_b f_{1b}) - f_a f_{1b} (1 + \theta_a f_a')(1 + \theta_b f_{1b}') \right] \Big\} \end{aligned} \tag{3.46}$$

The suppression factor $1/(1+\delta_{ab})$ is present in the case of scattering of identical particles $a = b$ to avoid double counting if a and b are indistinguishable. The δ-function imposes energy-momentum conservation. The product F of distribution functions

$$F = f_a' f_{1b}' (1 + \theta_a f_a)(1 + \theta_b f_{1b}) - f_a f_{1b} (1 + \theta_a f_a')(1 + \theta_b f_{1b}') \tag{3.47}$$

contains the statistical factor θ, which depends on the statistic of the particles,

$$\theta_a = \begin{cases} +1 & a \text{ bosons} \\ 0 & a \text{ classical particles} \\ -1 & a \text{ fermions} \end{cases} .$$

---

[5] Sometimes, the kinetic equation is not formulated in terms of particle number normalized distribution functions f_a, but in terms of phase space scaled distribution functions f_a. The relationship between these two is $f_a = g_a/(2\pi)^3 f_a$.

This product of distribution factors F can be interpreted as the change of particles with momentum p due to scattering processes. The first addend with a positive sign corresponds to the gain of particles with momentum p and p_1 by scattering from states p' and p'_1, whereas the second term with the minus sign correspond to the loss by the inverse scattering. For classical particles ($\theta = 0$), the collision term would only be proportional to these two functions f. However, for fermions ($\theta = -1$), one has to make sure that the final state is not occupied yet, and for bosons ($\theta = +1$), scattering is favored if the state is populated. Thus, the classical term is extended by the denoted suppression factor for fermions and by the denoted enhancement factor for bosons, respectively.

3.3.2 Chapman-Enskog expansion

The Chapman-Enskog expansion linearizes the kinetic equation (3.43) in order to find a solution for the distribution functions f_a. Besides the relativistic quantum formulation, it is also possible to treat the non-relativistic or the classical case in a similar way.

The expansion is based on an expansion of the distribution function f_a with the help of a book keeping parameter ϵ,

$$f = f^{(0)} + \epsilon f^{(1)} + \epsilon^2 f^{(2)} + \dots . \tag{3.48}$$

The parameter ϵ is also inserted in the Boltzmann-Uehling-Uhlenbeck-equation (3.43), where spatial and co-moving components defined in Eq. (3.45) are treated separately,

$$\frac{p_\mu}{p_0} U^\mu (\mathcal{D} f_a) + \epsilon \frac{p_\mu}{p_0} \nabla^\mu f_a = \sum_b C_{ab}[f_a, f_b]. \tag{3.49}$$

The convective derivative of f, $(\mathcal{D}f$ is expanded in a similar way.

$$(\mathcal{D}f) = \epsilon (\mathcal{D}f)^{(1)} + \epsilon^2 (\mathcal{D}f)^{(2)} + \dots \tag{3.50}$$

In an approximation scheme for the Uehling-Uhlenbeck equation, each approximation step has to fulfill conservation laws as the full equation does. The hydrodynamic conservation laws impose constraints on $(\mathcal{D}f)^{(i)}$. We see that lowest order of ϵ on the left-hand side of the expanded kinetic equation (3.49) is ϵ^1. The collision term on the right-hand side has to be analyzed by inserting the expansion of the distribution functions in Eq. (3.48) in the collision term in Eq. (3.46). The product of distribution functions leads to many different contributions to one ϵ-order, especially for higher orders. We call $C_{ab}^{(j)}$ a collision function contribution proportional to ϵ^j, it contains distribution function up to order j. The leading order in ϵ of C_{ab} is proportional to ϵ^0.

Thus, the expanded kinetic equation (3.49) contains many orders of ϵ on both sides of the equation. By sorting with respect to powers of ϵ, one obtains an infinite set of coupled equations,

$$\epsilon^j (\mathcal{D}f)^{(j)} + \epsilon^j \frac{p_\mu}{p_0} \nabla^\mu f_a^{(j)} = \quad \epsilon^j \textstyle\sum_b C_{ab}^{(j)} [f_a^{(0)}, \dots, f_a^{(j)}, f_b^{(0)}, \dots, f_a^{(j)}]. \tag{3.51}$$

The truncation of this infinite set of equations to a finite set up to order ϵ^j yields the order $j+1$ of the Chapman-Enskog expansion.

First order

If one only considers terms proportional to ϵ^0 in equation (3.49), on obtains the first order in the Chapman-Enskog expansion. There is only one equation per particle species for the distribution function $f_a^{(0)}$,

$$0 = \sum_b C_{ab}[f_a^{(0)}, f_b^{(0)}]. \tag{3.52}$$

This order corresponds to the free solution with no time evolution of f. The associated hydrodynamic equations are the Euler equations of a fluid. A direct result of equation (3.52) is the distribution function of a free gas in motion with four-velocity U_ν,

$$f_a^{(0)} = \frac{1}{e^{\beta(U_\nu p^\nu - \mu_a)} - \theta_a}. \tag{3.53}$$

In the rest frame of the gas,

$$U_\nu p^\nu = U_0 p^0 - \mathbf{U}\cdot\mathbf{p} = 1\cdot E - 0, \tag{3.54}$$

one directly obtains the more familiar expression for a gas at rest. This conclusion from equation (3.52) can be proved with use of the property

$$f_a^{(0)} f_{1b}^{(0)} (1+\theta_a f_a'^{(0)})(1+\theta_b f_{1b}'^{(0)}) = f_a'^{(0)} f_{1b}'^{(0)} (1+\theta_a f_a^{(0)})(1+\theta_b f_{1b}^{(0)}), \tag{3.55}$$

where $f_a^{(0)}$, $f_b^{(0)}$ are functions defined in Eq. (3.53).

Second order

One now considers terms of order ϵ^0 and ϵ^1 in the expansion (3.48) and sorts equation (3.49) with respect to the orders of ϵ. One obtains coupled equations for the second-order Chapman-Enskog expansion,

$$\begin{aligned} 0 &= \sum_b C_{ab}[f_a^{(0)}, f_b^{(0)}], && (3.56)\\ \frac{p_\mu}{p_0} U^\mu (\mathcal{D}f)^{(1)} + \frac{p_\mu}{p_0}\nabla^\mu f_a^{(0)} &= \sum_b \left(C_{ab}[f_a^{(0)}, f_b^{(1)}] + C_{ab}[f_a^{(1)}, f_b^{(0)}]\right). && (3.57) \end{aligned}$$

As equation (3.56) is the same as (3.52), $f^{(0)}$ stays the same as in the first-order Chapman-Enskog expansion. The remaining task is to determine $f^{(1)}$. We introduce the functions ϕ_a and rewrite the second-order correction of f,

$$f_a^{(1)} = f_a^{(0)} (1+\theta_a f_a^{(0)})\phi_a. \tag{3.58}$$

The F-function in the collision term, which was defined in Eq. (3.47), is linearized in ϕ with this choice of $f_a^{(1)}$,

$$F \to f_a^{(0)} f_{1b}^{(0)} (1+\theta_a f_a'^{(0)})(1+\theta_b f_{1b}'^{(0)}) \left[\phi_a' + \phi_{1b}' - \phi_a - \phi_{1b}\right]. \tag{3.59}$$

The full advective term is more complicated. As the shear component is hidden in the spatial derivative $\nabla^\mu f_a^{(0)}$, it is sufficient to concentrate on this part. Spatial derivatives of first-order distribution functions have the property

$$\partial_\nu f_a^{(0)} = -f_a^{(0)}(1+\theta_a f_a^{(0)})\partial_\nu\left(\frac{p^\lambda U_\lambda - \mu_a}{T}\right), \tag{3.60}$$

and with this expression, the shear part proportional to T^{ij}_{shear} can be extracted. The linearized Boltzmann-Uehling-Uhlenbeck equation for the shear component then reads

$$\begin{aligned} -\frac{p^i p^j}{p_0 T} f_a^{(0)}(1+\theta_a f_a^{(0)}) T^{ij}_{\text{shear}} = \sum_b \frac{g_b}{1+\delta_{ab}} \int & \frac{\mathrm{d}^3 p_1}{(2\pi)^3 2E_{1b}} \frac{\mathrm{d}^3 p'}{(2\pi)^3 2E_a'} \frac{\mathrm{d}^3 p_1'}{(2\pi)^3 2E_{1b}'} \times \\ & \times \Big\{ (2\pi)^4 \delta^{(4)}(p+p_1-p'-p_1')\, |\mathcal{M}_{ab}|^2 \times \\ & \times f_a^{(0)} f_{1b}^{(0)} (1+\theta_a f_a^{(0)\prime})(1+\theta_b f_{1b}^{(0)\prime}) \times \\ & \times \left[\phi_a' + \phi_{1b}' - \phi_a - \phi_{1b}\right] \Big\}. \end{aligned} \tag{3.61}$$

We rewrite ϕ by introducing two new functions[6], the tensor function B_a^{ij} and the scalar function $\mathcal{B}_a$,

$$\phi_a(\mathbf{p}) = \mathcal{B}_a(p)\left(\hat{p}^i\hat{p}^j - \frac{1}{3}\delta^{ij}\right) T^{ij}_{\text{shear}} = B_a^{ij}(\mathbf{p}) T^{ij}_{\text{shear}}, \tag{3.62}$$

---

[6] Sometimes, another definition of the scalar function is used [124]: $B_a^{ij} = \mathscr{B}(p)\left(p^i p^j - \frac{1}{3}\delta^{ij} p^2\right) T^{ij}_{\text{shear}}$.

where the traceless tensor T^{ij}_{shear} is again the shear component of the energy-momentum tensor. It is useful to define the vector

$$\vec{B}^{ij} = \left(B^{ij}_{P_1}, B^{ij}_{P_2}, \ldots, B^{ij}_{P_{N_p}}\right). \tag{3.63}$$

We observe that the right hand side of equation (3.61) acts as a linear integral operator on $\vec{B}^{ij}$,

$$\begin{aligned}
-\frac{p^i p^j}{p_0 T} f_a^{(0)}(1+\theta_a f_a^{(0)}) T^{ij}_{\text{shear}} = \sum_b \frac{g_b}{1+\delta_{ab}} \int & \frac{\mathrm{d}^3 p_1}{(2\pi)^3 2E_{1b}} \frac{\mathrm{d}^3 p'}{(2\pi)^3 2E'_a} \frac{\mathrm{d}^3 p'_1}{(2\pi)^3 2E'_{1b}} \times \\
& \times \Bigg\{ (2\pi)^4 \delta^{(4)}(p+p_1-p'-p'_1) \left|\mathcal{M}_{ab}\right|^2 \times \\
& \times f_a^{(0)} f_{1b}^{(0)} (1+\theta_a f_a^{(0)\prime})(1+\theta_b f_{1b}^{(0)\prime}) \times \\
& \times \left[B_a^{ij\prime} + B_{1b}^{ij\prime} - B_a^{ij} - B_{1b}^{ij}\right] T^{ij}_{\text{shear}} \Bigg\}.
\end{aligned} \tag{3.64}$$

We call the linear operator one the right-hand side $\Box_a$ and rewrite our linearized equation in terms of this operator, skipping T^{ij}_{shear} on both sides,

$$\Box_a \vec{B}^{ij} = -\frac{p^i p^j}{p_0 T} f_a^{(0)}(1+\theta_a f_a^{(0)}). \tag{3.65}$$

This is the final form of the second-order Chapman-Enskog expansion for the shear component. It is a set of linear equations for the distribution function corrections $f_a^{(1)}$, which are hidden in $\vec{B}^{ij}$. There are two remaining tasks if one tends to calculate the shear viscosity in this expansion scheme. First one has to solve this set of linear integral equations, and second one has to relate the resulting distribution functions to the shear viscosity coefficient. After a short outlook concerning higher order Chapman-Enskog expansions, we start with the derivation of the shear viscosity in terms of $f_a^{(1)}$.

Higher orders

Higher orders of the Chapman-Enskog expansion correspond to the Burnett- and Super-Burnett equations [121]. We limit the investigations to second order as it allows the calculation of linear transport coefficients.

Shear viscosity

The energy momentum tensor $T^{\mu\nu}$ in second-order Chapman-Enskog expansion can be expressed in terms of the distribution functions $f_a^{(0)}$ and $f_a^{(1)}$.

$$T^{\mu\nu} = \sum_a g_a \int \frac{\mathrm{d}^3 p}{(2\pi)^3 E_p} \left(f_a^{(0)} + f_a^{(1)}\right) p^\mu p^\nu = T^{(0)\mu\nu} + T^{(1)\mu\nu} \tag{3.66}$$

The tensor consists of the ideal hydrodynamic part (proportional to $f_a^{(0)}$) and the viscous correction part (proportional to $f_a^{(1)}$). The latter is subject of further investigations. We recall that in Eq. (3.16), the non-ideal part of $T^{\mu\nu}$ was related to the shear viscosity coefficient η by the equation

$$T^{(1)ij} = -2\eta T^{ij}_{\text{shear}} \tag{3.67}$$

if we only consider shear stress. We express first $f_a^{(1)}$ in Eq. (3.66) in terms of $\mathcal{B}_a$, as it is defined in Eqs. (3.62) and (3.58),

$$T^{(1)ij} = \sum_a g_a \int \frac{\mathrm{d}^3 p}{(2\pi)^3 E_p} f_a^{(0)}(1+\theta_a f_a^{(0)}) \mathcal{B}_a \left(\hat{p}^k \hat{p}^l - \frac{1}{3}\delta^{kl}\right) T^{ij}_{\text{shear}} p^i p^j. \tag{3.68}$$

After some algebra [121], we obtain

$$T^{(1)ij} = T^{ij}_{\text{shear}} \sum_a \frac{g_a}{5} \int \frac{\mathrm{d}^3 p}{(2\pi)^3 E_p} f_a^{(0)} (1 + \theta_a f_a^{(0)}) \mathcal{B}_a \left(\hat{p}^k \hat{p}^k - \frac{1}{3} \delta^{kl} \right) p_k p_l. \tag{3.69}$$

We perform the sum over k and l, use Eq. (3.67), and obtain the final expression for shear viscosity η in second order Chapman-Enskog expansion in terms of $\mathcal{B}_a$.

$$\eta = \sum_a \frac{g_a}{15} \frac{4\pi}{(2\pi)^3} \int_0^\infty \mathrm{d}p \frac{p^4}{E_p} f_a^{(0)} (1 + \theta_a f_a^{(0)}) \mathcal{B}_a \tag{3.70}$$

With this result, we arrive at an equation for the shear viscosity as a function of distribution function, here expressed in terms of $\mathcal{B}$. The only remaining problem is the determination of $\mathcal{B}$ in practice, starting from the linear equation (3.65). The next section, dedicated to the Sonine expansion, describes one possible solution.

3.3.3 Sonine expansion

In the previous section, we finally obtained a linear equation for the second-order Chapman-Enskog non-equilibrium distribution function (3.65). The unknown structure of the distribution function was mapped to the calculation of the unknown function $\mathcal{B}$,

$$f_a = f_a^{(0)} + f_a^{(1)} = f_a^{(0)} + f_a^{(0)} (1 + \theta_a f_a^{(0)}) \mathcal{B}_a(p) \left(\hat{p}^i \hat{p}^j - \frac{1}{3} \delta^{ij} \right) T^{ij}_{\text{shear}}. \tag{3.71}$$

$\mathcal{B}_a$ (p) is a set of real scalar functions of one variable. We now expand $\mathcal{B}_a$ in terms of orthogonal functions P_a^r,

$$\mathcal{B}_a(p) = \sum_r b_a^r P_a^r(p). \tag{3.72}$$

It is useful to define

$$B_a^{rij}(p) = P_a^r(p) \left(\hat{p}^i \hat{p}^j - \frac{1}{3} \delta^{ij} \right). \tag{3.73}$$

The orthogonality relations for the orthogonal functions P_a^r is

$$\int \mathrm{d}p \frac{p^4}{E_p} f_a^{(0)}(p) \left((1 + \theta_a f_a^{(0)}(p)) \right) P_a^r(p) P_a^s(p) = A_a^{rs} \delta^{rs}. \tag{3.74}$$

For the Boltzmann case, these functions (the *Sonine functions* [126]) are analytically known. This is not the case for the Boltzmann-Uehling-Uhlenbeck equation. But it is no problem to obtain orthogonal functions in a numerical way. These functions will be called generalized Sonine polynomials in this work, and we call the expansion (3.72) Sonine expansion in order to clarify the different kinds of expansions that enter the calculation of transport coefficients. For practical reasons, it is useful to chose a monic basis for the generalized Sonine functions,

$$\begin{array}{rcl} P_a^0(p) & = & 1 \\ P_a^1(p) & = & c_0^{(1)} + p \\ P_a^2(p) & = & c_0^{(2)} + c_1^{(2)} p + p^2 \\ \vdots & \vdots & \ddots \end{array} \tag{3.75}$$

The coefficients $c_{0,1,\ldots}^{(1),1(2),\ldots}$ are determined by the orthogonality relation (3.74). They depend on all parameters that enter this equation, i.e. T, μ_a, and m_a. It has been observed in the past that already few polynomials are sufficient to reach convergence [127, 125]. We see that, starting from Eqs. (3.70) and (3.72), the shear viscosity η is easily expressed in terms of polynomials and expansion coefficients b_a^r,

$$\eta = \sum_a \sum_r b_a^r \frac{g_a}{15} \frac{4\pi}{(2\pi)^3} \int_0^\infty \mathrm{d}p \frac{p^4}{E_p} f_a^{(0)} (1 + \theta_a f_a^{(0)}) P_a^r. \tag{3.76}$$

The calculation of the coefficients b_a^r is shown in the following.

Determination of coefficients

We are close to the work of [125] and [127] in the following lines. The idea is to project on the linearized transport equation in such a way that we obtain a set of linear equations for the coefficients b_a^r. We start with the linear equation for B_a^{ij},

$$\Box_a \vec{B}^{ij} = -\frac{p^i p^j}{p_0 T} f_a^{(0)}(1+\theta_a f_a^{(0)}). \tag{3.77}$$

Now we multiply both sides with the factor $g_a B_a^{rij}$ and integrate over p,

$$\int \frac{\mathrm{d}^3 p}{(2\pi)^3} g_a B_a^{rij} \Box_a \vec{B}^{ij} = -\int \frac{\mathrm{d}^3 p}{(2\pi)^3} g_a B_a^{rij} \frac{p^i p^j}{p_0 T} f_a^{(0)}(1+\theta_a f_a^{(0)}). \tag{3.78}$$

We write B_a^{ij} in terms of the Sonine expansion (3.72) and obtain a linear tensor equation for the Sonine expansion coefficients b_b^s:

$$A_{ab}^{rs} b_b^s = C_a^r. \tag{3.79}$$

The complete expressions of A_{ab}^{rs} and C_a^r are rather lengthy and are explicitly shown in the appendix D.2. The simplification and the methods of solution of the 12-dimensional integrals in the left hand side of Eq. (3.78) are also discussed in this appendix.

3.3.4 Range of validity

As already mentioned in the beginning, the kinetic approach is based on the assumption that each particle propagates classically between two collisions. Hence kinetic theory is valid if the mean free path λ is much larger than the typical range of the interaction d.

$$\frac{\lambda}{d} \gg 1 \tag{3.80}$$

For this reason, kinetic equations are applicable to rarefied gases. For a practical calculation using kinetic theory, it is inevitable to affirm the inequality (3.80). There, one needs an estimate of mean free path and interaction range. We limit the examination of these two quantities to the case of a single component gas, where we follow the methods of [125].
The mean free path λ is usually estimated by calculating

$$\lambda = \frac{1}{n\sigma} \tag{3.81}$$

where n is the particle density[7] and σ is the total cross section. The cross section in the center of mass frame and the invariant matrix element for binary collisions are connected (see e.g. [64]) by the equation

$$\left(\frac{\mathrm{d}\sigma_{ab}}{\mathrm{d}\Omega}\right)_{CM} = \frac{|\mathcal{M}_{ab}|^2}{64\pi^2 E_{CM}^2} \tag{3.82}$$

in the case of equal masses. Since the total cross section σ is momentum dependent, one has to specify the on-shell-momentum $\mathbf{p}$, or alternatively, the Mandelstam variable $s = (p+p_1)^2$. Usually [125], one uses thermal averages like

$$\bar{p} = \frac{\int \mathrm{d}^3\mathbf{p} f^{(0)}(p)|\mathbf{p}|}{\int \mathrm{d}^3\mathbf{p} f^{(0)}(p)} \tag{3.83}$$

or

$$\bar{s} = \frac{\int \mathrm{d}^3\mathbf{p}\mathrm{d}^3\mathbf{p}_1 f^{(0)}(p) f^{(0)}(p_1)(p+p_1)^2}{\int \mathrm{d}^3\mathbf{p}\mathrm{d}^3\mathbf{p}_1 f^{(0)}(p) f^{(0)}(p_1)}. \tag{3.84}$$

The range of interaction can be estimated with the Compton wavelength of the corresponding particle, in natural units just

$$d = \frac{1}{m}, \tag{3.85}$$

---

[7] The expression for a multicomponent gas is more complex; it is discussed in [125].

where m is the mass of the particle. Another possible way is to start from the cross section σ and estimate the range by the hard sphere limit,

$$d = \sqrt{\frac{\sigma}{\pi}}. \tag{3.86}$$

As one sees, the choice of the formulas is not unique. However, they all show the same qualitative behavior.

3.4 Qualitative properties

In the two preceding sections, different ways of calculating transport coefficients have been presented. In this section, qualitative properties of the different coefficients will be discussed, motivated by the fact that transport phenomena are not so familiar to many high-energy physicists. The sometimes counterintuitive dependency of transport phenomena on microscopic situations is reported as well as simple estimates for the different coefficients.

3.4.1 Estimates for transport coefficients

We begin with simple estimates for the various transport coefficients. Simple expressions, even though they are rough estimates of the true values or limited to special situations, are useful because the full expressions from Green-Kubo formalism or Chapman-Enskog expansion are not very clear. The main ingredient of these estimates from kinetic theory of gases is the mean free path

$$\lambda = \frac{1}{n\sigma}, \tag{3.87}$$

which describes the typical distance that a particle is propagating without interaction. The average time that is needed for this distance is called *relaxation time* τ,

$$\lambda = \bar{v}\tau. \tag{3.88}$$

We will call these classical, non-relativistic formulas *mean-free-path estimates* [121].

Electrical conductivity

We proceed in the same order as we did in the previous sections, starting with the electrical conductivity. The application of the kinetic theory of gases to the electrical conductivity of metals was introduced by Drude [128, 129], and the Drude model allows already a basic understanding of the microscopic mechanisms of transport phenomena of charged particles [130].

If one assumes an electron gas in an electric field, one can calculate the average velocity due to the acceleration in the field and the interrupting collisions after a mean free path λ. With the help of this one obtains the Drude formula for electrical conductivity,

$$\sigma_{el} \approx \frac{ne^2\lambda}{\bar{p}} = \frac{e^2}{\sigma\bar{p}}. \tag{3.89}$$

This formula has some shortcomings if the classical thermal average is used to calculate the momentum $\bar{p}$. The situation in metals is better described if the Fermi-Dirac statistic for a gas with high chemical potential and low temperature is used in the calculation. This is the so called Sommerfeld theory which leads to

$$\sigma_{el} \approx \frac{ne^2\lambda}{mv_\alpha}, \tag{3.90}$$

with

$$v_\alpha = \begin{cases} \bar{v} & \text{for classical gases} \\ v_F & \text{for Fermi gases with } T \ll \mu \end{cases},$$

where v_F is the Fermi velocity. The Drude formula expresses a relation that is intuitively clear: Metals with electrons which are less interacting have a better conductivity. This is manifest in Eq. (3.89), since the conductivity is inversely proportional to the total cross section.

Shear viscosity

A simple estimate for the shear viscosity is also found when the mean free path of a classical gas is considered. In contrast to the electrical conductivity σ_{el}, there is a transport of momentum and not of charge, and there is not a gradient in the electrical potential, but in the momentum distribution.
It is shown in elementary textbooks (see e.g. [131]) that one finds a momentum flow if such a gradient is present, and the flow can be associated with a viscosity of

$$\eta \approx \frac{1}{3} n \bar{p} \lambda = \frac{\bar{p}}{3\sigma}. \tag{3.91}$$

In a more careful estimate, one can obtain the more general formula

$$\eta \approx \sum_a \alpha_\eta n \bar{p}_a \lambda_a, \tag{3.92}$$

where the viscosities for different particle species a are summed, and the coefficient

$$\alpha_\eta = \begin{cases} 1/3 & \text{from simple estimate} \\ 4/15 & \text{for ultra-relativistic gases} \\ 0.21 & \text{for non-relativistic gases} \end{cases}$$

depends on the particles in the gas [132, 94, 133]. One should recall that these are expressions for the shear viscosity of a classical, dilute gas. As in section 3.3.4, $\bar{p}$ is the thermal average of the momentum.

Thermal conductivity

The derivation of the thermal conductivity in a mean-free-path estimate is again subject of standard textbooks (see e.g. [131]). The flow that results from a gradient in temperature leads to a thermal conductivity

$$\kappa \approx \frac{N}{12} n \bar{v} \lambda = \frac{N \bar{v}}{12\sigma}, \tag{3.93}$$

where N is the number of degrees of freedom of the particles. It is also possible to express this relation with the help of the shear viscosity coefficient η and the heat capacity c_V,

$$\kappa \approx \frac{1}{2} \alpha_\kappa \eta \frac{c_V}{m}, \tag{3.94}$$

where the factor α_κ depends on the nature of the particles or molecules in the gas,

$$\alpha_\kappa \approx \begin{cases} 2.4 & \text{for 1-atomic gases} \\ 1.9 & \text{for 2-atomic gases} \\ 1.6 & \text{for 3-atomic gases.} \end{cases}$$

In the same way as the electrical conductivity σ_{el} and the shear viscosity η, the thermal conductivity is inversely proportional to the cross section σ. As it was discussed in Sec. 3.1 and 3.2, a conserved current additional to energy density and momentum density is needed in order to have a heat conductivity in the system [133].

Bulk viscosity

The last discussion of qualitative properties concerns the bulk viscosity. Bulk viscosity plays an important role in damping processes of modes in compact stars, but only a minor role in the context of heavy-ion collisions. An important qualitative property of bulk viscosity is the behavior for large temperatures or small particle masses: The bulk viscosity coefficient ζ vanishes in ultra-relativistic systems [119].

3.4.2 Relations between transport coefficients

All transport phenomena with their associated coefficients rely on the same mechanisms: Electric charge, momentum or heat can flow, limited by the interactions of the elementary particles in the system. These interactions enter via a propagator dressing in case of the Green-Kubo method, via an on-shell scattering amplitude in case of the Chapman-Enskog method, or via a mean free path in case of the simple estimates. As these interactions are not influenced by the transport process itself, they are universal for all phenomena, and the question arises if the different coefficients are related to each other.

One of the oldest relation between transport coefficients is the Wiedemann-Franz law [134], which is a relation between the electrical conductivity σ_{el} and the thermal conductivity κ in a metal,

$$\frac{\kappa}{\sigma_{el}} = LT. \tag{3.95}$$

The factor L is called *Lorenz number*, and one of the advantages of the Drude model was the possibility of explaining the empirical formula of Wiedemann and Franz. One can construct the Lorenz number starting from Eq. (3.89) and (3.93).

In the same way, one can construct a relation between other transport coefficients. For instance, from Eq. (3.89) and (3.91), one can construct

$$q_{el}^2 \eta \approx \frac{1}{3} \bar{p}^2 \sigma_{el}, \tag{3.96}$$

which relates the shear viscosity η and the electrical conductivity σ of a dilute gas of particles that carry a charge q_{el}. One may construct more of these relations, but we limit this to Eq. (3.96) which will be used in the following.

3.4.3 Dependency on microscopic input

Density

The particle density in a system is one characteristic property. Naively one would expect that the effect on transport properties is important if the density is changed. It turns out that this is not the case in a wide regime. In a full quantum mechanical system it is difficult to change the particle density independently without modifying the average momentum because of the Pauli principle. However, the total particle number density can be changed by giving the particles more quantum numbers, i.e. by modifying the degeneracy g of each particle species.

This feature of transport in dilute gases can be studies directly from equations (3.64) and (3.70). Assume a single component gas and treat the degeneracy factor g_a as a free parameter. On the one hand, the solution B_a^{ij} of the linearized transport equation scales with g_a^{-1}. On the other hand, the shear viscosity is proportional to $g_a B_a^{ij}$, hence the viscosity does not depend on the degeneracy of the gas. In the mean free path estimates, we gave a formulation of each transport coefficient where the particle density n is canceled out in favor of the cross section σ, thus there is no dependency on density in a dilute classical gas.

This result, may be surprising, has a clear physical interpretation. If the gas is denser, more particles can transport momentum or charge, so the transport properties would increase. But the mean free path decreases in the case of more particles in exactly such a way that the effect is eliminated. This surprising result was first discussed by Maxwell [135, 136].

Coupling

One important property is the qualitative dependency of the transport coefficient η on the microscopic input of interaction. This interaction is coded in the propagator dressing used in the Green-Kubo formulas. It enters in terms of a differential cross section $\mathrm{d}\sigma/\mathrm{d}\Omega$ in the Chapman-Enskog expansion, and in terms of an average cross section in the simple mean free path estimates. A rigorous quantification of the influence of the dressing function at different interactions in time-correlation functions is quite annoying. It is easier to discuss the dependency of transport coefficients on the interaction for special choices of dressing functions, as it was done for example in [112, 107]. The correlators have been evaluated for fermionic and bosonic propagators that

Figure 3.3: Electric system illustrating the difference of an ideal fluid and an ideal gas.

are characterized by a spectral width $\varGamma$ that is related to the importance of interaction: A non-interacting particle would have zero width, and the larger the interaction becomes the more $\varGamma$ can increase. It has been shown in these works (see e.g. [112]) that transport coefficients like η decrease if the interaction is increased.

The demonstration of the influence of the coupling strength is much easier for the formula based on kinetic theory. From (3.61), one can learn that, if $|\mathcal{M}|^2$ or the cross section[8] σ is scaled by a global factor x, η will be scaled by a factor $1/x$. In this sense, we can write

$$\eta, \kappa, \ldots \propto \frac{1}{\sigma}. \tag{3.97}$$

The equation (3.97) becomes an exact algebraical relation in case of the simple mean free path estimates as it is directly seen from Eq. (3.89), (3.91), and (3.93).

Ideal gases and ideal fluids

In viscous hydrodynamics, entropy production and dissipation are included, in contrast to ideal hydrodynamics. Ideal hydrodynamics is the simplest description of a fluid, and an ideal gas is the simplest description of a thermodynamical system. However, these two systems are quite different. We will see that the ideal gas limit does not simply lead to an ideal fluid.

We derived that, if one takes a dilute, weakly interacting gas and studies the transport properties, the ability to transport momentum, charge or other quantities becomes better if the gas is weaker coupled. Thus, transport coefficients describing the gas will become larger if the interaction decreases. This behavior will be found in each microscopic approach. This relation between coupling and transport is counterintuitive especially for viscosity, where many people naively expect a smaller viscosity for fewer interactions. This motivates the more intense discussion of this property of transport phenomena in the following paragraphs, which is not done for shear viscosity, but for electrical conductivity. These coefficients are directly related as it was derived in Eq. (3.96), and it allows us to discuss the counterintuitive behavior of viscous fluids in a more familiar framework.

An example from everyday life which illustrates the behavior is a simple electric circuit, shown in figure 3.4.3. A voltage U is applied to a resistor R, the resulting current I is given by Ohm's law,

$$U = RI. \tag{3.98}$$

In the microscopic description, the electron fluid in the resistance that enables the charge current, has a specific electric conductivity. The conductivity is better if there are less collisions that prevent the electrons from flowing, and hence the resistance is lower. If the electrons interact stronger, the conductivity will decrease and the resistance R is higher. The energy dissipation in a resistor is given by

$$P = \frac{U^2}{R}. \tag{3.99}$$

We see that, if the electron gas is almost free, the resistance is low and lot of energy is dissipated in the system since $P \propto R^{-1}$. If the gas is strongly coupled, the resistance will be higher, leading to less dissipative processes in the hydrodynamical description. As it was discussed above, the

---

[8] It is favorable to formulate this relation in terms of the differential and total cross section than in terms of the invariant matrix element squared. The relation between the two quantities is shown in Eq (3.82).

dependency of transport coefficients on microscopic interactions is always like this, leading to the conclusion that strongly interacting particles form the most ideal fluids.

3.5 Relation between kinetic theory and Green-Kubo-method

In the preceding two sections, two different methods for the calculation of transport coefficients were shown: The time correlation function method and kinetic theory. Since in certain systems both methods apply, the natural question arises if both expressions yield the same results in these cases. First one has to recall that the range of application of both formalisms is not identical. Whereas the Green-Kubo formalism is universal, kinetic theory represents the dilute gas limit. In this section, an overview of different connections between kinetic theory and time-correlation function method is presented.

Already early after the works of Kubo and Green, it was shown that kinetic results can be obtained from Kubo formulas in some limits, which will be summarized first. In the next part, we refer to the calculation of transport in scalar theory using Kubo's method, where it is possible to make a direct connection to the associated kinetic expression. Finally, starting from kinetic theory, we summarize a construction scheme of correlation functions, resulting in a comparison with Green-Kubo formulas.

3.5.1 Low density limit

The comparison of transport theories based on kinetic theory of dilute gases or correlation functions began shortly after the works that established the latter [137]. This first work was based on the master equation and concentrated on a special type of constituents.

A more general derivation of this equivalence in the low-density limit was obtained later. These derivations either rely on diagrammatic expansions [138], or on a generalized master equation [139]. The latter identifies the appearing integral equations and expressions for transport coefficients to be the same as in a similar treatment starting with a Boltzmann equation. The observation of identical integral equations can also be present in a concrete situation, as it is discussed in the next paragraphs.

3.5.2 Identification of integral equations

For the precise demonstration of the equivalence of the time-correlation function method and the kinetic approach, one first has to find a theoretical model where both calculations can be performed. Elaborated calculations of transport in metals can be found in many textbooks about solid state physics (see e.g. [106]), using both methods for mainly electrical conductivity. As we are less interested in this topic and want to focus more on shear viscosity calculations in relativistic quantum field theory, we refer to the corresponding textbooks for these details.

A very simple field theoretical model is ϕ^4-theory or its natural generalization to N fields, the $O(N)$-model. Transport coefficients in scalar theories have been studied in detail in different works (see e.g. [140, 100, 141, 142]) in both frameworks. We follow the works of [142] and sketch the connection between kinetic theory and Green-Kubo correlators in the $O(N)$-model.

In a systematic expansion up to first nontrivial order in $1/N$, the Feynman diagrams contributing to the correlation function can be written as an equation of motion for the scalar propagator and a vertex dressing. Both equations involve an infinite series of iterated diagrams. By analysis of the vertex iteration prescription, one finds that the integral kernel contains the sum of scattering amplitudes and distribution functions that is also present in the collision term of the Boltzmann-Uehling-Uhlenbeck equation. That means that the corresponding interaction terms that would enter in a kinetic description are included in the Green-Kubo formalism because they enter in the vertex dressing.

This link between the two ways of calculating transport properties is made by identifying integral equations that occur in both approaches. Another connection between these fields in the context of scalar theories has been made in an earlier work [122, 143].

3.5.3 On-shell width from two-body cross section

A related approach is the parametrization of particle spectral functions with the help of kinetic theory inputs, i.e. masses and collision rates. Such a work was done in [144] for a description of a pion gas. The idea is sketched in the following, concentrating on (pseudo-)scalar particles. The simple Lorentzian spectral function parametrization

$$\rho(q_0, \mathbf{q}) = \frac{1}{E_q}\left[\frac{\Gamma(q_0,\mathbf{q})}{(q_0 - E_q)^2 + \Gamma(q_0,\mathbf{q}))^2} - \frac{\Gamma(q_0,\mathbf{q})}{(q_0 + E_q)^2 + \Gamma(q_0,\mathbf{q})^2}\right] \tag{3.100}$$

has the parameters m_B, the mass which enters in the energy $E_q = \sqrt{m_B^2 + \mathbf{q}^2}$, and the width Γ_p. This width is related to the complex self energy and can be calculated from the total cross section σ_{tot} for two-body collision. In the dilute gas limit, this yields

$$\Gamma(q_0, \mathbf{q}) = \frac{1}{2}\int \frac{\mathrm{d}^3 k}{(2\pi)^3} e^{-\beta E_k} \sigma_{tot} v_{rel} (1 - \mathbf{v}_q \cdot \mathbf{v}_k) \tag{3.101}$$

The velocities $v = p/E$ belonging to the two momenta are called $\mathbf{v}_q$ and $\mathbf{v}_k$, the relative velocity of the two momenta is called v_{rel}. If the width Γ_q is taken to be on-shell,

$$\Gamma_{on-shell} = \Gamma(E_q, \mathbf{q}), \tag{3.102}$$

the dependency of σ_{tot} even simplifies.

This spectral function can directly be implemented in the Green-Kubo relation for transport coefficients, which has been applied to pion gases [145, 107, 146].

Qualitatively, the result agrees with the transport properties obtained from Kinetic Theory, since

$$\Gamma \propto \sigma_{tot}, \tag{3.103}$$

and it is known that e. g. viscosity goes down as σ_{tot} increases in kinetic theory, and also goes down as the spectral width increases in Green-Kubo formalism. This gets explicit for the static shear viscosity in lowest-order resummation performed in [107],

$$\eta = \frac{1}{10\pi^2 T}\int_0^\infty \mathrm{d}|\mathbf{q}| \frac{|\mathbf{q}|^6}{E_q^2 \Gamma(E_q, \mathbf{q})} n_B(E_q)[1 + n_B(E_q)]. \tag{3.104}$$

In summary one can say that the usage of this parametrization generates the correct cross-section dependency of linear transport coefficients in Green-Kubo formalism.

3.6 Fluidity and Universality

The range of fluids that are candidates for a hydrodynamic description is very large, it reaches from materials known from all-day life, such as air, water, or honey, to very exotic ones, such as trapped cold atoms and quark gluon plasmas. Of course, the properties of all these materials are very different, resulting in the wide range of magnitudes for transport coefficients. In Tab. 3.1, some examples are listed for the viscosity η of different materials.

All these fluids are very different in the nature of their constituents and their macroscopic and microscopic behavior. The question arises if there is a natural fluidity measure[9] that characterizes the fluid. Such a quantity[10] would allow investigations if the (ideal) hydrodynamic description is applicable or how good ideal hydrodynamics works.

There are known examples of dimensionless numbers that characterize hydrodynamical behavior and motion of gases: the *Knudsen number* [149]

$$Kn = \frac{\lambda}{L_{\mathrm{macro}}}, \tag{3.105}$$

---

[9] Sometimes, the ratio $1/\eta$ is called fluidity [147], but here we focus on fluidity measures that are universal, dimensionless quantities that should become small if the ideal fluid is approached.

[10] We are using the term fluidity measure for this general purpose, although it was mainly introduced in one special context [148].

material	temperature T	viscosity η
Glass	$400°C$	$\approx 10^{16}\text{Nsm}^{-2}$
Ice	$-20°C$	$\approx 10^{14}\text{Nsm}^{-2}$
Pitch	$20°C$	$\approx 10^{8}\text{Nsm}^{-2}$
Honey	$20°C$	$\approx 3 \cdot 10^{0}\text{Nsm}^{-2}$
Mercury	$20°C$	$1.55 \cdot 10^{-3}\text{Nsm}^{-2}$
Water	$0°C$	$1.82 \cdot 10^{-3}\text{Nsm}^{-2}$
Water	$20°C$	$1.025 \cdot 10^{-3}\text{Nsm}^{-2}$
Water	$100°C$	$2.88 \cdot 10^{-4}\text{Nsm}^{-2}$
Air	$0°C$	$1.79 \cdot 10^{-5}\text{Nsm}^{-2}$
Hydrogen	$0°C$	$8.8 \cdot 10^{-6}\text{Nsm}^{-2}$

Table 3.1: Viscosity coefficient of different materials at the indicated temperatures. Data taken from [131] (water) and [147] (all other materials).

and the *Reynolds number* [147]

$$Re = \frac{\rho \bar{v} L_{\text{macro}}}{\eta}. \tag{3.106}$$

Both quantities are dimensionless and very important in many physical and technical contexts, but they involve a macroscopic scale of reference L_{macro}. The Knudsen number compares the mean free path λ to this, and in the hydrodynamic regime, $Kn \ll 1$ has to be fulfilled[11]. The Reynolds number is important for the description of turbulent flows. None the two concepts are convincing for a universal treatment because they depend on the macroscopic situation, for instance the cavities in which the fluids are situated. We are looking for intrinsic properties of the fluids.

The characteristic quantities that are related to the deviations of a fluid from the ideal hydrodynamical description are the transport coefficients η, κ, and ζ. The concept of heat conductivity κ is based on the existence of an additional conserved current in the system. Additionally, we saw that the bulk viscosity ζ can get arbitrarily small and vanishes exactly in the ultra-relativistic limit (see Sec. 3.4). Remarkably this does not hold for the shear viscosity — even the viscosity of superfluids is non-vanishing (see e.g. [150]). The possible construction of a fluidity measure based on that coefficient is discussed in the following.

3.6.1 Heisenberg uncertainty relation

A general statement can be derived from Heisenberg's uncertainty principle. In a relatively early work [133], it has been pointed out that quantum mechanical particles in a fluid that carry a momentum $\bar{p}$ cannot be localized in distances smaller than $\bar{p}^{-1}$, hence this limits the possible mean free paths λ to that value,

$$\lambda \bar{p} \geq 1. \tag{3.107}$$

If this limit is put in the viscosity estimate in Eq. (3.91), one obtains

$$\frac{\eta}{n} \gtrsim \frac{1}{3}. \tag{3.108}$$

It is possible to express this relation in terms of entropy density s instead of particle number density n, resulting in

$$\frac{\eta}{s} \gtrsim \frac{1}{15} \qquad \text{or} \qquad \frac{\eta}{s} \gtrsim 1, \tag{3.109}$$

according to the estimates from [151] and [152], respectively. One should emphasize that this estimate is obtained from general considerations of kinetic gas theory and quantum mechanics. All relations are not strict, but have to be understood as estimates up to factors of order unity. However, these relations indicate that η/n or η/s is a dimensionless quantity that cannot be

---

[11] The opposite limit, $Kn \gg 1$, is called the *Knudsen regime*.

arbitrarily small for physical reasons. This seems to be a reasonable fluidity measure, which takes a small value close to the absolute minimum in case of an almost ideal fluid.

Although nowadays this interpretation of the work [133] is common, one should not forget the fundamental assumptions of this estimate. The authors considered a system of "particles" and analyzed the range of quantum mechanical consistency with help of the "mean free path" of the particles. One should mention that the analysis can be understood as the identification of the breakdown of the concept of particles and the mean free path ansatz. Indeed, Eq. (3.107) resembles the estimate of the range of validity of relativistic kinetic theory, which yield $\lambda m \gg 1$ in case of the Compton wavelength estimate for the interaction range (see Sec. 3.3.4).

3.6.2 AdS/CFT Correspondence

A new insight in fluidity was gained by the conjecture of AdS/CFT correspondence [153, 154]. The basic idea is the duality of a conformal field theory on a flat space and a string theory in a higher-dimensional, curved anti-de Sitter space. Despite the lack of a strict proof for the conjecture, this was found to be a powerful technical tool to calculate certain properties of strong interacting field theories that are not accessible with perturbative approaches [155, 156, 157, 158]. The shear viscosity is obtained in the dual supergravity theory from properties of black branes.

Remarkably, the connection between viscosity and gravitation is not so weak. The Green-Kubo expression for shear viscosity, Eq. (3.23), involves a correlator of the energy-momentum tensor $T^{\mu\nu}$, which is coupled to gravity. The diagrammatic expression Eq. (3.38) takes the form of a fermion-loop or boson-loop, coupled to external tensor particles, such as gravitons. There were early derivations of Kubo's expression that used varying gravitational fields to generate a shear response [108], based on an idea that was even formulated earlier by Einstein [159].

After the calculation shear viscosity η in $N = 4$ supersymmetric Yang-Mills theory with a large number of colors in the strong coupling limit [158, 160, 50], it was conjectured that there is a universal lower bound for the ratio of shear viscosity and entropy density s,

$$\frac{\eta}{s} \geq \frac{1}{4\pi}. \tag{3.110}$$

This limit, which will be called *KSS-bound* in the following[12], can be understood as a normalization of viscosity, since the ratio η/s is dimensionless. As the entropy production in a hydrodynamical system is due to viscous effects in the fluid, one can see this quantity as the entropy production over the entropy content of matter.

In contrast to i. e. bulk viscosity which vanishes exactly in the conformal limit, there seems to be a lowest possible value for dissipation processes from shear flow, and an ideal fluid has not zero viscosity, but a small non-vanishing value. Unfortunately it is extremely difficult to calculate shear viscosity and other transport coefficients in candidates for this ideal fluid scenario since it is expected to be in the strong coupling limit. The viscosity estimate

$$\eta \approx \frac{1}{3} n \bar{p} \lambda \tag{3.111}$$

would construct an arbitrarily small value for η/s when n and s stays constant and $\lambda = 1/n\sigma$ is taken to a small value, but this limit violates the underlying assumptions of a classical, non-relativistic, dilute gas enormously, of course. The same statement holds for any application of relativistic kinetic theory, that is also an approach based on a dilute gas of quasi-free particles.

There have been several works concerning the test of this conjecture by investigating various materials that have been measured in experiment [109, 161, 162]. It has been found that a minimal value of η/s is well above the conjectured lower bound for each system that have been measured in experiment, even for counterintuitive cases as liquid helium and other superfluids. In the context of these investigations it was confirmed that the ratio of viscosity and entropy is extremal (mostly minimal) especially in the vicinity of phase transitions and critical points in the specific phase diagrams of the materials [161, 163, 164, 165]. Beside this experimental agreement with an lower bound of the shear viscosity coefficient, there are theoretical considerations indicating

---

[12] The initials KSS stand for Kovtun, Son, and Starinets, the authors of the main contribution to this topic.

that a lower limit for the shear viscosity is required in order to fulfill the Heisenberg uncertainty relation (see Sec. 3.6.1) as well as the generalized second law of thermodynamics [166].
As the underlying formalism is based on a conjecture and the universality of the shear viscosity value of a $N = 4$ supersymmetric Yang-Mills theory is in question, the lower bound of viscosity has been discussed critically. The limitations of the present derivation have been analyzed and possible violations in special systems have been constructed [167, 168, 169].
Finally, other measures of fluidity have been proposed that are inspired by the KSS-bound, but try to adapt the claims obtained from the special AdS/CFT framework to different limits [170, 148]. We will discuss one of these proposals in the following paragraph.

3.6.3 Relativistic and non-relativistic systems

In the following we summarize the fluidity measure proposed by [148]. The authors analyze the circumstances of the derivation of the KSS-bound and find that the conjecture is based on conformal, i. e. ultra-relativistic systems. A generalization to non-relativistic fluids requires a special treatment of the mass terms that enter in the quantities in both regimes in different ways. It is proposed to characterize relativistic and non-relativistic fluids not by their entropy density s, but by their enthalpy density h. This leads to the concept of the *kinematic viscosity*

$$\nu = \frac{\eta}{h}, \tag{3.112}$$

which is seen as a measure of dissipation in a fluid. Indeed, in the two different limits, one obtains

$$\nu = \begin{cases} \frac{\eta}{s} & \text{for the ultra-relativistic limit} \\ & \\ \frac{\eta}{\rho} & \text{for the non-relativistic limit} \end{cases},$$

where $\rho = mn$ is the mass density[13]. The kinematic viscosity ν is a quantity that is naturally discussed in the context of the Navier-Stokes equations. In these fluid equations, under certain side-conditions, only the kinematic viscosity enters. The considerations of the authors lead to the fluidity measure

$$\frac{L_\eta}{L_n} = L_\eta n^{1/3} = \begin{cases} \frac{\eta n^{1/3}}{h c_s} & \text{relativistic} \\ & \\ \frac{\eta n^{1/3}}{\rho c_s} & \text{non-relativistic} \end{cases},$$

which is small in nearly ideal fluids. The formula involves the mass density ρ as well as the speed of sound c_s.

---

[13] This non-relativistic limit assumes that $\mu \gtrsim m$

Chapter 4

Spectral functions

4.1 Properties of spectral functions

In this section, basic properties of spectral functions of scalar bosons and fermions are summarized. As it was motivated in the previous chapter in the calculation of the Kubo formula in Sec. 3.2.3, the main interest is in the NJL quark spectral functions. However, it is illustrative to compare the fermion spectra with the case of scalar theory. The content of this first section can be found to a large extend in [171, 172].

4.1.1 Scalar bosons

A scalar particle with the retarded propagator $D_B^R(q_0, \mathbf{q})$ has the spectral function

$$\rho_B(q_0, \mathbf{q}) = i[D_B^R(q_0, \mathbf{q}) - D_B^A(q_0, \mathbf{q})] = -2\mathrm{Im} D_B^R(q_0, \mathbf{q}). \tag{4.1}$$

The retarded propagator is related to the advanced propagator $D_B^A(q_0, \mathbf{q})$ by the symmetries

$$D_B^R(-q_0, \mathbf{q}) = D_B^{R*}(q_0, \mathbf{q}) = D_B^A(q_0, \mathbf{q}). \tag{4.2}$$

The inversion of the 3-momentum argument has no effect,

$$D_B^R(q_0, -\mathbf{q}) = D_B^R(q_0, \mathbf{q}). \tag{4.3}$$

Hence the symmetry of the scalar spectral function is

$$\rho_B(-q_0, -\mathbf{q}) = -\rho_B(q_0, \mathbf{q}). \tag{4.4}$$

The scalar spectral function obeys the sum rule

$$1 = \int_{-\infty}^{+\infty} \frac{\mathrm{d}q_0}{2\pi} q_0 \rho_B(q_0, \mathbf{q}), \tag{4.5}$$

which can be seen as a normalization condition to ρ_B.
The propagators of a free boson with mass m_B are

$$D_{B,free}(i\omega_q, \mathbf{q}) = \frac{1}{(i\omega_q)^2 - \mathbf{q}^2 - m_B^2} \tag{4.6}$$

$$D_{B,free}^R(q_0, \mathbf{q}) = \frac{1}{q_0^2 - \mathbf{q}^2 - m_B^2 + i\mathrm{sgn}(q_0)\epsilon} \tag{4.7}$$

$$D_{B,free}^A(q_0, \mathbf{q}) = \frac{1}{q_0^2 - \mathbf{q}^2 - m_B^2 - i\mathrm{sgn}(q_0)\epsilon}, \tag{4.8}$$

leading to a spectral function

$$\rho_{B,free}(q_0, \mathbf{q}) = 2\pi \mathrm{sgn}(q_0)\delta(q_0^2 - \mathbf{q}^2 - m_B^2). \tag{4.9}$$

4.1.2 Fermions

The spectral function of a fermion is given by

$$\rho_F(p_0,\mathbf{p}) = i[S_F^R(p_0,\mathbf{p}) - S_F^A(p_0,\mathbf{p})]. \tag{4.10}$$

As it is a matrix function in Dirac space, it is useful to decompose ρ in its different independent Dirac components

$$\rho_F(p_0,\mathbf{p}) = \rho_{F0}(p_0,\mathbf{p})\gamma^0 + \rho_{F3}(p_0,\mathbf{p})\mathbf{p}\cdot\boldsymbol{\gamma} + \rho_{Fs}(p_0,\mathbf{p})\mathbb{1}. \tag{4.11}$$

These components of ρ_F can be projected out using different projectors,

$$\begin{aligned}\rho_{F0}(p_0,\mathbf{p}) =& \frac{1}{4}\mathrm{tr}_{\mathrm{Dirac}}[\rho_F(p_0,\mathbf{p})\gamma_0]\\ \rho_{Fs}(p_0,\mathbf{p}) =& \frac{1}{4}\mathrm{tr}_{\mathrm{Dirac}}[\rho_F(p_0,\mathbf{p})\mathbb{1}].\end{aligned} \tag{4.12}$$

Simple formulas for the symmetries of S_F and ρ_F cannot be provided as easily as in the scalar case (see Eq. (4.2) and (4.4)), because the different Dirac components behave differently. In principle, these symmetries can be derived under the assumption of certain[1] symmetries [171]. A sum rule as in Eq. (4.5) for the Bose case exists for the component proportional to γ^0,

$$1 = \int_{-\infty}^{+\infty} \frac{\mathrm{d}p_{F0}}{2\pi}\rho_0(p_0,\mathbf{p}), \tag{4.13}$$

but not for the other components. A special case are the propagators of a free fermion with mass m_F.

$$S_{F,free}(i\omega_p,\mathbf{p}) = \frac{1}{i\omega_p\gamma^0 - \mathbf{p}\cdot\boldsymbol{\gamma} - m_F} \tag{4.14}$$

$$S^R_{F,free}(p_0,\mathbf{p}) = \frac{1}{(p_0+i\epsilon)\gamma^0 - \mathbf{p}\cdot\boldsymbol{\gamma} - m_F} = \frac{1}{p_0\gamma^0 - \mathbf{p}\cdot\boldsymbol{\gamma} - m_F + i\mathrm{sgn}(p_0)\epsilon\gamma^0} \tag{4.15}$$

$$S^A_{F,free}(p_0,\mathbf{p}) = \frac{1}{(p_0-i\epsilon)\gamma^0 - \mathbf{p}\cdot\boldsymbol{\gamma} - m_F} = \frac{1}{p_0\gamma^0 - \mathbf{p}\cdot\boldsymbol{\gamma} - m_F - i\mathrm{sgn}(p_0)\epsilon\gamma^0} \tag{4.16}$$

The spectral function of a free fermion reads

$$\rho_{F,free} = 2\pi(\not{p} + m_F)\mathrm{sgn}(p_0)\delta(p_0^2 - \mathbf{p}^2 - m_F^2), \tag{4.17}$$

so it has three non-vanishing components if $m_F \neq 0$ and two poles at positive and negative energy $\pm\sqrt{m_F^2 + \mathbf{p}^2}$.

4.1.3 Green's functions in the complex plane

We are now going to investigate the Fermi and Bose Green's functions for a complex energy argument,

$$S_F(z,\mathbf{p}), \qquad D_B(z,\mathbf{p}), \qquad z\in\mathbb{C}. \tag{4.18}$$

The continuation of two-point functions to complex arguments has a long history [173]. The Euclidean formulation of quantum field theory [174], which can be understood as a theory for imaginary 0-component of the 4-momenta, is an indispensable fundament for a nonperturbative treatment of quantum field theory, as it is done in lattice gauge theory or in the Dyson-Schwinger approach.

These properties of spectral functions are based on the assumption of observable degrees of freedom of the theory. This statement is natural for quantum electrodynamics, but applies not in general for quarks. Indeed, one confinement scenario predicts important modifications to spectral properties of confined particles [175, 87], namely the positivity axiom [176, 177], and there are indications that the positivity of quarks in the confined phase is violated [178].

---

[1] Beside parity and time reversal, charge conjugation and chirality may be symmetries of the theory, but are not present in general.

Since quarks in the Nambu-Jona-Lasinio model do not show confinement, it is correct to treat them as observable particles and let them have the same general spectral structure as electrons could have.

The Fermi and Bose propagators as functions of the complex energy variable are analytic in the upper half and in the lower half of the complex plane. They do not have to be analytic on the real axis. When the complex argument z approaches the real axis, one obtains the retarded and advanced propagator, depending on the direction of approach.

$$D_B^R(p_0,\mathbf{p}) = D_B(z\to p_0+i\epsilon,\mathbf{p}) \qquad D_B^A(p_0,\mathbf{p}) = D_B(z\to p_0-i\epsilon,\mathbf{p}) \tag{4.19}$$

$$S_F^R(p_0,\mathbf{p}) = S_F(z\to p_0+i\epsilon,\mathbf{p}) \qquad S_F^A(p_0,\mathbf{p}) = S_F(z\to p_0-i\epsilon,\mathbf{p}) \tag{4.20}$$

In the case of free propagators $S_{F,free}$ and $D_{B,free}$, the only non-analytic points are the mass poles on the real axis[2]. In the general case, both Fermi and Bose 2-point functions have a branch cut on the real z-axis. For scalars, the real part is continuous and the imaginary part changes its sign on the branch cut.

A second important property of S_F and D_B is the asymptotic behavior for large absolute values of the argument z. It is sufficient here to state that they have the same asymptotic behavior as the free propagators have. This topology in complex plane is sufficient to prove the Källen-Lehmann representation

$$S_F(z,\mathbf{p}) = \int_{-\infty}^{+\infty}\frac{\mathrm{d}\omega}{2\pi}\frac{\rho_F(\omega,\mathbf{p})}{z-\omega} \tag{4.21}$$

$$D_B(z,\mathbf{q}) = \int_{-\infty}^{+\infty}\frac{\mathrm{d}\omega}{2\pi}\frac{\rho_B(\omega,\mathbf{q})}{z-\omega} \tag{4.22}$$

with use of Cauchy's integral formula. The Källen-Lehmann representation is an essential identity for the understanding of Green's functions in the complex plane. In particular, one can see the restriction of Euclidean quantum field theory in these equations: Once the retarded function for real energies is obtained for ρ_F and ρ_B, any other object can be calculated by the Lehmann representation, which is an exact equation. Such a relation does not exist for imaginary time Green's functions, they cannot be used to determine exactly the Minkowski Green's functions.

4.2 Calculation of spectral functions

We will now discuss practical calculation of spectral functions for different cases and different frameworks. We will start with the known NJL-results in standard approximation and then switch to more general approaches.

4.2.1 Standard approximation NJL

At first, a summary of spectral functions in Hartree plus Random Phase Approximation is given. A selection of representative spectra is shown in Fig. 4.1. In the different plots, the spectral functions of quarks, pions, and σ-mesons are shown as a function of energy p_0. Due to the symmetries of the spectra, we restrict this to positive values of p_0 at a fixed 3-momentum of $|\mathbf{p}| = 50\,\mathrm{MeV}$. With this choice, we can investigate the spectra for time-like ($p_0 > |\mathbf{p}|$) as well as for space-like ($p_0 < |\mathbf{p}|$) momenta. We discuss the different spectra at the different temperatures in the following.

In vacuum, the δ-peak of the quark spectrum is at a relatively high energy $\sqrt{m_H^2+\mathbf{p}^2}$, and the spectral functions of the scalar and the pseudoscalar channel show a $q\bar{q}$-continuum for energies larger than $\sqrt{(2m_H)^2+\mathbf{p}^2}$. The first of these meson channels has a significant peak closely above the $q\bar{q}$-threshold, which is identified as the σ-mass peak, and the latter as a bound state at the pion mass. These are all spectral contributions at $T=\mu=0$, the imaginary parts of the

---

[2] One can verify this statement directly from Eqs. (4.7) and (4.8) for bosons, and from Eqs. (4.15) and (4.16) for fermions. Note that the sgn-function that is present in all retarded and advanced propagators would lead to an additional branch cut on the imaginary axis. However, this function is multiplied by an infinitesimal imaginary part, so the propagators are really analytic on the imaginary z-axis.

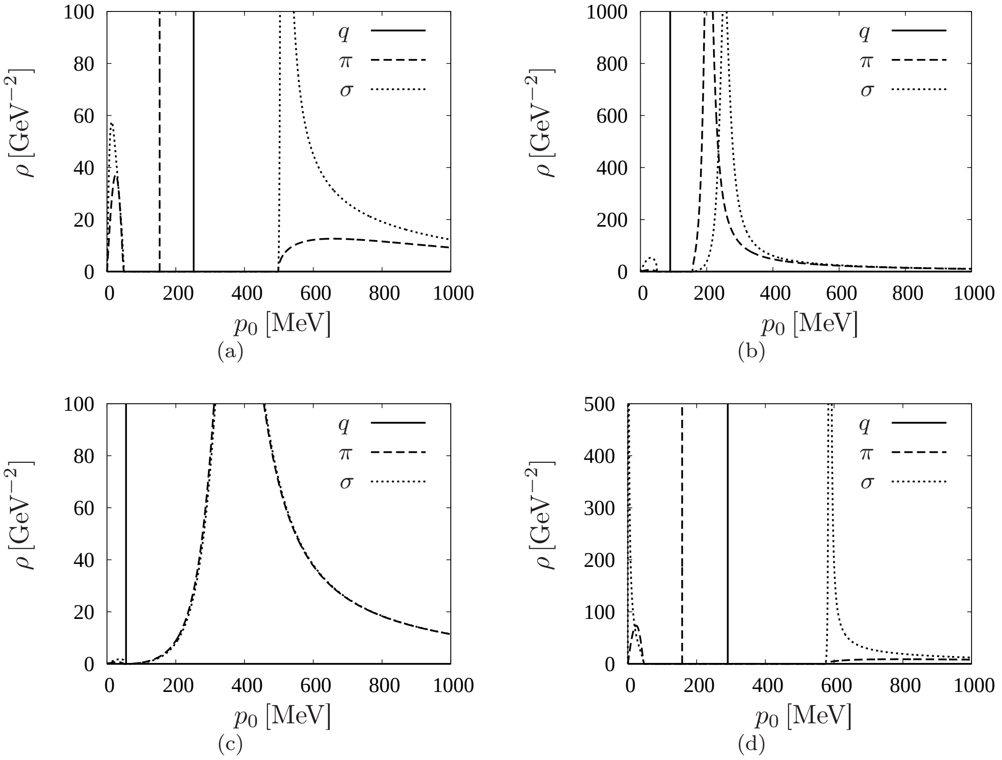

Figure 4.1: Spectral functions of Hartree-quark (or precisely, $\rho_{H\,s}/m_H$, solid line), pion (dashed line) and σ-meson (dotted line), plotted as functions of energy p_0 at 3-momentum $|\mathbf{p}| = 50\,\mathrm{MeV}$ for different values of temperature T and chemical potential μ. We used the Pauli-Villars parameter set 5 from Tab. 2.2, which yields relatively high temperatures for chiral symmetry restoration, but allows the investigation of a spectra at the critical end point. (a) $T = 250\,\mathrm{MeV}$, $\mu = 0$, (b) $T = 270\,\mathrm{MeV}$, $\mu = 0$, (c) $T = 300\,\mathrm{MeV}$, $\mu = 0$, (d) $T \approx T_{CEP}\,\mathrm{MeV}$, $\mu \approx \mu_{CEP}$.

propagators are zero elsewhere. At low temperatures (see Fig. 4.1(a)), the situation is similar as in vacuum, but there is an additional spectral contribution for space-like 4-momenta. This changes beyond the Mott transition where the pion can decay into a quark-antiquark pair since $m_\pi > 2m_H$. Closely above the Mott transition (see Fig. 4.1(b)), the pion mass pole enters the continuum. Sigma and pion are now resonant states with finite widths. The quark mass pole is pushed to lower energies due to restoration of chiral symmetry. At high temperatures in the restored phase (see Fig. 4.1(c)), the Hartree quark mass gets even smaller and the peak is close to $p^2 - \mathbf{p}^2 = 0$. Scalar and pseudoscalar meson are asymptotically degenerate, which is also seen in their spectra. The total spectral weight of the propagators[3] is decreasing at higher temperature. A very special situation is situated close to the critical end point (see Fig. 4.1(d)). As the transition is of second order at this point, a massless scalar excitation is expected in the spectrum. However, the σ mass pole is still slightly above the threshold, and the scalar meson seems to be far from a massless particle. This puzzle was solved [179] with the observation of an increasing spacelike spectral contribution of the σ-meson: The spectrum develops a peak close to $p_0 = 0$. This peak is clearly visible in Fig. 4.1(d).

The standard Nambu-Jona-Lasinio spectra are also affected by the regularization procedure, as it is shown in Fig. 4.2. At high energies, the meson spectra behave differently according to the chosen regularization scheme. For Pauli-Villars regularization, the contribution of the regulators deforms the spectrum in the continuum in such a way that ρ_M even changes its sign. That means that the regularization violates the positivity condition of bosonic spectral functions. This does

---

[3] Note that these meson spectra are not normalized since a coupling constant is involved, see Sec. 2.3.1 for this discussion.

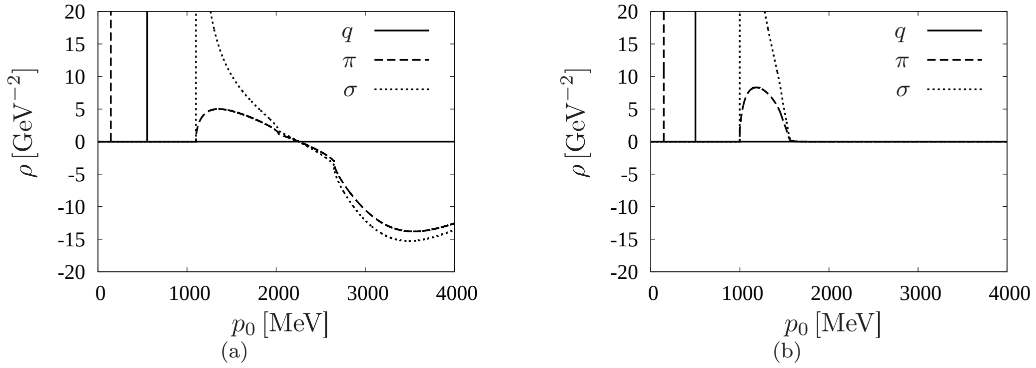

(a)

(b)

Figure 4.2: Spectral functions of π (dashed line) and σ (dotted line) in vacuum, plotted as functions of energy p_0 at $|\mathbf{p}| = 50\,\mathrm{MeV}$. As a comparison, the scalar part of the Hartree quark spectral function divided by m_H is plotted as solid line. (a) Pauli-Villars regularized (Parameters from Tab. 2.2 No 5), (b) Regularized with sharp 3-momentum cut-off (Parameters from Tab. 2.1 No 3).

not happen if the integrals are regularized with a sharp 3-momentum cut-off, but this prescription cuts off the imaginary part at high energies which leads to a vanishing spectral function at a certain energy scale.

4.2.2 NJL quark spectra beyond mean field

Our aim is the calculation of a non-trivial quark spectral function, as it was motivated by the previous chapter. Some general aspects of quark spectral functions and their calculations are found in [180, 181]. In Sec. 2.8, the self-consistent $1/N_c$-expansion up to next-to-leading order of the NJL model was discussed which would lead to propagator dressings with non-trivial spectral properties. The following part will focus on the difficulty of the direct calculation of spectral functions in the NJL model in this context, but the obstacles are quite general.

The direct way to calculate the spectral function is the calculation of the propagator and the successive extraction of the spectral function. The equation of motion for the fermion Green's function S_F reads

$$S_F(p_0, \mathbf{p})^{-1} = S_{F0}^{-1}(p_0, \mathbf{p}) - \Sigma[S_F](p_0, \mathbf{p}). \tag{4.23}$$

The retarded and advanced propagators are obtained for an external momentum $p_0 \to p_0 \pm i\epsilon$. The decomposition of S_F according to the Dirac structure simplifies the calculation, since there are only three and not 16 independent parts[4].

$$S_F(p_0 \pm i\epsilon, \mathbf{p}) = \frac{\gamma^0(p_0 - \Sigma_{F0}) - \boldsymbol{\gamma} \cdot \mathbf{p}(1 - \Sigma_{F3}) + \mathbb{1}(m_0 + \Sigma_{Fs})}{(p_0 - \Sigma_{F0})^2 - (1 - \Sigma_{F3})\mathbf{p}^2 - (m_0 + \Sigma_{Fs})^2 \pm i\mathrm{sgn}(p_0)\epsilon} \tag{4.24}$$

All self-energies $\Sigma_{0,3,s}$ depend on the common argument $(p_0 \pm i\epsilon, \mathbf{p})$. Hence the parts of the spectral function can be written

$$\rho_{0,3,s}(p_0, \mathbf{p}) = i\left[S_{F\,0,3,s}(p_0 + i\epsilon, \mathbf{p}) - S_{F\,0,3,s}(p_0 - i\epsilon, \mathbf{p})\right] \tag{4.25}$$

Thus the self-consistent spectral function requires the three retarded and advanced self-energies. Unfortunately, the calculation of this real momentum quantity is often impossible due to the numerical instability (see Sec. 2.8.4 for the NJL case). Indeed, calculations of quark spectral functions in the NJL model which are based on real-time quantities [182, 183] are not done in a self-consistent scheme. Only few works are dealing with concepts that allow the solution of Dyson-Schwinger equations in Minkowski space-time [184, 185, 186].

---

[4] Of course, the quark spectral function has also color- and isospin indices, but again we treat u and d-quarks as degenerate particles.

Thus, the solution of the self-consistent gap equation (4.23) in Minkowski space-time seems to be impossible in practice, and the spectral functions cannot be obtained directly from the dressed retarded two-point function S_F^R. However, the equation of motion for the propagators may be solved for Euclidean external momenta (see Sec. 2.8.3). The possibility of the reconstruction of spectral function from Euclidean solutions is discussed in the next section.

4.2.3 Spectra from Euclidean field theory

The usual way to solve Dyson-Schwinger equations and discretized quantum field theory on a lattice is the formulation in Euclidean space-time

$$p^2 = -\mathbf{p}^2 + p_0^2 = -\mathbf{p}^2 - p_4^2, \quad p_0 = ip_4, \tag{4.26}$$

that is for imaginary energy or spacelike 4-momentum. The functions $S_F(\mathbf{p}, p_4)$ or $\Sigma_F(\mathbf{p}, p_4)$ are connected to the retarded and advanced expressions, as they both result from the restriction of the functions

$$\mathbb{C}\backslash\mathbb{R} \ni z \mapsto S_F(z, \mathbf{p}) \quad \text{and} \quad \mathbb{C}\backslash\mathbb{R} \ni z \mapsto \Sigma_F(z, \mathbf{p}) \tag{4.27}$$

to two different lines of z in complex plane. As we point out in Sec. 4.1.3, no analytic expression for the reconstruction of the retarded expression from the Euclidean expressions exists. However, since a lot of research is dedicated to the calculation of Euclidean Green's functions, certain methods have been developed to extract the real momentum part anyway. Simple extrapolation schemes from $-p^2$ to $+p^2$, for example via a Padé extrapolation, only lead to the real part of the correlators and the imaginary part stays unknown. Thus we focus on more careful methods of extraction. Two prominent examples for these efforts are given in the following.

The first method which is presented is rather straight forward. It is possible to fit Euclidean two-point functions with some ansatz for the spectrum using the Källen-Lehmann representation (4.21),

$$S_F(\mathbf{p}, p_4) \approx \int_{-\infty}^{+\infty} \frac{\mathrm{d}\omega}{2\pi} \frac{\rho_F^{\text{ansatz}}(\omega, \mathbf{p})}{ip_4 - \omega}. \tag{4.28}$$

A popular ansatz for the spectral function is a two-pole structure [86, 187] which can be written as

$$\rho_F^{\text{ansatz}}(p_0, \mathbf{p}) = Z_1(\not{p} - m_1)\text{sgn}(p_0)\delta(p_0^2 - E_1^2) + Z_2(\not{p} - m_2)\text{sgn}(p_0)\delta(p_0^2 - E_2^2) \tag{4.29}$$

which is a spectrum containing two modes at $\pm\sqrt{m_1^2 + \mathbf{p}^2}$ and $\pm\sqrt{m_2^2 + \mathbf{p}^2}$ instead of a single one. The prefactors Z_1 and Z_2 and the energies of the modes m_1 and m_2 are fitting parameters. This ansatz for the quark spectrum is motivated by the existence of the plasmino mode also found in Hard Thermal Loop (HTL) calculations [172, 188]. However, this type of spectrum is not suitable for a transport calculation since both spectral peaks have zero width, these modes thus do not couple.

The Maximum Entropy Method (MEM)[189, 190, 187] determines the spectral function in a more sophisticated way. The spectral function is interpreted as a probability distribution and the most plausible spectrum for a given Euclidean correlator is determined. This method was even applied to the $1/N_c$ NJL problem [90]. The resulting spectral densities have a rich structure allowing the identification of different modes and excitations. While the position in energy of the spectral contribution is obtained quite well, the absolute height and width of these terms remain uncertain — a disadvantage that is especially present at finite temperature. Unfortunately, these properties of the spectrum are essential for the transport coefficients we tend to extract. Thus even this elaborated method is not suitable since it is not sensitive to the quantities influencing Green-Kubo formulas strongly.

We conclude that there is no method which allows the calculation of a spectral function in a self-consistent scheme that is adapted to the transport problem.

4.3 The method of Self-energy parametrization

In this section, a method for the calculation of a spectral function is presented.

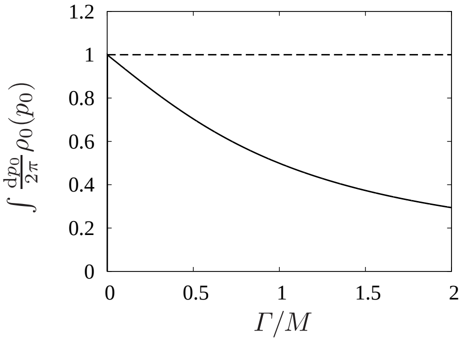

Figure 4.3: Check of the spectral function sum rule Eq. (4.13). The solid line corresponds to the propagator defined in Eq. (4.30), the dashed line to the one from Eq. (4.33), both as a function of the parameter Γ.

4.3.1 Propagator ansätze: Review of the literature

The calculation of the spectral function in a self-consistent scheme that can be used in a transport calculation requires a propagator with the correct analytic structure (because of self-consistency) and nontrivial spectral information (because of transport application). As the usual application of the Kubo formula in literature [142, 112, 113] is made with an ansatz function, one can try to adopt this approach for the solution of the self-consistent gap equation.

One important property of the spectrum ansatz is the validity of the Källen-Lehmann dispersion integral Eq. (4.21), which is a consequence of the analytic structure of the correlator in the complex plane. As the interest is focused on finite temperature and thermal properties the ansatz should also yield a well-behaved thermodynamic potential per volume Ω. It is not so easy to construct an ansatz-function that obeys all these conditions. We first investigate parametrizations of spectral functions used in comparable approaches to transport calculations. There have been several works concerning transport coefficients in quantum field theory with Green-Kubo relations, hence, there are some traditional parametrizations that have been used in practice.

A simple parametrization of a quark propagator is a Breit-Wigner type

$$S_F^R(p_0,\mathbf{p}) = \frac{1}{p_0\gamma^0 - \mathbf{p}\boldsymbol{\gamma} - M + i\mathrm{sgn}(p_0)\Gamma}, \tag{4.30}$$

with the two real constants

$$M > 0, \qquad \Gamma = const. \tag{4.31}$$

Such a parametrization has been used in NJL calculations of shear viscosity [112, 191, 114]. A related parametrization was used in [113], but with the momentum-dependent Γ parameter

$$M > 0, \qquad \Gamma = \frac{\lambda^2}{\sqrt{M^2 + \mathbf{p^2}}}, \qquad \lambda = const. \tag{4.32}$$

This parametrization is favorable because the spectral width Γ should decrease for high 3-momentum. Both parametrizations are not suitable for a self-consistent treatment of the gap equation. First of all, the sum rule (4.13) is violated as shown in Fig. 4.3. The sum rule integral should be equal to one for all parametrizations possible with the form Eq. (4.30) and (4.32). It is shown that this is only the case for small widths Γ, where the formulas take the form of a free Fermi propagator and the sum rule has to be fulfilled. For larger values of Γ the spectral weight decreases. While this normalization problem might be cured by introducing a certain prefactor, an additional complication is present in this parametrization. The form in the complex plane of Eq. (4.30) is not analytic at the places where it is required. There is a discontinuity of the spectral function at $p_0 = 0$ due to the sign-function. Indeed, this discontinuity is also present for the free Fermi propagator, but in that case, the gap is infinitesimally small because the imaginary part is infinitesimal. Furthermore, the polarization loop obtained with such a propagator shows an unexpected behavior because of these non-analyticities. This is discussed in Appendix E.1.

A naive construction for a spectral function is directly based on the expression for the free propagator, Eq. (4.15), by replacing the infinitesimal imaginary part ϵ by a finite value $\mathit{\Gamma}$.

$$S_F^R(p_0, \mathbf{p}) = \frac{1}{(p_0 + i\mathit{\Gamma})\gamma^0 - \mathbf{p}\boldsymbol{\gamma} - M}, \tag{4.33}$$

This parametrization has no discontinuity on the imaginary axis and no sum rule violation (see Fig. 4.3 for a demonstration). A severe artifact of this parametrization is the lack of a thermodynamic potential per volume $\mathit{\Omega}$, and hence all thermodynamic variables. The problem lies in the free part of the thermodynamic potential, which is always infinite. This complication is discussed in detail in Appendix E.2.

4.3.2 Self-energy dispersion relations

A solution to the problem of the propagator parametrization can be constructed by the investigation of the self-energy $\mathit{\Sigma}$. The self-energy has a structure in the complex plane similar to the propagator S: In general, there is a branch cut on the real axis. As it is discussed in appendix E.2, the imaginary part of the self-energy has to decrease for large momentum p_0. These properties are sufficient to state that there is a dispersion relation for the full self-energy

$$\mathit{\Sigma}_{0,3,s}(z, \mathbf{p}) = \sum_{j=0}^{\infty} \varsigma_{0,3,s;\,j} z^j + \int_{-\infty}^{+\infty} \frac{\mathrm{d}\omega}{2\pi} \frac{-2\mathrm{Im}\mathit{\Sigma}_{0,3,s}^R(\omega, \mathbf{p})}{z - \omega}, \tag{4.34}$$

quite similar to the dispersion relation of the propagator S. The subtracted part of the dispersion relation, the sum over the coefficients ς_j, corresponds to the analytic part and the dispersion integral to the part with a branch-cut on the real axis. The full propagator is then obtained by

$$S_F(z, \mathbf{p}) = \frac{1}{z\gamma^0 - \mathbf{p} \cdot \boldsymbol{\gamma} - m_F - \mathit{\Sigma}(z, \mathbf{p})}. \tag{4.35}$$

From arguments similar to the ones in Appendix E.2 one can see that only $\varsigma_{0,3,s;\,j=0}$ can contribute: this self-energy part is real-valued and constant, thus its scalar part $\varsigma_{s;\,j=0}$ is the shift in the effective mass. The functions $\mathrm{Im}\mathit{\Sigma}_{0,3,s}^R(p_0)$ are real functions of a single variable p_0 that are decreasing for large p_0. The Cauchy principle value of the integral in Eq. (4.34) is well defined if the functions $\mathrm{Im}\mathit{\Sigma}_{0,3,s}^R(p_0)$ are sufficiently smooth. The symmetries of these functions result from the symmetries of the propagator and read

$$\mathrm{Im}\mathit{\Sigma}_0^R(-p_0, \mathbf{p}) = +\mathrm{Im}\mathit{\Sigma}_0^R(p_0, \mathbf{p}) \tag{4.36}$$

$$\mathrm{Im}\mathit{\Sigma}_3^R(-p_0, \mathbf{p}) = -\mathrm{Im}\mathit{\Sigma}_3^R(p_0, \mathbf{p}) \tag{4.37}$$

$$\mathrm{Im}\mathit{\Sigma}_s^R(-p_0, \mathbf{p}) = -\mathrm{Im}\mathit{\Sigma}_s^R(p_0, \mathbf{p}) \tag{4.38}$$

The usage of self-energies and dispersion relations is a technique also known in many-body physics and self-consistent approaches in nuclear theory [192]. As a consequence, all analytic properties of the propagator are fulfilled by construction and the sum rule of the spectral function is correct. Self-energy dispersion relations determine solutions of self-consistent equations in a more practicable way than the direct calculation of the propagator S. Instead of calculating functions obeying several side conditions that even complicate the explicit construction of a nontrivial example, three continuous functions of a real variable with few constraints and a set of constants have to be determined. The imaginary parts of the retarded self-energy can be expanded in a function basis $f_{0,3,s}^{(j)}$

$$\mathrm{Im}\mathit{\Sigma}_{0,3,s}^R(p_0, \mathbf{p}) = \sum_j \varrho_{0,3,s}^{(j)}(\mathbf{p}) f_{0,3,s}^{(j)}(p_0) \tag{4.39}$$

with expansion coefficients $\varrho_{0,3,s}^{(j)}$, or a parametrization

$$\mathrm{Im}\mathit{\Sigma}_{0,3,s}^R(p_0, \mathbf{p}) = g_{0,3,s}(p_0, \mathbf{p})\Big|_{\{\mathit{\Gamma}_j\}} \tag{4.40}$$

with a set of parameters $\varGamma_j$ is taken.
With the help of this parametrization of the retarded self-energy, the gap equation can be solved by an iteration process. Starting with initial parameters $\varsigma_{0,3,s}^{(0)}$ and $\varrho_{0,3,s}^{(j)\;(0)}$, on can iterate the equation of motion (4.23). A projection scheme is required that identifies the parameters after each iteration,

$$S_F^{-1\,(a+1)} = S_0^{-1} - \varSigma\Big[S_F^{-1\,(a)}\Big[\varSigma^R_{0,3,s}[\varsigma^{(a)}_{0,3,s},\,\varrho^{(j)\;(a)}_{0,3,s}]\Big]\Big] \tag{4.41}$$

$$\varsigma_{0,3,s}^{(a+1)},\,\varrho_{0,3,s}^{(j)\;(a+1)} \longleftarrow S_F^{-1\,(a+1)}. \tag{4.42}$$

A more direct way of calculating the solution of the self-consistent problem with the parametrized self-energies is the minimization of the thermodynamic potential $\varOmega$ with respect to the expansion coefficients,

$$\min_{\varsigma_{0,3,s},\,\varrho^{(j)}_{0,3,s}} \varOmega\Big[S^R\big[\varsigma_{0,3,s}, \mathrm{Im}\varSigma^R_{0,3,s}[\varrho^{(j)}_{0,3,s}]\big]\Big] \tag{4.43}$$

for the expansion version or

$$\min_{\varsigma_{0,3,s},\,\varGamma_j} \varOmega\Big[S^R\big[\varsigma_{0,3,s}, \mathrm{Im}\varSigma^R_{0,3,s}[\varGamma_j]\big]\Big]. \tag{4.44}$$

for the restricted parametrization. Once this minimization is performed, the self-energy parameters $\varsigma_{0,3,s;\,0}$ and $\varrho^{(j)}_{0,3,s}$ or $\varGamma_j$ are known. The spectral function is obtained from the retarded and advanced propagator which can be calculated using Eq. (4.35) from the retarded self-energy

$$\varSigma^R_{0,3,s}(p_0,\mathbf{p}) = \sum_{j=0}^{\infty} \varsigma_{0,3,s;\,j}\, p_0^j + \int_{-\infty}^{+\infty} \frac{\mathrm{d}\omega}{2\pi}\, \frac{-2\mathrm{Im}\varSigma^R_{0,3,s}(\omega,\mathbf{p})}{p_0 + i\epsilon - \omega} \tag{4.45}$$

and the advanced one, which is obtained by complex conjugation of the integrand.
In summary, it can be said that the parametrization or expansion of the imaginary part of the retarded self-energy is a nice method to construct a valid propagator that is suitable for self-consistent calculations.

4.3.3 Optimization for the practical calculation

In the previous paragraphs, a method was presented which allowed the construction of ansätze for Green's functions with the correct analytic properties. Although these propagators fulfill the conditions that are necessary for the usage in the self-consistent scheme, the practical calculation seems to be still challenging. It seems that the numerical effort that is necessary for the computation of the spectral functions, compared to the prescription in Sec. 4.2.2 increased, since the retarded propagator itself is not known analytically but has to be determined from the dispersion integral in Eq. (4.45) for each evaluation. Moreover, the propagator is not directly obtained from the iteration prescription of an integral equation but from the minimization process in an abstract parameter space described in Eq. (4.43). Finally, the problem is still in a Minkowski formulation, so all appearing numerical integrations are not expected to be stable.
The first point is a technical detail. The parametrization of the imaginary part of the retarded self-energy can be chosen such that the integral (4.45) can be solved analytically. This restricts the set of possible ansatz-functions, but we will construct simple examples where these conditions are fulfilled.
The usage of real-momentum integrals is due to the choice of calculating the thermodynamic potential per volume $\varOmega$ from the real-time propagators. There is no need of this formulation — it has been shown in Sec. 2.8.3 and 2.8.4 that both Euclidean and Minkowski evaluation of the integrals are possible. They yield the same result.

$$\varOmega\Big[S^R\Big] = \varOmega\Big[S^{\mathrm{Matsubara}}\Big] \tag{4.46}$$

The Matsubara propagator $S(i\omega_p,\mathbf{p})$ is obtained by formula Eq. (4.35) from the Matsubara self-energy

$$\varSigma_{0,3,s}(i\omega_p,\mathbf{p}) = \sum_{j=0}^{\infty} \varsigma_{0,3,s;\,j}\,(i\omega_p)^j + \int_{-\infty}^{+\infty} \frac{\mathrm{d}\omega}{2\pi}\, \frac{-2\mathrm{Im}\varSigma^R_{0,3,s}(\omega,\mathbf{p})}{i\omega_p - \omega}. \tag{4.47}$$

If this integral is also analytically solvable, the resulting minimization procedure

$$\min_{\varsigma_{0,3,s},\,\varrho^{(j)}_{0,3,s}} \varOmega\Big[S^{\text{Matsubara}}\big[\varsigma_{0,3,s},\mathrm{Im}\varSigma^{\text{Matsubara}}_{0,3,s}[\varrho^{(j)}_{0,3,s}]\big]\Big] \tag{4.48}$$

or

$$\min_{\varsigma_{0,3,s},\,\varGamma_j} \varOmega\Big[S^{\text{Matsubara}}\big[\varsigma_{0,3,s},\mathrm{Im}\varSigma^{\text{Matsubara}}_{0,3,s}[\varGamma_j]\big]\Big] \tag{4.49}$$

requires only evaluations of Euclidean expressions — and the resulting quantities, the self-energy parameters, determine directly the spectral function without any computational effort or further assumptions. Thus, this self-energy parametrization (SEP) method determines the spectral function in a way such that only Euclidean integrals have to be evaluated.
The remaining task is the minimization of the thermodynamic potential with respect to the parameters. Minimization routines work well if the dependency of the function on the variables (the self-energy parameters) is smooth. It is helpful to choose

$$\mathbb{R}^n \ni \varrho_{0,3,s} \mapsto \mathrm{Im}\varSigma^R_{0,3,s}[\varrho_{0,3,s}] \quad \text{or} \quad \mathbb{R}^n \ni \varGamma_j \mapsto \mathrm{Im}\varSigma^R_{0,3,s}[\varGamma_j] \tag{4.50}$$

to be smooth or linear. The question arises if such a type of parametrization really exists. This question will be answered in the next section.

4.4 Self-energy parametrizations

In the following, three examples are presented fulfilling all conditions to imaginary parts of retarded self-energies mentioned above. We call the different self-energy parametrizations SEP1, SEP2, and SEP3.

4.4.1 Simplest version

The maybe simplest way (called SEP1 in the following) for a self-energy that conserves the analytic properties of the propagator and yields nontrivial transport coefficients is obtained by the two-parameter imaginary part

$$\mathrm{Im}\varSigma_s^{R,\,SEP1}(p_0,\mathbf{p}) = -\varGamma\frac{\lambda p_0}{1+\lambda^2 p_0^2}, \quad \mathrm{Im}\varSigma_0^{R,\,SEP1}(p_0,\mathbf{p}) = \mathrm{Im}\varSigma_3^{R,\,SEP1}(p_0,\mathbf{p}) = 0. \tag{4.51}$$

Only a scalar self-energy is included in this approach, and according to Eq. (4.34), we can add a constant real self-energy term which we call $M - m_0$. The parameters $\varGamma$ and M are the variational parameters of this parametrization while λ is just an arbitrary fixed constant ensuring the correct asymptotic behavior of the self-energy. From these prescriptions, by a dispersion integral (see Appendix E.3 for details) the retarded self-energy

$$\varSigma^{R,\,SEP1}(p_0,\mathbf{p}) = \left(M - m_0 - \varGamma\frac{1}{1+\lambda^2 p_0^2} - i\varGamma\frac{\lambda p_0}{1+\lambda^2 p_0^2}\right)\mathbb{1} \tag{4.52}$$

and the Matsubara self-energy

$$\varSigma^{R,\,SEP1}(i\omega_p,\mathbf{p}) = \left(M - m_0 - \varGamma\frac{1}{1+\lambda|\omega_p|}\right)\mathbb{1} \tag{4.53}$$

are obtained.
An illustration of typical functions resulting from this parametrization is shown in Fig. 4.4. The imaginary part of $\varSigma^R$ at positive p^2 is shown in Fig. 4.4(a), it is the simple parametrized function defined in Eq. (4.51). All other quantities can be derived from this function by the dispersion integral. Note that three rapidly varying complex functions obeying certain conditions are generated by this simple parametrization. The resulting spectral function (shown in Fig. Fig. 4.4(d)) has a peak with a certain width. The energy scale where the peak appears can be seen as the mass of the described particle. The mass is shifted with the parameters M and $\varGamma$[5]

---

[5] An estimate for the peak position for small widths is $M - \varGamma$

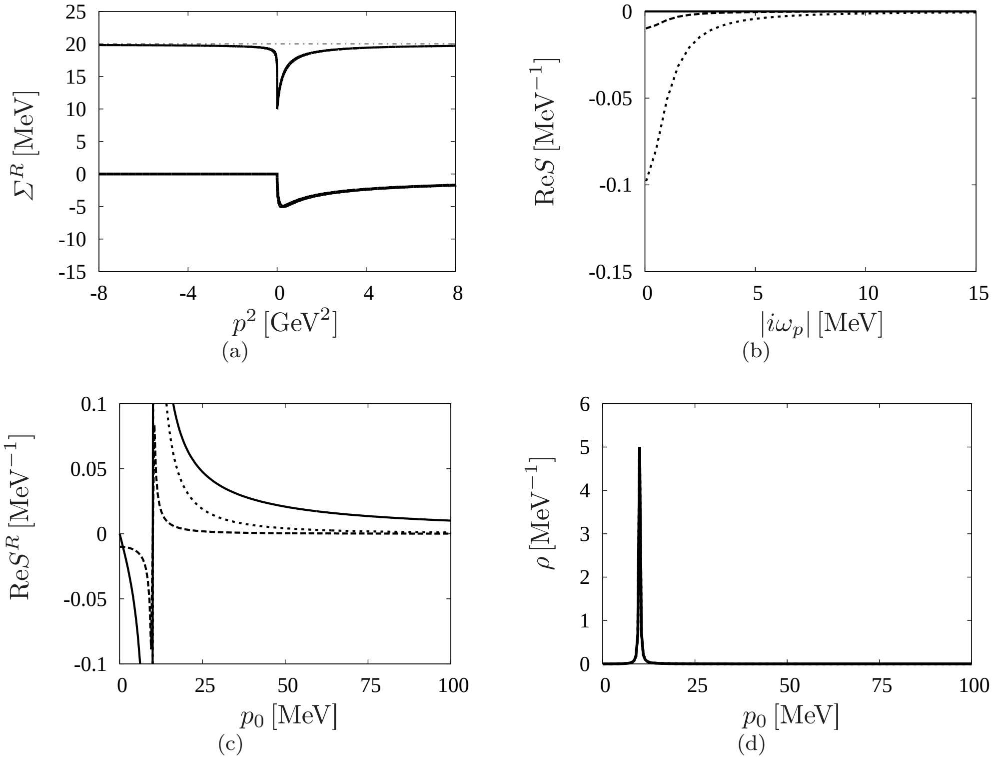

(a) (b)

(c) (d)

Figure 4.4: Illustration of the simplest presented self-energy parametrization SEP1 of Eq. (4.51). (a) Real part (thin line) and imaginary part (bold line) of the scalar self-energy as a function of $p^2 = (p_0 + i\epsilon, \mathbf{p} = 0)^2$. The parameter M is shown as a dotted line. (b) Real Matsubara propagator parts S_3 (dashed line) and S_s (dotted line) as functions of the imaginary frequency $i\omega_p$. (c) Real part of retarded propagator constituents S_0 (solid line), S_3 (dashed line) and S_s (dotted line) as functions of energy p_0 at $\mathbf{p} = 0$. (d) Spectral function ρ_s as a function of energy p_0 at $\mathbf{p} = 0$.

while the width is mainly proportional to the factor Γ. All possible parametrizations from that approach can only change the position and the width of the particle, so no further structure can be generated in this framework.

It is easily seen that Σ^{SEP1} depends smoothly on the two parameters Γ and M. The Hartree self-energy is obtained by the limit

$$\Sigma_H = \lim_{\Gamma\to 0} \lim_{M\to m_H} \Sigma^{SEP1}. \tag{4.54}$$

The construction of a whole basis of functions could be achieved by allowing different functions belonging to different values of the ultraviolet regulator λ. The imaginary part of the self-energy would then be written as

$$\mathrm{Im}\Sigma^{R,\,SEP1\,generalized}(p_0, \mathbf{p}) = \sum_j \Gamma_j \frac{\lambda_j p_0}{1 + \lambda_j^2 p_0^2} \mathbb{1}. \tag{4.55}$$

This idea will not be investigated further, another parametrization is constructed instead.

4.4.2 Grid interpolation

A more direct approach to the full representation of the imaginary part of the retarded self-energy is the usage of a discrete grid of points $(p_0)_i, (|\mathbf{p}|)_j$. The parametrization determines the values of $\Sigma_{0,3,s}$ at the grid points. In between they can be interpolated, outside of the grid an extrapolation can be defined.

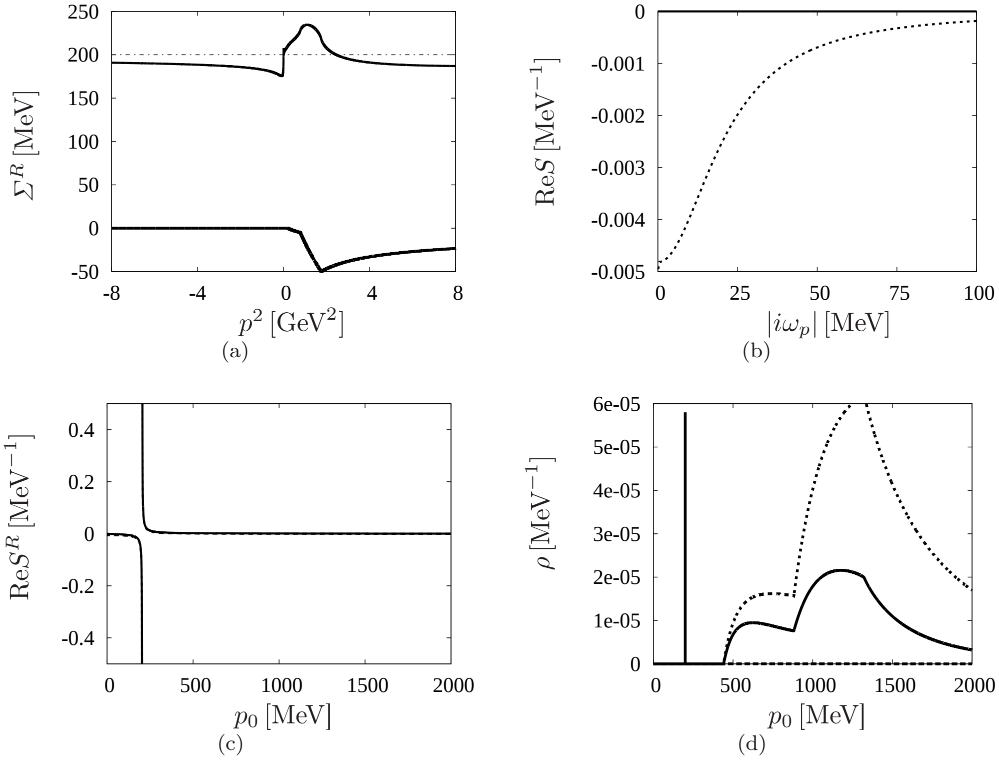

(a) (b) (c) (d)

Figure 4.5: Illustration of grid interpolated self-energy (SEP2). Only a scalar self-energy part is taken with four grid points. (a) Real part (thin line) and imaginary part (bold line) of the scalar self-energy as functions of $p^2 = (p_0 + i\epsilon, \mathbf{p} = 0)^2$. The parameter M_s is shown as a dotted line. (b) Real Matsubara propagator part S_s (dotted line) as a function of the imaginary frequency $i\omega_p$. (c) Real parts of the retarded propagator constituents S_0, S_3, and S_s as functions of the energy p_0 at $\mathbf{p} = 0$. All terms show a similar behavior. (d) Spectral function ρ as a function of the energy p_0 at $\mathbf{p} = 0$. The part ρ_0 is shown as a solid line, the dotted line denotes the scalar part ρ_s.

We restrict this approach (called SEP2 in the following) to a linear interpolated grid with $N_0 \times N_3$ points. The imaginary part of the retarded self-energy reads

$$\mathrm{Im}\Sigma^{R,\,SEP2}_{0,3,s}((p_0)_i, (|\mathbf{p}|)_j) = \Gamma_{0,3,s}((p_0)_i, (\mathbf{p})_j), \quad i,j \in \{1,\ldots,N_0\} \times \{1,\ldots,N_3\} \tag{4.56}$$

After linear interpolation, the imaginary part for $p_0 \in [(p_0)_i, (p_0)_{i+1}]$ and $|\mathbf{p}| \in [(|\mathbf{p}|)_j, (|\mathbf{p}|)_{j+1}]$ can be written as

$$\mathrm{Im}\Sigma^{R,\,SEP2}_{0,3,s}(p_0, \mathbf{p}) = (a^0_{i,j} p_0 + b^0_{i,j})(a^3_{i,j}|\mathbf{p}| + b^3_{i,j}), \tag{4.57}$$

which is a piecewise linear function that is continuous. The parameters $a^{0,3}_{i,j}$ and $b^{0,3}_{i,j}$ can easily be expressed in terms of grid points $\Gamma_{0,3,s}((p_0)_i, (\mathbf{p})_j)$. Outside the grid, the self-energy can be extrapolated in different ways. It is not possible to extrapolate the self-energy in p_0 direction constantly, but it is in principle possible to do this in $|\mathbf{p}|$-direction. One could set the imaginary part to zero outside, but one can also extrapolate it with a decreasing function, such as

$$\mathrm{Im}\Sigma^{R,\,SEP2}_{0,3,s}(p_0 > (p_0)_{N_0}, \mathbf{p}) = (c_j \frac{1}{p_0})(a^3_j|\mathbf{p}| + b^3_j). \tag{4.58}$$

The corresponding real parts are more difficult since all grid points enter into a single value of ReΣ. The derivation and the final result are explicitly shown in Appendix E.4.

In Fig. 4.5 an illustration of a typical self-energy on a grid is shown. For simplicity, the case is restricted to $\mathbf{p} = 0$ and only four grid points. The parametrized imaginary part of Σ^R is shown in

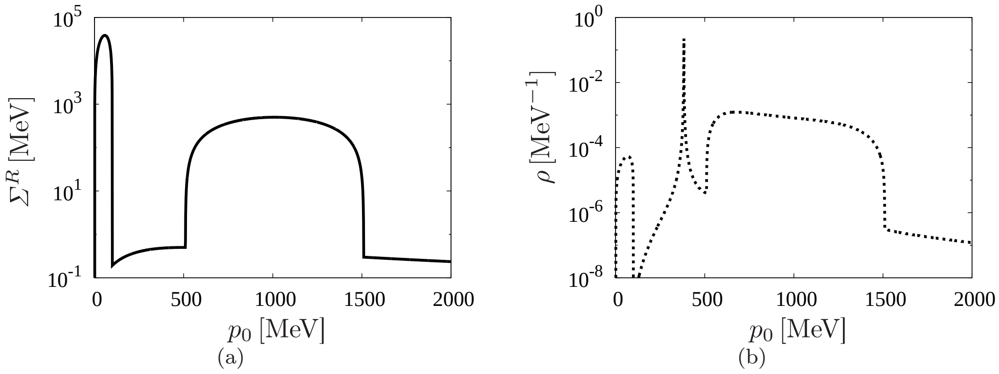

Figure 4.6: Illustration of the intuitive self-energy parametrization SEP3. (a) Imaginary part (bold line) of the scalar retarded self-energy as a function of p_0 at $\mathbf{p} = 100\,\mathrm{MeV}$. (b) Scalar component of the spectral function ρ_s as a function of the energy p_0 at $\mathbf{p} = 100\,\mathrm{MeV}$.

Fig. 4.5(a). The function is first zero, then it opens at a threshold and rises faster after a second threshold. After the last grid point, an extrapolation is performed. The resulting real part shown in the same figure has already a very complex structure. The mass parameter is chosen such that the propagator has a pole below the threshold. The resulting spectral function is shown in Fig. 4.5(d). There is a sharp mass pole and a continuum that opens at higher energies. Note that this complex behavior is modeled with only four self-energy parameters and the mass M.

Like SEP1, also this parametrization depends smoothly on the discrete self-energy values. The Hartree self-energy is obtained by setting the imaginary part to zero and the mass parameter M to the Hartree value m_H. It is obvious that this parametrization can approximate each allowed function in the limit of infinite grid points.

4.4.3 Intuitive parametrization

Although the parametrization SEP2 presented in the previous section is general enough to parametrize all possible forms of Σ, a large basis is needed in practice. On the other hand, guided by physical intuition and experience, one can guess what kind of structure one would expect to appear in spectral densities and complex self-energies (see for instance [64], Fig. 7.1 and 7.2). Considering the RPA meson spectral functions shown in Fig. 4.1, a mass peak is essential in the spectrum, which can be δ-like or broad. Furthermore, a multi-particle continuum at higher frequencies has to be modeled. It is favorable to allow an enhanced spacelike part as it was observed in the meson spectra.

The modeling of the imaginary part of a retarded self-energy which includes these structures is restricted to functions whose Cauchy integral can be solved analytically. One of these functions was presented in the first parametrization SEP1, it can be taken as a starting point in the development. In the grid-interpolated self-energy the imaginary part was a piecewise linear function, which works well. It turns out that the dispersion integral is also solvable analytically if the imaginary part of the retarded self-energy is piecewise a polynomial.

For the modeling of spectra it is sufficient to restrict oneself to the scalar self-energy and neglect vector parts in the self-energy. We write the new self-energy parametrization as a sum of three terms,

$$\begin{aligned}\mathrm{Im}\Sigma_s^{R,\,SEP3}(p_0,\mathbf{p}) =&\mathrm{Im}\Sigma_s^{R,\,SEP1}(p_0)+\\ &+\mathrm{Im}\Sigma_s^{R,\,SEP3,\,\mathrm{cont}}(p_0,\mathbf{p})+\mathrm{Im}\Sigma_s^{R,\,SEP3,\,\mathrm{space}}(p_0,\mathbf{p}),\end{aligned} \tag{4.59}$$

where the first one has exactly the form of SEP1. The second term is thought to model the multi-particle continuum, which is fulfilled with the ansatz

$$\begin{aligned}\mathrm{Im}\Sigma_s^{R,\,SEP3,\,\mathrm{cont}}(p_0,\mathbf{p}) =& -\Gamma_{\mathrm{cont}}(\mathbf{p})\mathrm{sgn}(p_0)\chi_{[E_{\tau_1},E_{\tau_2}]}(|p_0|)\times\\ &\times(p_0^2-(E_{\tau_1}+E_{\tau_2})|p_0|+E_{\tau_1}E_{\tau_2})\end{aligned} \tag{4.60}$$

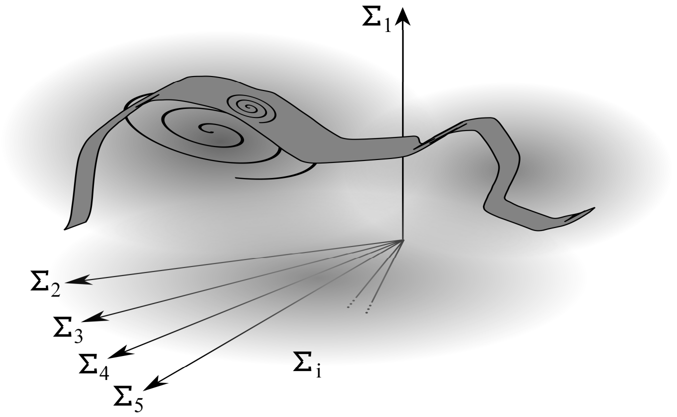

Figure 4.7: Illustration of the SEP method with a restricted parameter space.

where $E_{\tau_{1,2}1} = \sqrt{\tau_{1,2}^2(\mathbf{p}) + \mathbf{p}^2}$ and $\Gamma_{\text{cont}}(\mathbf{p})$, $\tau_1(\mathbf{p})$ and $\tau_2(\mathbf{p})$ are the parametrization inputs. It is possible to create a 3-momentum dependency using a grid interpolation method as it was done in the previous parametrization. This parametrization results in a spectral contribution between the energies τ_1 and τ_2, where $\tau_1 < \tau_2$. The third term is a spectral enhancement at spacelike momenta $p_0^2 - \mathbf{p}^2 < 0$ that can be obtained with the parametrization

$$\mathrm{Im}\Sigma_s^{R,\,SEP3,\,\text{space}}(p_0, \mathbf{p}) = -\Gamma_{\text{space}}(\mathbf{p})\theta(\mathbf{p}^2 - p_0^2)\left(\mathbf{p}^2 p_0 - p_0^3\right) \tag{4.61}$$

The sum of these three terms is the complete imaginary part of the retarded self-energy. The real part for real and complex momenta can be obtained by a dispersion integral that can be solved analytically, as it is shown in Appendix E.5. A typical spectral function obtained from the SEP3 version is shown in Fig. 4.6.

The five parameters of SEP3 are M_{SEP1}, Γ_{SEP1}, Γ_{cont}, τ_1, τ_2, and Γ_{space}. For practical calculation, these parameters are not all suitable for a direct minimization process. First, they do not have the same dimensions, which can be adapted easily by multiplying Γ_{cont} and Γ_{space} with the correct power of the cut-off Λ_q. Second, the condition $\tau_1 < \tau_2$ has to be fulfilled in the whole minimization procedure. Third, the Hesse matrix of the potential at the Hartree solution is singular due to the nonlinear dependency of $\mathrm{Im}\Sigma^R$ on τ_1 and τ_2. It is possible to avoid these complications that come from the non-linear dependency of Σ on the parameters by mapping the parameters to a more appropriate set. This idea will not be investigated further, since the numerical results of the practical calculations are not based on the parametrization SEP3.

4.5 Results

After the introduction of the self-energy parametrization method in Sec. 4.3 and the discussion of possible realizations in Sec. 4.4, we can apply the method to a certain system. We use the method to calculate the quark spectral function in the self-consistent $1/N_c$ expansion in next-to-leading order (see Sec. 2.8). In this section, the results for the calculation of this spectral function ρ_1 are shown, which result from the minimization of the $1/N_c$-corrected thermodynamic potential per volume Ω_1. All results use SEP1 and the Nambu-Jona-Lasinio parameters from Tab. 2.1 with a meson cut-off of $\Lambda_M = 300\,\text{MeV}$.

4.5.1 Interpretation

The practical calculation of the spectral function using the SEP method always requires a limitation in the parameter space. On a finite computer, not infinitely many basis functions or grid points can be used, but one has to restrict the parametrization and minimization of the thermodynamic potential per volume Ω to a finite dimension.

An artist's view of this restriction is shown in Fig. 4.7. The infinite dimensional self-energy parameter space is shown with its basis vectors in Σ_j direction, where Σ_j stands for a variable in a fixed self-energy parametrization. Ω is a scalar function of all these parameters with an absolute minimum, the fixed point of the gap equation, marked with the large spiral. If the self-energy is restricted to a finite set of parameters, the only available points in the self-energy parametrization are those in a small subspace or subset, indicated with a gray band-like structure in the figure. The solution of the minimization procedure will find the absolute minimum on the subspace, denoted with a small spiral within the gray parameter subset. It is obvious that the truncated parametrization will yield a satisfying result if the chosen parametrization is close enough to the real minimum, i. e. if the available spectral functions are realistic.

The solution of the self-consistent next-to-leading order $1/N_c$-expansion of the NJL gap equation was the motivation to develop the SEP method presented in this work. It was essential to treat the meson contributions not only in a perturbative, but in a full self-consistent way. However, in general, the absolute minimum of the thermodynamic potential is outside of the set of spectral functions that is generated with a chosen truncated parametrization of the retarded self-energy. Hence the solution of the minimization procedure with the SEP method does not have to be a fixed point of the NJL gap equation, and the full self-consistency is lost.

The loose of "full self-consistency" turns out to be not a true limitation of the method. First, one should notice that it is in principle a discretization error that is also present in Euclidean solutions — this effect vanishes for very fine discretization, that is for a large set of basis functions. But even in a small basis the obtained result has rich information for phenomenology. For the practical description, the behavior of the SEP-method solution for the propagator S in the gap equation is not the most important feature, but the fact that the mesons are back coupled. Thus the pion is really a composite particle of two fully dressed quarks, and this pion is fully back coupled to the quark again.

The absence of self-consistency affects also the thermodynamic properties, i.e. derivatives of Ω with respect to T and μ. This was already observed for the perturbative ring sum contribution in Sec. 2.7. For example, the temperature derivative of Ω[6] becomes

$$\frac{\mathrm{d}}{\mathrm{d}T}\Omega(\Sigma) = \frac{\partial \Omega}{\partial T} + \sum_j \frac{\partial \Omega}{\partial \Sigma_j}\frac{\partial \Sigma_j}{\partial T}, \tag{4.62}$$

where Σ_j again represents a self-energy parametrization basis. In the SEP method, Ω was minimized with respect to this basis, so all partial derivatives $\partial\Omega/\partial\Sigma_j$ are zero by construction. We conclude that the ambiguity of thermal derivatives in inconsistent potentials are not present in the meson back-coupled SEP method.

4.5.2 Minimization

The thermodynamic potential per volume Ω_1 is a scalar function of the self-energy parameters M and Γ_s. Thus a 2-dimensional minimization procedure can be applied to the problem. As a starting point, the Hartree solution for the same values of temperature and chemical potential can be taken as the initial values of a first calculation. Once a solution for a specific T and μ is obtained with the SEP method, it can be taken as an initial value for the minimization in the vicinity of the specified T-μ constellation. The dependency of Σ on M and Γ_s was chosen such that Σ is a smooth function, yielding a smooth dependency of Ω_1 on the two parametrization variables. There are different suitable algorithms for low-dimensional minimization of a smooth function. In contrast to many other optimization problems, the challenge in this minimization is not the complicated structure of the function Ω itself or the coexistence of many local minima, but the time-consuming evaluation of each point $\Omega(M, \Gamma_s)$. Thus, a good guess for the initial value and a rapid convergence in the vicinity of the fixed point without evaluating the function too often are essential.

For the numerical evaluation, a line search parallel to the M and Γ_s coordinates does not need derivatives of Ω, but is not efficient. The steepest-descent method is reasonable in the vicinity of the absolute minimum, but makes use of the gradients $\nabla_{M,\Gamma_s}\Omega_1$ that have to be determined

---

[6] This quantity is proportional to the entropy density: $s = -\partial\Omega/\partial T$.

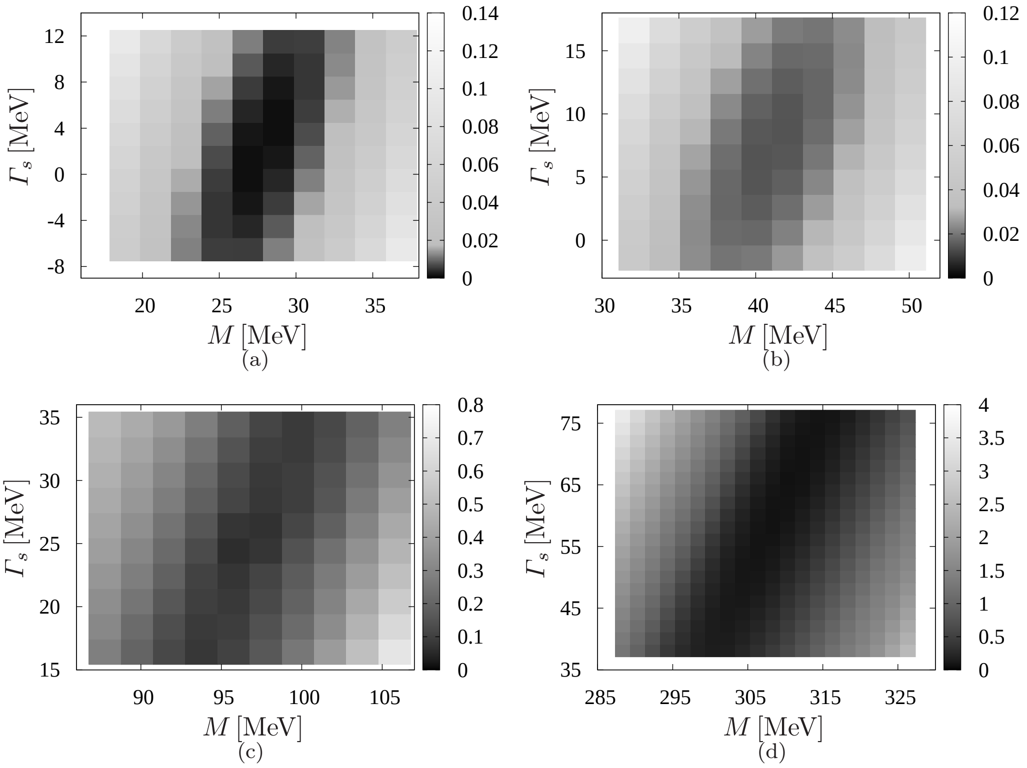

(a) (b) (c) (d)

Figure 4.8: The thermodynamic potential Ω_1 in MeVfm^{-3} as a function of the two SEP1-parameters M and Γ_s. Small values of Ω are coded in black, intermediate values in blue and high values in white. The different figures correspond to different temperatures at $\mu = 0$: (a) $T = 300\,\text{MeV}$, (b) $T = 250\,\text{MeV}$, (c) $T = 200\,\text{MeV}$, and (d) $T = 150\,\text{MeV}$.

by numerical differentiation. The smooth structure of the potential is an advantage when a quasi-Newton method is used, but even for a quasi-Newton algorithm as the Broyden-Fletcher-Goldfarb-Shanno prescription much more evaluations of Ω are needed.

It turns out that at high temperatures[7] the minimum is found quickly, since the starting guess — the Hartree solution — is close enough to the $1/N_c$ corrected solution. The algorithms converge quickly to the minimum nearby. From general considerations, one can expect that the discretization error due to the restricted parametrization basis is not severe at temperatures deeply in the restored phase. For temperatures above the crossover, convergence is reached faster when the initial value for the minimization routine is chosen to be the solution at a proximate temperature. This works for temperatures down to the crossover region.

At low temperatures, the minimization of the thermodynamic potential per volume as a function of the self-energy parameters M and Γ_s fails. The problem is explained in Fig. 4.8 by showing the minimal region of the thermodynamic potential Ω_1 as a function of the two SEP variables for different temperatures. At high temperatures, shown in Fig. 4.8(a) and 4.8(b), the minimum of Ω_1 is clearly visible in a well-behaved minimal region, whereas at low temperatures, see Fig. 4.8(c) and 4.8(d), there is not a well defined minimum anymore, but a large flat region.

The failure of the SEP method using the simplest SEP1 version at low temperatures is not unexpected. The range of spectral functions that can be obtained with this parametrization is limited, all spectra consist of a mass peak with a certain width, even though a richer structure in the spectrum is expected at low temperatures: a pion-quark continuum and a spacelike contribution due to scattering effects with the medium have to be mentioned. Referring to Fig. 4.7 one can say that the subset of allowed parametrized spectral functions is far away from the global minimum

---

[7] The numerical evaluation of the potential Ω_1 is also fast at high temperatures due to the distance between two Matsubara frequencies.

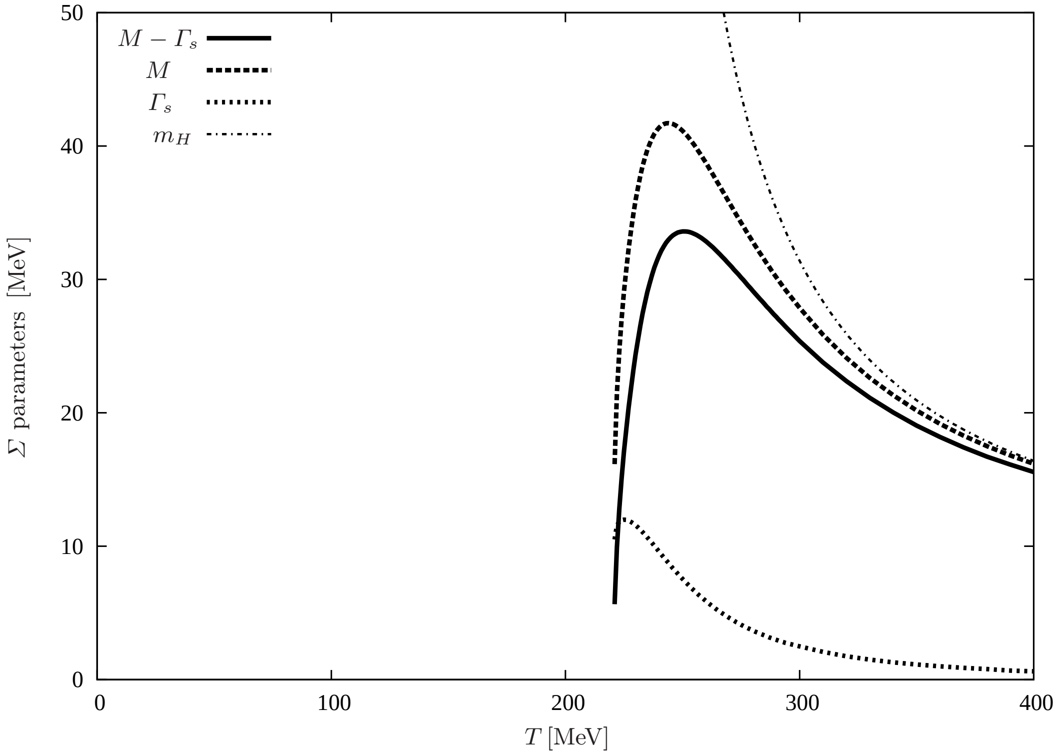

Figure 4.9: SEP 1 parameters as a function of temperature. As a comparison, the Hartree mass for the same NJL parameter set is shown as a thin line.

of Ω_1, so the distance between the projected solution and the real solution increases when the temperature is lowered. Hence, the restriction of the SEP1 choice to the restored phase can be understood as an artifact of the simplicity of the available spectra. Concluding that the meson back coupled self-energies can be calculated for high temperatures, the resulting spectra can be analyzed.

4.5.3 Spectra

The convincing advantage of the SEP method is the immediate access to Minkowski Green's functions and hence to spectral densities, when the self-energy parameters are determined. The parameters M and Γ_S have been calculated in a way sketched in the previous section, their temperature dependency is shown in Fig. 4.9.

In this figure, the constant self-energy part M and the width Γ_s are plotted as well as the approximate peak position $M-\Gamma_s$. For a comparison with the mean-field case the Hartree mass m_H is shown in the plot, too. As in the previous section, the discussion of the result begins at high temperatures, at 400 MeV. The SEP1-parameter M and the Hartree mass m_H are almost equal, the width parameter Γ_s is very small. If the minimum of Hartree thermodynamic potential Ω_H was calculated with the same method, the result would be $M=m_H$ and $\Gamma_s=0$. One observes that the solution of the minimization procedure approaches the mean-field value in the limit of high temperatures. When the temperature decreases, the difference between the Hartree and the $1/N_c$ corrected values grows. The mass parameter M, which is a signal of chiral symmetry breaking, increases, but less strong than in the Hartree case. The width, a pure effect of the mesonic ring sum contribution to the thermodynamic potential, is also increasing, which can be understood as the growing importance of mesonic correlations at lower temperatures. The mass peak position, which is estimated to be the difference of the two minimization parameters, is also increasing. This behavior changes at temperatures directly above the crossover region. The width increases stronger, affirming the assumption that meson effects are strong at the crossover

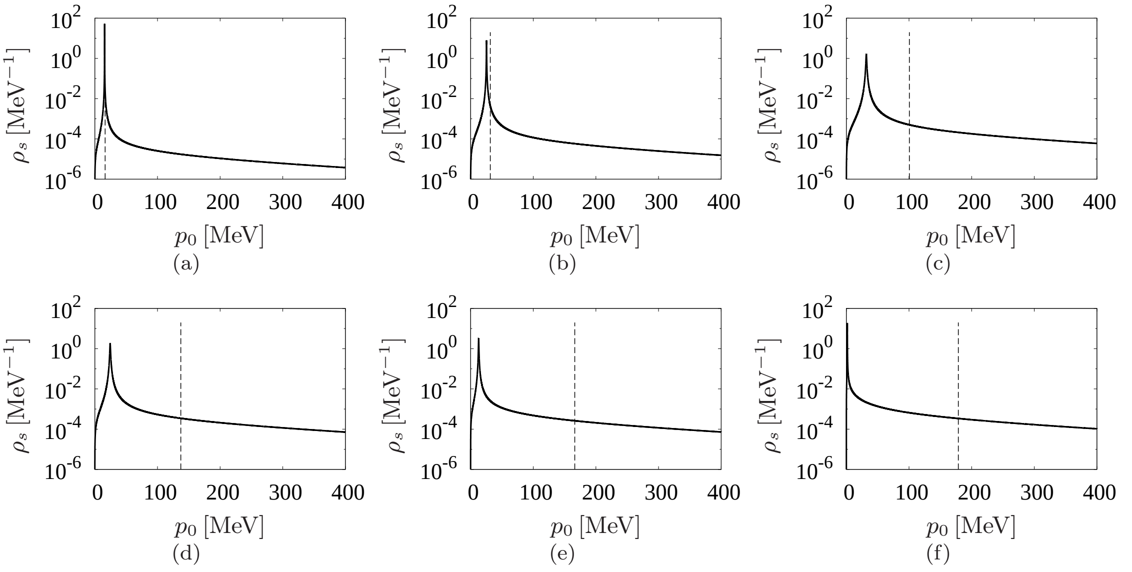

(a) (b) (c) (d) (e) (f)

Figure 4.10: Scalar part of the spectral function ρ_{1s} (solid line) as a function of the frequency p_0 at $\mathbf{p} = 0$ for different temperatures. As a comparison, the δ-like Hartree spectral functions are indicated with dashed lines. (a) $T = 400\,\mathrm{MeV}$, (b) $T = 300\,\mathrm{MeV}$, (c) $T = 240\,\mathrm{MeV}$, (d) $T = 230\,\mathrm{MeV}$, (e) $T = 223\,\mathrm{MeV}$, (f) $T = 220\,\mathrm{MeV}$. Parameter set from Tab. 2.1 No 2.

and in the chirally broken phase. The real self-energy part M decreases when the temperature becomes lower than about 240 MeV, resulting in a mass peak position of $M - \mathit{\Gamma}_s$ that becomes very low. This behavior continues up to the breakdown of the SEP method at about 220 MeV. The spectral functions are obtained by inserting these parameters into the expression for the retarded self-energy. A selection of spectra at representative temperatures is shown in Fig. 4.10. In these plots, the scalar part of the quark spectral function ρ_{1s} is shown as a function of energy. The vector parts would lead to similar curves as it was demonstrated in Fig. 4.4(d). A comparison to the mean-field case can be made since the scalar part of the Hartree quark spectral function at the specific temperature is shown in the same plot. The behavior at high temperature (Fig. 4.10(a)) is not surprising: As it was already understood from the plain parameters the leading order in $1/N_c$ resembles the next-to-leading order. The spectrum constructed from $\mathit{\Omega}_1$ is a narrow peak at low energies, which has approximately the same position as the δ-peak of the Hartree spectral function. The spectral width of the peak is very small. For lower temperatures (see Fig. 4.10(b) and 4.10(c)) the spectrum broadens and the maximum is shifted to higher energies, though the position of the Hartree mass peak moves faster. At even lower temperatures (see Fig. 4.10(d) and 4.10(e)) the difference in the peak positions of ρ_{1s} and ρ_{Hs} becomes more significant, because the mass-peak of the SEP1 solution stops its movement to higher energy and even turns back to lower values, while the Hartree mass continues its growth. In the end (see Fig. 4.10(f)) the peak position falls even below the value for 400 MeV, the highest temperature shown here (Fig. 4.10(a),) and approaches zero.

4.5.4 Thermodynamics

The minimization procedure of the SEP method provides the parameters of the retarded self-energy which allows the calculation of the spectral function. The value of $\mathit{\Omega}_1$ at the minimum is a side product of the calculation. For a homogeneous system, this value is directly connected to the thermodynamic pressure of the system

$$p_1 = -(\mathit{\Omega}_1 - \mathit{\Omega}_1^{vac}) \tag{4.63}$$

in the same way as it was discussed in the case of Hartree thermodynamic quantities in Sec. 2.5.3. The problem is that the value of the vacuum normalization $\mathit{\Omega}_1^{vac}$ is not available because the

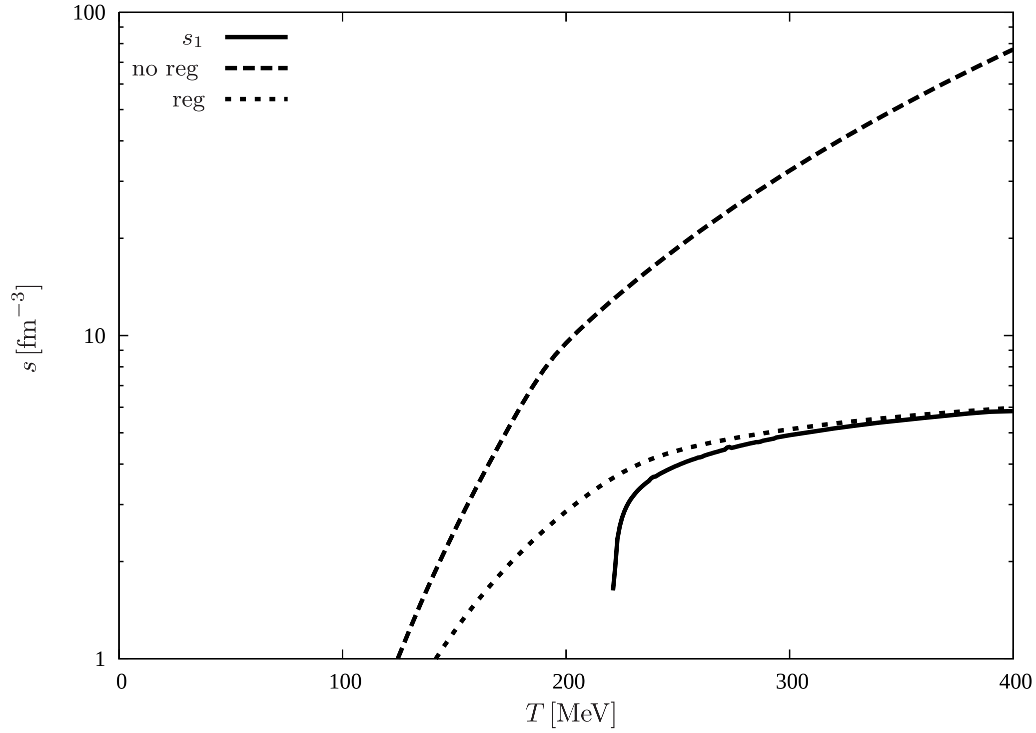

Figure 4.11: Entropy density as a function of the temperature. The values obtained with the SEP method are shown as a bold line, the mean-field results are shown as a dashed line for unregularized medium part (no reg), and dotted line for regularized medium part (reg).

specific ansatz for the method used here turns out to be only applicable at higher temperatures. However, this vacuum constant is not present for derivatives of the thermodynamic potential, for instance for entropy density $s = -\partial\Omega/\partial T$, because the additive constant vanishes in the derivation.

The entropy density s as a function of the temperature T for the results obtained with the SEP method is shown in Fig. 4.11. The SEP-curve is shown as a bold line, and the Hartree curve for the same NJL parameter set is also shown for comparison. As already stated in Fig. 2.9, there is a severe difference at high temperatures between the calculations with regularized medium part and unregularized medium part, so both results are plotted. One observes that the entropy density calculated from Ω_1 is almost equal to the entropy density of a mean-field NJL system — with regularized medium. The asymptotic approach of the $1/N_c$ corrected quantities to the mean-field values was already known from potential, parameters and spectral density, and the fact that it is the entropy density with regularization artifacts that is reached in the restored phase can also be understood. As the SEP method calculates Ω always in the Euclidean formulation, the separation of vacuum and medium is not possible since these parts can only be distinguished in a Minkowski formulation. Thus the medium is regularized in the SEP calculation and the entropy density is clearly below the more physical curve with unregularized medium part. For smaller temperatures approaching the crossover, the SEP curve deviates from the mean-field result to smaller entropy densities. This can be understood as an effect of smaller mass change in $1/N_c$ corrected system, compared to the mean-field constituent quark mass. The Hartree mass peak goes quickly to higher values when approaching the chirally broken region, while the position of the peak in the quark spectrum obtained with the meson-back coupled equation changes less. The more the two spectra differ, the more the corresponding entropy densities deviate from each other.

Chapter 5

Results

5.1 Perturbative NJL viscosity

The simplest transport calculation that can be made within the Nambu-Jona-Lasinio model is probably relativistic kinetic theory applied to bare quarks and antiquarks and their bare scattering amplitudes. For a first study this simple system will be investigated.

5.1.1 Particles and interaction

We decide to describe a system of quarks and antiquarks, hence the degrees of freedom from spin, isospin and color are averaged. We do not average over quarks and antiquarks because their interaction differs fundamentally. For the kinetic approach explained in Sec. 3.3, we need the scattering amplitudes for quarks which interact with quarks and antiquarks, and the scattering amplitudes for antiquarks which interact with quarks and antiquarks. The lowest order diagrams in the coupling g are shown in Fig. 5.1. The $q\bar{q}$-scattering exists in the s- and t-channel. The bare quark propagator is called S_0, so the scattering amplitudes of bare quarks and antiquarks will be called $\mathcal{M}_{q_0\bar{q}_0}$. It is the sum of both terms and reads

$$i\mathcal{M}_{q_0\bar{q}_0} = \sum_M \left[(\bar{v}_1 \varGamma_M u) 2g (\bar{u}' \varGamma_M v_1') + (\bar{v}_1 \varGamma_M v_1') 2g (\bar{u}' \varGamma_M u)\right], \tag{5.1}$$

where the usual notation (for example $v_1' = v(p_1')$) of the Uehling-Uhlenbeck momentum labeling is taken (see Fig. 3.2). The bare scattering of qq has no s-channel but a t- and a u-channel. The summed quark-quark scattering amplitude reads

$$i\mathcal{M}_{q_0 q_0} = \sum_M \left[(\bar{u}' \varGamma_M u) 2g (\bar{u}_1' \varGamma_M u_1) + (\bar{u}_1' \varGamma_M u) 2g (\bar{u}' \varGamma_M u_1)\right]. \tag{5.2}$$

The antiquark-antiquark scattering is obtained by changing the direction of all fermion lines. The spin-averaging of the squared amplitudes are performed in Appendix F.2 for quark-antiquark

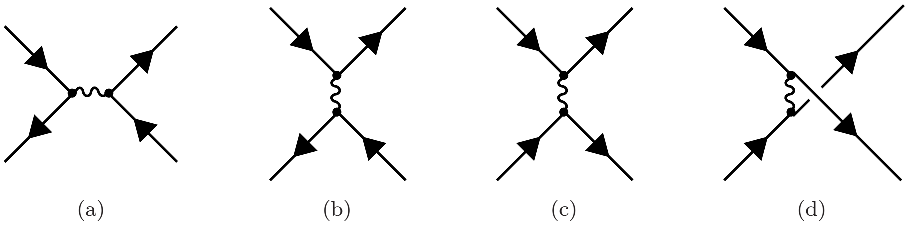

Figure 5.1: Diagrams contributing to $q\bar{q}$-scattering (where (a) correspond to the s-channel and (b) to the t-channel), and to the qq-scattering (where (c) correspond to the t-channel and (d) to the u-channel). The diagrams for $\bar{q}\bar{q}$-scattering are obtained analogously. These are all diagrams up to order g^1 in perturbation theory.

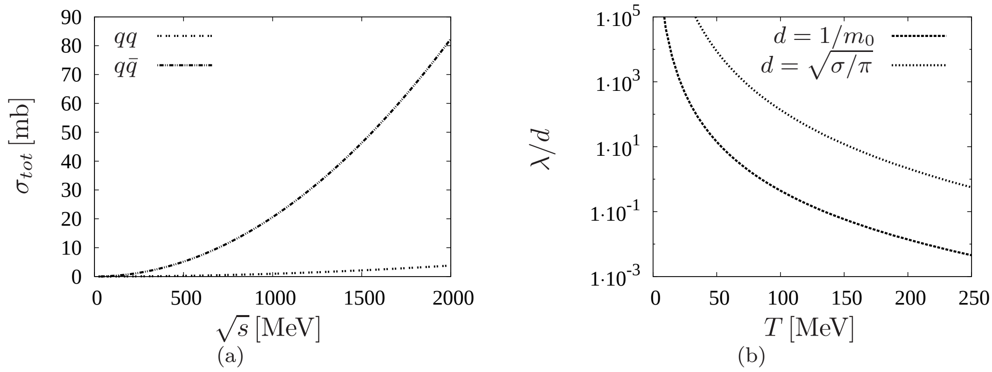

(a) (b)

Figure 5.2: (a) Total cross section of qq- and $q\bar{q}$-scattering in vacuum in lowest order perturbation theory in the NJL model. Note that the cross section increases monotonic with the external momentum. (b) Estimate of λ/d for two different formulas. Parameters from Tab. 2.1 No 2.

scattering, and F.3 for the quark-quark term, respectively. The resulting matrix element square for $q\bar{q}$-processes is

$$\begin{aligned}|\mathcal{M}_{q_0\bar{q}_0}|^2 =& 16g^2\sum_M \left(|\mathcal{M}^s_{q_0\bar{q}_0}|^2\right)_M + \left(|\mathcal{M}^t_{q_0\bar{q}_0}|^2\right)_M \\ &+ \left(\mathcal{M}^s_{q_0\bar{q}_0}\mathcal{M}^{t\,*}_{q_0\bar{q}_0}\right)_M + \left(\mathcal{M}^t_{q_0\bar{q}_0}\mathcal{M}^{s\,*}_{q_0\bar{q}_0}\right)_M,\end{aligned} \tag{5.3}$$

with the direct terms

$$\left(|\mathcal{M}^s_{q_0\bar{q}_0}|^2\right)_M = 4(p_1\cdot p \mp m_0^2)(p'\cdot p'_1 \mp m_0^2) \tag{5.4}$$

and

$$\left(|\mathcal{M}^t_{q_0\bar{q}_0}|^2\right)_M = 4(p_1\cdot p'_1 \pm m_0^2)(p\cdot p' \pm m_0^2) \tag{5.5}$$

and the interference terms

$$\begin{aligned}\left(\mathcal{M}^s_{q_0\bar{q}_0}\mathcal{M}^{t\,*}_{q_0\bar{q}_0}\right)_M =& \left(\mathcal{M}^t_{q_0\bar{q}_0}\mathcal{M}^{s\,*}_{q_0\bar{q}_0}\right)_M = p_1\cdot pp'\cdot p'_1 - p_1\cdot p'p\cdot p'_1 + p_1\cdot p'_1p\cdot p' + m_0^4 \\ &+ m_0^2(\mp p_1\cdot p - p_1\cdot p' \pm p_1\cdot p'_1 \pm p\cdot p' - p\cdot p'_1 \mp p'\cdot p'_1).\end{aligned} \tag{5.6}$$

The resulting matrix element square for qq-processes is

$$|\mathcal{M}_{q_0q_0}|^2 = 16g^2\sum_M \left(|\mathcal{M}^t_{q_0q_0}|^2\right)_M + \left(|\mathcal{M}^u_{q_0q_0}|^2\right)_M + \left(\mathcal{M}^t_{q_0q_0}\mathcal{M}^{u\,*}_{q_0q_0}\right)_M + \left(\mathcal{M}^u_{q_0q_0}\mathcal{M}^{t\,*}_{q_0q_0}\right)_M, \tag{5.7}$$

with the direct terms

$$\left(|\mathcal{M}^t_{q_0q_0}|^2\right)_M = 4(p'\cdot p \mp m_0^2)(p'_1\cdot p_1 \mp m_0^2) \tag{5.8}$$

and

$$\left(|\mathcal{M}^u_{q_0q_0}|^2\right)_M = 4(p'_1\cdot p \pm m_0^2)(p'\cdot p_1 \pm m_0^2) \tag{5.9}$$

and the interference terms

$$\begin{aligned}\left(\mathcal{M}^t_{q_0q_0}\mathcal{M}^{u\,*}_{q_0q_0}\right)_M =& \left(\mathcal{M}^u_{q_0q_0}\mathcal{M}^{t\,*}_{q_0q_0}\right)_M = p'\cdot pp'_1\cdot p'_1 - p'\cdot p'_1p\cdot p_1 + p'\cdot p_1p\cdot p'_1 + m_0^4 \\ &+ m_0^2(\pm p'\cdot p + p'\cdot p'_1 \pm p'\cdot p_1 \pm p\cdot p'_1 + p\cdot p_1 \pm p'_1\cdot p_1).\end{aligned} \tag{5.10}$$

The different signs correspond to the two different interaction channels $\mathit{\Gamma}_\pi$ and $\mathit{\Gamma}_\sigma$, the mass m_0 is the bare quark mass from the Nambu-Jona-Lasinio Lagrangian. In addition to spin averaging, one has to average over isospin and color quantum numbers. The squared invariant matrix elements

$|\mathcal{M}_{q_0\bar{q}_0}|^2$ and $|\mathcal{M}_{q_0 q_0}|^2$ depend on all four relevant momenta[1], hence it is difficult to visualize the behavior of the function. Therefore, the total cross section σ_{tot} is calculated and plotted as a function of Mandelstam-variable s in Fig. 5.2(a). The total cross section increases monotonically with the total energy $\sqrt{s}$. Such a dependency is unphysical because unitarity is violated: the total cross section has to decrease for large momenta. On the one hand, this is an artifact of the Born approximation. On the other hand, the fact that the NJL model can not be renormalized has the same origin. The bare NJL coupling is constant and has no momentum-dependency, thus the interaction stays very strong even for very large momenta. This would not be the case if the coupling is realized by a (heavy) boson: For large momenta, the propagator of the boson would damp the amplitude. One possibility to avoid this effect is the introduction of a cut-off, similar to the regularization of mean-field NJL model: All amplitudes with a 3-momentum larger than a fixed cut-off Λ_q are set to zero. The same cut-off as in the NJL parameters can be used for this purpose.

It is important to check the validity of the kinetic approach for the perturbative NJL quark-antiquark gas (see Sec. 3.3.4). Therefore, the mean-free-path λ and an estimate for the typical range of the interaction are calculated for different temperatures. We use the estimates from Eqs. (3.85) and (3.86) for the interaction range d. The ratio λ/d is shown in Fig. 5.2(b) as a function of temperature T at $\mu = 0$. This ratio is assumed to be large for the kinetic treatment. In the figure, one sees that λ/d for the two different estimates has the same qualitative behavior: A very large value for small temperatures is is going to values smaller than 10 for a temperature of roughly 50 MeV, or 150 MeV, depending on the estimate. The ratio becomes much smaller for larger temperatures. There are two effects driving λ/d down for high temperatures. The thermal momentum increases at higher temperatures and as the cross section gets larger for higher s (see Fig. 5.2(a) discussed in the paragraph above), thus the typical cross section is higher in a hot NJL quark system. The other effect influences the mean free path λ that is inversely proportional to the particle density n_{q_0}. The density of thermally generated quarks and antiquarks is zero in vacuum and rises strongly[2] if temperature increases, and the mean free path of quarks and antiquarks reduces in the dense system. The resulting application range for kinetic theory is limited to low temperature of some tens of MeV. This result is disappointing because the only region in the QCD phase diagram where the idea of perturbative quarks would be realistic is the phase at very high temperatures.

One has to conclude that the kinetic approach with perturbative NJL input works only in the region where it is a unphysical description. In the hot and dense systems, where a perturbative approach may be a better concept, the kinetic description fails. Nevertheless, the results for the shear viscosity η and the ratio η/s are discussed in short in the following, because they will be useful for the understanding of the further investigations in the following sections.

5.1.2 Perturbative viscosity

Shear viscosity of the quark-antiquark system in the NJL model is calculated with relativistic kinetic theory in this section. In the language of Sec. 3.3 this corresponds to $N_P = 2$ with particle species $a \in \{q_0\bar{q}_0\}$. All collision rates $C[f_a, f_b]$ are nonzero. For the solution of the linearized Boltzmann-Uehling-Uhlenbeck equation the non-equilibrium part of the distribution functions (see Sec. 3.3.3) is expanded in generalized Sonine polynomials. This expansion has to be truncated to a finite number of polynomials N_S. We find that the difference in η for $N_S = 1$ and $N_S = 3$ is of the order of 1 %, thus the series converges rapidly.

The shear viscosity η as a function of temperature T is shown in Fig. 5.3 at chemical potential $\mu = 0$. There are three different curves. The first curve uses the full $N_S = 3$ calculation of the Chapman-Enskog expansion with the perturbative NJL scattering kernel calculated in Sec. 5.1.1. As a comparison, the simple estimate from Eq. (3.91) is also plotted. Because of the ultraviolet behavior of the NJL point interaction, a calculation was added which uses a 3-momentum cut-off at Λ_q. All resulting viscosities increase for low temperatures. For very low temperatures one would expect a decreasing viscosity, but this is out of the range of $T > 5$MeV shown here because

---

[1] The momenta of the two particles before and after the cattering, p, p_1, p', and p'_1, are not all independend because of energy-momentum conservation.

[2] Bare quarks are used as interacting particles of the system, so temperature excesses the value of the bare quark mass of few MeV very early.

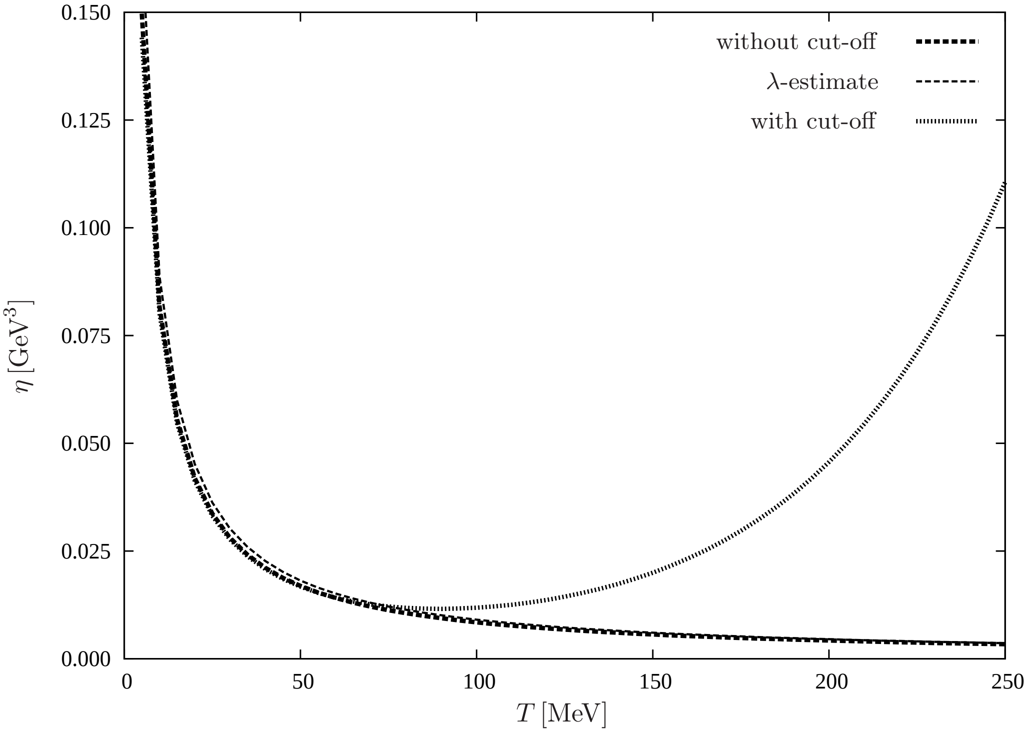

Figure 5.3: Shear viscosity of NJL quarks in lowest order perturbation theory as a function of temperature T at $\mu = 0$. The different lines correspond to the calculation without cut-off, the estimate using the formula $\eta = \bar{p}/3\sigma$ and the regularized scattering amplitudes. Recall the validity range estimate in Fig. 5.2(b). Parameters from Tab. 2.1 No 2.

the bare quark mass is so small. All three formulas for shear viscosity yield a similar result in the low-temperature regime. Close to the vacuum, the two calculation with different cross sections are very similar, because the high momenta where the regularized and the unregularized matrix element differ are not occupied thermally. When temperature increases, the calculation without cut-off is still very close to the estimate $\eta = \bar{p}/3\sigma$, and both curves continue their drop. This is mainly an effect of the total cross section shown in Fig. 5.2(a). The cross section increases if momentum increases, and the hotter the system gets the harder the momenta become. With increasing averaged cross section, viscosity has to go down. The η-curve for the calculation including a 3-momentum cut-off deviates visibly from the two other curves for temperatures higher than about 70 MeV. For higher temperatures the qualitative behavior of viscosity for the different scattering amplitudes differs: The transport coefficient with regularized couplings has a minimum at $T \approx 90\,\mathrm{MeV}$ and increases if the system becomes hotter. This behavior is a result of the modified ultraviolet part of the regularized cross section: The thermal average of the cross section involves harder momenta for higher temperatures, and the drop in $|\mathcal{M}|^2$ results in an increasing shear viscosity. This is a general statement for temperature-independent inputs of kinetic theory, because this qualitative behavior of averaged momentum $\bar{p}$ and UV-behavior of $|\mathcal{M}|^2$ is universal.

With the entropy density s of the system, the ratio of shear viscosity over entropy density η/s can be calculated as well. This plot is shown in Fig. 5.4. The two curves correspond to the scattering without cut-off, and with cut-off, respectively. As it was pointed out in the discussion of shear viscosity in Fig. 5.3, both calculations are very similar at low temperatures. Entropy density increases rapidly at low temperature and approaches quickly the ultra-relativistic Stefan-Boltzmann limit because of the small bare quark masses. This leads to a very large ratio η/s for low temperatures. As temperature increases, the shear viscosity over entropy density becomes smaller. This drop stops for the regularized cross section at about $\eta/s = 1$ for T between 100 MeV and 250 MeV while η/s of unregularized $|\mathcal{M}|^2$ continues its decline. The latter even falls

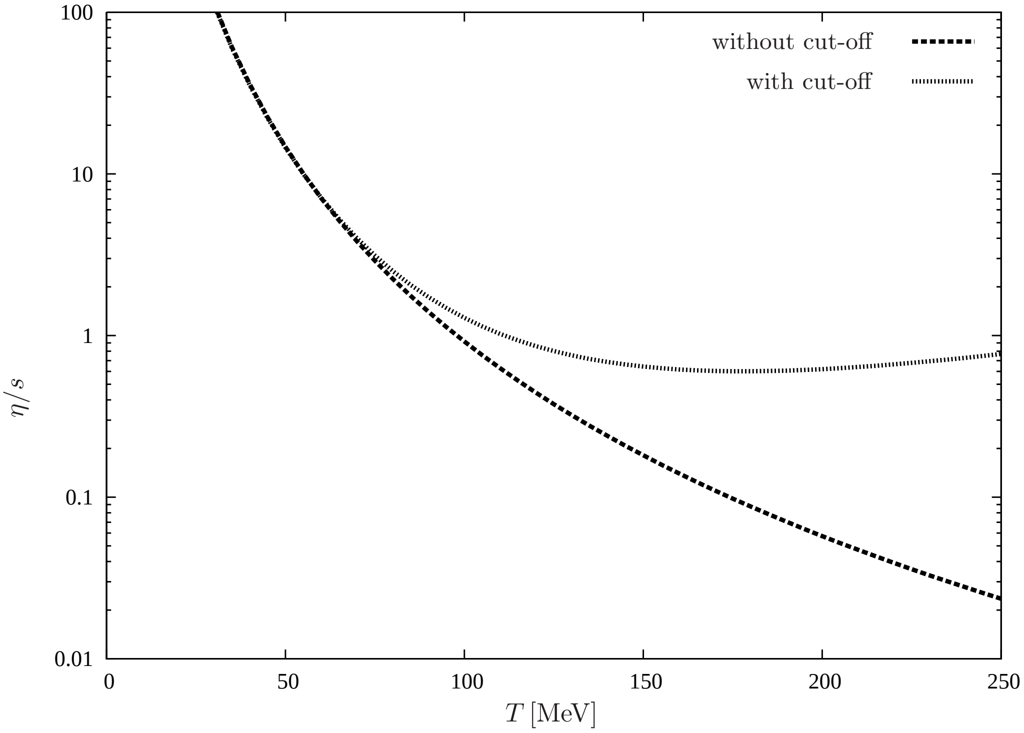

Figure 5.4: Ratio of shear viscosity η and entropy density s as a function of temperature T at $\mu = 0$. Particles and interactions are obtained from the NJL model in lowest order perturbation theory. The different lines correspond to the calculation without cut-off and the regularized scattering amplitude. Recall the validity range estimate in Fig. 5.2(b). Parameters from Tab. 2.1 No 2.

below the value of $1/4\pi$, but only at values for T where the kinetic description can not be applied and the whole calculation is not valid.

5.2 Quarks exchanging RPA mesons

In the previous section bare NJL quarks interacting via their perturbative coupling were investigated. A more accurate system is a system of Hartree quarks and antiquarks. Their scattering was described as the exchange of an RPA meson in Sec. 2.3. The transport properties of such a system are discussed in the following.

5.2.1 Scattering amplitudes

The Nambu-Jona-Lasinio model in Hartree approximation was presented in Sec. 2.2. The dressed propagator has a large constituent quark mass m_H in vacuum. The quark-antiquark interaction is resummed to an RPA meson exchange. If one restricts the terms to one-meson exchange, the possible diagrams are listed in Fig. 5.5. As the RPA meson is an s-channel resummed bare amplitude, the same types of diagrams as for the bare interaction discussed in the previous section appear.
$q\bar{q}$-scattering in s- and t-channel yields a scattering amplitude $\mathcal{M}_{q_H\bar{q}_H}$ of

$$i\mathcal{M}_{q_H\bar{q}_H} = \sum_M \left[(\bar{v}_1 \mathit{\Gamma}_M u) D_M(s) (\bar{u}' \mathit{\Gamma}_M v_1') + (\bar{v}_1 \mathit{\Gamma}_M v_1') D_M(t) (\bar{u}' \mathit{\Gamma}_M u)\right], \tag{5.11}$$

The summed quark-quark scattering amplitude of t- and u-channel reads

$$i\mathcal{M}_{q_H q_H} = \sum_M \left[(\bar{u}' \mathit{\Gamma}_M u) D_M(t) (\bar{u}_1' \mathit{\Gamma}_M u_1) + (\bar{u}_1' \mathit{\Gamma}_M u) D_M(u) (\bar{u}' \mathit{\Gamma}_M u_1)\right]. \tag{5.12}$$

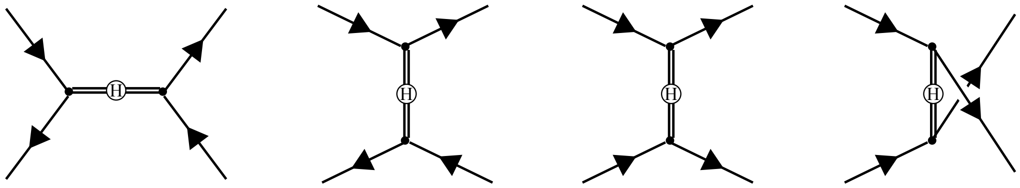

(a) (b) (c) (d)

Figure 5.5: Diagrams contributing to $q\bar{q}$-scattering (Fig. 5.1(a) in s-channel and 5.1(b) in t-channel) and qq-scattering (Fig. 5.1(c) in t-channel and 5.1(d) u-channel). The diagrams for $\bar{q}\bar{q}$-scattering are obtained by inversion of the qq terms. These are all possible diagrams constructed by a one-meson exchange.

The spin-averaging of the squared amplitudes is calculated in Appendix F.2 and F.3. The resulting matrix element square for $q\bar{q}$-processes is

$$|\mathcal{M}_{q_H\bar{q}_H}|^2 = 4\sum_M \Big(|\mathcal{M}^s_{q_H\bar{q}_H}|^2\Big)_M + \Big(|\mathcal{M}^t_{q_H\bar{q}_H}|^2\Big)_M + \Big(\mathcal{M}^s_{q_H\bar{q}_H}\mathcal{M}^{t\,*}_{q_H\bar{q}_H}\Big)_M + \Big(\mathcal{M}^t_{q_H\bar{q}_H}\mathcal{M}^{s\,*}_{q_H\bar{q}_H}\Big)_M, \tag{5.13}$$

with the direct terms

$$\Big(|\mathcal{M}^s_{q_H\bar{q}_H}|^2\Big)_M = 4(p_1\cdot p \mp m_H^2)(p'\cdot p_1' \mp m_H^2)|D_M(s)|^2 \tag{5.14}$$

and

$$\Big(|\mathcal{M}^t_{q_H\bar{q}_H}|^2\Big)_M = 4(p_1\cdot p_1' \pm m_H^2)(p\cdot p' \pm m_H^2)|D_M(t)|^2 \tag{5.15}$$

and the interference terms

$$\begin{aligned}\Big(\mathcal{M}^s_{q_H\bar{q}_H}\mathcal{M}^{t\,*}_{q_H\bar{q}_H}\Big)_M =&\Big(\mathcal{M}^t_{q_H\bar{q}_H}\mathcal{M}^{s\,*}_{q_H\bar{q}_H}\Big)_M, = \Big[p_1\cdot pp'\cdot p_1' - p_1\cdot p'p\cdot p_1' + p_1\cdot p_1'p\cdot p' \\ &+ m_H^2(\mp p_1\cdot p - p_1\cdot p' \pm p_1\cdot p_1' \pm p\cdot p' - p\cdot p_1' \mp p'\cdot p_1') \\ &+ m_H^4\Big]D_M(s)D_M^*(t).\end{aligned} \tag{5.16}$$

The resulting matrix element square for qq-processes with a single meson exchange is

$$|\mathcal{M}_{q_Hq_H}|^2 = 4\sum_M \Big(|\mathcal{M}^t_{q_Hq_H}|^2\Big)_M + \Big(|\mathcal{M}^u_{q_Hq_H}|^2\Big)_M + \Big(\mathcal{M}^t_{q_Hq_H}\mathcal{M}^{u\,*}_{q_Hq_H}\Big)_M + \Big(\mathcal{M}^u_{q_Hq_H}\mathcal{M}^{t\,*}_{q_Hq_H}\Big)_M, \tag{5.17}$$

with the first terms

$$\Big(|\mathcal{M}^t_{q_Hq_H}|^2\Big)_M = 4(p'\cdot p \mp m_H^2)(p_1'\cdot p_1 \mp m_H^2)|D_M(t)|^2 \tag{5.18}$$

and

$$\Big(|\mathcal{M}^u_{q_Hq_H}|^2\Big)_M = 4(p_1'\cdot p \pm m_H^2)(p'\cdot p_1 \pm m_H^2)|D_M(u)|^2 \tag{5.19}$$

and the terms corresponding to interference of the two diagrams

$$\begin{aligned}\Big(\mathcal{M}^t_{q_Hq_H}\mathcal{M}^{u\,*}_{q_Hq_H}\Big)_M =&\Big(\mathcal{M}^u_{q_Hq_H}\mathcal{M}^{t\,*}_{q_Hq_H}\Big)_M, = \Big[p'\cdot pp_1'\cdot p_1' - p'\cdot p_1'p\cdot p_1 + p'\cdot p_1p\cdot p_1' \\ &+ m_H^2(\pm p'\cdot p + p'\cdot p_1' \pm p'\cdot p_1 \pm p\cdot p_1' + p\cdot p_1 \pm p_1'\cdot p_1) \\ &+ m_H^4\Big]D_M(t)D_M^*(u).\end{aligned} \tag{5.20}$$

The different signs belong to the two different mesons D_π and D_σ, the mass m_H is the Hartree quark mass. These expressions are similar to the perturbative NJL viscosity (see Sec. 5.1).

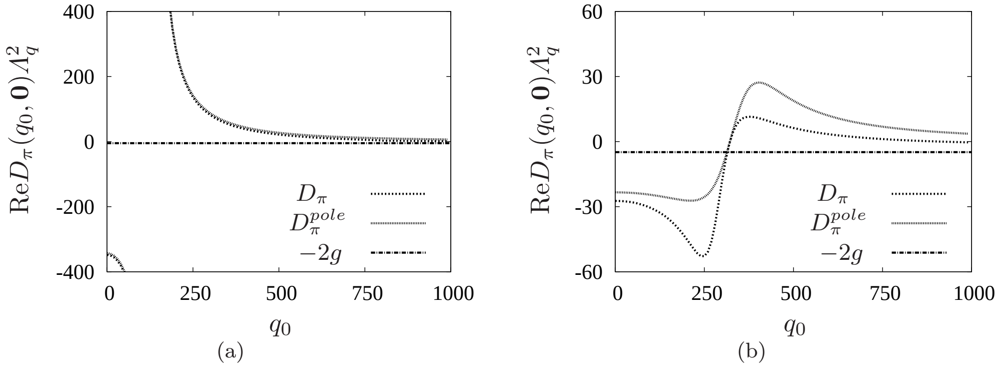

Figure 5.6: Real part of the full RPA pion propagator D_π and real part of the RPA pion propagator in resonance approximation D_π^{pole} as functions of the zero-component of the external momentum q_0 at $|\mathbf{q}| = 0$. The bare NJL coupling ($-2g\Lambda^2 = -4.88$) is also shown. All values are normalized by multiplying the cut-off square Λ_q^2. The left figure is in vacuum ($T = \mu = 0$), the right figure is at $T = 300$ MeV and $\mu = 0$. Parameters from Tab. 2.1 No 2.

Indeed, the only difference is the fermion coupling, the whole kinematics and momentum dependency is analogical to the perturbative case. One obtains the perturbative result by setting

$$m_H \to m_0 \qquad , \qquad D_M(s,t,u) \to -2g. \tag{5.21}$$

The interaction in the $q\bar{q}$ system with one-meson exchange is the resummed perturbative interaction. One can see from Fig. 5.6 that the resummed interaction is really much stronger than the bare interaction. The pion propagator D_π is shown as a function of q_0 and compared to the bare NJL coupling $-2g$. For small momenta, bare quark coupling and pion propagator differ by many orders of magnitude in vacuum (see Fig. 5.6(a)) and still by a large factor at high temperatures (Fig. 5.6(b)). At high momenta, all RPA propagators fall to the bare coupling. As it was discussed in the previous section, this high-momentum limit causes some artifacts because the Nambu-Jona-Lasinio model is not renormalizable. Therefore the resonance approximation for the RPA meson propagator is also shown in Fig. 5.6. The resonance approximation turns out to be a good replacement in vacuum for low momenta. In the ultraviolet the interaction shows a physical asymptotic behavior. This approximation has also the advantage that no additional evaluation of a complicated function has to be done in the Monte-Carlo integrand. The only practical disadvantage of the usage of the resonance approximation is found in the asymptotic high-temperature behaviour of the transport coefficients. At high temperatures, the average thermal momenta are very large and the meson propagators are evaluated mainly in the ultraviolet, where the amplitude approaches the bare scattering amplitude. Thus, one would find the perturbative result in the high temperature phase if the full RPA propagators were used, whereas this limit is not obtained in the resonance approximation. That is not a severe problem because the kinetic approach for extremely high temperatures where both interactions would lead to the same results is not valid. All calculations that follow are done in resonance approximation.

Because the resummation increases the effective coupling of quarks and antiquarks strongly, one expects a similar behavior for the scattering cross section. The total cross section for qq-scattering and $q\bar{q}$-scattering in vacuum is shown in Fig. 5.7(a). In comparison to the previous calculation (see Fig. 5.2(a)), σ_{tot} is several orders of magnitude larger. The cross section decreases at high momenta as a consequence of the resonance approximation for the RPA meson propagators.

Before applying the kinetic formulas for the shear viscosity the validity of the underlying assumptions has to be checked. Therefore, the ratio of mean free path λ and the typical range of interaction d of quarks and antiquarks has to be calculated. Compared to the calculation in lowest order perturbation theory one can expect that the mean free path is smaller and the range of interaction is larger because all interaction channels are stronger. Therefore λ/d has smaller values for the single meson exchange interaction, and the region where the kinetic condition $\lambda/d \gg 1$ if fulfilled will be smaller.

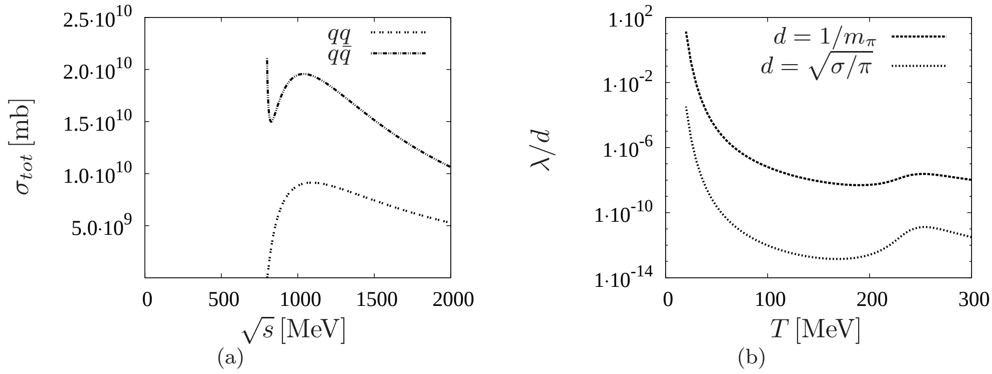

(a) (b)

Figure 5.7: (a) Total cross section of qq-scattering, and $q\bar{q}$-scattering in vacuum calculated with the one-meson exchange diagrams from Fig. 5.5. (b) Estimate of λ/d with the two different formulas. Parameters from Tab. 2.1 No 2.

The different estimates (see Sec. 3.3.4 for details) for λ and d are shown in Fig. 5.7(b). The ratio of mean free path and interaction range is shown as a function of temperature for chemical potential $\mu = 0$. The ratio is much smaller than unity for most of the temperatures. It has a small maximum at the crossover temperature and increases close to the vacuum. This is in agreement with the considerations in the previous paragraph: The quark-antiquark system coupled so strongly that the dilute gas limit of kinetic theory fails for almost all temperatures. Only for very small temperatures the density of heavy Hartree constituent quarks gets small enough to increase the mean free path sufficiently for fulfilling the kinetic theory assumptions. In the restored phase the increase in density is stronger than the reduction in interaction, and the kinetic fails again.

5.2.2 Viscosity

The estimate for mean free path and range of interaction showed that the system of quarks and antiquarks interacting via one meson exchange diagrams can not be described in kinetic theory even at intermediate temperatures. However, we can perform the calculation and discuss the result in short. These results will deliver insight into the application range of kinetic theory and the consequences of its failure.

The results of the calculation in kinetic theory are summarized in Fig. 5.8. In Fig. 5.8(a) the shear viscosity η is shown as a function of temperature T. The lines for different numbers of generalized Sonine functions used in the expansion of the distribution functions show the same qualitative behavior, as well as the estimate $\eta = \bar{p}/3\sigma$. The viscosity η is small for low temperatures and increases in the crossover region. A maximum is located close to the Mott temperature, before the viscosity decreases for higher temperatures. The ratio of viscosity and entropy density is shown in Fig. 5.8(b). η/s as a function of temperature is decreasing for low temperatures and shows a large flat structure in the broken phase. The maximum in viscosity at the crossover temperature is still visible in this plot. The absolute value of the ratio is very small, but the formulas used here should not be applied in this range. Once again we find that η/s is small in strongly coupled systems, kinetic theory even can construct arbitrarily small values for the ratio η/s but is not applicable because the underlying assumptions are not fulfilled.

5.3 Pion gas

For a moment we leave the Nambu-Jona-Lasinio model and investigate a gas of pions. One the one hand, this is a preparatory act for the section thereafter, but on the other hand it allows the application of the mathematical tools developed in Sec. 3.3 in a system of reference.

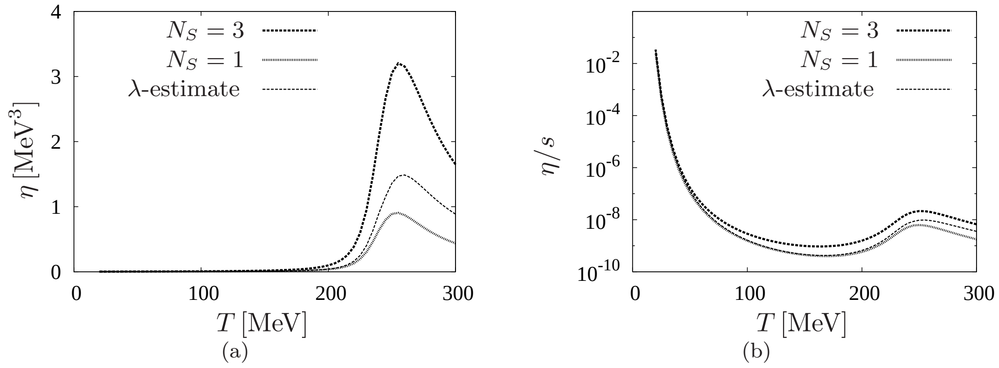

(a)
(b)

Figure 5.8: Results for shear viscosity η with RPA meson exchange as interaction. The estimate in Fig. 5.7(b) has shown that the kinetic approach used for the interaction is not valid. (a) Shear viscosity as a function of temperature T at $\mu = 0$. The different lines correspond to the complete calculation using one and three generalized Sonine-polynomials, and the estimate using the formula $\eta = \bar{p}/3\sigma$. (b) Ratio of shear viscosity and entropy density η/s as a function of temperature T at $\mu = 0$. The two lines show the result for one and three Sonine-polynomials. Parameters from Tab. 2.1 No 2.

Particle	π^0	$\pi^\pm$	$K^\pm$	K^0, $\bar{K}^0$	η
Mass [MeV]	134.98	139.57	493.7	497.6	574.9

Table 5.1: Table of the lightest hadrons with their rounded masses. Data taken from [193].

5.3.1 Introduction

In the previous two sections kinetic theory was applied to the quark-antiquark system. It turned out that the system interacts so strongly that the kinetic approach can only be applied in a very dilute system, that is realized at low temperatures and chemical potentials. Unfortunately, one does not expect that strongly interacting matter at low temperatures behaves like a quark gas because of confinement. In the hadronic phase at low temperature, quarks are confined and thermodynamic properties, as well as transport coefficients, should be governed by the lightest degrees of freedoms. The lightest hadrons (see Tab. 5.3.1) are the pions, so we will concentrate on these mesons in this section.

The particle density at zero chemical potential is purely generated by thermal effects, so it is exponentially suppressed close to the vacuum, when the hadron mass is much higher than the temperature of the hadron gas. In this region, the hadron gas is expected to be very dilute, and low momenta govern the dynamics of the system. But the dilute gas limit is exactly the physics where kinetic theory can be applied[3], so we can be sure that there is a regime where the results for transport coefficients of a pion gas within kinetic theory are reasonable.

In the chiral limit, the pions are the Goldstone bosons of the spontaneously broken chiral symmetry and have zero mass. As a additional consequence, their scattering has to vanish for small E_{cm}. Hence, the pion scattering for slow kinematics depends on the pion mass.

In all the calculation we will treat non-chiral pions in the isospin limit. That means that we treat the three different pions as degenerate indistinguishable particles, and one has to average out the isospin quantum number for all appearing formulas.

The only conserved quantity of such a degenerate pion gas is charge. However, sometimes it is useful to introduce a pion chemical potential μ_π. This assumption of particle number conservation can be motivated from experimental results as well as from considerations of chemical equilibration [194, 195, 196, 197], and finds also its application in literature [198].

---

[3] When temperatures are very low, one can approximate the system by a non-relativistic gas. This idea will not be followed in this work, see e.g. [127] for such a pion gas.

The hadron gas can be seen as a generalization of the pion gas concept, involving kaons, η, or nucleons, depending on the region of QCD phase diagram that is under investigation. Baryons should be included at higher baryon chemical potential μ_B, whereas heavier mesons play an important role for higher temperatures already for small μ_B.

5.3.2 Review of the literature

Important literature concerning interacting pions is summarized in the following. The basis for the theoretical description of pion scattering is given by Weinberg [199] using current algebra. The idea of chiral symmetry and deviation from chiral symmetry, including chiral perturbation theory, led to the extension of this work [200, 201, 202, 203]. These interaction terms even have been used for calculations of transport properties [127, 145]. Beside these fundamental considerations there have been different efforts to extract pion scattering amplitudes from experimental measurements. Prominent examples are models from empirical phase shifts [204], the inverse amplitude method (IAM) [205, 198, 124], and fits of phenomenological amplitudes to experimental data [125].

All these pion descriptions are performed in vacuum, pion mass and invariant matrix elements are constantly extrapolated to finite temperature or baryon chemical potential. An intrinsic dependency on temperature is obtained with a microscopic description of the scattering process, for example with the Linear σ-model [146].

The extension of a pion gas to a hadron gas need additional information about particle scattering. The same ideas as for the pion gas can be used for these additional degrees of freedom, see [204, 124, 125, 107, 206] for interactions in hadron gases.

5.3.3 Pion scattering

The invariant matrix element of $\pi\pi$-scattering according to leading-order chiral perturbation theory (LO-ChPT) is given by

$$|\mathcal{M}_{\pi\pi}^{LO-ChPT}|^2 = \frac{1}{9f_\pi^4}\left[21m_\pi^4 + 9s^2 - 24m_\pi^2 s + 3(t-u)^2\right]. \tag{5.22}$$

As it was discussed before, the pion mass m_π enters in the matrix element, as well as the pion decay constant f_π. The Mandelstam variables s, t and u introduce a momentum dependency in the invariant matrix element. By setting the external 3-momenta to zero[4], one obtaines the matrix element that also enters in the Weinberg $\pi\pi$-scattering length,

$$|\mathcal{M}_{\pi\pi}^{\text{Weinberg}}|^2 = \frac{23m_\pi^4}{3f_\pi^4}. \tag{5.23}$$

We will call this constant scattering amplitude Weinberg interaction. It is obvious that the scattering vanishes in chiral limit, where $m_\pi = 0$. We take these two scattering terms as different descriptions of the pion interaction, although it is clear that the Weinberg interaction is the low-momentum limit of the LO-ChPT result.

The two scattering amplitudes lead to scattering cross sections that are only identical for $s = 4m_\pi$. The total cross section σ_{tot} as a function of $\sqrt{s}$ is shown in Fig. 5.9(a). Because $\mathcal{M}_{\pi\pi}^{\text{Weinberg}}$ is constant the total cross section decreases for growing s (see Eq. (3.82)). In contrast, as $\mathcal{M}_{\pi\pi}^{LO-ChPT}$ rises with center-of-mass momentum, the total cross section in leading-order chiral perturbation theory increases.

This totally different behavior of the scattering cross section will leads to a significant difference in the dependency of viscosity and temperature. As we saw already in Sec. 5.1, a larger temperature lead to a population of larger momenta. The cross section decreases for larger momenta for the Weinberg interaction, and increases for leading-order chiral perturbation theory, thus the effective coupling at a thermal momentum for the two interactions differ.

We first check if the kinetic framework can be applied to the system. Therefore, the usual estimates for mean free path λ and interaction range d are plotted in Fig. 5.9(b). As it was expected, kinetic theory seems to work perfectly at low temperatures because of the low density

---

[4] That means $s = 4m_\pi^2$, $t = u = 0$

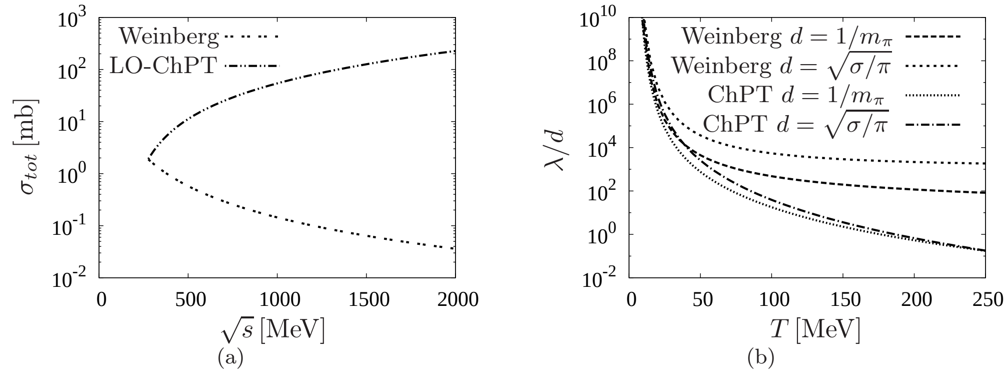

Figure 5.9: $\pi\pi$-scattering for Weinberg result Eq. (5.23), and leading-order chiral perturbation theory Eq. (5.22), respectively. (a) Total cross section for $\pi\pi$-scattering as a function of Mandelstam-variable s. (b) Estimate of mean free path λ and interaction range d as a function of temperature for $\mu_\pi = 0$.

of the system. At larger temperatures, the Weinberg term allows a calculation up to very high temperatures, whereas the LO-ChPT result predicts a range of applicability up to temperatures about 100 MeV. This difference of the two formulas is easily understood because the average momentum rises with temperature T, and the LO-ChPT-scattering is enhanced for larger momenta. Because of the important difference between the LO-ChPT interaction and the Weinberg interation, we investigate the pion system for both interactions separately. We begin with the constant scattering amplitude. Of course, both results agree at low temperatures, where the thermal momentum is very small. At higher temperatures, the LO-ChPT interaction should give a more reliable result, however, the monotonic increase of the cross section in this approximation limits the range of a reasonable application.

5.3.4 Weinberg interaction

We first investigate the role of the Sonine expansion in the well-studied pion system. Therefore we investigate the viscosity as a function of temperature for different expansions. The analysis of shear viscosity and its temperature dependency in the best Sonine expansion is done afterward. The calculation of shear viscosity in kinetic theory with the two interactions has already been documented in literature [125, 124], although the focus in the two cited works is different.

A calculation for different Sonine expansions and the Weinberg interaction is presented in Fig. 5.10. In the left plot, we chose a single monome

$$P_j(p) = p^j \tag{5.24}$$

as a basis function and neglect all other functions, such that $N_S = 1$. We see that the choice of $P(p) = p^2$, as it was used in [124] includes the most contributions, all other choices of j lead to smaller results. In the other plot, Fig. 5.10(b), the basis is constructed from orthogonalized monic polynomials from $j = 0$ up to $j = N_S - 1$. One can see that the difference in the result for η is huge for N_S between one and three, but is converged if $N_S > 2$. As a demonstration, some points for $N_S = 5$ are plotted, and one can see that they are in good agreement with $N_S = 3$. The crosses in both plots correspond to the estimated $\eta = \bar{p}/3\sigma$, which is in the same order of magnitude but lower than the exact result. We conclude that η is calculated to a satisfying accuracy with $N_S = 3$, and approximately by $N_S = 1$ when p^2 is taken as the basis function.

Now it is possible to calculate the shear viscosity and the thermal conductivity for different values of chemical potential μ_π. Of course we first have to check the validity of the kinetic approach again for each calculation because the variation in density will change the mean free path.

The Sonine-converged calculation of shear viscosity with pions interacting with the constant Weinberg scattering amplitude is shown in Fig. 5.11(a). The calculation was done for chemical

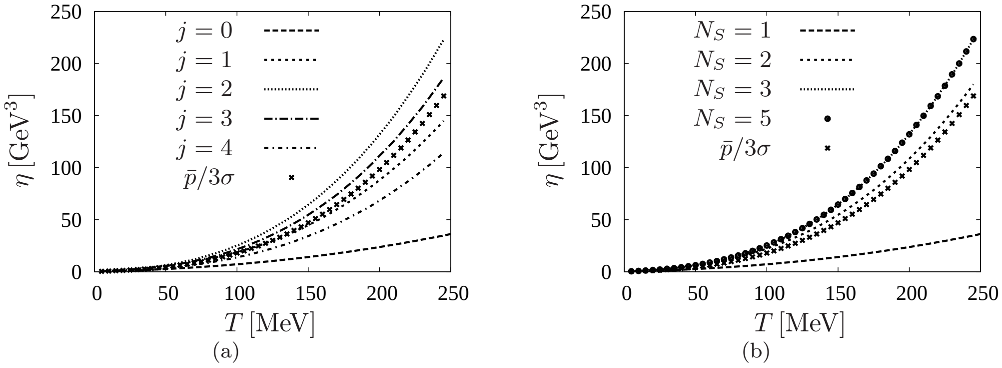

(a) (b)

Figure 5.10: Different Sonine-expansions are tested in the viscosity calculation for a pion gas with Weinberg $\pi\pi$-interaction. Shear viscosity is plotted as a function of temperature T at $\mu_\pi = 0$. The different lines and points correspond to different truncations. Crosses denote the mean free path estimate $\bar{p}/3\sigma$. (a) One monomial $P_j(p) = p^j$ is used for different values of j. (b) The polynomial $P_{N_S}(p) = \sum_{j=0}^{N_S-1} c_j p^j$ is used for different values of N_S.

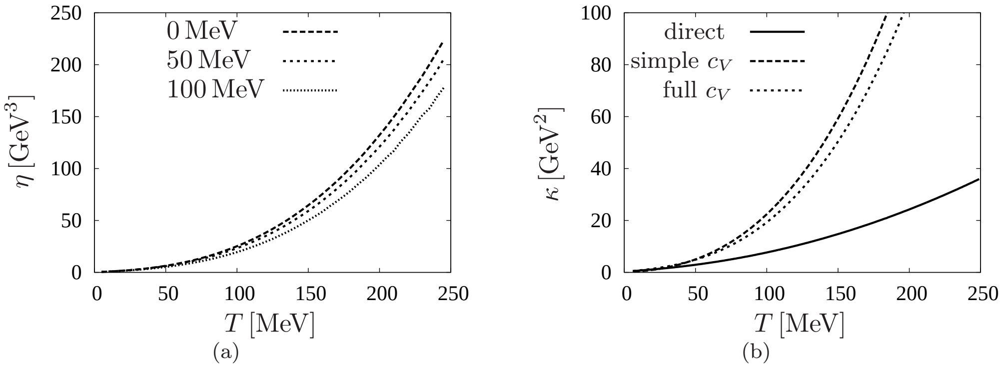

(a) (b)

Figure 5.11: Transport coefficients of a gas of pions interacting via the Weinberg scattering amplitude. (a) Shear viscosity η for different pion chemical potentials μ_π. (b) Estimates for the thermal conductivity κ of a pion gas with Weinberg $\pi\pi$-interaction as a function of temperature. The different lines correspond to the different values of μ_π indicated in the figure.

potentials

$$\mu_\pi \in \{0\,\mathrm{MeV}, 50\,\mathrm{MeV}, 100\,\mathrm{MeV}\}, \tag{5.25}$$

so no condensation of the boson takes place. The estimates for λ/d indicate that the kinetic approach is reasonable even for the highest chemical potential shown in the plot, even for temperatures above 250 MeV. In the figure, one sees that a higher pion chemical potential leads to a lower viscosity, although the changes in viscosity are not very large. This change reminds to a calculation [124] with varying pion fugacity

$$z_\pi = \exp\left(\frac{\mu_\pi - m_\pi}{T}\right), \tag{5.26}$$

where it was also found that a denser system of pions interacting with a constant invariant matrix element has a lower viscosity than a dilute one.

The thermal conductivity κ is calculated from its mean free path estimate as it was discussed in Sec. 3.4.1. We do not use a systematic Chapman-Enskog expansion but restrict the calculation to the estimates, motivated by the fact that the results for the shear viscosity coefficient indicate that the mean free path estimate and the full calculation are in good agreement. In Fig. 5.11(b),

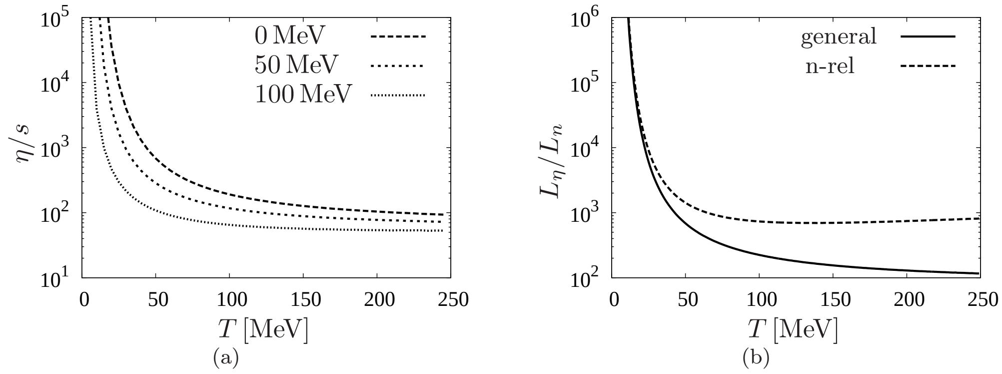

Figure 5.12: Fluidity of a pion gas interacting via the Weinberg scattering amplitude. The different dimensionless fluidity measures are shown as a function of temperature T. (a) η/s for different values μ_π, (b) L_η/L_n calculated from the general formula (solid line) and from the non-relativistic limit (dashed line).

the results for κ for the estimate from Eq. (3.93) are shown as well as the estimate from Eq. (3.94). For the latter, we did two calculations, which differ in a different treatment of the heat capacity c_V. Beside the full value

$$c_V = T\frac{\partial s}{\partial T}, \tag{5.27}$$

we also used the simple relation from a classical free gas, $c_V = N/2$, where the number of degrees of freedom is set to $N = 3$. The three different curves are shown in Fig. 5.11(b) for pions interacting by the Weinberg scattering amplitude. We find that the three estimates all lead to a thermal conductivity that increases with temperature. Indeed, the qualitative behaviour of the estimates is similar to the shape of the shear viscosity curve, as one would expect from the relation between the different transport coeffients. The quantitative differences between the three estimates are relatively large.

In Fig. 5.12(a) the ratio of shear viscosity and entropy density for the pion system is plotted for the same chemical potentials as in Fig. 5.11(a). The ratio is large in the dilute system at low temperatures and becomes smaller for higher values of T. Remarkably the fluidity measure η/s flattens at some point, staying on values of the order of magnitude of 10^1 to 10^2. We can conclude that pions with the constant $\pi\pi$-scattering amplitude are not coupled very strongly, even in a system that is expected to be considerably hot and dense. This motivates the investigation of the LO-ChPT interaction which becomes much stronger even for moderate momenta.

The fluidity measure L_η/L_n as a function of the temperature T is shown in Fig. 5.12(b). We have to restrict this calculation to $\mu_\pi = 0$ because the concept of a pion chemical potential causes severe artifacts in the thermodynamic relations of p, ϵ, and c_s. We show the general curve related to η/h as well as the non-relativistic limit, which involves η/ρ. One can see that the relativistic corrections become important at temperatures of a few tens of MeV. The general curve decreases monotonically with temperature T, no plateau-like structure like in η/s is observed. This can be understood as $h = Ts$ for zero pion chemical potential, thus if η/s does not change with temperature, η/h will decrease as $1/T$.

5.3.5 Leading-order chiral perturbation theory

We now investigate the pion gas that interacts via the scattering amplitude in leading-order chiral perturbation theory. We proceed in the same order as in the preceding part concerning the Weinberg scattering amplitude.

The investigation of the Sonine-expansion is visualized in Fig. 5.13 for the $\pi\pi$-interaction from leading-order chiral perturbation theory. The different Sonine basis functions, corresponding to different values of j in Fig. 5.13(a), again show a different behavior. For low temperatures, $j = 1$ and $j = 2$ pic up the most contributions, whereas the largest values at higher temperatures

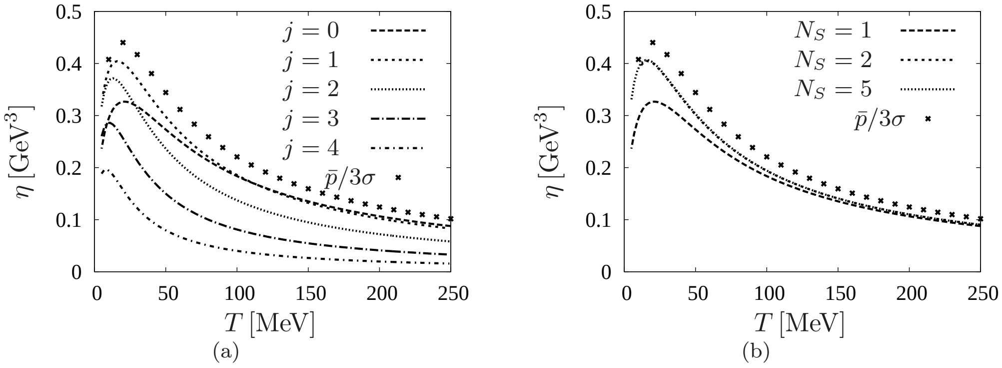

Figure 5.13: Different Sonine-expansions are tested in the viscosity calculation for a pion gas with LO-ChPT $\pi\pi$-interaction. The shear viscosity is plotted as a function of temperature T at $\mu_\pi = 0$, the different lines correspond to different truncations. The Points show the value of the estimate $\eta = \bar{p}/3\sigma$. (a) One monomial $P_j(p) = p^j$ is used for different values of j. (b) The polynomial $P_{N_S}(p) = \sum_{j=0}^{N_S-1} c_j p^j$ is used for different values of N_S.

are obtained by $j = 0$ and $j = 1$. Different sizes of the basis have an effect that differs from the influence in the Weinberg interaction calculation. The convergence is already reached with $N_s = 2$, as it can be seen in Fig. 5.13(b) where the lines for $N_S = 1$, $N_S = 2$, and $N_S = 5$ are shown. The viscosity estimate is denoted with crosses in both figures, and in contrast to the Weinberg interaction, it is found that the estimate is larger than the exact result, although it is in the same order of magnitude. One can conclude that the choice $N_S = 2$ is sufficient for the calculation of η with LO-ChPT interaction.

The Sonine-converged calculation of shear viscosity using the leading-order chiral perturbation theory is shown in Fig. 5.14(a). The chemical potentials of the pions are

$$\mu_\pi \in \{0\,\mathrm{MeV},\, 50\,\mathrm{MeV},\, 100\,\mathrm{MeV},\, 135\,\mathrm{MeV}\}, \tag{5.28}$$

indicated by different lines in the figure. Although the LO-ChPT interaction is reliable for a larger temperature range than the Weinberg interaction, it turns out that the range of applicability due to the estimate of λ and d is more restricted than for the Weinberg calculation. If one takes $\lambda/d > 10$ as a courageous limit of kinetic theory[5], one finds that $T < 150\,\mathrm{MeV}$ for $\mu_\pi = 0$, and $T < 80\,\mathrm{MeV}$ for $\mu_\pi = 135\,\mathrm{MeV}$, all other are in between these extreme cases. The behavior that is found for $\mu_\pi = 0$ is that the viscosity is low for small temperatures and has a maximum at a temperature of a few tens of MeV. The viscosity becomes smaller for high temperatures because the interaction increases for larger thermal momentum. Only few changes in the behavior of the viscosity appear if the chemical potential μ_π takes a small value. While these curves in Fig. 5.14(a) are close to the curve of $\mu_\pi = 0$, the viscosity is affected stronger close to the condensation point $\mu_\pi = m_\pi$. The general behavior is similar to the result for Weinberg interaction: A system with higher particle chemical potential has a lower shear viscosity.

The thermal conductivity of a pion system interacting by the leading-order chiral perturbation theory scattering amplitude is shown in Fig. 5.14(b). We restrict this investigation to $\mu_\pi = 0$ and use the same estimates as discussed in Sec. 5.3.4. The curves different curves resemble the shear viscosity curves shown in Fig. 5.14(a) in their qualitative behaviour: The thermal conductivity increases for small temperatures, has a maximum at temperatures of a few tens of MeV, and is decreasing for larger temperatures. This behavior is similar for all heat conductivity estimates, while the absolute values of the three curves differ.

The shear viscosity divided by entropy density for the same temperatures T and chemical potentials μ_π as in Fig. 5.14(a) is shown in Fig. 5.15(a). Starting from $T = 0$, one finds a decreasing curve that falls below the values of η/s obtained from the calculation using the Weinberg interaction (see Fig. 5.12(a)) already for small temperatures. The curves decrease monotonically, and

---

[5] The same limit has been used in a similar calculation of pions and hadrons [125], where the LO-ChPT interaction was used for the shear viscosity of a pion gas at $\mu_\pi = 0$.

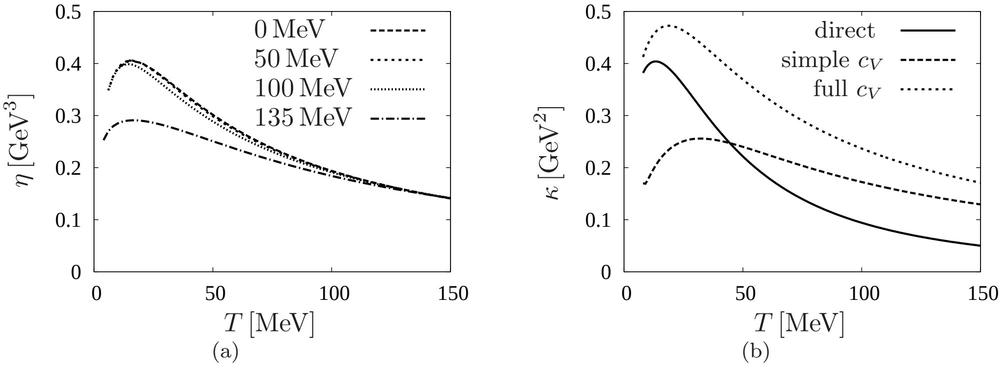

(a) (b)

Figure 5.14: Results for transport coefficients of a pion gas with LO-ChPT $\pi\pi$-interaction as a function of temperature. (a) Shear viscosity η, where the different lines correspond to the different values of μ_π indicated in the figure. (b) Mean free path estimates for the thermal conductivity κ. The different curves in the figures correspond to different estimate. The direct calculation evaluates Eq. (3.93), while the two other lines result from Eq. (3.94). The thermal conductivity is just $N/2$ in the simple case, and calculated from the thermodynamic relations in the full case.

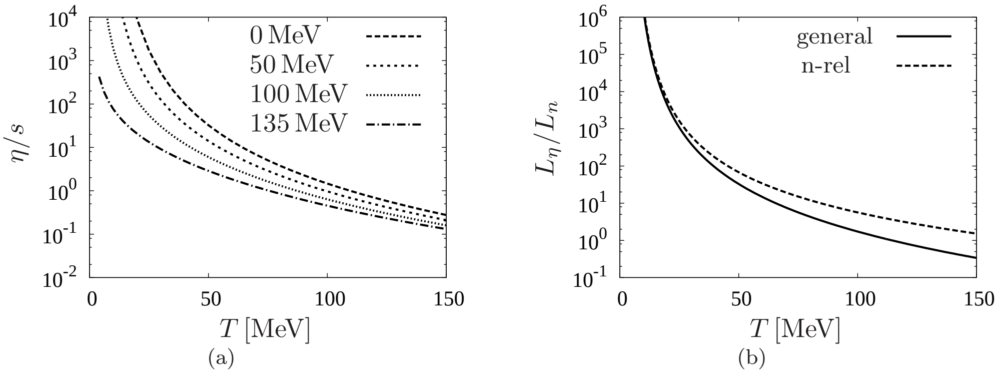

(a) (b)

Figure 5.15: Fluidity measures of a pion gas interacting via the LO-ChPT scattering amplitude. All dimensionless measures are shown as a function of temperature T. (a) η/s for different values of pion chemical potential μ_π. (b) Fluidity measure L_η/L_n (solid line) and its nonrelativistic limit (dashed line) for $\mu_\pi = 0$.

if one evaluate the plot for the limiting temperature for kinetic theory, one finds values of order one. Again, η/s is smaller if the density and the chemical potential are higher.

The fluidity measure L_η/L_n as a function of temperature is shown in Fig. 5.15(b). As we restrict this estimate to $\mu_\pi = 0$ as in Sec. 5.3.4, we only show the general curve obtained from η/h, and the non-relativistic curve which is obtained from η/ρ. Both curves coincide for small temperatures, where the non-relativistic description is reasonable. L_η/L_n decreases at higher temperatures, and reach a small value in the region where we have to stop the investigation in the kinetic theory because we exit the dilute gas limit. If one compares the absolute values of L_η/L_n with the ones from the Weinberg interaction, one sees that the fluidity measure is significantly smaller. For temperatures of about 150 MeV, the ratio becomes smaller than one, as it was also observed for critical and supercritical fluids [148].

5.4 NJL pion gas

The pion-pion interaction in the NJL model is interesting because it is not an elementary interaction of the model but an effective interaction between effective degrees of freedom.

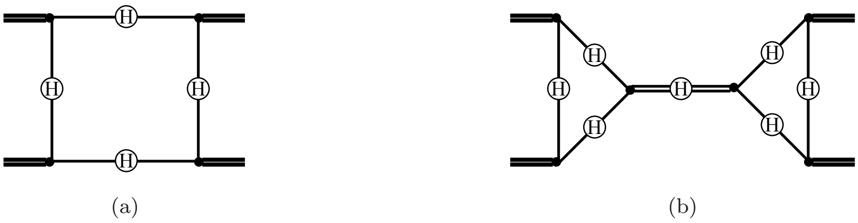

Figure 5.16: Diagrams contributing to $\pi\pi$-scattering in Nambu-Jona-Lasinio model: the box-diagram (a), and the σ-propagation diagram (b). Both diagrams are taken in s-, t-, and u-channel, resulting in different contributions to different isospin amplitudes.

Thus, the pions are particles containing a quark and an antiquark which are influenced by chiral symmetry breaking and restoration, which implies a dramatic temperature dependency. The calculation of the pion includes medium effects, resulting in a nontrivial pion propagator. Even when this propagator is approximated by a simpler function in order to interprete the quark-antiquark scattering channel as a particle, the pion mass that is deduced from this formulation has an important temperature dependency. The effective interactions between these NJL pions are not elementary, but consist of elementary quark diagrams that have an intrinsic dependency on temperature and quark chemical potential. The calculations with Weinberg interaction and LO-ChPT made use of pion masses and interactions in vacuum and generated all temperature dependency via the occupation number in the distribution functions in kinetic theory, whereas a calculation with these quantities in the NJL model would include medium modifications of the particles themselves.

5.4.1 $\pi\pi$ cross-section

The construction of effective $\pi\pi$-interaction diagrams in the NJL model can be done in many ways. The aim is to find the correct scattering in vacuum, as it is required from chiral symmetry. In order to obtain this limit correctly, a systematic and consistent choice of Feynman diagrams is needed. An expansion scheme in the NJL-model was already presented in the chapter 2, the $1/N_c$-counting, summarized in Tab. 2.3. The leading-order diagrams for the $\pi - \pi$ scattering in this counting scheme can be constructed according to [207, 208][6] which are described by the two diagrams shown in Fig. 5.16. The first diagram (Fig. 5.16(a)) is called *box-diagram* and consists of a quark-box (or an antiquark-box) with four fermion propagators. The second diagram (Fig. 5.16(b)) is called *σ-propagation diagram* because the pions couple to a scalar meson through a quark-triangle, and a σ-exchange takes place.

In our work, the diagrams are evaluated in the same way as for the calculation of the $\pi - \pi$ scattering length [207, 208]. This can be seen as the static limit of the whole diagrams, with all momenta going to their lowest possible value. An overview over possible extensions of this scheme is given in the end of this section.

The evaluation of the box diagram makes use of different crossing symmetries. A detailed derivation of the possible combinations is gived in [207]. The process

$$\pi^a + \pi^b \to \pi^c + \pi^d \tag{5.29}$$

with isospin indices a, b, c, and d, leads to the amplitudes

$$i\mathcal{M}^{NJL\,(1)}_{\pi\pi\,ab;cd} = -4N_cN_f i(\delta_{ab}\delta_{cd} + \delta_{ac}\delta_{bd} - \delta_{ad}\delta_{bc})g^4_{\pi qq}\left[iI(0) + iI(p_{thr}) - p^2_{thr} iK(p_{thr})\right], \tag{5.30}$$

$$i\mathcal{M}^{NJL\,(2)}_{\pi\pi\,ab;cd} = -4N_cN_f i(\delta_{ab}\delta_{cd} - \delta_{ac}\delta_{bd} - \delta_{ad}\delta_{bc})g^4_{\pi qq}\left[iI(0) + iI(p_{thr}) - p^2_{thr} iK(p_{thr})\right], \tag{5.31}$$

---

[6] There are also other works dealing with $\pi - \pi$ scattering in NJL-type models, see for example [209] and [210]. An earlier work describing meson interactions in the model is [211].

and

$$i\mathcal{M}^{NJL\,(3)}_{\pi\pi\,ab;cd} = -8N_cN_f i(-\delta_{ab}\delta_{cd} + \delta_{ac}\delta_{bd} + \delta_{ad}\delta_{bc})g^4_{\pi qq}\left[iI(0) + \frac{1}{2}p^4_{thr} iL(p_{thr}) - 2p^2_{thr} iK(p_{thr})\right]. \tag{5.32}$$

The 4-momentum p_{thr} is defined by

$$p_{thr} = (2m_\pi, \mathbf{0}), \tag{5.33}$$

so it is the total 4-momentum of two pions at rest. The elementary integral iI was already defined earlier (see Sec. 2.3), the two additional elementary integrals

$$iK(i\omega_p, \mathbf{p}) = -T\sum_{i\omega_k}\int\frac{\mathrm{d}^3k}{(2\pi)^3}\frac{1}{[(i\omega_k+\mu)^2 - \mathbf{k}^2 - m_H^2]^2[(i\omega_k + i\omega_p + \mu)^2 - (\mathbf{k}+\mathbf{p})^2 - m_H^2]} \tag{5.34}$$

and

$$iL(i\omega_p, \mathbf{p}) = -T\sum_{i\omega_k}\int\frac{\mathrm{d}^3k}{(2\pi)^3}\frac{1}{[(i\omega_k+\mu)^2 - \mathbf{k}^2 - m_H^2]^2[(i\omega_k + i\omega_p + \mu)^2 - (\mathbf{k}+\mathbf{p})^2 - m_H^2]^2} \tag{5.35}$$

are evaluated in Appendix B.6, and B.7, respectively. An analytic continuation to real momenta $i\omega_p \to p_0 \pm i\epsilon$ is necessary since the external momentum p_{thr} is timelike. For the specific constellation of external momenta and $\mu = 0$, this leads to

$$iK(p_0, \mathbf{0}) = \int\frac{\mathrm{d}^3k}{(2\pi)^3}\left\{\frac{n_F(E_k) - n_F(-E_k)}{4E_k^3}\left[\frac{1}{p_0^2 - 4E_k^2} - \frac{8E_k^2}{(p_0^2-4E_k^2)^2} + \frac{2E_k n_F(E_k)n_F(-E_k)}{T(p_0^2 - 4E_k^2)}\right]\right\} \tag{5.36}$$

and

$$\begin{aligned} iL(p_0, \mathbf{0}) = \int\frac{\mathrm{d}^3k}{(2\pi)^3}\Bigg\{&\frac{n_F(E_k) - n_F(-E_k)}{4E_k^3 - P0^2}\Bigg[\frac{1}{p_0^2 - 4E_k^2} - \frac{12E_k^2}{(p_0^2-4E_k^2)^2} - \frac{64E_k^4}{(p_0^2-4E_k^2)^3} \\ &+ \frac{E_k n_F(E_k)n_F(-E_k)}{T}\left(\frac{1}{p_0^2-4E_k^2} + \frac{8E_k^2}{(p_0^2-4E_k^2)^2}\right)\Bigg]\Bigg\}. \end{aligned} \tag{5.37}$$

The evaluation of the σ-propagation diagram for the same reaction process (see [207]) leads to the amplitudes

$$i\mathcal{M}^{NJL\,(4)}_{\pi\pi\,ab;cd} = \delta_{ab}\delta_{cd}g^4_{\pi qq}\mathit{\Gamma}^2_{\sigma\pi\pi}(p_{thr}, -p_{thr})iD_\sigma(2p_{thr}) \tag{5.38}$$

and

$$i\mathcal{M}^{NJL\,(5)}_{\pi\pi\,ab;cd} = \delta_{ab}\delta_{cd}g^4_{\pi qq}\mathit{\Gamma}^2_{\sigma\pi\pi}(p_{thr}, p_{thr})iD_\sigma(0), \tag{5.39}$$

where D_σ is the RPA propagator of the σ-meson[7]. The $\sigma\pi\pi$-vertex $\mathit{\Gamma}_{\sigma\pi\pi}$ is calculated from the quark triangle. It can be expressed in terms of elementary integrals,

$$i\mathit{\Gamma}_{\sigma\pi\pi}(p, -p) = -8N_cN_f m_H iI(p) \tag{5.40}$$

for the s-channel, and

$$i\mathit{\Gamma}_{\sigma\pi\pi}(p, p) = -8N_cN_f m_H[iI(0) - p^2 iK(p)] \tag{5.41}$$

for t-channel, respectively. The full scattering amplitudes of these different isospin channels are obtained by

$$i\mathcal{M}^{NJL,\,0}_{\pi\pi} = 6i\mathcal{M}^{NJL\,(1)}_{\pi\pi\,ab;cd} - i\mathcal{M}^{NJL\,(3)}_{\pi\pi\,ab;cd} + 3i\mathcal{M}^{NJL\,(4)}_{\pi\pi\,ab;cd} + 2i\mathcal{M}^{NJL\,(5)}_{\pi\pi\,ab;cd} \tag{5.42}$$

for $I = 0$, and

$$i\mathcal{M}^{NJL,\,2}_{\pi\pi} = 2i\mathcal{M}^{NJL\,(3)}_{\pi\pi\,ab;cd} + 2i\mathcal{M}^{NJL\,(5)}_{\pi\pi\,ab;cd} \tag{5.43}$$

$i\mathcal{M}^{NJL\,(1)}_{\pi\pi\,ab;cd}$	$i\mathcal{M}^{NJL\,(3)}_{\pi\pi\,ab;cd}$	$i\mathcal{M}^{NJL\,(4)}_{\pi\pi\,ab;cd}$	$i\mathcal{M}^{NJL\,(5)}_{\pi\pi\,ab;cd}$	$a^{NJL,\,0}_{\pi\pi}[m_\pi^{-1}]$	$a^{NJL,\,2}_{\pi\pi}[m_\pi^{-1}]$
-72.5	-77.0	74.5	74.9	0.153	-0.0407

Table 5.2: $\pi\pi$-scattering amplitudes, their different contributions and the resulting scattering length. All quantities are calculated in vacuum using the parameters from Tab. 2.1 No 2.

for $I = 2$, while the amplitude is identically zero for $I = 1$.
The different contributions to the scattering amplitudes are listed in Tab. 5.2. One sees that they all have absolute values that are close to each other. That is important since in the chiral limit, the scattering amplitude at threshold vanishes while the single diagrams still have a finite contribution, hence the total amplitude has to vanish by destructive interference of the different terms.
The $\pi\pi$-scattering lengths $a_{\pi\pi}$ for the different isospins are

$$a^{0,2} = \frac{1}{32\pi m_\pi} i\mathcal{M}^{NJL,\,0,2}_{\pi\pi}(s = p^2_{thr} = 4m^2_\pi, t = u = 0). \tag{5.44}$$

The result for the NJL calculation of the scattering lengths $a^{NJL,\,0}_{\pi\pi}$ and $a^{NJL,\,2}_{\pi\pi}$ is also found in Tab. 5.2. Both values can be compared to the Weinberg result$\pi\pi$-scattering length

$$a^{\text{Weinberg},\,0}_{\pi\pi} = \frac{7m_\pi}{32\pi f^2_\pi} \qquad a^{\text{Weinberg},\,2}_{\pi\pi} = -\frac{2m_\pi}{32\pi f^2_\pi}, \tag{5.45}$$

which yields[8] $a^{\text{Weinberg},\,0}_{\pi\pi} = 0.149$ and $a^{\text{Weinberg},\,2}_{\pi\pi} = -0.0425$. The agreement of NJL model and the general prediction is very good, although there is a difference which may arise from the truncation of the scattering diagrams or from deviation from chiral symmetry [208]. There is also a dependency of the scattering length on the NJL parameter set [207], but we find that the chosen values are reasonable.
In the same way as in Sec. 5.3, we want to treat the pions in isospin limit. For the differential cross section $\mathrm{d}\sigma/\mathrm{d}\Omega$, we have to average over all isospins [125]. This leads to the sum

$$\frac{\mathrm{d}\sigma}{\mathrm{d}\Omega} = \frac{1}{\sum_{I'=0}^{2}(2I'+1)} \sum_{I=0}^{2}(2I+1)\frac{\left|i\mathcal{M}^{NJL,\,I}_{\pi\pi}\right|^2}{64\pi^2 E^2_{cm}}. \tag{5.46}$$

The expressions for the scattering amplitudes $i\mathcal{M}_{\pi\pi}$ calculated in the NJL model are fully temperature dependent. We will investigate the implications of the thermal modifications of the scattering length and the consequences for transport properties in the next section.

5.4.2 Temperature dependent scattering

Using the temperature-dependent NJL expressions for scattering matrices $i\mathcal{M}_{\pi\pi}$, we can calculate the $\pi\pi$-scattering lengths $a^{I=0,2}$ as functions of temperature. We restrict our investigations to the case of $\mu = 0$ for the same parameter set as it was used in Tab. 5.2.
The numerical results for the scattering length are shown in Fig. 5.17(a), where $a^{NJL,\,0}_{\pi\pi}$ and $a^{NJL,\,2}_{\pi\pi}$ as functions of temperature T are compared to $a^{\text{Weinberg},\,0}_{\pi\pi}$ and $a^{\text{Weinberg},\,2}_{\pi\pi}$. For temperatures up to 120 MeV it is difficult to distinguish the NJL-result from the Weinberg value in the plot. This changes dramatically for higher temperature. Close to the dissociation temperature[9] T_{diss}, the $I = 0$-length increases strongly, changes its sign and takes a large negative values, while the isospin-2-length decreases smoothly in this region. Close to the Mott temperature T_{Mott}, both scattering lengths $a^{NJL,\,0}_{\pi\pi}$ and $a^{NJL,\,2}_{\pi\pi}$ diverge. This behavior is understood if one considers the temperature dependency of the masses of pions, σ-mesons and constituent quarks, which is pictured in Fig. 5.17(b). In this figure, besides the three above-mentioned masses, the values of $2m_H$ and $1/2\, m_\sigma$ are shown in the plot in order to identify the two transition temperatures T_{diss}

---

[7] The same notation is used as in Sec. 2.3.

[8] We set m_π and f_π to the value used as a fitting condition in the NJL parameter set for consistency.

[9] More details about the meson transition temperatures T_{diss} and T_{Mott} can be found in Secs. 2.5.3 and 2.5.4.

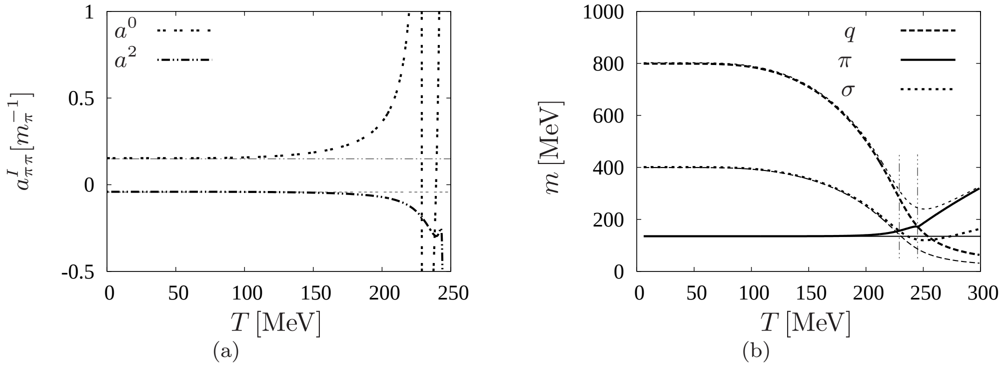

(a)

(b)

Figure 5.17: Investigation of medium modifications of $\pi\pi$-scattering for $\mu = 0$. (a) Scattering length a^0 and a^2 as functions of temperature. Bold lines denote the NJL calculation, the thin lines extrapolate the Weinberg-value from $T = 0$. (b) Masses of different particles. The bold q-line shows the value of $2m_H$, the thin q line the value of m_H. The bold π-line corresponds to the medium dependent pion mass, the thin line is the extrapolation of the vacuum value. The bold σ line is $1/2\, m_\sigma$, and the thin σ-line shows m_σ. The two vertical lines indicate the σ-dissociation temperature ($T_{diss} \approx 230\,\mathrm{MeV}$), and the Mott temperature (at $T_{Mott} \approx 245\,\mathrm{MeV}$), respectively.

and T_{Mott} (indicated with vertical lines). The dissociation temperature separates the regions where the scalar meson is stable and the region where it is unstable with respect to decays into two pions. At T_{diss}, the process

$$\pi(p_1) + \pi(p_2) \to \sigma(p_1 + p_2) \tag{5.47}$$

is resonant at threshold, i. e. the σ-meson is on-shell for two pions at rest. The process described in the reaction (5.47) is present in the σ-propagation diagram shown in Fig. 5.16(b) in the s-channel. Indeed, the scattering matrix $\mathcal{M}^{(4)}$ involves a σ-propagator at its mass peak at T_{diss}, leading to a strongly increasing contribution. As this scattering matrix only enters in $a_{\pi\pi}^{NJL,0}$, only the scattering length for isospin $I = 0$ is sensitive to the σ-dissociation transition.

The divergences of $a_{\pi\pi}^{NJL,0}$ and $a_{\pi\pi}^{NJL,2}$ at T_{Mott} result from the scattering amplitudes of Eq. (5.32) and Eq. (5.39). The process that is at threshold at the Mott transition is

$$\pi(p_1 + p_2) \to q(p_1) + \bar{q}(p_2), \tag{5.48}$$

leading to a divergence of the intermediate quark loops in the effective meson-meson vertices. As the corresponding amplitudes enter in both isospin states, both scattering lengths are affected by this process. For higher temperatures, π is no longer a stable particle but has a finite width. The kinetic approach treating the pions as a quasi-free gas of stable particles ends here.

We can now analyze the pion gas and test whether it is suitable for a kinetic description or not. We first analyze the particle number density n and the entropy density s pictured in Fig. 5.18(a). Both quantities are not modified by the $\pi\pi$-scattering processes discussed in Fig. 5.17(a), but are affected by the change of the effective pion mass in medium (see e. g. Fig. 5.17(b)). In the temperature range $0 < T < T_{Mott}$, this variation is small, and indeed it is hard to see the differences in n and s between the medium-dependent m_π and the vacuum-extrapolated curve.

The validity of the assumptions of the kinetic approach has to be verified again, since the pion properties are modified at finite temperature. We can use the inverse σ-mass as an estimate of the range of interaction generated by the σ-propagation diagram. Additionally, the hard sphere estimate $\sigma = \pi d^2$ can be calculated. In Fig. 5.18(b), the estimates for the ratio of mean free path λ and interaction range d are shown, again for the full-temperature dependent NJL calculation in bold lines and the Weinberg-values in thin lines[10]. The behavior for small values of T is similar

---

[10] The result for $d = 1/m$ is not comparable directly. For the Weinberg case, we estimate the range of interaction to be the Compton wavelength $1/m_\pi$. In the NJL calculation, the effective range $1/m_\sigma$ is motivated by the σ-propagation diagram.

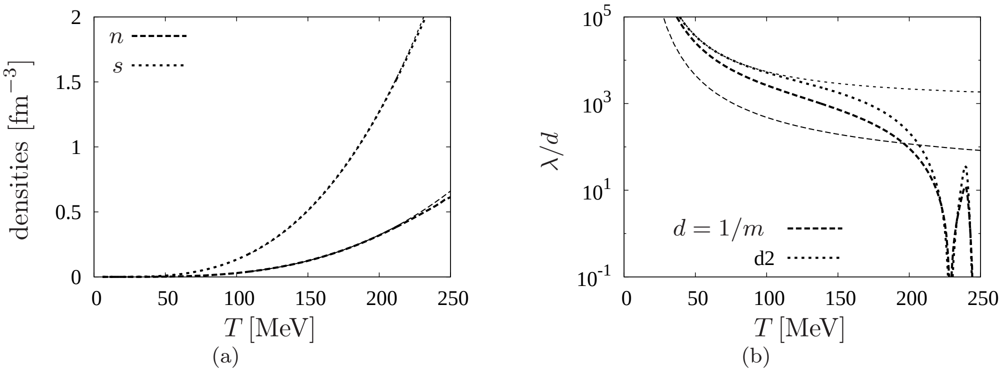

Figure 5.18: Properties of the pion gas calculated from the Nambu-Jona-Lasinio model. (a) Particle number density n and entropy density s of the NJL calculation (bold lines) and of the extrapolated vacuum value of m_π (thin lines). (b) Estimates for λ/d of the NJL calculation (bold lines) and the extrapolated (Weinberg) vacuum values (thin lines). The interaction range $d = 1/m$ is set to the inverse σ-mass in the first case, and to the Compton wavelength of the pion in the latter.

for both systems, and we find a large mean free path leading to a huge value of λ/d close to the vacuum. For higher temperatures, the deviation of the fully temperature-dependent NJL pion gas from the Weinberg-system increases. The strong enhancement of $a_{\pi\pi}^{NJL,0}$ at T_{diss} leads to a longer range of the $\pi\pi$-interaction estimate and a smaller mean free path λ, thus the ratio falls far below 1. Between the two transition temperatures, a value of about 1 is reached again before the λ/d-estimates fall to zero at the Mott temperature T_{Mott}. We can conclude that the kinetic treatment of the system used for shear viscosity calculation is reasonable for temperatures $T \lesssim 215\,\text{MeV}$.

5.4.3 Viscosity and entropy density

The scattering matrix can be used as an input for the shear viscosity formulation in kinetic theory. The numerical results for $N_S = 3$ and the parameters from Tab. 2.1 No 2 are presented in this section.

In Fig. 5.19, the shear viscosity η is plotted as a function of temperature T. One sees that at low temperatures, the full kinetic calculation of the shear viscosity coefficient using the NJL scattering amplitudes and pion masses resembles the results obtained with vacuum masses and the Weinberg scattering term. This is in agreement with the behavior of densities and λ/d shown in Fig. 5.18: Both frameworks are constructed such that they coincide in vacuum and are similar at low temperatures. The two curves begin to differ visibly for temperatures T larger than about 100 MeV, and show a significantly different behavior thereafter. While Weinberg viscosity continues to grow with temperature (this is shown in Fig. 5.11(a) in detail), the NJL viscosity ceases its increase and has a maximum at about 160 MeV. The drop ends at a very small value at the σ-dissociation transition at T_{diss}, and between T_{diss} and T_{Mott}, a second maximum occurs before η falls again in the vicinity of the Mott temperature. However, one should recall that the strict range of application of the kinetic treatment is limited to $0 < T \lesssim 215\,\text{MeV}$, as it was derived in Fig. 5.18(b), hence the behavior of the curve around and in between T_{diss} and T_{Mott} has no meaning. However, it is possible to understand the viscosity minima at the transition temperatures as effects of the enhancement of scattering length at these points shown in Fig. 5.17(a): The strong coupling induced by the large scattering amplitude lead to a small shear viscosity. Beside the two lines indicating calculations in the Sonine-expanded Chapman-Enskog treatment, points mark the shear viscosity estimate $\eta = \bar{p}/3\sigma$. The qualitative behavior is very similar to the one found for the simple Weinberg result: The mean free path estimate is in the same order of magnitude but smaller than the full result.

In Fig. 5.20, the ratio of shear viscosity η and entropy density s is shown for the same data. In the

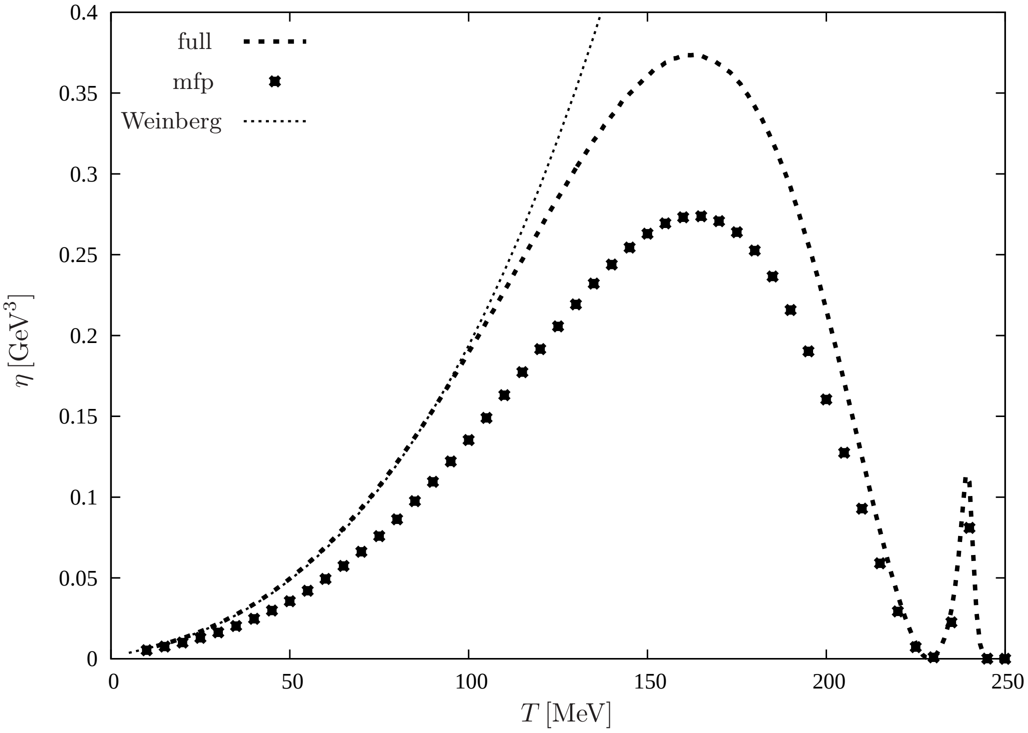

Figure 5.19: Shear viscosity of a pion gas calculated from the NJL model. The line named 'full' is the full calculation in kinetic theory, the mean free path (mfp) estimate $\eta = \bar{p}/3\sigma$ is shown as points. The pure Weinberg scattering term, identical to the NJL result in vacuum, is also shown.

region of small temperatures the two calculations lie on top of each other and result in quite high values for η/s. While the Weinberg interaction settles at values of about 10^2 in the temperature range that is investigated, the NJL calculation is affected by the increasing coupling close to the transition temperatures and bends down. At the σ-dissociation temperature the ratio falls to a very small value, and the same behavior is found at the Mott-transition. However, the kinetic theory already broke down before, thus the lowest value of η/s that is found in the presented calculation is between 10^0 and 10^1 - more than one order of magnitude below the Weinberg result. We conclude that the introduction of a fully temperature-dependent scattering amplitude and fully temperature-dependent effective particle masses affect the behavior of shear viscosity enormously. The effect of chiral symmetry breaking and restoration is modeled in the Nambu-Jona-Lasinio model, and the resulting temperature dependent interaction- and decay-channels absent in the simple vacuum extrapolation are included in the presented calculation. The natural transition temperatures of the system are characterized by minima in η/s, but the immediate vicinity of these transitions is not accessible in kinetic theory.

5.4.4 Thermal conductivity and fluidity

The numerical results for the shear viscosity and the ratio of shear viscosity over entropy density gave an insight in the medium modifications of pions. As in Sec. 5.3, we also calculate the thermal conductivity κ, and the fluidity measure L_η/L_n. The results of these calculations are shown in Fig. 5.21.

The heat conductivity of the NJL pions, which is shown in Fig. 5.21(a), shows important modifications compared to the pion gas with the Weinberg-scattering amplitude, due to the temperature-dependend corrections. While the agreement at low temperature is rather good, even the qualitative behavior of the variation of κ with temperature T changes. The similarity of the curves for η (see Fig. 5.19) and κ are obvious: Both deviate from the vacuum-extrapolation at intermediate temperatures and have very small values at the crossover temperatures. Even the position of the

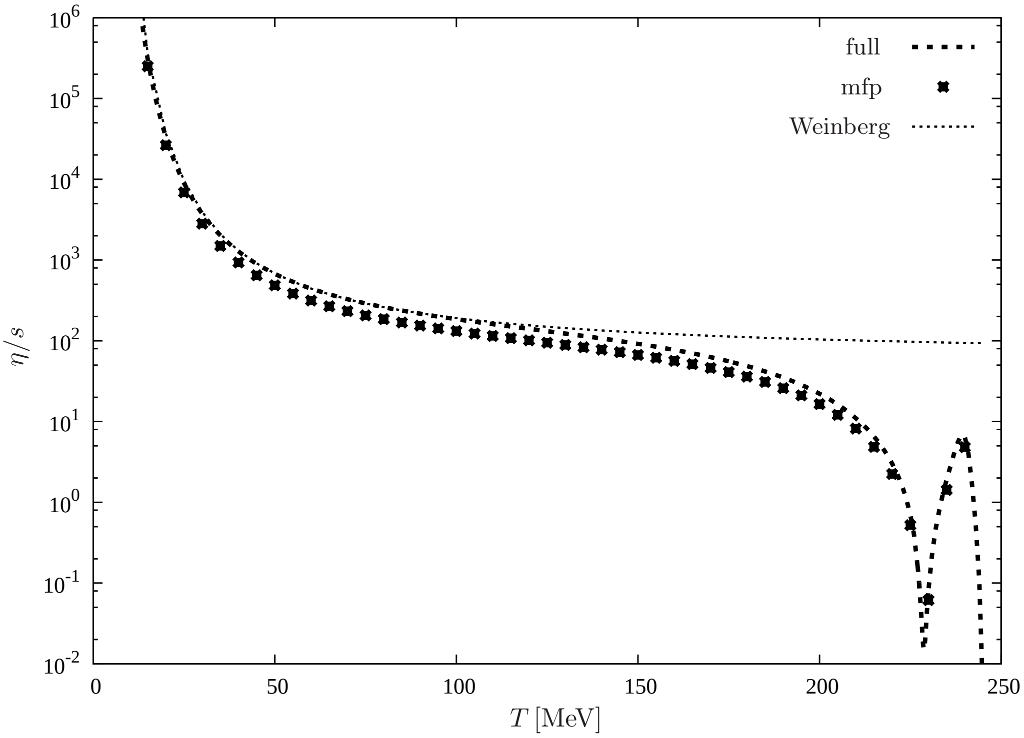

Figure 5.20: Ratio of shear viscosity and entropy density of a pion gas calculated from the NJL model. As in Fig. 5.19, the full calculation in kinetic theory is compared to the the mean free path (mfp) estimate $\eta = \bar{p}/3\sigma$ and viscosity from the Weinberg scattering term. Note that the underlying assumptions are only valid for $T \lesssim 215\,\mathrm{MeV}$.

maxima of η and κ are similar. This fact underlines the assumption that the most-ideal fluid is found at transitions: The viscous corrections in the hydrodynamic equations are negligable if all prefactors, the transport coefficients η, κ, and ζ, are small.

In Fig. 5.21(b), the fluidity measure L_η/L_n is shown in its non-relativistic version as well as in its relativistic form. The ratio is shown as a function of temperature, and the vacuum-extrapolated function, which correspond to the Weinberg scattering amplitude, is indicated as well. The curves show a convincing similarity with the curves for η/s, which are shown in Fig. 5.20. While the values for L_η/L_n from the Weinberg scattering amplitude stay higher than 10^2 in the investigated temperature region, the NJL result drops at the two transition temperatures T_{diss} and T_{Mott} to values below one. This result affirms the conclusion from the discussion of the ratio η/s: The pion gas in the NJL calculation behaves like an almost ideal fluid in the chiral crossover region due to the medium modifications of the particle masses and transition rates.

5.4.5 Possible extensions of the calculation

There are different possibilities to extend the calculation of the shear viscosity of pions in the Nambu-Jona-Lasinio model. First we will discuss if it is possible to avoid certain additional approximations that were done in the framework, other ways of calculation of kinetic theory-input from the NJL model will be presented thereafter.

A strong limitation of the whole calculation in this section was the extrapolation of the scattering matrix of pions at rest to pions at finite 3-momentum. This was due to the previous works concerning the $\pi\pi$-scattering length in the NJL model that can directly be used for transport calculations in the presented framework. A more exact approach would require the calculation of the full momentum-dependent quark-boxes, quark-triangles and meson propagators. Especially the quark-polygons are difficult to calculate for real external momenta if one relaxes the approximation of infinitely heavy quarks.

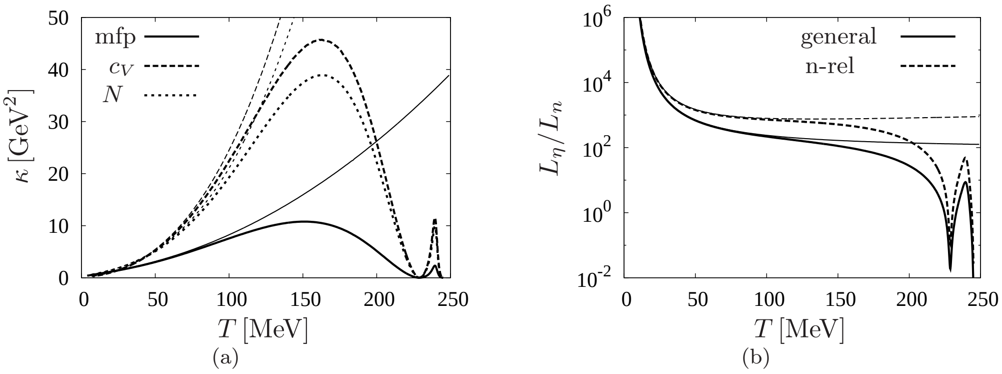

Figure 5.21: Transport properties of a NJL pion gas (bold lines) and a Weinberg pion gas (thin lines) as functions of temperature. (a) Thermal conductivity estimates, where the mfp-curve is obtained from $\kappa = \bar{v}/4\sigma$, the c_V-curve by $\kappa = 1.2\eta c_V/m$ and the N-curve by $\kappa = \bar{p}/4m\sigma$. (b) Fluidity measure L_η/L_n (solid line) and its nonrelativistic limit (dashed line) for $\mu_\pi = 0$.

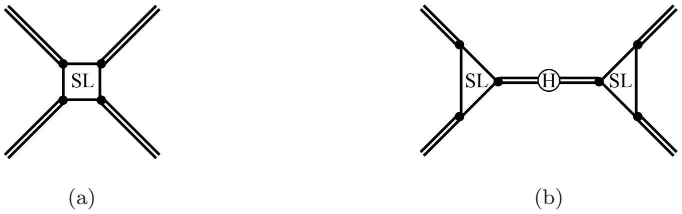

Figure 5.22: $\pi\pi$-scattering diagrams in Nambu-Jona-Lasinio model in static limit, which is the sum of the box-diagram (a) and the σ-propagation diagram (b). The meson-meson vertices labeled "SL" are the quark box and the quark triangle in static limit.

An easier way of including more microscopic information from the scattering processes is the static limit of quark-boxes and quark-triangles while the propagator of the σ-meson is taken fully momentum-dependent. This would correspond to scattering amplitudes represented by Feynman diagrams shown in Fig. 5.22: The quarks parts of the diagrams are shrunk to effective meson-meson vertices and the RPA σ-meson is taken without further approximations. These diagrams lead to a momentum-dependent scattering amplitude where the σ-resonance mass pole would appear. However, this scheme can not be implemented without additional tricks because the calculation of the propagator of the scalar meson is too time-consuming for a invocation inside the 5-dimensional integral used in relativistic kinetic theory. Moreover, the resonance approximation of D_σ is not suitable for the calculation because the connection to the Weinberg term in vacuum is lost: The resonance approximation fits the propagator of σ at its mass m_σ, but in the diagrams for the scattering length, the propagator is evaluated at 0 and at $2m_\pi$. The resulting deviations are important since the different contributions to $i\mathcal{M}$ are sensitive to small changes in some of them, as it is shown in Tab. 5.2.

Another way of extending the calculation of $\pi\pi$-scattering is the resummation of the calculated cross section, diagrammatically expressed in Fig. 5.23. Such a treatment of the $\pi\pi$-scattering in transport calculation has been performed in the linear σ-model [146]. Although the resummation technique gives rise to a momentum-dependent scattering amplitude, an immediate use of the NJL scattering results is not suitable in this context because the low-momentum regime of the scattering is considerably affected by this procedure while the ultraviolet result falls to the bare scattering kernel. But the bare scattering amplitude in NJL fits the zero-momentum Weinberg term, thus the resummed scattering will differ from it, and the Weinberg scattering is obtained at high momenta where it is not convincing. Hence a refit of the NJL parameters has to be performed to allow the resummation of the $\pi\pi$-scattering amplitude.

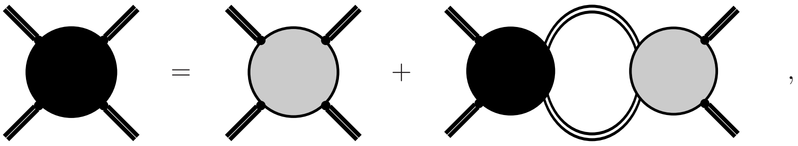

Figure 5.23: Resummation of the $\pi\pi$-scattering cross section. The gray circle denotes the scattering amplitude obtained from box-diagram and σ-propagation diagram, and the black circle denotes the resummed scattering amplitude.

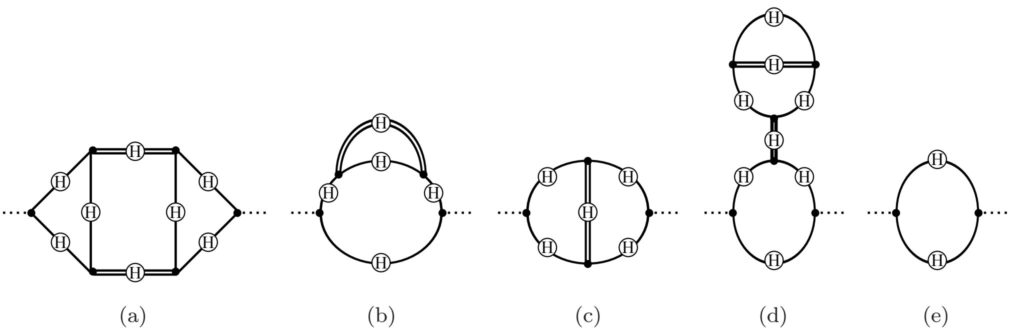

Figure 5.24: Expansion of the polarization loop of the Kubo-Green formula in $1/N_c$. The last diagram (e) is the leading-order contribution, the diagrams (a) to (d) are of next-to-leading order.

Lastly, on has to mention that the restriction to quarks, pions and σ-mesons comes from the choice of the NJL Lagrangian. It is possible to include also the ρ-channel in the $\pi\pi$-scattering. Therefore, one has to include a vector interaction term in $\mathscr{L}$. A calculation of this contribution was done in a similar framework as it was presented for the $\pi\pi$-scattering length [212]. Beside the extension of the model to more interaction terms, it is also possible to include more quark flavors. A calculation of the $\pi - K$ scattering length in a $SU(3)$-NJL model is found in [213].

5.5 Meson-quark contribution

In the previous four sections, several calculations of transport properties in relativistic kinetic theory were discussed. Although the calculation of some aspects from the NJL model were possible, the results were limited to the kinetic regime, where the dilute gas condition $\lambda/d \gg 1$ was fulfilled. For calculations beyond this limitation, we have to leave kinetic theory behind and consider the exact formulas for the transport coefficients given by the time-correlation function method.

Transport coefficients in Green-Kubo formalism are given by the evaluation of Feynman-diagrams of the type shown in Fig. 3.1. For a systematic approximation scheme in the framework of the NJL model, a truncation has to be found that leads to a finite set of contributing terms. The choice of diagram used in this section has already been used earlier [115]. However, some aspects have not been discussed yet.

5.5.1 Expansion scheme

The idea is to expand the dressed quark loop $\varPi$ shown in Fig. 3.1 in terms of $1/N_c$. Such an approximation scheme was already discussed in the context of $1/N_c$-corrections to meson properties [214, 215]. The leading-order contribution is the RPA quark loop. The diagrams to next-to-leading order $\varPi^{(a)}$ to $\varPi^{(d)}$ are shown in Fig. 5.24. Then the full polarization loop reads

$$\varPi = \varPi^{\mathrm{RPA}} + \varPi^{(a)} + \varPi^{(b)} + \varPi^{(c)} + \varPi^{(d)}. \tag{5.49}$$

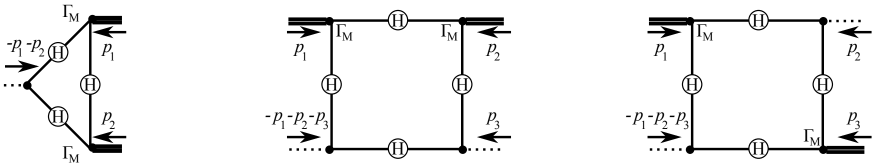

(a) (b) (c)

Figure 5.25: Momentum labeling in the triangle diagram and in the box diagrams. (a) correspond to the triangle vertex $\Gamma_{\gamma^2 MM}$, (b) correspond to $\Gamma_{\gamma^2 MM\gamma^2}$, and (c) correspond to $\Gamma_{\gamma^2 M\gamma^2 M}$.

The expressions for $\Pi^{(a,b,c,d)}$ for an external momentum $(i\omega_e, \mathbf{0})$ as it is needed in the shear viscosity correlation function can all be written in the form

$$\Pi^{(a,b,c,d)}(i\omega_e, \mathbf{0}) = \sum_M T \sum_{i\omega_q} \int \frac{\mathrm{d}^3 q}{(2\pi)^3} P_M^{(a,b,c,d)}(i\omega_e, i\omega_q), \tag{5.50}$$

where we suppress the dependency on the 3-momentum $\mathbf{q}$ in the integrand symbols $P_M^{(a,b,c,d)}$. The integrand $P_M^{(a)}$ corresponding to the first diagram is defined as

$$\begin{aligned} P_M^{(a)}(i\omega_e, i\omega_q) =& \frac{1}{2} \Gamma_{\gamma^2 MM}(i\omega_e + i\omega_q, \mathbf{q}; -i\omega_q, -\mathbf{q}) D_M(i\omega_q, \mathbf{q}) \times \\ & \times \Gamma_{\gamma^2 MM}(-i\omega_e - i\omega_q, -\mathbf{q}; i\omega_q, \mathbf{q}) D_M(i\omega_e + i\omega_q, \mathbf{q}). \end{aligned} \tag{5.51}$$

The RPA meson propagator D_M couples to the external vertices via the quark triangle diagram $\Gamma_{\gamma^2 MM}(p_1; p_2)$,

$$\begin{aligned} \Gamma_{\gamma^2 MM}(p_1; p_2) = -T \sum_{i\omega_k} \int \frac{\mathrm{d}^3 k}{(2\pi)^3} \mathrm{Tr}\Big[& k_x \gamma^2 S_H(i\omega_k + i\omega_{p_1} + i\omega_{p_2} + \mu, \mathbf{k} + \mathbf{p}_1 + \mathbf{p}_2) \times \\ & \times \Gamma_M S_H(i\omega_k + i\omega_{p_1} + \mu, \mathbf{k} + \mathbf{p}_1) \Gamma_M S_H(i\omega_k + \mu, \mathbf{k}) \Big] + ex., \end{aligned} \tag{5.52}$$

where the remark $+ex.$ indicates that both directions of fermion propagators in the diagram are included. The underlying momentum labeling is of the two independend momenta p_1 and p_2 is shown in Fig. 5.25(a). The second diagram of Fig. 5.24 has the integrand

$$P_M^{(b)}(i\omega_1, i\omega_2) = \Gamma_{\gamma^2 MM\gamma^2}(-i\omega_q, -\mathbf{q}; i\omega_q, \mathbf{q}; -i\omega_e, \mathbf{0}) D_M(i\omega_q . \mathbf{q}) \tag{5.53}$$

which involves the quark box diagram

$$\begin{aligned} \Gamma_{\gamma^2 MM\gamma^2}(p_1; p_2; p_3) =& T \sum_{i\omega_k} \int \frac{\mathrm{d}^3 k}{(2\pi)^3} \mathrm{Tr}\Big[k_x \gamma^2 S_H(i\omega_k + \mu, \mathbf{k}) \Gamma_M S_H(i\omega_k + i\omega_{p_1} + \mu, \mathbf{k} + \mathbf{p}_1) \times \\ & \times \Gamma_M S_H(i\omega_k + i\omega_{p_1} + i\omega_{p_2} + \mu, \mathbf{k} + \mathbf{p}_1 + \mathbf{p}_2) \times \\ & \times k_x \gamma^2 S_H(i\omega_k + i\omega_{p_1} + i\omega_{p_2} + i\omega_{p_3} + \mu, \mathbf{k} + \mathbf{p}_1 + \mathbf{p}_2 + \mathbf{p}_3) \Big]. \end{aligned} \tag{5.54}$$

The definition of the momenta p_1, p_2 and p_3 are shown in Fig. 5.25(b). The integrand of $\Pi^{(c)}$ is similar,

$$P_M^{(c)}(i\omega_1, i\omega_2) = \Gamma_{\gamma^2 M\gamma^2 M}(-i\omega_q, -\mathbf{q}; -i\omega_e, \mathbf{0}; i\omega_q, \mathbf{q}) D_M(i\omega_q . \mathbf{q}), \tag{5.55}$$

and involves a similar quark box diagram $\Gamma_{\gamma^2 M\gamma^2 M}$, where the only difference to $\Gamma_{\gamma^2 MM\gamma^2}$ is the order of the vertices,

$$\begin{aligned} \Gamma_{\gamma^2 M\gamma^2 M}(p_1; p_2; p_3) =& T \sum_{i\omega_k} \int \frac{\mathrm{d}^3 k}{(2\pi)^3} \mathrm{Tr}\Big[k_x \gamma^2 S_H(i\omega_k + \mu, \mathbf{k}) \Gamma_M S_H(i\omega_k + i\omega_{p_1} + \mu, \mathbf{k} + \mathbf{p}_1) \times \\ & \times k_x \gamma^2 S_H(i\omega_k + i\omega_{p_1} + i\omega_{p_2} + \mu, \mathbf{k} + \mathbf{p}_1 + \mathbf{p}_2) \times \\ & \times \Gamma_M S_H(i\omega_k + i\omega_{p_1} + i\omega_{p_2} + i\omega_{p_3} + \mu, \mathbf{k} + \mathbf{p}_1 + \mathbf{p}_2 + \mathbf{p}_3) \Big]. \end{aligned} \tag{5.56}$$

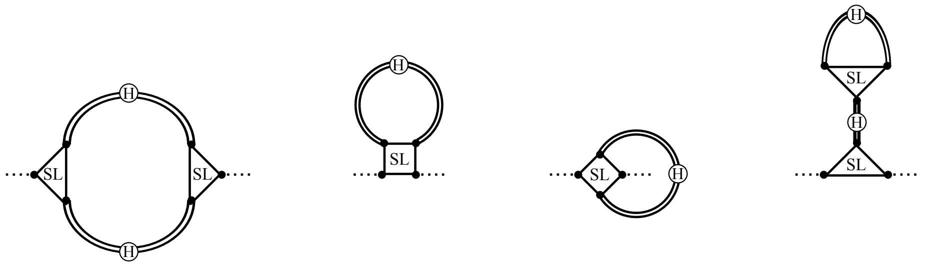

(a) (b) (c) (d)

Figure 5.26: Diagrams contributing to the viscosity polarization loop (see Fig. 5.24) in the static limit. It turns out that only the first diagram (a) yield a contribution to rhe shear viscosity.

The momentum labeling in this vertex is found in Fig. 5.25(c).The exact form of the last correction diagram $\Pi^{(d)}$ is not important because it does not yield a contribution to shear viscosity. This is easily seen because the loop can be seen as a quark loop including two quark propagators that are dressed in different ways. One is the Hartree quark propagator S_H, the other one is dressed with a simple self-energy diagram that leads to a constant, real self-energy. Thus the spectral functions of the two dressed propagators are δ-like with peaks at different positions, hence their product vanishes. A more explicit derivation of this result is found in [115].

In summary, the shear viscosity η in this expansion can be expressed as a sum over three terms

$$\eta = \eta^{(a)} + \eta^{(b)} + \eta^{(c)}, \tag{5.57}$$

where each contribution

$$\eta^{(a,b,c)} = - \lim_{\omega_e \to 0} \frac{\mathrm{d}}{\mathrm{d}\omega_e} \mathrm{Im} \Pi^{(a,b,c)}(\omega_e + i\epsilon) \tag{5.58}$$

could be expressed as a sum over mesonic parts $\Pi_M^{(a,b,c)}(\omega_e)$ corresponding to the four RPA meson channels of the 2-flavor Nambu-Jona-Lasinio model.

5.5.2 Simplification and calculation

The three non-vanishing contributions $\Pi^{(a,b,c)}$ to the shear viscosity η formulated in the previous section are highly nontrivial diagrams. The continuation to real frequencies, the calculation of the imaginary part and the numerical computation are complicated tasks. This can be simplified much by taking a systematic approximation often used in the NJL model involving meson propagators in diagrams: the static limit. This corresponds to the limit of vanishing external momentum[11], or equivalently to the limit of infinitely heavy constituent quarks. One can express this limit diagrammatically by contracting all quark boxes and triangles to effective meson-meson vertices, as it is shown in Fig. 5.26.

Thus the effective meson vertices $\Gamma_{\gamma^2 MM}$, $\Gamma_{\gamma^2 MM\gamma^2}$, and $\Gamma_{\gamma^2 M\gamma^2 M}$ are expanded in powers of the external momentum q/m. It is found that the static-limit expressions of these vertices are independent of q_0 and depend on the 3-components of q like

$$\Gamma^{SL}_{\gamma^2 MM}\big(p_1 = (i\omega_{p_1}, \mathbf{p}); p_2 = (i\omega_{p_1}, -\mathbf{p})\big) \propto p_x p_y \tag{5.59}$$

$$\Gamma^{SL}_{\gamma^2 MM\gamma^2}\big(p_1 = (i\omega_{p_1}, \mathbf{p}); p_2 = (i\omega_{p_2}, -\mathbf{p}); p_3 = (i\omega_{p_3}, \mathbf{0})\big) \propto p_x^2 p_y^2 \tag{5.60}$$

$$\Gamma^{SL}_{\gamma^2 M\gamma^2 M}\big(p_1 = (i\omega_{p_1}, \mathbf{p}); p_2 = (i\omega_{p_2}, \mathbf{0}); p_3 = (i\omega_{p_3}, -\mathbf{p})\big) \propto p_x^2 p_y^2 \tag{5.61}$$

---

[11] The static limit correspond to the limit of minimal external 4-momentum. In the case of external on-shell mesons coupling to quark boxes and quark triangles as they were discussed in Sec. 5.4.5, the vanishing 3-momentum lead to the momentum of an external on-shell meson at rest, $q = (m_M, \mathbf{0})$. For the expanded shear viscosity quark loop, there is no restriction to on-shell particles, thus the minimal external momentum is $q = (0, \mathbf{0})$.

The practical evaluations of η in static limit is done in Appendix G. This leads to

$$\begin{aligned}\eta^{(a)} =& -\sum_M \int \frac{\mathrm{d}^3 q}{(2\pi)^3} \Big(\Gamma^{SL}_{\gamma^2 MM}(\mathbf{q})\Big)^2 \Big(T D_M(0,\mathbf{q}) \mathrm{Im} D_M(0,\mathbf{q}) + \\ &+ \int_{-\infty}^{+\infty} \frac{\mathrm{d}q_0}{2\pi} n'_B(q_0) [\mathrm{Im} D_M(q_0,\mathbf{q})]^2\Big) \qquad (5.62)\\ \eta^{(b)} =& 0 \qquad (5.63)\\ \eta^{(c)} =& 0 \qquad (5.64)\end{aligned}$$

Thus the only remaining diagram in the expansion of the Kubo-formula quark loop in next-to-leading order $1/N_c$ is the meson loop in Fig. 5.26(a). This diagram can be interpreted as the contribution of a meson gas with particles that interact via effective vertices. If one looks more carefully to the evaluation of the diagram, writing the external vertex

$$\Gamma^{SL}_{\gamma^2 MM} = \Lambda^{SL}_{\gamma^2 MM} p_x p_y \qquad (5.65)$$

one can identify with help of the notation introduced in Eq. (2.38) the expression

$$\begin{aligned}\Pi^{(a),\,SL}(i\omega_e, \mathbf{0}) = \sum_M \big(\Lambda^{SL}_{\gamma^2 MM}\big)^2 T \sum_{i\omega_q} \int \frac{\mathrm{d}^3 q}{(2\pi)^3} \Big[g^2_{Mqq}(i\omega_e + i\omega_q, \mathbf{q}) g^2_{Mqq}(i\omega_q, \mathbf{q}) \times \\ \times\, q_x q_y \mathcal{D}_M(i\omega_e + i\omega_q, \mathbf{q}) q_x q_y \mathcal{D}_M(i\omega_q, \mathbf{q})\Big]. \qquad (5.66)\end{aligned}$$

The same quantity for a bosonic field theory with scalar mesons described by dressed propagators D_a and a dressed vertex Γ_a would read

$$\Pi^{Scalars}(i\omega_e, \mathbf{0}) = \sum_a T \sum_{i\omega_q} \int \frac{\mathrm{d}^3 q}{(2\pi)^3} \Big[\Gamma_a q_x q_y D_a(i\omega_e + i\omega_q, \mathbf{q}) q_x q_y D_a(i\omega_q, \mathbf{q})\Big], \qquad (5.67)$$

so we can identify the supplemental terms in Eq. (5.66) as a dressed vertex.

In the restored phase, there is no problem in calculating (5.62), but in the chirally broken phase, the pion mass pole is present in the spectral function of the pion. This mass pole causes the same problems as the poles in the Hartree quark spectral function: A product of two δ-functions appears in the correlator. Technically it is possible to avoid the δ-peak in the same way as for the case of free fermion (see Sec. 3.2.3). Nevertheless, the viscosity contribution from on-shell pion interacting is missing if this treatment is applied. Therefore the interpretation of shear viscosity from formula (5.62) in the chirally broken phase has to be done with care. The spectral weight of on-shell pions in systematically ignored in the broken phase, while it is taken into account in the restored phase. One could imagine that it is possible to add these missing contributions in the low-temperature region by including some processes to allow on-shell pions to interact, but such terms are not present in this current approximation scheme.

The qualitative understanding of the shear viscosity obtained from the presented treatment of the time-correlation function method is a rather difficult issue. In contrast to the results obtained with kinetic theory (see Sec. 5.1, 5.2, 5.3, and 5.4) it is difficult to identify the origin of the interactions entering in the calculation. What enters is the meson-quark coupling (hidden in D_M and $\Gamma_{\gamma^2 MM}$) and the decays of π and σ into quarks (hidden in $\mathrm{Im}D_M$). What does not enter is any meson-meson scattering, especially no $\pi\pi$-scattering as it was essential in Sec. 5.4.

We conclude that the approximations leading to the shear viscosity formula (5.62) is very natural and systematic in the context of the NJL model, but it will be difficult to interprete the results presented in the next section.

5.5.3 Viscosity for $\mu = 0$

We first focus on the region relevant for heavy-ion collisions at small chemical potential μ. We set $\mu = 0$ for simplicity and use the parameter set from Tab. 2.2 No 2 with a mesonic cut-off $\Lambda_M = 300\,\mathrm{MeV}$.

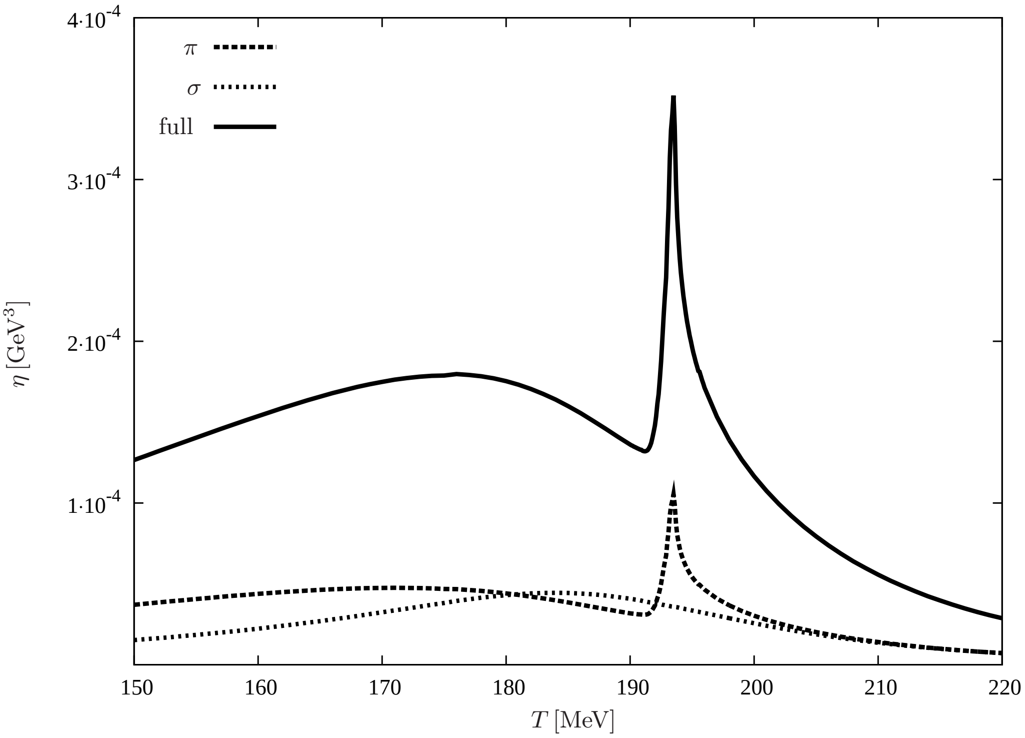

Figure 5.27: Shear viscosity coefficient η as a function of temperature, calculated from the expanded Kubo-correlation function in static limit. The quark chemical potential is set to $\mu = 0$, the parameters used here are found in Tab. 2.2 No 2 with a mesonic cut-off $\Lambda_M = 300\,\mathrm{MeV}$. The sum of σ-contributions and the three pions gives the full result.

The resulting viscosity from Eq. (5.62) as a function of temperature T is shown in Fig. 5.27. We begin the discussion of this plot at elevated temperatures. We find that in the restored phase, the contributions of the mesonic resonances π and σ are degenerate asymptotically and the summed shear viscosity of them decreases with temperature. This behavior can be understood when the temperature-dependency of meson spectral functions (see Sec. 4.2.1 and Fig. 4.1) are considered. In the restored phase, π and σ can decay into a quark-antiquark pair. The broadening of the spectra due to these decays increases the higher the temperature T becomes, and the broader spectral function ρ_M leads lower viscosity than a spectrum with a smaller width. When one approaches the crossover temperature, the viscosity rises: While the σ-meson shows a smooth behavior of $\eta(T)$, the pion contribution rises very strongly. This is an effect of the Mott transition[12], that is smeared over the temperature range

$$T \in [T_{Mott}(|\mathbf{q}| = 0),\, T_{Mott}(|\mathbf{q}| = \Lambda_M)] \tag{5.68}$$

because RPA mesons with different 3-momentum $\mathbf{q}$ enter in the viscosity formula (5.62). As it was discussed in the previous section, the contributions from the pion mass peak in the spectrum do not contribute to η. Therefore, in Fig. 5.27 this on-shell contribution of the π-meson is missing at temperatures $T < T_{Mott}(|\mathbf{q}| = \Lambda_M)$, but in the Mott transition range, there are mesons with a certain $|\mathbf{q}|$ that are exactly at threshold

$$m_\pi(\mathbf{q}) = 2\sqrt{m_H^2 + \mathbf{q}^2}. \tag{5.69}$$

These constellations lead to a strong increase of the spectral density at the continuum threshold which enters quadratically in the Kubo formula, and we find an enhancement in the shear viscosity. In the restored phase, close to the transition temperature, the viscosity coefficient has a minimum

---

[12] The small window of Mott transition was not resolved in the previous work [115]

as a result mainly from the continuum- and particle-hole-branch contribution of the pion spectra. For lower temperatures, η_σ again falls below η_π.

It would be interesting to study the ratio of shear viscosity and entropy density η/s for the Kubo formula results, especially because we saw in the results with kinetic theory that the region where η/s is expected to be small is out of the range of validity of the approximations. Unlike in kinetic theory, it is not obvious which entropy density s has to be taken, because no quasi-free gas of particles was assumed. As it was shown in Sec. 2.7, there is also a perturbative $1/N_c$-correction to the thermodynamic potential in the NJL model, hence one can calculate a $1/N_c$-corrected entropy density. However, in the evaluation of Kubo-formula additional approximations were made, i.e. the static limit which lead to effective meson-meson vertices. This limit of infinitely heavy quarks has to be translated to the calculation of entropy density and thermodynamic quantities, too. Moreover, the result has been interpreted as viscosity of bosonic fields with a certain dressing of propagators and their vertices, and the thermodynamic potential should be truncated in the same way. Finally, in the chirally broken phase the on-shell contribution of the pions is missing. Even if one could separate the different contributions in the thermodynamic potential per volume, the meaning of the resulting ratio is unclear since

$$\frac{\eta}{s} = \frac{\eta^{(a)} + \eta^{rest}}{s^{(a)} + s^{rest}} \neq \frac{\eta^{(a)}}{s^{(a)}} + \frac{\eta^{rest}}{s^{rest}}. \tag{5.70}$$

Despite these difficulties in interpreting the meson-contributions to the shear viscosity obtained with the Kubo formula, an amazing result is obtained in the neighborhood of the critical end-point of the phase diagram. This is discussed in the following section.

5.5.4 The critical end point

We calculate the shear viscosity with the same method used in the previous paragraphs in the vicinity of the critical end point. Therefore we take the parameter set from Tab. 2.2 No 5 with a mesonic cut-off $\Lambda_M = 700\,\mathrm{MeV}$. The phase diagram for this parameter set is found in Fig. 2.11(c).

We vary the temperature T at $\mu \lessapprox \mu_{crit}$ around $T_c \approx 120\,\mathrm{MeV}$, thus in the cross over region. The result is shown in Fig. 5.28. The first observation is that the shear viscosity is strongly varying in the relatively small temperature range: The total shear viscosity varies by a factor of more than 10^3, the single contributions of σ and π even more. Beside the rapid variations of thermodynamic quantities in the critical region, a special input naturally included in the Kubo formula result Eq. (5.62) is essential for the behavior. We first analyze the integrand of the mentioned equation close to $q_0 = 0$. With help of L'Hôpital's rule, we obtain

$$\lim_{q_0 \to 0} n'_B(q_0)[\mathrm{Im}D_M(q_0, \mathbf{q})]^2 \propto [\mathrm{Im}D'_M(q_0, \mathbf{q})]^2, \tag{5.71}$$

where all primes denote derivatives with respect to q_0. As it was discussed in Sec. 4.2.1, the spectral function of the σ-meson

$$\rho_\sigma(q_0, \mathbf{q}) = -2\mathrm{Im}D_\sigma(q_0, \mathbf{q}) \tag{5.72}$$

has a special behavior at the critical point: It develops a pole at $q_0 = 0$ due to the second-order phase transition. One can estimate from Fig. 4.1(d) that the closer one approaches the critical end point, the larger the derivative of the spectrum at $q_0 = 0$ will become. Thus we find even with this limited approach that the contribution of the σ-meson at the critical point will lead to a divergence of the shear viscosity η. In the vicinity of this point, as it is investigated in Fig. 5.28, a strong enhancement of the σ-contribution to η is found, that is dominating the complete transport coefficient behavior, different from $\mu = 0$ where the scalar meson played a minor role. A minimum in viscosity is found below the critical temperature.

5.6 Green-Kubo formalism with SEP-method

In this section the shear viscosity is calculated in NJL model using Green-Kubo formalism. We apply the systematic approximation schemes developed in chapter 2 to the Green-Kubo correlator and calculate the dressed Green's functions with the SEP-method introduced in chapter 4.

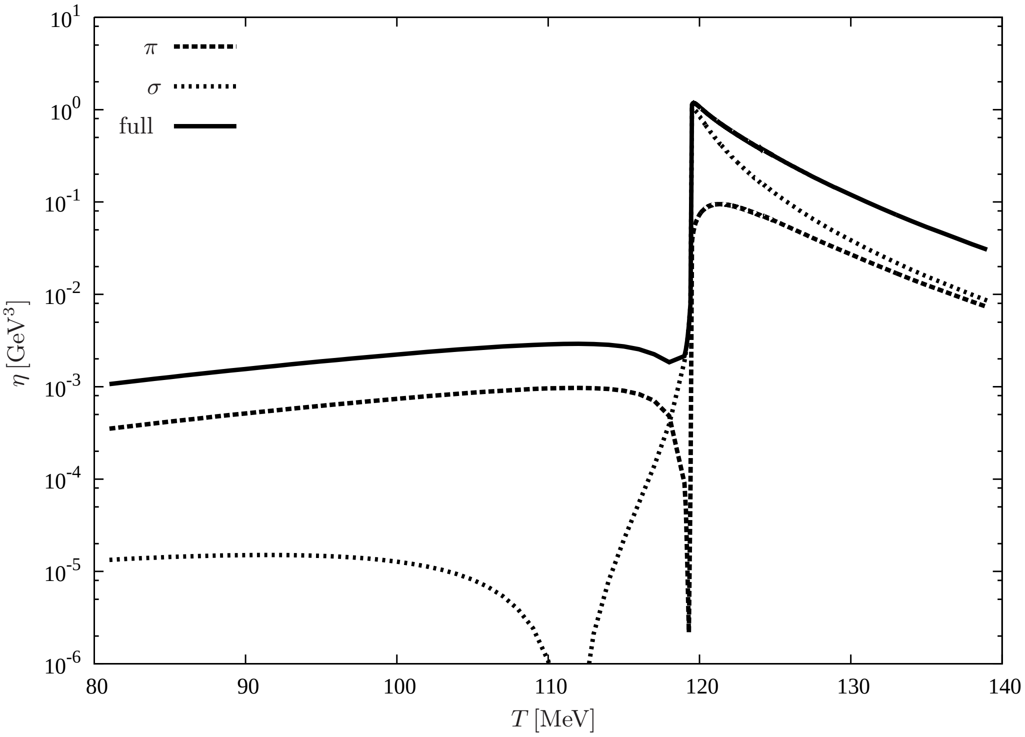

Figure 5.28: Shear viscosity close to the critical end point of the phase diagram. η was calculated from the with Kubo-formula from Eq. (5.62) at $\mu = 430\,\mathrm{MeV} \lessapprox \mu_{crit}$. The parameters used here are found in Tab. 2.2 No 5 using a meson cut-off $\Lambda_M = 700\,\mathrm{MeV}$.

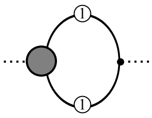

Figure 5.29: This diagram enters in the Green-Kubo formula in next-to-leading in $1/N_c$.

5.6.1 Framework

The shear viscosity of NJL quarks in Green-Kubo formulation makes use of the quark spectral function ρ_{full}. In Chap. 2, different dressings for the quark 2-point functions have been presented, but it was pointed out that the spectral function for this purpose should not be a spectrum of non-interacting particles since this yields trivial results. As a consequence neither the bare quark spectrum nor the Hartree quark spectrum can be used as input for the time correlator. The simplest systematic expansion that is suitable here is the next-to-leading order in the inverse number of colors presented in Sec. 2.8. In a diagrammatic expansion, the expression for the static shear viscosity can be written

$$\eta = - \lim_{q_0 + i\epsilon \to 0 + i\epsilon} \lim_{\mathbf{q} \to 0} \mathrm{Im} \Pi^R(q_0, \mathbf{q}), \tag{5.73}$$

where the function Π^R is the retarded version of the diagram shown in Fig. 5.29
The dressed vertex can be derived from the Φ-functional as it was done for the corrected Bethe-Salpeter-equation in Sec. 2.8.5,

$$\Gamma_\eta^{ij} = \Gamma_{\eta\,\mathrm{loop}\,M}^{ij} + \Gamma_{\eta\,\mathrm{loop}\,M}^{ij}[\Gamma_\eta] + \Gamma_{\eta\,1\ \mathrm{meson}\,M}^{ij}[\Gamma_\eta] + \Gamma_{\eta\,2\ \mathrm{mesons}\,M_1 M_2}^{ij}[\Gamma_\eta] \tag{5.74}$$

The diagrammatic version of the vertex dressing equation for the vertex in the Green-Kubo formula with the correct order in $1/N_c$ is shown in Fig. 5.30. This integral equation for the

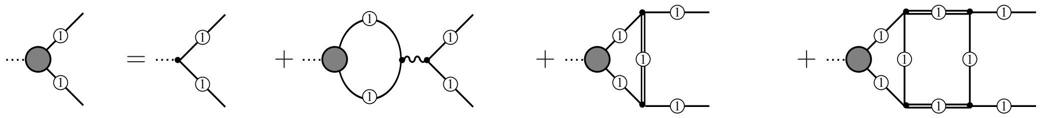

Figure 5.30: Integral equation for the dressing of the vertex in the Green-Kubo formula (see Fig. 5.29).

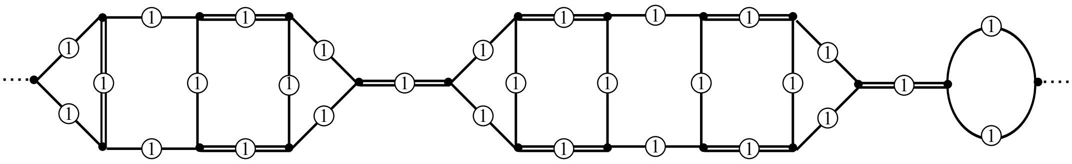

Figure 5.31: Example for a typical diagram contributing to η in the self-consistent $1/N_c$-expansion in next-to-leading order. Note the $\pi\pi$-scattering elements similar to the diagrams shown in Fig. 5.16.

vertex leads to a large set of contributions to the shear viscosity. For an illustration of the various diagrams resulting from this self-consistent vertex dressing, a typical contribution[13] to η is shown in Fig. 5.31. There are dressed quark propagators and RPA mesons containing dressed quarks in different diagrams. On can identify diagrams resembling different meson scattering processes.
Before entering into details of calculation, one can first estimate the importance of terms in different regions in the phase diagram. In the restored phase at high temperatures, meson contributions are vanishing since the weight decreases and the masses grow. The propagators approach their Hartree values and the vertex get back to the bare one, neglecting all terms involving meson propagators. Thus at high temperature one expects that all observables behave like a gas of light, weakly interacting fermions. In the chirally broken phase at low temperatures, mesons are the less massive degrees of freedom, so they will govern the thermodynamic quantities as pressure and entropy density. Dissipative quantities such as shear viscosity are then dominated by the interaction of these light bosons. As the density of the system rises thermally starting from vacuum, one expects the behavior of a dilute pion gas — that should coincide with the relativistic kinetic description.

5.6.2 The vertex

The calculation of the dressed vertex starts with the analysis of the Dirac structure. This is a nontrivial task since the bare vertex in the integral equation is anisotropic. It can be simplified to some extent if the energy-momentum tensor T^{ij} is symmetrized. Then the spacelike components of a Lorentz-vector x can be decomposed in a part $x^{\parallel}$ which is in the $i-j$ plane and a part $x^{\perp}$ which is perpendicular to the $i-j$-plane. With this step, the vertex can be written as a sum of scalar, vector and tensor components. The functions $\Gamma^{s,V0,\cdots}$ proportional to these Dirac structures,

$$\begin{aligned}\Gamma^{ij}_{\eta} = p^{\perp}\Big[&\Gamma^{s}\mathbb{1} + \Gamma^{V0}\gamma^{0} + \Gamma^{V\parallel}\gamma^{\parallel} + \Gamma^{V\perp}\gamma^{\perp} + \\ &+ \Gamma^{T0\parallel}\sigma^{0\parallel} + \Gamma^{T0\perp}\sigma^{0\perp} + \Gamma^{T\perp\parallel}\sigma^{\perp\parallel} + \Gamma^{T\parallel\parallel}\sigma^{\parallel\parallel}\Big], \qquad (5.75)\end{aligned}$$

are called *form factors*. The short hand notation used for example for $\Gamma^{V\parallel}\gamma^{\parallel}$ indicates that the prefactor of the Dirac components γ^{i} and γ^{j} are the same. The different components can be projected out by the usage of the projectors

$$\Gamma^{s,\,V0,\,V\parallel,\,\cdots} = \mathrm{tr}_{\mathrm{Dirac}}\left[\mathcal{P}^{s,\,V0,\,V\parallel,\,\cdots}\Gamma\right]. \qquad (5.76)$$

---

[13] A similar illustration of a typical contribution was shown for the $O(N)$-model in [142].

The projectors $\mathcal{P}$ are the Dirac matrices listed in the following,

$$\begin{aligned}
\mathcal{P}^{s} &= \frac{1}{4}\mathbb{1} & \mathcal{P}^{V0} &= \frac{1}{4}\gamma^{0} \\
\mathcal{P}^{V\parallel} &= \frac{1}{4}\gamma^{\parallel} & \mathcal{P}^{V\perp} &= \frac{1}{4}\gamma^{\perp} \\
\mathcal{P}^{T0\parallel} &= \frac{1}{32}\sigma^{0\parallel} & \mathcal{P}^{T0\perp} &= \frac{1}{32}\sigma^{0\perp} \\
\mathcal{P}^{T\perp\parallel} &= \frac{1}{32}\sigma^{\perp\parallel} & \mathcal{P}^{T\parallel\parallel} &= \frac{1}{32}\sigma^{ij}.
\end{aligned} \tag{5.77}$$

Finally, the different components of the vertex defined in Eq. (5.74) have to be calculated. The external momentum is set to $(i\omega_e, \mathbf{0})$. The bare vertex, which is denoted by a small point in the diagrammatic equation, reads

$$\mathit{\Gamma}_{\text{bare}} = p^i \gamma^j \tag{5.78}$$

in its unsymmetrical form, as it was formulated in Sec. 3.2.3. The imaginary time expression second term of Eq. (5.74) reads

$$\mathit{\Gamma}^{ij}_{\eta\,\text{loop}\,M} = \sum_M (-T) \sum_{i\omega_l} \int \frac{\mathrm{d}^3 l}{(2\pi)^3} 2g K^{ij}_{\text{loop}\,M}\big((i\omega_l + \mu, \mathbf{l}), (i\omega_l + i\omega_e + \mu, \mathbf{l})\big) \mathit{\Gamma}_M \tag{5.79}$$

with the kernel

$$K^{ij}_{\text{loop}\,M}(k_1, k_2) = \mathrm{Tr}\left[\mathit{\Gamma}^{ij}_{\eta}(k_1, k_2) S(k_2) \mathit{\Gamma}_M S(k_1)\right]. \tag{5.80}$$

Since there is no external momentum, the spatial arguments of $K^{ij}_{\text{loop}\,M}$ can be suppressed because they are always equal to $\mathbf{l}$. In Appendix H.1 is is shown how to perform the analytic continuation to the real momentum q_0. This results in a splitting of the vacuum and the medium part,

$$\begin{aligned}
\mathit{\Gamma}^{ij}_{\eta\,\text{loop}\,M} = \sum_M 2g\mathit{\Gamma}_M \int \frac{\mathrm{d}^3 l}{(2\pi)^3} \int_0^\infty \frac{dl_0}{2\pi i} \Bigg\{ & \Big[1 - n_F(l_0 + \mu)\Big] \Big[K^{ij}_{\text{loop}\,M}(-l_0 + i\epsilon, -l_0 + q_0 + i\epsilon) \\
& - K^{ij}_{\text{loop}\,M}(-l_0 - i\epsilon, -l_0 + q_0 + i\epsilon) + K^{ij}_{\text{loop}\,M}(-l_0 - q_0 - i\epsilon, -l_0 + i\epsilon) \\
& - K^{ij}_{\text{loop}\,M}(-l_0 - q_0 - i\epsilon, -l_0 - i\epsilon)\Big] \\
& + n_F(l_0 - \mu)\Big[K^{ij}_{\text{loop}\,M}(l_0 + i\epsilon, l_0 + q_0 + i\epsilon) \\
& - K^{ij}_{\text{loop}\,M}(l_0 - i\epsilon, l_0 + q_0 + i\epsilon) + K^{ij}_{\text{loop}\,M}(l_0 - q_0 - i\epsilon, l_0 + i\epsilon) \\
& - K^{ij}_{\text{loop}\,M}(l_0 - q_0 - i\epsilon, l_0 - i\epsilon)\Big]\Bigg\}.
\end{aligned} \tag{5.81}$$

This first loop diagram is rather simple, and has a trivial Dirac structure. The next diagram containing one meson,

$$\mathit{\Gamma}^{ij}_{\eta\,1\text{ meson}\,M} = \sum_M (-T) \sum_{i\omega_l} \int \frac{\mathrm{d}^3 l}{(2\pi)^3} K^{ij}_{\text{loop}\,M}\big((i\omega_l + i\omega_{p_2} + \mu, \mathbf{p} + \mathbf{l}), (i\omega_l, \mathbf{l}), (i\omega_l + i\omega_{p_1} + \mu, \mathbf{p} + \mathbf{l})\big) \tag{5.82}$$

in imaginary time, has the Kernel

$$K^{ij}_{1\text{ meson}\,M}(k_1, k_2, k_3) = \mathit{\Gamma}^{ij}_{\eta}(k_1, k_3) S(k_1) \mathit{\Gamma}_M D_M(k_2) \mathit{\Gamma}_M S(k_3). \tag{5.83}$$

The continuation to real energies is performed in Appendix H.2. On obtains the retarded expression

$$
\begin{aligned}
\mathit{\Gamma}^{ij}_{\eta\,1\ \mathrm{meson}\,M} = -\sum_M \int \frac{\mathrm{d}^3 l}{(2\pi)^3} \int_0^\infty \frac{\mathrm{d}l_0}{2\pi i} \Bigg\{ & [1-n_B(l_0)] \times \\
& \times \Big[K^{ij}_{1\ \mathrm{meson}\,M}(-l_0+\mu+i\epsilon, -l_0+i\epsilon, -l_0+q_0+\mu+i\epsilon) \\
& - K^{ij}_{1\ \mathrm{meson}\,M}(-l_0+\mu+i\epsilon, -l_0-i\epsilon, -l_0+q_0+\mu+i\epsilon) \\
& - n_B(l_0) \Big[K^{ij}_{1\ \mathrm{meson}\,M}(l_0+\mu+i\epsilon, l_0+i\epsilon, l_0+q_0+\mu+i\epsilon) \\
& - K^{ij}_{1\ \mathrm{meson}\,M}(l_0+\mu+i\epsilon, l_0-i\epsilon, l_0+q_0+\mu+i\epsilon) \Big] \\
& - [1-n_F(l_0)] \Big[K^{ij}_{1\ \mathrm{meson}\,M}(-l_0-q_0+\mu+i\epsilon, -l_0-q_0-i\epsilon, -l_0+\mu+i\epsilon) \\
& - K^{ij}_{1\ \mathrm{meson}\,M}(-l_0-q_0+\mu+i\epsilon, -l_0-q_0-i\epsilon, -l_0+\mu-i\epsilon) \\
& + K^{ij}_{1\ \mathrm{meson}\,M}(-l_0+\mu+i\epsilon, -l_0-i\epsilon, -l_0+q_0+\mu-i\epsilon) \\
& - K^{ij}_{1\ \mathrm{meson}\,M}(-l_0+\mu-i\epsilon, -l_0-i\epsilon, -l_0+q_0+\mu-i\epsilon) \Big] \\
& - n_F(l_0) \Big[K^{ij}_{1\ \mathrm{meson}\,M}(l_0-q_0+\mu+i\epsilon, l_0-q_0-i\epsilon, l_0+\mu+i\epsilon) \\
& - K^{ij}_{1\ \mathrm{meson}\,M}(l_0-q_0+\mu+i\epsilon, l_0-q_0-i\epsilon, l_0+\mu-i\epsilon) \\
& + K^{ij}_{1\ \mathrm{meson}\,M}(l_0+\mu+i\epsilon, l_0-i\epsilon, l_0+q_0+\mu-i\epsilon) \\
& - K^{ij}_{1\ \mathrm{meson}\,M}(l_0+\mu-i\epsilon, l_0-i\epsilon, l_0+q_0+\mu-i\epsilon) \Big] \Bigg\}
\end{aligned}
\tag{5.84}
$$

for external momentum $q_0+i\epsilon$. The last diagram $\mathit{\Gamma}^{ij}_{\eta\,2\ \mathrm{mesons}\,M_1 M_2}$ of the vertex equation, involving two meson propagators, can be written as Matsubara sums

$$
\begin{aligned}
\mathit{\Gamma}^{ij}_{\eta\,2\ \mathrm{mesons}\,M_1 M_2} = \sum_{M_1,\,M_2} (-T) \sum_{i\omega_l} \int \frac{\mathrm{d}^3 l}{(2\pi)^3} (-T) \sum_{i\omega_k} \int \frac{\mathrm{d}^3 k}{(2\pi)^3} \times & \\
\times \Big\{ \mathit{\Lambda}^{ij}_{2\ \mathrm{mesons}\,M_1 M_2}(i\omega_l + i\omega_{p_1} + \mu, i\omega_l - i\omega_k + \mu, i - \omega_l + i\omega_{p_2} + \mu) \times & \\
\times K_{2\ \mathrm{mesons}\,M_1 M_2}(i\omega_k + i\omega_{p_1}, i\omega_k + \mu, i\omega_k + i\omega_{p_2}) \Big\} &
\end{aligned}
\tag{5.85}
$$

with the two functions in the integrand

$$
\mathit{\Lambda}^{ij}_{2\ \mathrm{mesons}\,M_1 M_2}(k_1,k_2,k_3) = \mathrm{Tr}\left[\mathit{\Gamma}^{ij}_{\eta}(k_1,k_3), S(k_1)\mathit{\Gamma}_{M_2} S(k_2) \mathit{\Gamma}_{M_1} S(k_3)\right] \tag{5.86}
$$

and

$$
K_{2\ \mathrm{mesons}\,M_1 M_2}(k_1,k_2,k_3) = D_{M_1}(k_1)\mathit{\Gamma}_{M_1} S(k_2) \mathit{\Gamma}_{M_2} D_{M_2}(k_3) \tag{5.87}
$$

One can estimate (see Appendix H.3 for details) that the continuation to real frequencies would lead to a sum of 80 terms.

We cease continuing the demonstration of the realization of the present approximation and turn to the practical calculation. The statement for the NJL-Dyson equation in next-to-leading order in $1/N_c$, Eq. (2.127), is also true for the self-consistent vertex iteration: The Minkowski formulation of the iteration prescription is not numerically stable and is extremely difficult to compute. The vertex $\mathit{\Gamma}^{ij}_{\eta}$ is even more complex than the quark propagator, it depends on four variables (instead of two), has eight Dirac components (instead of three) and is anisotropic, so more integrals remain to the numerical evaluation. Additionally, the required diagrams for the dressed vertex involve more loops than the self-energy in next-to-leading order in $1/N_c$.

The spectral function was only obtained by using the new method of self-energy parametrization. It was based on the existence of a thermodynamic potential $\mathit{\Omega}$, such that the propagator S could be found in a minimization procedure. Such a potential does not exist for the vertex, so an other method should be developed. Indeed, a similar problem in $O(N)$ model was solved approximately in [142], based on a variational formulation of the self-consistent vertex equation. However, in scalar theories no spontaneous symmetry breaking and no complication due to the Dirac decomposition of all parts have to be taken into account.

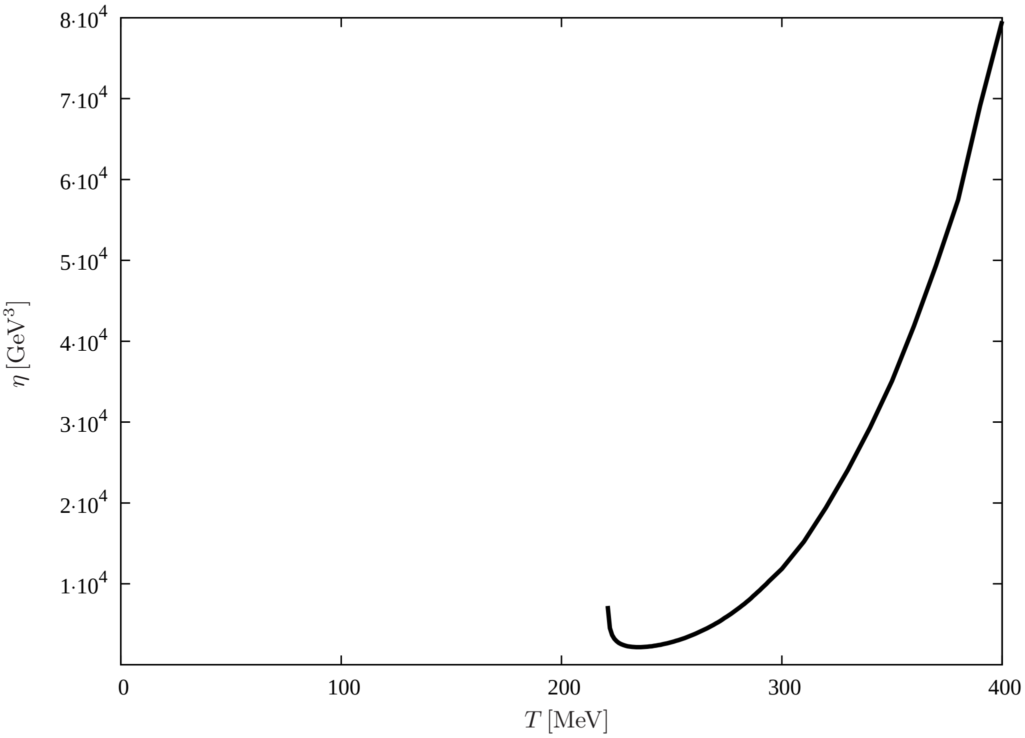

Figure 5.32: Shear viscosity.

5.6.3 Shear viscosity

For the computation of shear viscosity within the framework presented in this section, one needs the dressed quark propagator and the dressed vertex in next-to-leading order in $1/N_c$. For the quark propagator and the spectral function, we can use the results obtained with the self-energy parametrization method SEP1 in Sec. 4.5. We saw in the previous subsection that the numerical calculation of the fully dressed vertex causes problems. As in previous works of shear viscosity in the NJL model [112, 191, 114, 113], we restrict the calculation to the bare vertex. This approximation corresponds to the of Eq. (5.74) after the second term, because the higher order loops in an iteration of the bare vertex are vanishing. Thus, all diagrams involving meson propagators are neglected. These iterated diagrams are very important at low temperatures since they are expected to introduce meson-meson scattering effects into the calculation of shear viscosity (see e.g. Fig. 5.31). However, the SEP1-result was only successful at high temperatures, where one can estimate that the vertex corrections that are not present in our truncation play a minor role.

The calculated shear viscosity η is shown in Fig. 5.32 as a function of temperature. The same parameter set as in Sec. 4.5 is used, it can be found in Tab. 2.1 No 2. We begin with the discussion at high temperatures where η rapidly grows when the temperature T is increased. It is helpful to compare this behavior to the temperature-dependency of the quark spectra shown in Fig. 4.10. At high temperatures, the quark spectra resemble more and more the spectrum of Hartree constituent quarks, the width of the mass peak gets smaller the larger temperature T becomes. The small width of ρ_1 is a signature of few interactions in the chirally restored quark gas, leading to a large shear viscosity η. For smaller temperatures, the mesonic contributions to the self-energy that are essential since meson resonances are more important close to the hadronic phase. This leads to a smaller shear viscosity if one approaches the crossover region. When the peak in spectral function ceases its movement to higher energies and turns back to lower values (see the spectral functions plotted in Figs. 4.10(e) and 4.10(f) where this behavior can be observed), the main contributions in the Kubo formula are shifted to lower energies. Therefore, η has a minimum close to the crossover and rises strongly when the mass peak of the spectrum moves to small values of energy, before the SEP1-method fails.

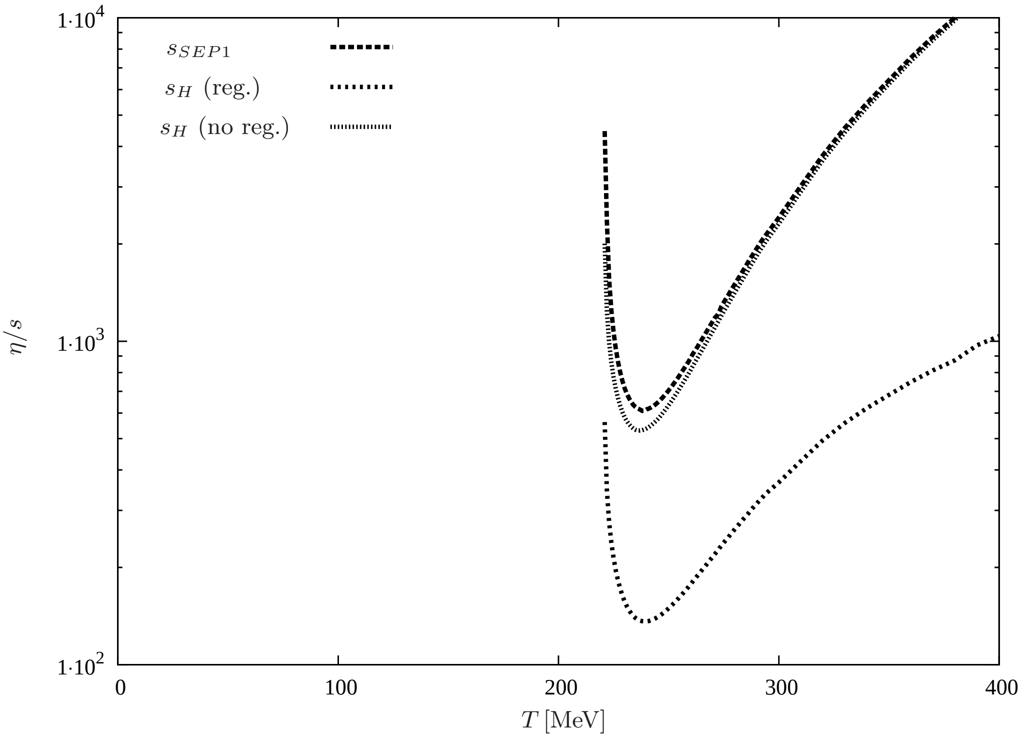

Figure 5.33: Shear viscosity over entropy density.

Not only shear viscosity, but also shear viscosity over entropy density is an interesting quantity to study. The entropy density from the SEP1-calculation was already discussed earlier (see Sec. 4.5.4), but it is worth the effort to analyze the calculation of s and η a bit more in detail. In both calculations, the meson-back coupled self-energy of quarks was included in a simple parametrization, thus there is a systematic error present in both calculations, which is thought to be less important in the high temperature regime. Beside this systematic limitation of both quantities, s is strongly affected by regularization artifacts as is was shown in Fig. 4.11. The Green-Kubo expression of η to the same order in $(1/N_c)$ was truncated because the meson-scattering effects in the calculation caused a severe complication of the computation of the fully dressed vertex. In summary, one can say that the regulator artifacts of Ω_1 lead to an entropy density that is too small, and the cancellation of coupling terms due to the truncation of the vertex equation leads to a shear viscosity that is too large, hence η/s will be much larger than in an exact calculation.

The ratio η/s is plotted as a function of temperature in Fig. 5.33. Beside the problematic ratio η_1/s_1, also the ratio of shear viscosity and mean-field entropy density is shown: As is was discussed in Fig. 4.11, the difference in entropy density between Hartree- and self-consistent $1/N_c$-result is smaller than the difference in s between the version regularized medium part and the version without medium regularization. Both versions of s_H are used in the figure, leading to quite different results. Besides the fact that the absolute value of η/s is quite high due to the absence of meson scattering effects, one sees that the ratio rises for high temperatures and exhibits a minimum at the transition to the chirally broken phase.

The high-temperature behavior of the shear viscosity seems to have a reasonable behavior because it approaches a free quark gas asymptotically. This feature implemented with help of the exchange of an RPA meson in the quark self-energy arises naturally in the $1/N_c$-expansion to next-to-leading order in the NJL model, but has a different origin than asymptotic freedom in full QCD. Hence it is impossible to find the asymptotic behavior of perturbative QCD at high temperatures. Additionally, the contributions of gluons are not present in the NJL calculation, especially important at high temperatures.

Investigations of fermions in lattice QCD indicate that quarks in the high-temperature phase do not show many signals of strong coupling: Quark fluctuations reach rapidly the Stefan-Boltzmann limit of a non-interacting Fermi gas [216]. This seems not to be the case for the gauge part: One finds that gluons behave differently in this region of the phase diagram [217]. From the result for the shear viscosity obtained with the NJL model, one can say that our model calculation confirms the observation of quark fluctuations that fall rapidly to the free Stefan-Boltzmann limit.

Chapter 6

Summary and conclusions

In this thesis, we studied the non-equilibrium properties of strongly interacting matter, inspired by recent results and conjectures in the context of heavy-ion collisions. We focused on the transport properties close to equilibrium, and on the microscopic calculation of the linear transport coefficients, especially of the shear viscosity. The microscopic calculation of viscous properties allowed the comparison with new ideas of universality of almost ideal fluids and propositions concerning fluidity.

The analysis was mainly based on the Nambu-Jona-Lasinio model, which had the advantage that it can describe a hadronic phase, a quark phase, and different transition scenarios between these two. The ability to work in the transition region was the main advantage of the model, since it described pions as bound quark states in the one regime, and chirally restored quarks with mesonic resonances in the other regime. Thus we could find consequences of hadronization when approaching the crossover zone from high temperatures, and consequences from meson dissociation when we approached from low temperatures. These were effects that are not included in simpler models where quarks and mesons are equally treated as elementary particles.

Although the usage of the NJL model as an effective description of strongly interacting particles simplified the calculation of various thermal properties significantly, the remaining task of finding nontrivial spectral functions in a self-consistent scheme is still hard. Therefore, we developed the self-energy parametrization method (SEP), which allowed the calculation of spectral functions by only dealing with integrals in Euclidean space-time. This was demonstrated by introducing several self-energy expansions and the application to the NJL model in next-to-leading order in $1/N_c$.

The numerical results of the different approaches gave insights to transport processes and theoretical concepts of strongly interacting matter as well as to the NJL model. We first demonstrated that the application of relativistic kinetic theory to the quark phase of the NJL model in lowest-order perturbation theory and in mean-field is not possible. The reason was mainly that the decreasing interaction at higher energies was compensated by a particle density that increased much faster with temperature, thus the dilute-gas limit is never reached.

Therefore, the low-temperature phase, where the correct description was given by an arbitrarily rarefied pion gas when the temperature and chemical potential are sufficiently small, seemed to be promising for the application of kinetic theory. We summarized the results obtained with chiral perturbation theory to leading-order and with the Weinberg interaction. We investigated the effects of the Sonine-expansion truncation of the distribution function corrections of the Chapman-Enskog expansion in these pion descriptions. We then used the NJL model for the description of pions and their interactions, based on earlier works concerning the $\pi\pi$-scattering length. This allowed not only the reproduction of the Weinberg interaction in vacuum, but also the inclusion of effects that come from the restoration of chiral symmetry which strongly affected the properties of the mesons. This is in contrast to many other approaches, which treat pions and their interaction in vacuum and generate a temperature-dependent shear viscosity by solely changing the average momentum and the different thermal occupation of states. We observed a strong change of the viscosity curve due to the dissociation of the σ-meson into two pions, and due to the Mott transition. We observed a minimal ratio of η/s in the vicinity of the transitions, although the kinetic approach is not valid at these points. We conclude that we could observe a mechanism that changes the behavior of a pion gas from its properties in vacuum to the crossover-region enormously because the pion was really described as a composite particle.

Our first application of the Green-Kubo method to the NJL-model was done in a very classical, systematic expansion scheme of the model. The interpretation of the result was clarified, and we pointed out that this scheme is equivalent to a meson gas, where the mesons are have nontrivial spectra due to their interaction with quarks. The identified mechanisms that were included in this systematic loop expansion in static limit are not thought to be the dominant contributions to transport properties. However, these methods can reveal properties of different regions of the phase diagram. The Mott transition region was resolved in more details than in the past, although the important on-shell meson-meson scattering contribution is excluded in the work. Finally, the shear viscosity coefficients as been calculated at the critical end point, and a minimum in the vicinity was observed as well as one could show the divergence at this point in an analytical way. The comparison of shear viscosity and entropy density turned out to be not directly possible, since the additional approximation of the static limit affects the systematics.

The last calculation used the SEP-results for the quark spectral function in order to calculate the shear viscosity with the Green-Kubo method. These pion-back coupled quark spectral functions were used in the expansion up to next-to-leading order in $1/N_c$ of the Green-Kubo correlation function. The lack of a method similar to the new SEP-approach which can be used in the calculation of the $1/N_c$-dressed vertex led to an additional truncation. Luckily, the restriction to the special type of self-energy parametrization and the additional vertex truncation were both reasonable in the high-temperature limit, thus the calculation in the restored phase was in that sense consistent. The resulting η/s showed a minimum in the vicinity of the crossover region and an increasing value for higher temperatures like one would expect it from asymptotic freedom. However, absolute value of η/s was questionable since some additional mechanisms become important in these two limits. Like in the previous application of the Green-Kubo formula, the approximation schemes of η and s were different, thus the ratio of the two quantities is not follow a systematic expansion.

This is a good point to rediscuss the application of the Green-Kubo formalism and the relativistic kinetic theory in certain situations. We can draw some general conclusions concerning the two methods and their usage in the context of strongly interacting matter, based on the summarized observation of this study. The conclusions in the following paragraphs allow the investigation of this task from a more general perspective.

Kinetic theory is a good description in dilute systems, for example in a pion gas close to the vacuum (see Secs. 5.3 and 5.4). However, it cannot be applied in a dense and strongly coupled system, which are the interesting objects for the question of ideal fluids and universal lower bounds for the ratio of shear viscosity over entropy density. This qualitative statement that purely relies on the dependency of transport coefficients on the coupling strength (see Sec. 3.4.3) and the range of applicability of kinetic theory (see Sec. 3.3.4). The results discussed in chapter 5 allow a more quantitative statement: All curves for λ/d which indicated the validity of the kinetic approach resemble the curves of η/s for a given system. One can verify this observation from the comparison of Fig. 5.2(b) with 5.4, Fig. 5.7(b) with 5.8(b), Fig. 5.9(b) with 5.12(a) and 5.15(a), and Fig. 5.18(b) with 5.20. The similarity of η/s and λ/d affirms the impossibility of studying the region of nearly ideal fluids within kinetic theory, since the former is found in the region of $\eta/s < 1$, while the latter is valid for $\lambda/d \gg 1$. Indeed, the minimal value of η/n that was formulated from considerations of the Heisenberg uncertainty principle (see Sec. 3.6.1) was identified as an estimate for the breakdown of the picture of the kinetic theory of particles. As one can relate the minimal viscosity from the Heisenberg uncertainty relation estimate to the ratio of shear viscosity over entropy density, this observation is well in agreement with the different concepts of fluidity that were discussed in Sec. 3.6.

Although the kinetic description of NJL quarks that was discussed in Secs. 5.1 and 5.2 was not satisfying, one can learn something from these results. Assume that the ratio of shear viscosity over entropy density is small in the chiral crossover region, and the quarks and gluons are strongly coupled. All qualitative arguments as well as all results in this work indicate that the description of this matter cannot be done with kinetic theory since the matter is very dense and strongly interacting. When the temperature is increased, the coupling is expected to decrease because of asymptotic freedom, however, the density is strongly increasing with temperature due to thermally

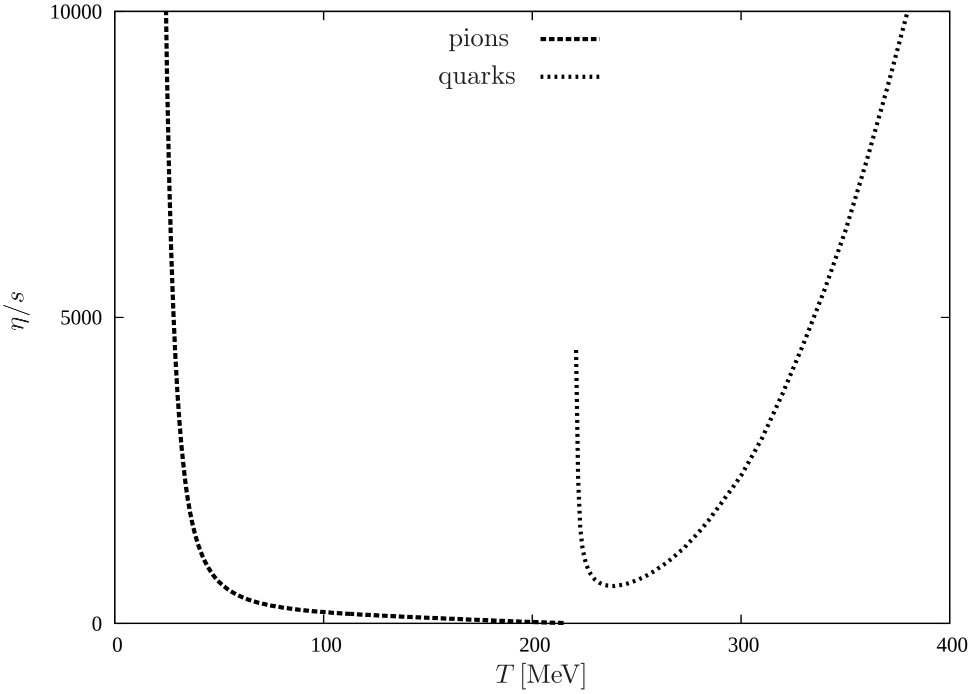

Figure 6.1: Shear viscosity over entropy density at high temperature and at low temperature. The low temperature region was obtained from the kinetic approach for the NJL pion gas discussed in Sec. 5.4, whereas the high temperature region is the result for the quark phase that was calculated from the Green-Kubo. This is a synopsis of Figs. 5.33 and 5.20, which both were calculated from the parameter set No 2 from Tab. 2.1.

produced particles. In order to enter the kinetic regime, the mean-free path, which is affected by the density as well as by the coupling, has to become larger than the typical interaction range, which is related to the coupling. Thus, the coupling has to decrease stronger that the density is increasing, starting from the strongly coupled cross over region, in order to achieve a situation where relativistic kinetic theory may be applied. Although the estimates from perturbative QCD indicate justifiable conditions for the application of the kinetic concept for asymptotically high temperatures, we can conclude that the point from which on a kinetic treatment make sense has to be chosen with care.

The time-correlation function method does not have the limitation of relativistic kinetic theory, and can be applied in a dilute gas as well as a strongly coupled medium. The experiences that were made in past when applying the method to a concrete model could be verified in our calculation: The technical efforts that are needed are considerably higher, compared to kinetic theory. The approximation schemes that could be realized in this work lead to results of the Green-Kubo formula which showed additional troubles. Although very systematic expansion and truncation schemes were used that were known to work in several situations, the interpretation of the obtained viscosity coefficient and its relation to the microscopic physics was a difficult issue. Even after identifying the physical processes and interactions that are included in the Green-Kubo correlator, the consequences of the systematic truncation schemes remained confusing. Furthermore, the calculation of η/s, which could in principle be done in the limit of strong coupling, yields another ambiguity that is related to the problem of relating the input of the Green-Kubo correlator to the qualitative understanding of the physics. The truncation schemes that were necessary to calculate η numerically were different from that which were used to calculate s, hence the resulting value of η/s is not reliable. This is a completely new situation, compared to the application of relativistic kinetic theory, where thermodynamic quantities like entropy density are taken in the free gas limit systematically.

After this critical discussion of the different theoretical transport concepts, we want to underline three important results that were obtained by the presented study. First, we calculated the low-temperature region and the high-temperature region within the same model. This ability is the convincing advantage of the NJL model. The results are not obtained within the same approximations, but at least with the same set of parameters. The two results are summarized in Fig. 6.1. Second, we studied many different systems and calculated the ratio of shear viscosity over entropy density in each of them. We always found that there is an extremal value of η/s in the vicinity of a (phase) transition: The fluidity measure was minimal in the chiral crossover region and in the vicinity of the meson transition temperatures, and diverged at the critical end point due to the contribution of the σ-meson. Third, the self-energy parametrization method allowed the calculation of real-frequency Green's function by only evaluating integrals in Euclidean space-time. The application to other models and to contexts different than transport phenomena seems to be promising, though it was developed for shear viscosity in the NJL model. Additionally, there are more possible parametrizations of imaginary parts of retarded self-energies than the ones that have been investigated in this study, and there may be versions that are even more suitable or successful than the first examples presented in this work.

The last lines are dedicated to a further outlook. Beside an improvement of the SEP methods and its application to other problems, the results of this thesis can be seen as a starting point for further investigations of transport properties. The calculation of the fully dressed vertex in next-to-leading order in $1/N_c$ that is necessary for the Green-Kubo correlator would require a simplificating technique similar to the SEP method. Although the variational approach used in scalar theories might be a promising candidate for such a task, the adaption to fermions is surely still difficult. A clearly more direct and relatively simple extension of this thesis can be done in the kinetic approach. The investigation of a pion gas in the NJL model already revealed a number of interesting features. These calculations can be extended in order to give a even more precise description of transport coefficients in the hadronic phase. The inclusion of kaons modifies the behavior at higher temperatures. The improvement of the modeling of the $\pi\pi$ interaction a very promising point, because the momentum-dependency of the cross section from leading-order chiral perturbation theory has some disadvantages. Resummation techniques, but especially the inclusion of a ρ-meson exchange lead to a more realistic momentum-dependency — the latter can even link this results to calculations with phenomenological scattering amplitudes. Lastly, an interdisciplinary aspect of the calculation of transport coefficients in a NJL pion gas has to be mentioned. The pion interaction is characterized by a scattering length, that diverges at some point, and a minimum of η/s is found. A similar situation is found in cold fermion gases in the vicinity of the Feshbach resonance. Thus, our result relates strongly interacting matter at the chiral crossover region to the unitary limit of a gas of cold fermionic atoms. One might expect that it is possible to study the transport coefficients in cold atomic gases with methods similar to the ones that have been developed in this thesis. The kinetic approach is even more justifiable in this context, since it is well under control that a cold gas at low pressure is sufficiently rarefied.

Appendix A

Conventions

The notations and conventions that are used in this work are summarized here. We use a metric tensor of space-time that is defined as

$$g^{\mu\nu} = \begin{pmatrix} 1 & 0 & 0 & 0 \\ 0 & -1 & 0 & 0 \\ 0 & 0 & -1 & 0 \\ 0 & 0 & 0 & -1 \end{pmatrix}.$$

We chose natural units and set

$$\hbar = c = k_B = 1. \tag{A.1}$$

In the evaluations of Feynman diagrams, several different traces appear. The functional trace over the total phase space is noted $\mathcal{T}r$, the trace over quark operators in Dirac-, color-, and flavor-space will be called Tr. Sometimes, the trace over the spinor indices solely is needed, which will be abbreviated with $\mathrm{tr}_{\mathrm{Dirac}}$.

Appendix B

Calculation of elementary integrals

In this part, the calculation of certain quantities in the standard approximation of the NJL model is presented. Most of them can be expressed in terms of so called elementary integrals.

B.1 Techniques in the complex plane

It is useful to summarize some basic properties of the Fermi and Bose distribution functions

$$n_F(z) = \frac{1}{e^{\beta z}+1} \qquad\qquad n_B(z) = \frac{1}{e^{\beta z}-1} \tag{B.1}$$

for complex arguments $z \in \mathbb{C}$. In the following, z denotes a complex number and

$$i\omega_F = (2n+1)i\pi T \qquad\qquad n \in \mathbb{Z} \tag{B.2}$$

$$i\omega_B = 2ni\pi T \qquad\qquad n \in \mathbb{Z} \tag{B.3}$$

are arbitrary fermionic and bosonic Matsubara frequencies, for the temperature $T = 1/\beta$.

B.1.1 Properties of distribution functions

The distribution functions have the following properties for inversion of their arguments,

$$n_F(-z) = 1 - n_F(z) \qquad\qquad n_B(-z) = -1 - n_B(z). \tag{B.4}$$

An important issue is to note the behavior under shifts by Matsubara frequencies,

$$n_F(z+i\omega_B) = n_F(z) \qquad\qquad n_B(z+i\omega_B) = n_B(z) \tag{B.5}$$

$$n_F(z+i\omega_F) = -n_B(z) \qquad\qquad n_B(z+i\omega_F) = -n_F(z). \tag{B.6}$$

Sometimes, the integrals over the plain distribution functions are needed. The solutions of the integrals are known analytically,

$$\int \mathrm{d}x\, n_F(x) = -T\ln\left(1+e^{-x/T}\right) \tag{B.7}$$

$$\int \mathrm{d}x\, n_B(x) = +T\ln\left(1-e^{-x/T}\right). \tag{B.8}$$

The Fermi distribution function and the Bose distribution function have a set of poles at $i\omega_F$ and $i\omega_B$, respectively, and are analytic elsewhere.

B.1.2 Contour integral trick

A useful trick for the calculations in the appendix is the formulation of Matsubara sums as a contour integrals. We consider the Matsubara sums

$$-T\sum_{i\omega_k\in FMF} f_F(i\omega_k+\mu) \qquad \text{and} \qquad -T\sum_{i\omega_q\in BMF} f_B(i\omega_q) \tag{B.9}$$

over Fermionic Matsubara frequencies (FMF), or Bosonic Matsubara frequencies (BMF), respectively. Each term belonging to $i\omega_k$ or $i\omega_q$ in the sums can be written as an integration over a closed path $\mathcal{C}_0$ in the complex plane if the functions f_F or f_B are analytic in $i\omega_k$ or $i\omega_q$.

$$f_F(i\omega_k+\mu)=\int_{\mathcal{C}_0}\frac{\mathrm{d}z}{2\pi i}\frac{f_F(z+\mu)}{z-i\omega_k}, \qquad f_B(i\omega_q)=\int_{\mathcal{C}_0}\frac{\mathrm{d}z}{2\pi i}\frac{f_B(z)}{z-i\omega_q} \tag{B.10}$$

The integration contour $\mathcal{C}_0$ is a small circle around the Matsubara frequency $i\omega_k$ or $i\omega_q$. For the full sum over all frequencies a function with the required residuals at all Matsubara frequencies is needed. The Bose distribution function has poles at all Bose Matsubara frequencies, while the Fermi distribution function has poles at all Fermi Matsubara frequencies. The residua are

$$\mathrm{Res}_{z\in FMF}\, n_F(z)=-T, \qquad \mathrm{Res}_{z\in BMF}\, n_B(z)=+T. \tag{B.11}$$

Hence under the the assumptions of analyticity at the Matsubara frequencies the Matsubara sum can be generally expressed as a contour integral

$$-T\sum_{i\omega_k\in FMF} f_F(i\omega_k+\mu)=\int_{\mathcal{C}_F}\frac{\mathrm{d}z}{2\pi i}n_F(z)f_F(z+\mu) \tag{B.12}$$

$$-T\sum_{i\omega_q\in BMF} f_B(i\omega_q)=-\int_{\mathcal{C}_B}\frac{\mathrm{d}z}{2\pi i}n_B(z)f_B(z). \tag{B.13}$$

The contours $\mathcal{C}_B$ and $\mathcal{C}_B$ are now a combination of all circles around Matsubara frequencies on the imaginary axis in the complex z-plane.
This contour integration trick is a convincing technique because the contour can be deformed in regions where the function $n_F(z)f_F(z)$ or $n_B(z)f_B(z)$ are holomorphic. This simplifies the calculation of elementary integrals.

B.2 Elementary integral iI_1

The elementary integral iI_1 arising in Hartree self-energy and polarization loop is defined as

$$iI_1=-T\sum_{i\omega_k}\int\frac{\mathrm{d}^3k}{(2\pi)^3}\frac{1}{(i\omega_k+\mu)^2-E_k^2} \tag{B.14}$$

with the energy $E_k=(m_H^2+\mathbf{k}^2)^{1/2}$ depending on Hartree quark mass m_H. The Matsubara sum is rewritten as contour integral

$$iI_1=\int\frac{\mathrm{d}^3k}{(2\pi)^3}\oint_{\mathcal{C}} n_F(z)\frac{\mathrm{d}z}{2\pi i}\frac{1}{(z+\mu)^2-E_k^2}. \tag{B.15}$$

The integration contour $\mathcal{C}$ is shown in Fig. B.1(a). The integrand has two poles in the complex plane at $z_{1,2}=\pm E_k-\mu$. After the deformations sketched in Fig. B.1(b) and B.1(c), on arrives at the sum over two residua.

$$iI_1=-\int\frac{\mathrm{d}^3k}{(2\pi)^3}\sum_{z_1,z_2}\mathrm{Res}\frac{1}{2E_k}\left(\frac{1}{z+\mu-E_k}-\frac{1}{z+\mu+E_k}\right)n_F(z) \tag{B.16}$$

The residua are easily calculated, and one obtains

$$iI_1=-\int\frac{\mathrm{d}^3k}{(2\pi)^3}\frac{1}{2E_k}\left(n_F(E_k-\mu)-n_F(-E_k-\mu)\right). \tag{B.17}$$

With help of the symmetry relation (B.4), one can separate the temperature independent part,

$$iI_1=\int\frac{\mathrm{d}^3k}{(2\pi)^3}\frac{1}{2E_k}\left(1-n_F(E_k-\mu)-n_F(E_k+\mu)\right). \tag{B.18}$$

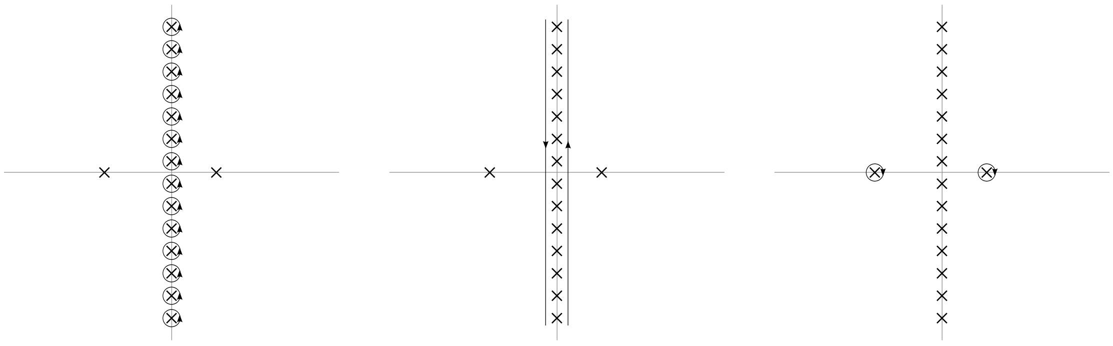
(a) (b) (c)

Figure B.1: Integration contours for the elementary integral iI_1. The different integration paths in the figure are the initial path $\mathcal{C}$ from Eq. (B.15) in (a), the path in (b) is obtained by merging all circles around the poles of n_F, and (c) is the final form leading to Eq. (B.16).

This is the final form for the integral iI_1. The integrand depends only on the absolute value of the momentum $\mathbf{k}$, so it can be written as

$$iI_1 = \frac{4\pi}{(2\pi)^3} \int_0^\infty \mathrm{d}|\mathbf{k}| \frac{1}{2E_k} \left(1 - n_F(E_k - \mu) - n_F(E_k + \mu)\right) \tag{B.19}$$

The integral is UV-divergent[1] and hence a regularization is needed in order to obtain a finite result. The integrand has no singularity and the result is purely real. It is obvious that iI_1 is symmetric under the change of sign of μ. An interesting case is the limit $T \to 0$ with a finite chemical potential.

$$\lim_{T\to 0,\, \mu\neq 0} iI_1 = \begin{cases} \frac{4\pi}{(2\pi)^3} \int_0^\infty \mathrm{d}|\mathbf{k}| \frac{1}{2E_k} & \text{for } |\mu| < m_H \\ \frac{4\pi}{(2\pi)^3} \int_{\sqrt{\mu^2 - m_H^2}}^\infty \mathrm{d}|\mathbf{k}| \frac{1}{2E_k} & \text{for } |\mu| > m_H \end{cases}$$

One sees that iI_1 stays at its vacuum value till the chemical potential μ gets larger than the energy gap - which is the Hartree quark mass m_H.

B.3 Polarization loop

The polarization loop $\mathit{\Pi}_M$ is defined as

$$\begin{aligned} \mathit{\Pi}_M(i\omega_q, \mathbf{q}) = -T \sum_{i\omega_k} \int \frac{\mathrm{d}^3 k}{(2\pi)^3} \frac{1}{\left[(i\omega_q + i\omega_k + \mu)^2 - (\mathbf{q} + \mathbf{k})^2 - m_H^2\right]\left[(i\omega_k + \mu)^2 - \mathbf{k}^2 - m_H^2\right]} \times \\ \times \mathrm{Tr}\left[\big((i\omega_q + i\omega_k + \mu)\gamma^0 - \boldsymbol{\gamma}(\mathbf{q} + \mathbf{k}) + m_H\big)\mathit{\Gamma}_M\big((i\omega_k + \mu)\gamma^0 - \boldsymbol{\gamma}\mathbf{k} + m_H\big)\mathit{\Gamma}_M\right]. \end{aligned} \tag{B.20}$$

This expression can be written as a linear combination of the elementary integrals iI_1 and iI. We concentrate on the integrand and switch to the 4-momentum notation for simplicity. The integrand is

$$\frac{\mathrm{Tr}\left[\big((\not{q} + \not{k}) + m_H\big)\big(\not{k} \pm m_H\big)\right]}{\left[(q + k)^2 - m_H^2\right]\left[k^2 - m_H^2\right]}, \tag{B.21}$$

where the upper sign correspond to the scalar channel, $\mathit{\Pi}_\sigma$, and the lower one the the pseudoscalar polarization functions $\mathit{\Pi}_\pi^a$. After the calculation of the trace, the integrand reads

$$4N_c N_f \frac{k^2 + k \cdot q \pm m_H^2}{\left[(q + k)^2 - m_H^2\right]\left[k^2 - m_H^2\right]}, \tag{B.22}$$

---

[1] The UV-divergence is not present for the terms containing a Fermi distribution function

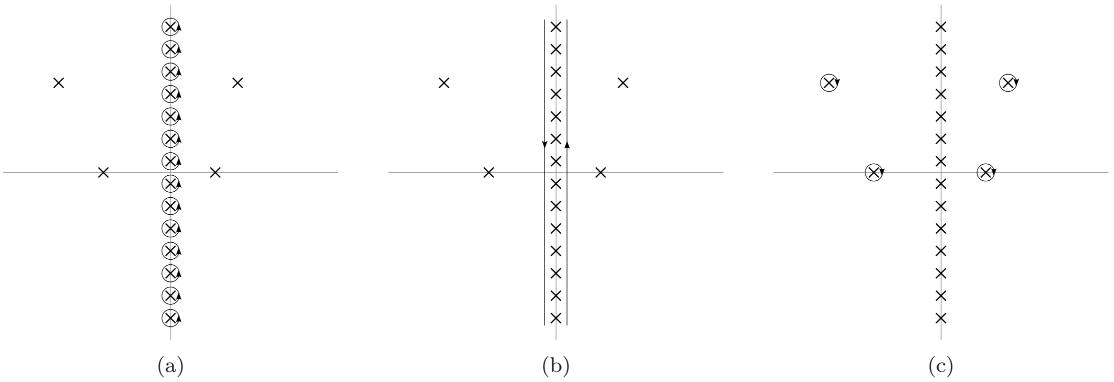

Figure B.2: Integration contours for the elementary integral iI. (a) shows the initial path C, which is deformed in (b) and (c) such that one arrives at Eq. (B.29).

which can be written as

$$2N_cN_f\left\{\frac{1}{k^2-m_H^2}+\frac{1}{(q+k)^2-m_H^2}+\frac{-q^2+2m_H^2\pm 2m_H^2}{\left[(q+k)^2-m_H^2\right]\left[k^2-m_H^2\right]}\right\}. \tag{B.23}$$

We shift the integration variable in the second term by $-q$ and extract the constant prefactors in the third term. This leads to the final results for the polarization loops

$$\Pi_{\pi^i} = 4N_cN_f iI_1 - 2N_cN_f(q^2)iI(q) \tag{B.24}$$

$$\Pi_\sigma = 4N_cN_f iI_1 - 2N_cN_f(q^2-4m_H^2)iI(q), \tag{B.25}$$

where the elementary integral iI_1 is calculated in Sec. B.2, and iI is discussed in the next section.

B.4 Elementary integral iI

In this section, the integral

$$iI(i\omega_q,\mathbf{q}) = -\int\frac{\mathrm{d}^3k}{(2\pi)^3}T\sum_{i\omega_k}\frac{1}{[(i\omega_k+\mu)-\mathbf{k}^2-m_H^2][(i\omega_k+i\omega_q+\mu)-(\mathbf{k}+\mathbf{q})^2-m_H^2]} \tag{B.26}$$

is evaluated.

B.4.1 Contour integration

With help of the energies E_k and E_{kq}, defined as $E_k^2=\mathbf{k}^2+m_H^2$ and $E_{kq}^2=(\mathbf{k}+\mathbf{q})^2+m_H^2$, the integral iI can be written in a more compact form,

$$iI(i\omega_q,\mathbf{q}) = -\int\frac{\mathrm{d}^3k}{(2\pi)^3}T\sum_{i\omega_k}\frac{1}{[(i\omega_k+\mu)-E_k^2][(i\omega_k+i\omega_q+\mu)-E_{kq}^2]}. \tag{B.27}$$

The Matsubara sum is expressed as the contour integral

$$iI(i\omega_q,\mathbf{q}) = \int\frac{\mathrm{d}^3k}{(2\pi)^3}\oint_C\frac{\mathrm{d}z}{2\pi i}n_F(z)\frac{1}{[(z+\mu)^2-E_k^2][(z+i\omega_q+\mu)^2-E_{kq}^2]}, \tag{B.28}$$

with the integration path C shown in Fig. B.2(a). We analyze the structure of the integrand in the complex plane. Beside the poles of the Fermi distribution function, there are four poles at $z_{1,2}=\pm E_k-\mu$ and $z_{3,4}=\pm E_{kq}-i\omega_q-\mu$. After the deformations of the integration contour shown in Fig. B.2(b) and B.2(c), the integral takes the form of a sum over the four residua,

$$iI(i\omega_q,\mathbf{q}) = -\int\frac{\mathrm{d}^3k}{(2\pi)^3}\sum_{z\in\{z_1,z_2,z_3,z_4\}}\mathrm{Res}\,n_F(z)\frac{1}{[(z+\mu)^2-E_k^2][(z+i\omega_q+\mu)^2-E_{kq}^2]}. \tag{B.29}$$

After the evaluation of the residua the result reads

$$\begin{aligned} iI(i\omega_q,\mathbf{q}) &= -\int \frac{\mathrm{d}^3k}{(2\pi)^3}\frac{1}{4E_kE_{kq}}\times \\ &\left\{\frac{n_F(E_k-\mu)}{i\omega_q-d_E}-\frac{n_F(E_{kq}-\mu)}{i\omega_q+d_E}-\frac{n_F(E_k-\mu)}{i\omega_q+s_E}+\frac{n_F(-E_{kq}-\mu)}{i\omega_q+s_E}\right. \\ &\left.-\frac{n_F(E_k-\mu)}{i\omega_q-s_E}+\frac{n_F(E_{kq}-\mu)}{i\omega_q-s_E}+\frac{n_F(-E_k-\mu)}{i\omega_q+d_E}-\frac{n_F(-E_{kq}-\mu)}{i\omega_q+d_E}\right\}. \end{aligned} \tag{B.30}$$

The new symbols s_E and d_E correspond to the sum and the difference of the energies, respectively: $s_E = E_{kq}+E_k$ and $d_E = E_{kq}-E_k$. The periodicity of distribution functions in imaginary arguments from Eq. (B.5) and (B.6) has been used. The terms in the sum can be split in a suitable way, and the energy E_{kq} can be eliminated in the argument of n_F by a substitution $\mathbf{k}'=\mathbf{k}+\mathbf{q}$,

$$\begin{aligned} iI(i\omega_q,\mathbf{q}) &= -\int \frac{\mathrm{d}^3k}{(2\pi)^3}T\sum_{i\omega_k}\frac{1}{4E_kE_{kq}}\left\{\vphantom{\frac{1}{1}}\right. \\ & n_F(E_k-\mu)\left(\frac{1}{i\omega_q-d_E}-\frac{1}{i\omega_q+d_E}-\frac{1}{i\omega_q+s_E}+\frac{1}{i\omega_q-s_E}\right) \\ & \left.+n_F(-E_k-\mu)\left(\frac{1}{i\omega_q+s_E}-\frac{1}{i\omega_q-s_E}+\frac{1}{i\omega_q+d_E}-\frac{1}{i\omega_q-d_E}\right)\right\}. \end{aligned} \tag{B.31}$$

The temperature-independent part can be separated with the formula (B.4).

$$\begin{aligned} iI(i\omega_q,\mathbf{q}) = \int \frac{\mathrm{d}^3k}{(2\pi)^3}&\left\{\left(\frac{1}{E_k}-\frac{n_F(E_k-\mu)+n_F(E_k+\mu)}{2E_kE_{kq}}s_E\right)\frac{1}{(i\omega_q)^2-s_E^2}\right. \\ &\left.-\frac{n_F(E_k-\mu)+n_F(E_k+\mu)}{2E_kE_{kq}}d_E\frac{1}{(i\omega_q)^2-d_E^2}\right\}. \end{aligned} \tag{B.32}$$

This is the final result for imaginary external momentum $i\omega_q$. For the expression for real momentum q_0, we calculate for example the retarded[2] expression by analytical continuation $i\omega_q \rightarrow q_0+i\epsilon$.

$$\begin{aligned} iI(q_0+i\epsilon,\mathbf{q}) = \int \frac{\mathrm{d}^3k}{(2\pi)^3}&\left\{\left(\frac{1}{E_k}-\frac{n_F(E_k-\mu)+n_F(E_k+\mu)}{2E_kE_{kq}}s_E\right)\frac{1}{(q_0+i\epsilon)^2-s_E^2}\right. \\ &\left.-\frac{n_F(E_k-\mu)+n_F(E_k+\mu)}{2E_kE_{kq}}d_E\frac{1}{(q_0+i\epsilon)^2-d_E^2}\right\} \end{aligned} \tag{B.33}$$

The real part is given by the Cauchy principle value

$$\begin{aligned} \mathrm{Re}\,iI(q_0,\mathbf{q}) = \mathrm{Pr}\int \frac{\mathrm{d}^3k}{(2\pi)^3}&\left\{\left(\frac{1}{E_k}-\frac{n_F(E_k-\mu)+n_F(E_k+\mu)}{2E_kE_{kq}}s_E\right)\frac{1}{q_0^2-s_E^2}\right. \\ &\left.-\frac{n_F(E_k-\mu)+n_F(E_k+\mu)}{2E_kE_{kq}}d_E\frac{1}{q_0^2-d_E^2}\right\}. \end{aligned} \tag{B.34}$$

The imaginary part is calculated in the next paragraphs.

B.4.2 Imaginary part

In this section the imaginary part of $iI(q_0+i\epsilon,\mathbf{q})$ is derived from Eq. (B.33). The identity

$$\lim_{\epsilon\rightarrow 0}\mathrm{Im}\frac{1}{x+i\epsilon} = -\pi\delta(x) \tag{B.35}$$

---

[2] The advanced expression would be obtained by the prescription $i\omega_q \rightarrow q_0 - i\epsilon$. As it can always be obtained from the retarded iI by complex conjugation, we restrict this demonstration to the retarded case.

for the infinitesimal imaginary part leads to

$$
\begin{aligned}
\mathrm{Im}\, iI(q_0,\mathbf{q}) = -\int \frac{d^3k}{(2\pi)^3}\Bigg\{ & \frac{\pi}{2s_E}\left(\frac{1}{E_k} - \frac{n_F(E_k-\mu)+n_F(E_k+\mu)}{2E_{kq}E_k}s_E\right)\times \\
& \times\left(\delta(q_0-s_E)-\delta(q_0+s_E)\right) \\
& -\frac{\pi}{2d_E}\frac{n_F(E_k-\mu)+n_F(E_k+\mu)}{2E_{kq}E_k}d_E\times \\
& \times\left(\delta(q_0-d_E)-\delta(q_0+d_E)\right)\Bigg\}.
\end{aligned} \tag{B.36}
$$

We switch to spherical coordinates for the integration variable $\mathbf{k}$. We chose them such that $\mathbf{q}$ is parallel to k_z, yielding

$$
\mathbf{q}\cdot\mathbf{k} = |\mathbf{q}||\mathbf{k}|\cos\theta_k. \tag{B.37}
$$

First the θ_k-integration is performed, eliminating the δ-functions. From now on, one has to distinguish between spacelike q^2 and timelike q^2.
If $q^2 = q_0^2 - \mathbf{q}^2 > 0$:

$$
\begin{aligned}
\mathrm{Im}\, iI(q_0,\mathbf{q}) = & -\frac{1}{8\pi}\int_m^\infty \mathrm{d}E_k \frac{\sqrt{E_k^2-m_H^2}}{|\mathbf{k}|\cdot|\mathbf{q}|}\theta(q^2-4m^2)\times \\
& \times\Bigg\{\theta(q_0-E_k)(q_0-E_k)\left(\frac{1}{q_0}-\frac{n_F(E_k-\mu)+n_F(E_k+\mu)}{2(q_0-E_k)}\right)\chi_{[\frac{q_0}{2}\pm\sqrt{\triangle}]}(E_k) \\
& -\theta(-q_0-E_k)(-q_0-E_k)\left(\frac{1}{-q_0}-\frac{n_F(E_k-\mu)+n_F(E_k+\mu)}{2(-q_0-E_k)}\right)\chi_{[-\frac{q_0}{2}\pm\sqrt{\triangle}]}(E_k) \\
& +\theta(q_0+E_k)(q_0+E_k)\left(-\frac{n_F(E_k-\mu)+n_F(E_k+\mu)}{2(q_0+E_k)}\right)\chi_{[-\frac{q_0}{2}\pm\sqrt{\triangle}]}(E_k) \\
& -\theta(-q_0+E_k)(-q_0+E_k)\left(-\frac{n_F(E_k-\mu)+n_F(E_k+\mu)}{2(-q_0+E_k)}\right)\chi_{[\frac{q_0}{2}\pm\sqrt{\triangle}]}(E_k)\Bigg\}
\end{aligned} \tag{B.38}
$$

If $q^2 = q_0^2 - \mathbf{q}^2 < 0$:

$$
\begin{aligned}
\mathrm{Im}\, iI(q_0,\mathbf{q}) = & -\frac{1}{8\pi}\int_m^\infty \mathrm{d}E_k \frac{\sqrt{E_k^2-m_H^2}}{|\mathbf{k}|\cdot|\mathbf{q}|}\theta(-q^2)\times \\
& \times\Bigg\{\theta(q_0-E_k)(q_0-E_k)\left(\frac{1}{q_0}-\frac{n_F(E_k-\mu)+n_F(E_k+\mu)}{2(q_0-E_k)}\right)\times \\
& \times\left(1-\chi_{[\frac{q_0}{2}\pm\sqrt{\triangle}]}(E_k)\right) \\
& -\theta(-q_0-E_k)(-q_0-E_k)\left(\frac{1}{-q_0}-\frac{n_F(E_k-\mu)+n_F(E_k+\mu)}{2(-q_0-E_k)}\right)\times \\
& \times\left(1-\chi_{[-\frac{q_0}{2}\pm\sqrt{\triangle}]}(E_k)\right) \\
& +\theta(q_0+E_k)(q_0+E_k)\left(-\frac{n_F(E_k-\mu)+n_F(E_k+\mu)}{2(q_0+E_k)}\right)\left(1-\chi_{[-\frac{q_0}{2}\pm\sqrt{\triangle}]}(E_k)\right) \\
& -\theta(-q_0+E_k)(-q_0+E_k)\left(-\frac{n_F(E_k-\mu)+n_F(E_k+\mu)}{2(-q_0+E_k)}\right)\left(1-\chi_{[\frac{q_0}{2}\pm\sqrt{\triangle}]}(E_k)\right)\Bigg\}
\end{aligned} \tag{B.39}
$$

The new symbol $\sqrt{\triangle}$ is defined as

$$
\sqrt{\triangle} = \frac{|\mathbf{q}|}{2}\sqrt{\frac{q^2-4m_H^2}{q^2}}. \tag{B.40}
$$

The integration range[3] is restricted by the step functions θ and the indicator functions χ.
If $q^2 = q_0^2 - \mathbf{q}^2 > 0$:

$$\begin{aligned}\mathrm{Im} iI(q_0,\mathbf{q}) =& -\frac{1}{8\pi}\theta(q_0^2-\mathbf{q}^2-4m^2)\frac{1}{|\mathbf{q}|}\\ &\times\left\{\theta(q_0)\int_{[\frac{q_0}{2}\pm\sqrt{\triangle}]}\mathrm{d}E_k\left(1-\frac{E_k}{q_0}-\frac{1}{2}(n_F(E_k-\mu)+n_F(E_k+\mu))\right)\right.\\ &\left.+\theta(-q_0)\int_{[-\frac{q_0}{2}\pm\sqrt{\triangle}]}\mathrm{d}E_k\left(1+\frac{E_k}{q_0}-\frac{1}{2}(n_F(E_k-\mu)+n_F(E_k+\mu))\right)\right\} \qquad \text{(B.41)}\end{aligned}$$

If $q^2 = q_0^2 - \mathbf{q}^2 < 0$:

$$\begin{aligned}\mathrm{Im} iI(q_0,\mathbf{q}) =& \frac{1}{16\pi|\mathbf{q}|}\int_{-\frac{q_0}{2}+\sqrt{\triangle}}^{\infty}\mathrm{d}E_k(n_F(E_k-\mu)+n_F(E_k+\mu))\\ &-\frac{1}{16\pi|\mathbf{q}|}\int_{\frac{q_0}{2}+\sqrt{\triangle}}^{\infty}\mathrm{d}E_k(n_F(E_k-\mu)+n_F(E_k+\mu)) \qquad \text{(B.42)}\end{aligned}$$

After algebraical simplifications one obtains momentum integrals over finite intervals.
If $q_0^2 - \mathbf{q}^2 > 0>$

$$\begin{aligned}\mathrm{Im} iI(q_0,\mathbf{q}) =& \frac{1}{16\pi}\theta(q_0^2-\mathbf{q}^2-4m_H^2)\mathrm{sgn}(q_0)\times\\ &\times\left(-\sqrt{1-\frac{4m_H^2}{q_0^2-\mathbf{q}^2}}+\frac{1}{|\mathbf{q}|}\int_{|\frac{q_0}{2}|-\sqrt{\triangle}}^{|\frac{q_0}{2}|+\sqrt{\triangle}}\mathrm{d}E_k(n_F(E_k-\mu)+n_F(E_k+\mu))\right), \qquad \text{(B.43)}\end{aligned}$$

If $q_0^2 - \mathbf{q}^2 < 0$

$$\mathrm{Im} iI(q_0,\mathbf{q}) = \frac{1}{16\pi|\mathbf{q}|}\mathrm{sgn}(q_0)\int_{\sqrt{\triangle}-|\frac{q_0}{2}|}^{\sqrt{\triangle}+|\frac{q_0}{2}|}\mathrm{d}E_k(n_F(E_k-\mu)+n_F(E_k+\mu)) \qquad \text{(B.44)}$$

The integral over the Fermi distribution function n_F is known analytically, see Eq. (B.7).
If $q_0^2 - \mathbf{q}^2 > 0$:

$$\begin{aligned}\mathrm{Im} iI(q_0,\mathbf{q}) =& -\frac{1}{16\pi}\theta(q_0^2-\mathbf{q}^2-4m_H^2)\mathrm{sgn}(q_0)\left[\sqrt{1-\frac{4m_H^2}{q_0^2-\mathbf{q}^2}}\right.\\ &\left.+\frac{T}{|\mathbf{q}|}\ln\left(\frac{1+e^{-\frac{1}{T}(\frac{q_0}{2}+\sqrt{\triangle}-\mu)}}{1+e^{-\frac{1}{T}(|\frac{q_0}{2}-\sqrt{\triangle}-\mu}}\right)+\frac{T}{|\mathbf{q}|}\ln\left(\frac{1+e^{-\frac{1}{T}(\frac{q_0}{2}+\sqrt{\triangle}+\mu)}}{1+e^{-\frac{1}{T}(|\frac{q_0}{2}-\sqrt{\triangle}+\mu)}}\right)\right] \qquad \text{(B.45)}\end{aligned}$$

If $q_0^2 - \mathbf{q}^2 < 0$:

$$\mathrm{Im} iI(q_0,\mathbf{q}) = -\frac{T}{16\pi|\mathbf{q}|}\mathrm{sgn}(q_0)\left[\ln\left(\frac{1+e^{-\frac{1}{T}(\sqrt{\triangle}+|\frac{q_0}{2}-\mu)}}{1+e^{-\frac{1}{T}(\sqrt{\triangle}-|\frac{q_0}{2}-\mu)}}\right)+\ln\left(\frac{1+e^{-\frac{1}{T}(\sqrt{\triangle}+|\frac{q_0}{2}+\mu)}}{1+e^{-\frac{1}{T}(\sqrt{\triangle}-|\frac{q_0}{2}+\mu)}}\right)\right] \qquad \text{(B.46)}$$

These expressions are understood to be regularized. For the Pauli-Villars scheme, the sum over regulator masses can be applied directly. For a sharp 3-momentum cut-off, the integration ranges in Eq. (B.43) and Eq. (B.44) must be analyzed more carefully.

B.4.3 Numerical integration

The numerical integration of the integral iI with its real and imaginary part is an important issue because this expression enters in various expressions in the NJL model. While the imaginary part was derived analytically, the real part has two nontrivial integrals remaining (one if $\mathbf{q} = 0$) for a numerical treatment. If the imaginary part for the given external momentum $(q_0, \mathbf{q})$ is zero, there

---

[3] We postpone the discussion of regulators to the end of this section.

is no difficulty. If the imaginary part ImiI is nonzero, there are singularities in the integrand and the integration procedure becomes more involved. We present three different methods to treat such a type of numerical challenge.

A direct calculation that is implemented easily is the replacement of the imaginary part in Eq. (B.33) by a finite value $\mathcal{E}$,

$$iI(q_0 + i\epsilon) \longrightarrow iI(q_0 + i\mathcal{E}). \tag{B.47}$$

The choice of an appropriate value of $\mathcal{E}$ depends on the other relevant scales in the expression as well as on the required accuracy. The replaced integrand has no singularities any more but more or less sharp maxima, depending on the magnitude of $\mathcal{E}$. In general, the numerical accuracy that can be obtained with this method is limited; it is better if $\mathcal{E}$ is small, but such a choice increases the integration effort. An improvement in accuracy is obtained if the replacement is done for several different values of $\mathcal{E}$ is obtained and an extrapolation for $\mathcal{E} \to 0$ is performed,

$$iI(q_0 + i\epsilon) \longrightarrow \lim_{\mathcal{E}\to 0} iI(q_0 + i\mathcal{E}). \tag{B.48}$$

In this case, even the imaginary part has a reasonable accuracy. However, this treatment requires a multidimensional integration over an integrand with different maxima, and the procedure has to be repeated several times if the extrapolation method is used.

For a more exact solution of the problem, the integrand can not be replaced by a simplifying expression but has to be integrated with its singularities. For practical calculation, this can be done with the replacement

$$\int_a^b f(x)\mathrm{d}x \to \int_a^b \left(f(x) - \frac{f'(x_s)}{x - x_s} \right) \mathrm{d}x + \int_a^b \frac{f'(x_s)}{x - x_s} \mathrm{d}x, \tag{B.49}$$

where f has a first-order singularity[4] in x_s. The integrand of the first integral on the right hand side of Eq. is now well-behaved in the limit $x \longrightarrow x_s$ and the second one can be solved analytically. However, if one has two integrations, there may remain a logarithmic divergence that has to be subtracted in a similar way in the next integral. The analysis of the pole position as well as the implementation is clearly more involved, whereas the numerical effort is smaller than in the previous method.

The last method makes use of complex analysis. As the elementary integral iI has the properties

$$iI(q_0 + i\epsilon, \mathbf{q}) = (iI)^*(q_0 - i\epsilon, \mathbf{q}) \tag{B.50}$$

and

$$\lim_{|q_0|\to\infty} iI = 0 \tag{B.51}$$

faster that $1/q_0$, there exists a type of Lehmann representation for the integral,

$$iI(q_0 + i\epsilon, \mathbf{q}) = \int_{-\infty}^{+\infty} \frac{\mathrm{d}\omega}{2\pi} \frac{-2\mathrm{Im}iI(\omega, \mathbf{q})}{q_0 + i\epsilon - \omega}. \tag{B.52}$$

Thus, the real part is obtained from the integral

$$\mathrm{Re}iI(q_0, \mathbf{q}) = \mathrm{Pr} \int_{-\infty}^{+\infty} \frac{\mathrm{d}\omega}{2\pi} \frac{-2\mathrm{Im}iI(\omega, \mathbf{q})}{q_0 - \omega}, \tag{B.53}$$

which is a 1-dimensional integral with no (if the imaginary part of iI is zero) ore one (if the imaginary part is nonzero) first-order singularity. This is the way the integral is evaluated the fastest and the most exactly[5].

---

[4] The generalization to higher orders poles or several of them is obvious

[5] A similar method was applied in [143].

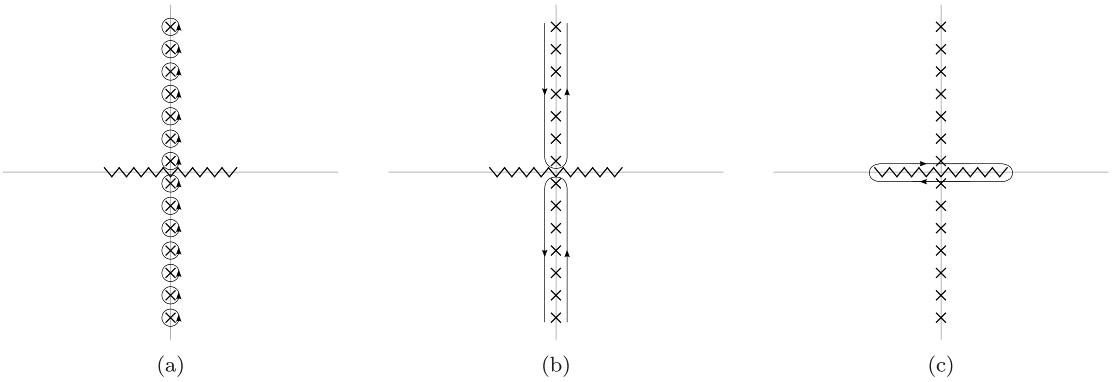

Figure B.3: Integration contours for the free thermodynamic potential Ω. In (a), the contour C used in Eq. (B.57) consists of circles around the fermionic Matsubara frequencies. After the merging of the circles on the positive and negative half plane in (b), the integration contours are bend to the branch cuts on the real axis as shown in (c).

B.5 Mean-field thermodynamic potential

B.5.1 Free part

The free part of the thermodynamic potential per volume is also derived in textbooks (see e.g. [218]), but it is instructive to use a similar technique as in the rest of the work. The part of Ω can be written[6] as

$$i\mathcal{Tr}\ln iS_H^{-1} = -T\sum_{i\omega_k}\int\frac{\mathrm{d}^3k}{(2\pi)^3}\ln\det S_H^{-1}(i\omega_k+\mu,\mathbf{k}). \tag{B.54}$$

The evaluation of the determinant in the integrand yields

$$\det S_H^{-1}(i\omega_k+\mu,\mathbf{k}) = \left[(i\omega_k+\mu)^2-\mathbf{k}^2-m_H^2\right]^{2N_cN_f}, \tag{B.55}$$

leading to the contribution of the thermodynamic potential per volume

$$i\mathcal{Tr}\ln iS^{-1} = -2N_cN_fT\sum_{i\omega_k}\int\frac{\mathrm{d}^3k}{(2\pi)^3}\ln\left[(i\omega_k+\mu)^2-E_k^2\right], \tag{B.56}$$

with the usual notation $E_k^2 = \mathbf{k}^2 - m_H^2$. The Matsubara sum can be written in the form of a contour integration with a contour C shown in Fig. B.3(a),

$$i\mathcal{Tr}\ln iS^{-1} = 2N_cN_f\int\frac{\mathrm{d}^3k}{(2\pi)^3}\oint_C\frac{\mathrm{d}z}{2\pi i}n_F(z)\ln\left[(z+\mu)^2-E_k^2\right]. \tag{B.57}$$

The integrand of Eq. (B.57) will be analyzed now in order to simplify the expression. The logarithm is analytic in the complex plane without the negative real axis[7] where it has a branch cut: The imaginary part jumps from $-\pi$ to π. Thus, the integrand has a branch cut on the real axis between $-E_k-\mu$ and $+E_k-\mu$, as it is shown in Fig. B.3(a). In Fig. B.3(b) and B.3(c), it is shown how to deform the integration path to arrive at the expression

$$\begin{aligned} i\mathcal{Tr}\ln iS^{-1} = 2N_cN_f\int\frac{\mathrm{d}^3k}{(2\pi)^3}\int_{-E_k-\mu}^{+E_k-\mu}\frac{\mathrm{d}k_0}{2\pi i}\Big\{&n_F(k_0+i\epsilon)\ln\left[(k_0+i\epsilon+\mu)^2-E_k^2\right]\\ &-n_F(k_0-i\epsilon)\ln\left[(k_0-i\epsilon+\mu)^2-E_k^2\right]\Big\}. \end{aligned} \tag{B.58}$$

---

[6] The presented expression is not finite in the way it is written here. As usual, a infinite "vacuum term" has to be subtracted in order to bring it to a finite value and makes all algebra valid performed in this section. Since this term can be chosen to be $-i\mathcal{Tr}\ln iS_H^{\mathrm{vac}\,-1}$ or $-i\mathcal{Tr}\ln iS_0^{-1}$ that have the have the same structure, the terms are omitted here.

[7] This is a special choice of a branch of the complex logarithm, another choice correspond to another fixing of the thermodynamic potential per volume.

As the continuation of the Fermi distribution function to real values is analytic, and the logarithm has the property

$$\ln(z) = \ln(|z|) + i\arg(z) = \big[\ln(z^*)\big]^*, \tag{B.59}$$

Eq. (B.58) can be written as

$$i\mathcal{T}r\ln iS^{-1} = 2N_cN_f\int\frac{\mathrm{d}^3k}{(2\pi)^3}\int_{-E_k-\mu}^{+E_k-\mu}\frac{\mathrm{d}k_0}{2\pi i}\Big\{n_F(k_0)2i\arg\big[(k_0+i\epsilon+\mu)^2-E_k^2\big]\Big\}. \tag{B.60}$$

We first shift the integration variable by μ, which leads to the more symmetric expression

$$i\mathcal{T}r\ln iS^{-1} = 2N_cN_f\int\frac{\mathrm{d}^3k}{(2\pi)^3}\int_{-E_k}^{+E_k}\frac{\mathrm{d}k_0}{2\pi i}\Big\{n_F(k_0-\mu)2i\arg\big[(k_0+i\epsilon)^2-E_k^2\big]\Big\}. \tag{B.61}$$

Now, one can identify the angle $\mathrm{sgn}(k_0)\pi$ in the integrand, and the integral takes the simple form

$$i\mathcal{T}r\ln iS^{-1} = 2N_cN_f\int\frac{\mathrm{d}^3k}{(2\pi)^3}\int_{-E_k}^{+E_k}\mathrm{d}k_0\mathrm{sgn}(k_0)n_F(k_0-\mu). \tag{B.62}$$

It is useful to split the integral into two intervals, where property of the Fermi distribution function from Eq. (B.4) can be used,

$$i\mathcal{T}r\ln iS^{-1} = -2N_cN_f\int\frac{\mathrm{d}^3k}{(2\pi)^3}\int_0^{+E_k}\mathrm{d}k_0\left[1-n_F(k_0-\mu)-n_F(k_0+\mu)\right]. \tag{B.63}$$

This type of integral can be solved analytically as shown in Eq. (B.7),

$$i\mathcal{T}r\ln iS^{-1} = -2N_cN_f\int\frac{\mathrm{d}^3k}{(2\pi)^3}\Big[E_k+T\ln(1+e^{-\frac{1}{T}(E_k-\mu)})+T\ln(1+e^{-\frac{1}{T}(E_k+\mu)})\Big]. \tag{B.64}$$

The numerical treatment of this integrand is rather simple since only one integration remains,

$$\int\frac{\mathrm{d}^3k}{(2\pi)^3}\rightarrow\int_0^\infty\mathbf{k}^2\mathrm{d}|\mathbf{k}|, \tag{B.65}$$

and the integrand has no singularities. However, the regularization has to be applied at least for the vacuum part, leading to a finite integration interval

$$\int_0^\infty\mathrm{d}|\mathbf{k}|f_{m_H^2}(k)\rightarrow\int_0^{\Lambda_q}\mathrm{d}|\mathbf{k}|f_{m_H^2}(k) \tag{B.66}$$

for the 3-momentum cut-off scheme. The Pauli-Villars prescription requires the subtraction of an additional constant, for example the vacuum value.

$$\int_0^\infty\mathrm{d}|\mathbf{k}|f_{m_H^2}(k)\rightarrow\int_0^\infty\mathrm{d}|\mathbf{k}|\sum_{j=0}^{2}\Big(c_jf_{m_H^2+j\Lambda_{PV}^2}(k)-c_jf_{m_H^{\mathrm{vac}\;2}+j\Lambda_{PV}^2}(k)\Big) \tag{B.67}$$

This sum over six terms, which rise cubically each separately leads to a well-behaved ultraviolet behavior. The vacuum integral can be solved analytically,

$$\int\mathrm{d}|\mathbf{k}||\mathbf{k}|^2E_k = \frac{1}{4}E_k|\mathbf{k}|-\frac{1}{8}m_H^2E_k|\mathbf{k}|-\frac{1}{8}m_H^4\ln\left(2E_k+2|\mathbf{k}|\right) \tag{B.68}$$

For the 3-momentum cut-off regularization, the primitive is evaluated at 0 and Λ_q, whereas for the Pauli-Villars regularization the regulator terms at 0 are summed.

B.5.2 Self-energy term

The second term in the thermodynamic potential contains the self-energy $\mathit{\Sigma}$, which is the Hartree self-energy $\mathit{\Sigma}_H$ in case of the mean field thermodynamic potential per volume,

$$\mathcal{Tr}(\mathit{\Sigma}_H iS_H) = -T \sum_{i\omega_k} \int \frac{\mathrm{d}^3k}{(2\pi)^3} \mathit{\Sigma}_H \frac{\mathrm{Tr}\big[(i\omega_K + \mu)\gamma^0 - \mathbf{k}\boldsymbol{\gamma} + m_H\big]}{(i\omega_K + \mu)^2 - \mathbf{k}^2 - m_H^2}. \tag{B.69}$$

Because the mean field self-energy is constant,

$$\mathit{\Sigma}_H = m_H - m_0, \tag{B.70}$$

the integral simplifies and one obtains

$$\mathcal{Tr}(\mathit{\Sigma}_H iS_H) = -4N_c N_f \mathit{\Sigma}_H T \sum_{i\omega_k} \int \frac{\mathrm{d}^3k}{(2\pi)^3} \frac{m_H}{(i\omega_K + \mu)^2 - \mathbf{k}^2 - m_H^2}. \tag{B.71}$$

In this integral, one can identify the elementary integral iI_1,

$$\mathcal{Tr}(\mathit{\Sigma}_H iS_H) = 4N_c N_f \mathit{\Sigma}_H iI_1. \tag{B.72}$$

This expression is closely related to the Hartree self-energy $\mathit{\Sigma}_H$ again. Therefore, one can write the self-energy term of the thermodynamic potential per volume

$$\mathcal{Tr}(\mathit{\Sigma}_H iS_H) = \frac{1}{2g}\mathit{\Sigma}_H^2 = \frac{(m_H - m_0)^2}{2g}. \tag{B.73}$$

A similar term is obtained by the evaluation of the $\mathit{\Phi}$-functional where the Hartree self-energy enters, too. This is discussed in the next paragraphs.

B.5.3 Glasses diagram

The glasses diagram is the only contribution to the $\mathit{\Phi}$-functional in mean field approximation. It takes the form

$$\mathit{\Phi}_H = -\sum_M 2g\frac{1}{2}\left(-T\sum_{i\omega_k}\int \frac{\mathrm{d}^3k}{(2\pi)^3}\mathrm{Tr}\big[\mathit{\Gamma}_M iS(i\omega_k + \mu, \mathbf{k})\big]\right)^2, \tag{B.74}$$

where only the scalar term in the sum over all interaction channels M contribute. This consideration leads to

$$\mathit{\Phi}_H = -g\left(T\sum_{i\omega_k}\int \frac{\mathrm{d}^3k}{(2\pi)^3}\frac{\mathrm{Tr}\big[(i\omega_k + \mu)\gamma^0 - \boldsymbol{\gamma}\mathbf{k} + m_H\big]}{(i\omega_k + \mu)^2 - \mathbf{k}^2 - m_H^2}\right)^2, \tag{B.75}$$

which resembles the expression obtained in Eq. (B.69). Indeed, the integral in the parenthesis can be simplified in the same way as in Sec. B.5.2 , leading to

$$\mathit{\Phi}_H = -\frac{\mathit{\Sigma}_H^2}{4g} = -\frac{(m_H - m_0)^2}{4g}. \tag{B.76}$$

Thus, the sum of the self-energy term and the glasses diagram lead to the contribution

$$\mathcal{Tr}(\mathit{\Sigma}_H iS_H) + \mathit{\Phi}_H[S_H] = \frac{(m_H - m_0)^2}{4g}, \tag{B.77}$$

which is the mass-dependent shift additional to the free fermions in the thermodynamic potential per volume $\mathit{\Omega}_H$.

B.6 Elementary integral iK

The elementary integral iK is defined as

$$iK(i\omega_q,\mathbf{q}) = -\int \frac{\mathrm{d}^3k}{(2\pi)^3} T \sum_{i\omega_k} \frac{1}{[(i\omega_k+\mu)^2-\mathbf{k}^2-m_H^2]^2[(i\omega_k+i\omega_q+\mu)^2-(\mathbf{k}+\mathbf{q})^2-m_H^2]}, \tag{B.78}$$

where m_H is the Hartree quark mass. In the usual manner, we write the sum over the Matsubara frequencies as

$$iK(i\omega_q,\mathbf{q}) = \int \frac{\mathrm{d}^3k}{(2\pi)^3} \oint_C \frac{\mathrm{d}z}{2\pi i} n_F(z) \frac{1}{[(z+\mu)^2-E_k^2]^2[(z+i\omega_q+\mu)^2-E_{kq}^2]}, \tag{B.79}$$

where we use the same notation for the energies as in Sec. B.4. For further investigations, the structure of the integrand in the complex z-plane has to be analyzed. It is found that the integrand has two poles of first order at

$$z_{1,2} = \pm E_{kq} - i\omega_q - \mu, \tag{B.80}$$

and two poles of second order at

$$z_{3,4} = \pm E_k - \mu. \tag{B.81}$$

Besides the orders of the poles, the structure in the complex plane is equivalent to Fig. B.2, and we can perform the same contour deformations as in Sec. B.4. This leads to the result

$$iK(i\omega_q,\mathbf{q}) = \int \frac{\mathrm{d}^3k}{(2\pi)^3} \sum_{z_i} \mathrm{Res} \frac{n_F(z)}{[(z+\mu)^2-E_k^2]^2[(z+i\omega_q+\mu)^2-E_{kq}^2]}. \tag{B.82}$$

The explicit form is significantly more lengthy than the result for iI. We limit the derivation to the special case

$$i\omega_q \to q_0 + i\epsilon, \quad \mathbf{q}=0, \quad \mu=0, \quad T>0, \tag{B.83}$$

which is needed in the work. According to [208], we write the result

$$iK(q_0,\mathbf{0}) = \int \frac{\mathrm{d}^3k}{(2\pi)^3} \left\{ \frac{n_F(E_k)-n_F(-E_k)}{4E_k^3} \left[\frac{1}{q_0^2-4E_k^2} - \frac{8E_k^2}{(q_0^2-4E_k^2)^2} + \frac{2E_k n_F(E_k) n_F(-E_k)}{T(q_0^2-4E_k^2)} \right] \right\} \tag{B.84}$$

for this special parameters.

B.7 Elementary integral iL

In this section, the elementary integral iL is evaluated. It is defined as

$$iL(i\omega_q,\mathbf{q}) = -\int \frac{\mathrm{d}^3k}{(2\pi)^3} T \sum_{i\omega_k} \frac{1}{[(i\omega_k+\mu)-\mathbf{k}^2-m_H^2]^2[(i\omega_k+i\omega_q+\mu)-(\mathbf{k}+\mathbf{q})^2-m_H^2]^2}, \tag{B.85}$$

thus it is very similar to iI and iK. Indeed, if one uses the contour integral trick

$$iL(i\omega_q,\mathbf{q}) = \int \frac{\mathrm{d}^3k}{(2\pi)^3} \oint_C \frac{\mathrm{d}z}{2\pi i} n_F(z) \frac{1}{[(z+\mu)^2-E_k^2]^2[(z+i\omega_q+\mu)^2-E_{kq}^2]^2}, \tag{B.86}$$

one encounters the same structure in complex plane, but all four poles are of second order. This is an additional complication to the evaluation of the expression after contour deformation,

$$iL(i\omega_q,\mathbf{q}) = \int \frac{\mathrm{d}^3k}{(2\pi)^3} \sum_{z_i} \mathrm{Res} \frac{n_F(z)}{[(z+\mu)^2-E_k^2]^2[(z+i\omega_q+\mu)^2-E_{kq}^2]^2}, \tag{B.87}$$

where the same deformations have been performed as in the previous section concerning iK. For a vanishing external 3-momentum and zero chemical potential, we can use [208] and obtain

$$iL(q_0,\mathbf{0}) = \int \frac{\mathrm{d}^3k}{(2\pi)^3} \Bigg\{ \frac{n_F(E_k) - n_F(-E_k)}{4E_k^3 - q_0^2} \Big[\frac{1}{q_0^2 - 4E_k^2} - \frac{12E_k^2}{(q_0^2 - 4E_k^2)^2} - \frac{64E_k^4}{(q_0^2 - 4E_k^2)^3} + \frac{E_k n_F(E_k) n_F(-E_k)}{T} \Big(\frac{1}{q_0^2 - 4E_k^2} + \frac{8E_k^2}{(q_0^2 - 4E_k^2)^2} \Big) \Big] \Bigg\} \tag{B.88}$$

for real external momentum q_0.

Appendix C

Calculation of the NLO integrals

In this part, we derive expressions for the different integrals that appear in the evaluation of Feynman diagrams in the NJL model in next-to-leading order in $1/N_c$-counting. The first section concerns the perturbative ring sum contribution, all other sections deal with quantities in the self-consistent scheme.

C.1 Ring sum

The evaluation of the ring sum leads to one contribution for each meson channel M, where these contributions read

$$\Omega_M = \frac{1}{2} T \sum_{i\omega_q} \int \frac{\mathrm{d}^3 q}{(2\pi)^3} \ln\left[1 - 2g\Pi_M(i\omega_q, \mathbf{q})\right]. \tag{C.1}$$

It is possible write the Matsubara sum as a contour integral in the complex plane,

$$\Omega_M = \frac{1}{2} \int \frac{\mathrm{d}^3 q}{(2\pi)^3} \oint_C \frac{\mathrm{d}z}{2\pi i} n_B(z) \ln\left[1 - 2g\Pi_M(z, \mathbf{q})\right], \tag{C.2}$$

where the contour C consists of circles around the bosonic Matsubara frequencies $i\omega_q$. We analyze the integrand in the complex plane to perform a contour deformation. The logarithm has a branch cut on the negative real axis, thus we have branch cuts in the complex plane where the argument of the logarithm is real and negative, and where the argument of the logarithm is complex and changes its sign. As the argument is related to the RPA meson propagator,

$$1 - 2g\Pi_M(z, \mathbf{q}) = \frac{-2g}{D_M(z, \mathbf{q})}, \tag{C.3}$$

we can use our knowledge about the meson propagator to identify the structure in the complex plane. In Hartree approximation and RPA, the meson propagator $D_M(z, \mathbf{q})$ is real for

$$z = q_0 \pm i\epsilon, \qquad q_0 \in \left[|\mathbf{q}|, \sqrt{\mathbf{q}^2 + 4m_H^2}\right] \subset \mathbb{R}. \tag{C.4}$$

The sign of $\mathrm{Re}D_M$ is negative if $q_0^2 + \mathbf{q}^2 < m_M^2$, and positive elsewhere. This situation is rather complex, since different cases for π and σ for different values of T and μ have to be distinguished. Therefore, we first assume the most general case for Π_M, which will help us in the self-consistent approximation scheme, too. The specialization to the perturbative ring sum can be done later.

In the general case, the meson propagator D_M has a branch cut on the real axis, where the retarded and advanced propagator are above and below the axis, respectively. The imaginary part of the meson propagator changes its sign when $\mathrm{Im}z$ changes its sign, and therefore a branch cut is found on the real axis. The situation, including the integration contour C, is sketched in Fig. C.1(a). We merge the different circles as it is shown in Fig. C.1(b), and deform the resulting

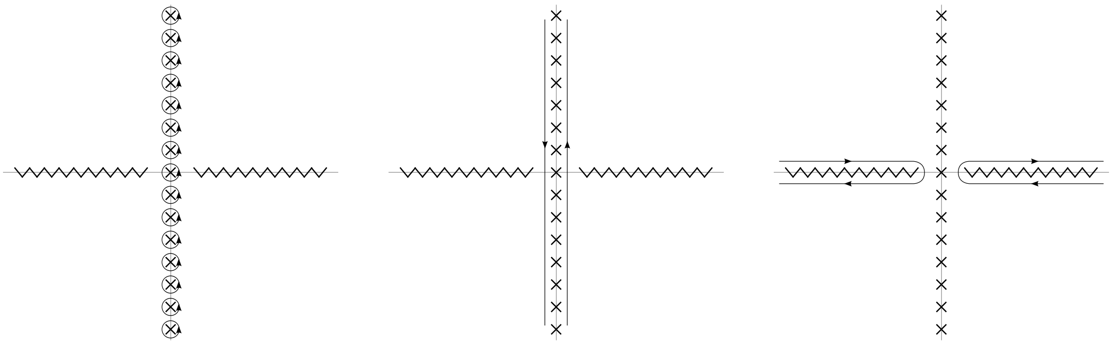

Figure C.1: Integration contours for the calculation of the ring sum contribution to the thermodynamic potential per volume. (a) is the contour integral equivalent of the Matsubara sum, which is, after the intermediate step (b), deformed to (c).

path in a way that the integration is done along the real axis. This integration path, which is shown in Fig. C.1(c), leads to the integral

$$\varOmega_M = \frac{1}{2}\int\frac{\mathrm{d}^3q}{(2\pi)^3}\int_{-\infty}^{+\infty}\frac{\mathrm{d}q_0}{2\pi i}\Big\{+n_B(q_0+i\epsilon)\ln\left[1-2g\varPi_M(q_0+i\epsilon,\mathbf{q})\right] \\ - n_B(q_0-i\epsilon)\ln\left[1-2g\varPi_M(q_0-i\epsilon,\mathbf{q})\right]\Big\}. \tag{C.5}$$

The infinitesimal arguments in the Bose distribution function n_B can be omitted, and we write the result as

$$\varOmega_M = \frac{1}{2}\int\frac{\mathrm{d}^3q}{(2\pi)^3}\int_{-\infty}^{+\infty}\frac{\mathrm{d}q_0}{2\pi i}n_B(q_0)\ln\frac{1-2g\varPi_M(q_0+i\epsilon,\mathbf{q})}{1-2g\varPi_M(q_0-i\epsilon,\mathbf{q})}. \tag{C.6}$$

We can split the integration of q_0 in two parts,

$$\varOmega_M = \frac{1}{2}\int\frac{\mathrm{d}^3q}{(2\pi)^3}\Big\{\int_{-\infty}^{0}\frac{\mathrm{d}q_0}{2\pi i}n_B(q_0)\ln\frac{1-2g\varPi_M(q_0+i\epsilon,\mathbf{q})}{1-2g\varPi_M(q_0-i\epsilon,\mathbf{q})} \\ + \int_{0}^{+\infty}\frac{\mathrm{d}q_0}{2\pi i}n_B(q_0)\ln\frac{1-2g\varPi_M(q_0+i\epsilon,\mathbf{q})}{1-2g\varPi_M(q_0-i\epsilon,\mathbf{q})}, \tag{C.7}$$

and use the symmetries of the Bose distribution function to write

$$\varOmega_M = \frac{1}{2}\int\frac{\mathrm{d}^3q}{(2\pi)^3}\Big\{n_B(q_0)\ln\frac{1-2g\varPi_M(q_0+i\epsilon,\mathbf{q})}{1-2g\varPi_M(q_0-i\epsilon,\mathbf{q})} \\ - \left[1+n_B(q_0)\right]\ln\frac{1-2g\varPi_M(-q_0+i\epsilon,\mathbf{q})}{1-2g\varPi_M(-q_0-i\epsilon,\mathbf{q})}. \tag{C.8}$$

The polarization loop $\varPi_M$ has the property

$$\varPi_M(q_0\pm i\epsilon,\mathbf{q}) = \varPi_M(-q_0\mp i\epsilon,\mathbf{q}), \tag{C.9}$$

thus we can write the result as

$$\varOmega_M = \int\frac{\mathrm{d}^3q}{(2\pi)^3}\int_{0}^{+\infty}\frac{\mathrm{d}q_0}{2\pi i}\left(n_B(q_0)+\frac{1}{2}\right)\ln\frac{1-2g\varPi_M(q_0+i\epsilon)}{1-2g\varPi_M(q_0-i\epsilon)}. \tag{C.10}$$

We can try to relate this expression to the RPA meson propagators D_M. Therefore, we add and subtract a term $\ln -2g$ in the integrand,

$$\varOmega_M = -\int\frac{\mathrm{d}^3q}{(2\pi)^3}\int_{0}^{+\infty}\frac{\mathrm{d}q_0}{2\pi i}\left(n_B(q_0)+\frac{1}{2}\right)\Big\{+\ln\left[\frac{-2g}{1-2g\varPi_M(q_0+i\epsilon,\mathbf{q})}\right] \\ - \ln\left[\frac{-2g}{1-2g\varPi_M(q_0-i\epsilon,\mathbf{q})}\right]\Big\}, \tag{C.11}$$

where we can identify the arguments of the logarithm as the retarded and advanced meson propagator D^R_M and D^A_M,

$$\Omega_M = -\int \frac{\mathrm{d}^3 q}{(2\pi)^3} \int_0^{+\infty} \frac{\mathrm{d}q_0}{2\pi i} \left(n_B(q_0) + \frac{1}{2} \right) \left[\ln D^R_M(q_0, \mathbf{q}) - \ln D^A_M(q_0, \mathbf{q}) \right]. \tag{C.12}$$

The difference of retarded and advanced boson propagator is the sign of the imaginary part. We write the logarithms of the propagators as

$$\ln D_M(q_0 \pm i\epsilon, \mathbf{q}) = \ln |D^R_M(q_0, \mathbf{q})| \mp i\phi_M(q_0, \mathbf{q}) \tag{C.13}$$

and obtain the thermodynamic potential per volume in terms of scattering phases ϕ_M,

$$\Omega_M = \int \frac{\mathrm{d}^3 q}{(2\pi)^3} \int_0^{+\infty} \frac{\mathrm{d}q_0}{\pi} \left(n_B(q_0) + \frac{1}{2} \right) \phi_M(q_0, \mathbf{q}). \tag{C.14}$$

We have a choice in a constant shift of the thermodynamic potential per volume, which correspond to the fixing of the definition of ϕ_M. An angle in the complex plane is defined up to a multiple of 2π, and we want to take the constant that sets Eq. (C.14) to a finite value. In the Nozière-Schmitt-Rink contribution

$$\Omega^{NSR}_M = \int \frac{\mathrm{d}^3 q}{(2\pi)^3} \int_0^{\infty} \frac{\mathrm{d}q_0}{\pi} n_B(q_0) \phi_M, \tag{C.15}$$

the Bose distribution function n_B is present, which has a pole at zero. We obtain a finite value if we chose the scattering phase such that

$$\lim_{q_0 \to 0} \phi_M(q_0) = 0 \quad \Rightarrow \quad \lim_{q_0 \to 0} n_B(q_0)\phi_M(q_0) = T\phi'_M(x). \tag{C.16}$$

The integration in the quantum fluctuation part

$$\Omega^{qfl}_M = \int \frac{\mathrm{d}^3 q}{(2\pi)^3} \int_0^{\infty} \frac{\mathrm{d}q_0}{2\pi} \phi_M. \tag{C.17}$$

has now an infrared divergence. For a well-defined potential, it is required that ϕ_M vanishes for large q_0. This can be obtained by a phase convention that fulfills the Levinson theorem.
We turn back to the special case of the perturbative ring sum, where we know more about the structure of the scattering phases and propagators. The integral has a contribution for momenta in the continuum and for spacelike momenta. There is an additional term for pions in the chirally broken phase, since

$$\arg \left[D^R_\pi(q_0, \mathbf{q}) \right] = \begin{cases} -i\pi & \text{for } \mathbf{q}^2 < q_0^2 < m_\pi^2 + \mathbf{q}^2 \\ 0 & \text{for } m_\pi^2 + \mathbf{q}^2 < q_0^2 < 4m_H^2 + \mathbf{q}^2 \end{cases}.$$

With these considerations, some parts of the q_0-integral can be solved analytically in the case of the perturbative ring sum contribution.

C.2 Hartree self-energy

The Hartree self-energy for a dressed propagator S_1 has only a scalar contribution, like in the case of mean field approximation. Therefore, we can write

$$\Sigma_H = 8N_c N_f g T \sum_{i\omega_k} \int \frac{\mathrm{d}^3 k}{(2\pi)^3} S_s(i\omega_k + \mu, \mathbf{k}), \tag{C.18}$$

thus only the scalar component of the propagator S_s enters in the calculation. In principle, one can use the equation above for the calculation of the Hartree self-energy Σ_H: one only has to evaluate the Matsubara sum and one integral in a numerical way,

$$\Sigma_H = 8N_c N_f g \frac{4\pi}{(2\pi)^3} \int_{-\infty}^{+\infty} \mathrm{d}|\mathbf{k}|\, \mathbf{k}^2 T \sum_{i\omega_k} S_s(i\omega_k + \mu, \mathbf{k}). \tag{C.19}$$

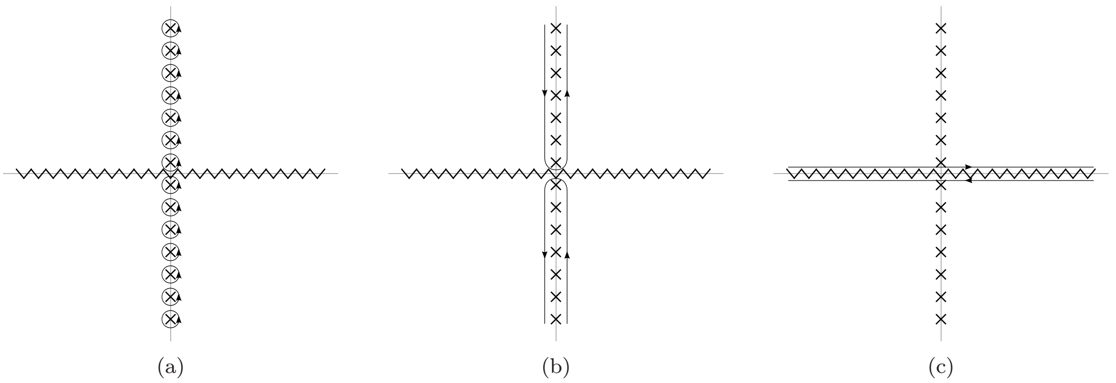

Figure C.2: Integration contours for calculation of $\Sigma_H(S_1)$. (a) shows the contour introduced in Eq. (C.20), which is deformed in (b) and (c).

However, we can try to rewrite the expression as an integral in the complex plane to obtain a significant simplification of the self-energy. As usual, we start with

$$\Sigma_H = 8N_cN_fg\int\frac{\mathrm{d}^3k}{(2\pi)^3}\oint_C\frac{\mathrm{d}z}{2\pi i}n_F(z)S_s(z+\mu,\mathbf{k}), \tag{C.20}$$

where the closed integration contour C is a set of circles around fermionic Matsubara frequencies. We want to deform this integration contour and therefore, the structure of the integrand in the complex plane has to be investigated. The poles of n_F on the imaginary axis are known, what is left is the scalar part of the dressed quark propagator. The exact analytic structure S_1 is unknown, but from reasons of analyticity, the most general form of S_1 has a branch cut on the real axis, where the change between retarded and advanced propagators occurs. The contour C in the complex plane is shown in Fig. C.2(a) as well as the poles and the branch cut. With this knowledge, the contour can be deformed as it shown in Figs. C.2(b) and C.2(c). This leads to the integral

$$\begin{aligned}\Sigma_H = 8N_cN_fg\int\frac{\mathrm{d}^3k}{(2\pi)^3}\int_{-\infty}^{+\infty}\frac{\mathrm{d}k_0}{2\pi i}\Big\{&+n_F(k_0+i\epsilon)S_s(k_0+\mu+i\epsilon,\mathbf{k})\\ &-n_F(k_0-i\epsilon)S_s(k_0+\mu-i\epsilon,\mathbf{k})\Big\},\end{aligned} \tag{C.21}$$

where the two contributions with different signs come from the two integration paths close to the real axis, which have different directions. Because the Fermi distribution function is continuous on the real axis, we can perform the limit $\epsilon\to 0$ in this function and obtain

$$\Sigma_H = 8N_cN_fg\int\frac{\mathrm{d}^3k}{(2\pi)^3}\int_{-\infty}^{+\infty}\frac{\mathrm{d}p_0}{2\pi i}n_F(k_0-\mu)\big[S_s(k_0+i\epsilon,\mathbf{k})-S_s(k_0-i\epsilon,\mathbf{k})\big], \tag{C.22}$$

where the integration variable k_0 was shifted by μ. The two propagators can be identified as the retarded and the advanced propagators, and their difference is related to the spectral function ρ,

$$S(k_0+i\epsilon,\mathbf{k})-S(k_0-i\epsilon,\mathbf{k}) = S^R(k_0,\mathbf{k})-S^A(k_0,\mathbf{k}) = -i\rho(k_0,\mathbf{k}). \tag{C.23}$$

Therefore, the Hartree self-energy can be written in terms of the scalar part of the quark spectral function,

$$\Sigma_H = -8N_cN_fg\int\frac{\mathrm{d}^3k}{(2\pi)^3}\int_{-\infty}^{+\infty}\frac{\mathrm{d}k_0}{2\pi}n_F(k_0-\mu)\rho_s(k_0+i\epsilon,\mathbf{k}), \tag{C.24}$$

which is nice to interpret because it is a phase space integral over a thermal distribution function times a density of states. We can identify a part that is independent of temperature and chemical potential by the separation of the integral over k_0,

$$\Sigma_H = -8N_cN_fg\int\frac{\mathrm{d}^3k}{(2\pi)^3}\Bigg\{\int_{-\infty}^{0}\frac{\mathrm{d}k_0}{2\pi}n_F(k_0-\mu)\rho_s(k_0+i\epsilon,\mathbf{k}) + \int_{0}^{+\infty}\frac{\mathrm{d}k_0}{2\pi}n_F(k_0-\mu)\rho_s(k_0+i\epsilon,\mathbf{k})\Bigg\}. \tag{C.25}$$

We rewrite this expression as one single integral,

$$\Sigma_H = -8N_cN_fg\int\frac{\mathrm{d}^3k}{(2\pi)^3}\int_0^{+\infty}\frac{\mathrm{d}k_0}{2\pi}\Big\{n_F(k_0-\mu)\rho_s(k_0,\mathbf{k}) + [1-n_F(k_0+\mu)]\rho_s(-k_0,\mathbf{k})\Big\}, \tag{C.26}$$

and can see the temperature-independent part clearly. In contrast to the Hartree self-energy with Hartree propagators, there are two and not one remaining integrals that have to be solved numerically. From Eq. (C.26) one can see that Σ_H is real and constant like in Hartree approximation, so no nontrivial structure in the spectral function is generated from this self-energy term.

Special case of Hartree approximation

As a check of the calculation, we specialize the result obtained for a general propagator S_1 to the case of a Hartree dressing. The Hartree spectral function ρ_H is just the spectrum of a free fermion with mass m_H, and the scalar component reads

$$\rho_{H,s} = \frac{\pi m_H}{E_k}\left[\delta(k_0-E_k)-\delta(k_0+E_k)\right]. \tag{C.27}$$

When the δ-function is inserted in Eq. (C.26), the integral over k_0 can be performed analytically, yielding

$$\Sigma_H = -8N_cN_fg\int\frac{\mathrm{d}^3k}{(2\pi)^3}\frac{m_H}{2E_k}\big\{n_F(E_k-\mu)-[1-n_F(E_k+\mu)]\big\}. \tag{C.28}$$

One can directly identify the elementary integral iI_1 in its form from Eq. (B.19).

C.3 Polarization loop

The polarization loop Π_M, with the dressed propagator S_1 in the internal lines, reads

$$\Pi_M(i\omega_q,\mathbf{q}) = -T\sum_{i\omega_p}\int\frac{\mathrm{d}^3p}{(2\pi)^3}\mathrm{Tr}\left[S_1(i\omega_p+\mu,\mathbf{p})\Gamma_M S_1(i\omega_p+i\omega_q+\mu,\mathbf{p}+\mathbf{q})\Gamma_M\right] \tag{C.29}$$

for external momentum $(i\omega_q,\mathbf{q})$. The trace P in the integrand

$$P(i\omega_p+\mu,\mathbf{p};i\omega_p+i\omega_q+\mu,\mathbf{p}+\mathbf{q}) = \mathrm{Tr}\left[S_1(i\omega_p+\mu,\mathbf{p})\Gamma_M S_1(i\omega_p+i\omega_q+\mu,\mathbf{p}+\mathbf{q})\Gamma_M\right], \tag{C.30}$$

can be simplified using the decomposition of the propagator S_1 with respect to the different Dirac components,

$$\begin{aligned}P(i\omega_p+\mu,\mathbf{p};i\omega_p+i\omega_q+\mu,\mathbf{p}+\mathbf{q}) =& 4N_cN_f\big[S_0(i\omega_p+\mu,\mathbf{p})S_0(i\omega_p+i\omega_q+\mu,\mathbf{p}+\mathbf{q})\\ &- S_3(i\omega_p+\mu,\mathbf{p})S_3(i\omega_p+i\omega_q+\mu,\mathbf{p}+\mathbf{q})\mathbf{p}(\mathbf{p}+\mathbf{q})\\ &\pm S_s(i\omega_p+\mu,\mathbf{p})S_s(i\omega_p+i\omega_q+\mu,\mathbf{p}+\mathbf{q})\big].\end{aligned} \tag{C.31}$$

The upper sign stands for the σ-channel, and the lower sign for the π^a-channels. By the choice of a coordinate system for $\mathbf{p}$ such that $\mathbf{q}$ points in p_z-direction, one can write the expression for Π_M in the form

$$\Pi_M(i\omega_q,\mathbf{q}) = -\frac{T}{(2\pi)^2}\sum_{i\omega_p}\int_0^{+\infty}\mathrm{d}|\mathbf{p}|\int_{-1}^{+1}\mathrm{d}(\cos\theta_p)\mathbf{p}^2P(i\omega_p+\mu,\mathbf{p};i\omega_p+i\omega_q+\mu,\mathbf{p}+\mathbf{q}), \tag{C.32}$$

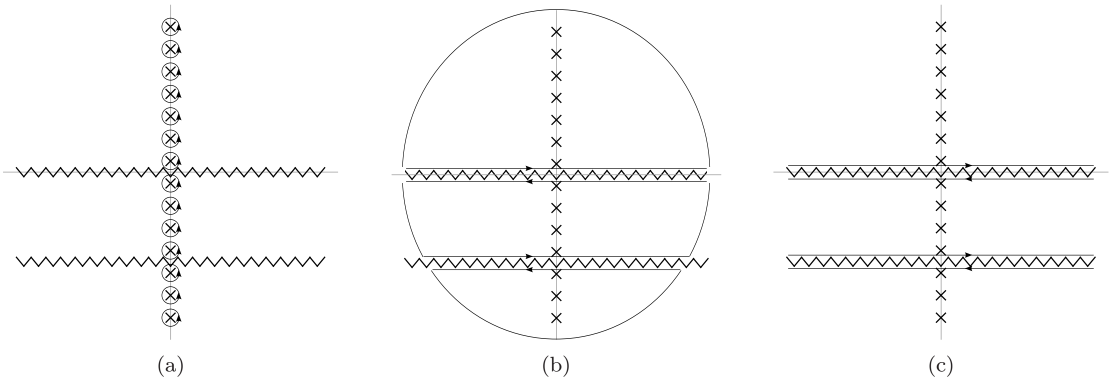

Figure C.3: Integration contours for the calculation of Π_M. The rewriting of the Matsubara sum leads to (a), which can be deformed into (b) by merging the circles that are not separated by branch cuts. Since the path elements at large $|z|$ do not contribute, one arrives finally at (c).

which is already the final result for Euclidean external momenta.

If we want to calculate the quantity for real external frequencies, the starting point is to express Eq. (C.29) as a contour integral,

$$\Pi_M(i\omega_q, \mathbf{q}) = \int \frac{\mathrm{d}^3p}{(2\pi)^3} \oint_C \frac{\mathrm{d}z}{2\pi i} n_F(z) P(z+\mu, \mathbf{p}; z+i\omega_q+\mu, \mathbf{p}+\mathbf{q}). \tag{C.33}$$

The contour C is a set of circles around the fermionic Matsubara frequencies, where n_F has first order poles. We analyze the integrand in the rest of the plane of complex z. The propagator S_1 appears twice in P for different arguments, there is a branch cut if the argument of one propagator is real. Hence, we find two branch cuts, one for real z, one for real $z+i\omega_q$. The situation, including the integration contour, is figured in Fig. C.3(a). We can deform the integration contour as it is shown in Figs. C.3(b) and C.3(c), which leads to a sum of four integrals,

$$\begin{aligned}\Pi_M(i\omega_q, \mathbf{q}) = \int \frac{\mathrm{d}^3p}{(2\pi)^3} \int_{-\infty}^{+\infty} \frac{\mathrm{d}p_0}{2\pi i} \Big\{ & + n_F(p_0+i\epsilon) P(p_0+\mu+i\epsilon, \mathbf{p}; p_0+i\omega_q+\mu+i\epsilon, \mathbf{p}+\mathbf{q}) \\ & - n_F(p_0-i\epsilon) P(p_0+\mu-i\epsilon, \mathbf{p}; p_0+i\omega_q+\mu-i\epsilon, \mathbf{p}+\mathbf{q}) \\ & + n_F(p_0-i\omega_q+i\epsilon) P(p_0+\mu-i\omega_q+i\epsilon, \mathbf{p}; p_0+\mu+i\epsilon, \mathbf{p}+\mathbf{q}) \\ & - n_F(p_0-i\omega_q-i\epsilon) P(p_0+\mu-i\omega_q-i\epsilon, \mathbf{p}; p_0+\mu-i\epsilon, \mathbf{p}+\mathbf{q}) \Big\}. \end{aligned} \tag{C.34}$$

We first eliminate all infinitesimal imaginary parts in the arguments when a finite imaginary part due to the Matsubara frequency $i\omega_q$ is present, and use the continuity of n_F on the real axis. With this simplification

$$\begin{aligned}\Pi_M(i\omega_q, \mathbf{q}) = \int \frac{\mathrm{d}^3p}{(2\pi)^3} \int_{-\infty}^{+\infty} \frac{\mathrm{d}p_0}{2\pi i} \Big\{ n_F(p_0) \big[& + P(p_0+\mu+i\epsilon, \mathbf{p}; p_0+i\omega_q+\mu, \mathbf{p}+\mathbf{q}) \\ & - P(p_0+\mu-i\epsilon, \mathbf{p}; p_0+i\omega_q+\mu, \mathbf{p}+\mathbf{q}) \\ & + P(p_0+\mu-i\omega_q, \mathbf{p}; p_0+\mu+i\epsilon, \mathbf{p}+\mathbf{q}) \\ & - P(p_0+\mu-i\omega_q, \mathbf{p}; p_0+\mu-i\epsilon, \mathbf{p}+\mathbf{q}) \big] \Big\}, \end{aligned} \tag{C.35}$$

we are ready to perform the analytical continuation to real external frequencies

$$i\omega_q \to q_0 + i\epsilon, \tag{C.36}$$

where we choose the positive sign to obtain the retarded polarization loop — the advanced loop is obtained by a minus sign. Thus, the retarded polarization loop $\mathit{\Pi}_M^R$ reads

$$\begin{aligned}\mathit{\Pi}_M(q_0,\mathbf{q}) = \int \frac{\mathrm{d}^3p}{(2\pi)^3}\int_{-\infty}^{+\infty}\frac{\mathrm{d}p_0}{2\pi i}\Big\{n_F(p_0-\mu)\big[&+ P(p_0+i\epsilon,\mathbf{p};p_0+q_0+i\epsilon,\mathbf{p}+\mathbf{q})\\ &- P(p_0-i\epsilon,\mathbf{p};p_0+q_0+i\epsilon,\mathbf{p}+\mathbf{q})\\ &+ P(p_0-q_0-i\epsilon,\mathbf{p};p_0+i\epsilon,\mathbf{p}+\mathbf{q})\\ &- P(p_0-q_0-i\epsilon,\mathbf{p};p_0-i\epsilon,\mathbf{p}+\mathbf{q})\big]\Big\}, \end{aligned}\tag{C.37}$$

where the integration variable p_0 was shifted in order to put the μ-dependency in the Fermi distribution function solely. A further simplification is obtained by reconsidering the exact form of P, which leads to

$$\begin{aligned}\mathit{\Pi}_M^R(q_0,\mathbf{q}) =& \int \frac{\mathrm{d}^3p}{(2\pi)^3}\int_{-\infty}^{+\infty}\frac{\mathrm{d}p_0}{2\pi i}\Big\{n_F(p_0-\mu)\times\\ &\times \mathrm{Tr}\big[\big(S_1(p_0+i\epsilon,\mathbf{p})-S_1(p_0-i\epsilon,\mathbf{p})\big)\mathit{\Gamma}_M S_1(p_0+q_0+i\epsilon,\mathbf{p}+\mathbf{q})\mathit{\Gamma}_M\\ &+ S_1(p_0-q_0-i\epsilon,\mathbf{p}\mathit{\Gamma}_M\big(S_1(p_0+i\epsilon,\mathbf{p}+\mathbf{q})-S_1(p_0-i\epsilon,\mathbf{p}+\mathbf{q})\big)\mathit{\Gamma}_M\big]\Big\}.\end{aligned}\tag{C.38}$$

The difference of retarded and advanced quark propagator is related to the spectral function ρ_1,

$$\begin{aligned}\mathit{\Pi}_M^R(q_0,\mathbf{q}) = -\int \frac{\mathrm{d}^3p}{(2\pi)^3}\int_{-\infty}^{+\infty}\frac{\mathrm{d}p_0}{2\pi}\Big\{&n_F(p_0-\mu)\mathrm{Tr}\big[\rho_1(p_0,\mathbf{p})\mathit{\Gamma}_M S_1(p_0+q_0+i\epsilon,\mathbf{p}+\mathbf{q})\mathit{\Gamma}_M\\ &+ S_1(p_0-q_0-i\epsilon,\mathbf{p})\mathit{\Gamma}_M\rho_1(p_0,\mathbf{p}+\mathbf{q})\mathit{\Gamma}_M\big]\Big\}.\end{aligned}\tag{C.39}$$

By the substitution in the 3-momentum integral

$$-\mathbf{p}' = \mathbf{p}+\mathbf{q}\tag{C.40}$$

for the second term, the rotation and the final reunion of both terms, one obtains

$$\begin{aligned}\mathit{\Pi}_M^R(q_0,\mathbf{q}) = -\int \frac{\mathrm{d}^3p}{(2\pi)^3}\int_{-\infty}^{+\infty}\frac{\mathrm{d}p_0}{2\pi}\Big\{&n_F(p_0-\mu)\mathrm{Tr}\Big[\rho_1(p_0,\mathbf{p})\times\\ &\times \mathit{\Gamma}_M\big[S_1(p_0+q_0+i\epsilon,\mathbf{p}+\mathbf{q})+S_1(p_0-q_0-i\epsilon,\mathbf{p}+\mathbf{q})\big]\mathit{\Gamma}_M\Big]\Big\}.\end{aligned}\tag{C.41}$$

This is the final expression for the retarded polarization loop $\mathit{\Pi}_M^R$, which contains a distribution function times a density of state as was found in the calculation of $\mathit{\Sigma}_H$. The evaluation of the trace is analog to Eq. (C.31),

$$\begin{aligned}&\mathrm{Tr}\Big[\rho_1(p_0,\mathbf{p})\mathit{\Gamma}_M\big[S_1(p_0+q_0+i\epsilon,\mathbf{p}+\mathbf{q})+S_1(p_0-q_0-i\epsilon,\mathbf{p}+\mathbf{q})\big]\mathit{\Gamma}_M\Big]\\ =&4N_cN_f\Big[\rho_0(p_0,\mathbf{p})\big[S_0(p_0+q_0+i\epsilon,\mathbf{p}+\mathbf{q})+S_0(p_0-q_0-i\epsilon,\mathbf{p}+\mathbf{q})\big]\\ &-\rho_3(p_0,\mathbf{p})\big[S_3(p_0+q_0+i\epsilon,\mathbf{p}+\mathbf{q})+S_3(p_0-q_0-i\epsilon,\mathbf{p}+\mathbf{q})\big](\mathbf{p}+\mathbf{q})\mathbf{p}\\ &\pm\rho_s(p_0,\mathbf{p})\big[S_s(p_0+q_0+i\epsilon,\mathbf{p}+\mathbf{q})+S_s(p_0-q_0-i\epsilon,\mathbf{p}+\mathbf{q})\big]\Big],\end{aligned}\tag{C.42}$$

where we used the same conventions for the sign as above.

C.4 Thermodynamic potential

C.4.1 Free part

The free part of thermodynamic potential per volume $\mathit{\Omega}_1$ reads

$$i\mathcal{T}r\ln iS_1^{-1} = -T\sum_{i\omega_k}\int\frac{\mathrm{d}^3k}{(2\pi)^3}\ln\det S_1^{-1}(i\omega_k+\mu,\mathbf{k}),\tag{C.43}$$

where the infinite constant that has to be subtracted was omitted. The determinant was already evaluated in the mean-field case, the Dirac components of the inverse propagator are similar. This consideration leads to

$$i\mathcal{T}r \ln iS_1^{-1} = -2N_cN_fT\sum_{i\omega_k}\int\frac{\mathrm{d}^3k}{(2\pi)^3}\ln\left[a_0^2 - a_3^2\mathbf{k}^2 - a_s^2\right]\Big|_{(i\omega_k+\mu,\mathbf{k})}, \tag{C.44}$$

where all $a_{0,3,s}$-functions depend on the common variables $(i\omega_k + \mu, \mathbf{k})$. This is already the final expression for the thermodynamic potential per volume in terms of the Matsubara propagator $S_1(\omega_k, \mathbf{k})$. In the following, it is shown how to rewrite the expression in terms of the retarded and advanced propagators $S_1(k_0 \pm i\epsilon, \mathbf{k})$.

We begin with the introduction of a contour C around the Fermi Matsubara frequencies and write the Matsubara sum as

$$i\mathcal{T}r \ln iS_1^{-1} = 2N_cN_f\int\frac{\mathrm{d}^3k}{(2\pi)^3}\oint_C\frac{\mathrm{d}z}{2\pi i}n_F(z)\ln\left[a_0^2 - a_3^2\mathbf{k}^2 - a_s^2\right]\Big|_{(z+\mu,\mathbf{k})}. \tag{C.45}$$

For further investigations, the structures of the integrand in the complex z-plane have to be identified. Beside the poles of $n_F(z)$ on the imaginary axis, the logarithm can have a branch cut when the imaginary part of the argument changes its sign. This is the case on the real axis, thus we find a situation that was already shown in Fig. C.2 in the context of the Hartree self-energy. The contour C shown in Fig. C.2(a) is deformed as it is shown in Fig. C.2(b) and C.2(c), and we arrive at

$$\begin{aligned} i\mathcal{T}r \ln iS_1^{-1} = 2N_cN_f\int\frac{\mathrm{d}^3k}{(2\pi)^3}\int_{-\infty}^{+\infty}\frac{\mathrm{d}k_0}{2\pi i}\Bigg\{ & n_F(k_0+i\epsilon)\ln\left[a_0^2 - a_3^2\mathbf{k}^2 - a_s^2\right]\Big|_{(k_0+\mu+i\epsilon,\mathbf{k})} \\ & - n_F(k_0+i\epsilon)\ln\left[a_0^2 - a_3^2\mathbf{k}^2 - a_s^2\right]\Big|_{(k_0+\mu-i\epsilon,\mathbf{k})}\Bigg\}. \end{aligned} \tag{C.46}$$

The imaginary part in the distribution function can be omitted, and the integration variable k_0 can be shifted by μ:

$$i\mathcal{T}r \ln iS_1^{-1} = 2N_cN_f\int\frac{\mathrm{d}^3k}{(2\pi)^3}\int_{-\infty}^{+\infty}\frac{\mathrm{d}k_0}{2\pi i}n_F(k_0-\mu)\ln\left\{\frac{\left[a_0^2 - a_3^2\mathbf{k}^2 - a_s^2\right]\big|_{(k_0+i\epsilon,\mathbf{k})}}{\left[a_0^2 - a_3^2\mathbf{k}^2 - a_s^2\right]\big|_{(k_0-i\epsilon,\mathbf{k})}}\right\}. \tag{C.47}$$

The separation in vacuum and medium part can be done with the splitting of the integration range,

$$\begin{aligned} i\mathcal{T}r \ln iS_1^{-1} = 2N_cN_f\int\frac{\mathrm{d}^3k}{(2\pi)^3}\int_{0}^{+\infty}\frac{\mathrm{d}k_0}{2\pi i}\Bigg\{ & [1-n_F(k_0+\mu)]\ln\left(\frac{\left[a_0^2 - a_3^2\mathbf{k}^2 - a_s^2\right]\big|_{(-k_0+i\epsilon,\mathbf{k})}}{\left[a_0^2 - a_3^2\mathbf{k}^2 - a_s^2\right]\big|_{(-k_0-i\epsilon,\mathbf{k})}}\right) \\ & + n_F(k_0-\mu)\ln\left(\frac{\left[a_0^2 - a_3^2\mathbf{k}^2 - a_s^2\right]\big|_{(k_0+i\epsilon,\mathbf{k})}}{\left[a_0^2 - a_3^2\mathbf{k}^2 - a_s^2\right]\big|_{(k_0-i\epsilon,\mathbf{k})}}\right)\Bigg\}. \end{aligned} \tag{C.48}$$

This formulation is in terms of real-momentum Green's functions, and the temperature-independent part and the medium contribution are clearly visible.

Special case of Hartree approximation

The specialization to the mean field case is done in order to check the result in Eq. (C.48). The arguments in the logarithm take the form

$$\left[a_0^2 - a_3^2\mathbf{k}^2 - a_s^2\right]\big|_{(k_0\pm i\epsilon,\mathbf{k})} = (k_0\pm i\epsilon)^2 - \mathbf{k}^2 - m_H^2 = (k_0\pm i\epsilon)^2 - E_k^2, \tag{C.49}$$

thus the logarithm-functions in the integrand can be written as

$$\ln\left(\frac{(k_0+i\epsilon)^2 - E_k^2}{(k_0-i\epsilon)^2 - E_k^2}\right) = 2i\arg\left[(k_0+i\epsilon)^2 - E_k^2\right] = 2i\pi\mathrm{sgn}(k_0)\theta(E_k^2 - k_0^2). \tag{C.50}$$

The same arguments as in Sec. B.5 can be used for the complex angles. We write the free part of the thermodynamic potential per volume as a k_0-integral over a finite range with help of the θ-function,

$$i\mathcal{T}r \ln iS_1^{-1} = 2N_cN_f \int \frac{\mathrm{d}^3k}{(2\pi)^3} \int_0^{E_k} \mathrm{d}k_0 \Big\{[1 - n_F(k_0+\mu)]\mathrm{sgn}(-k_0) + n_F(k_0-\mu)\mathrm{sgn}(k_0)\Big\}. \quad \text{(C.51)}$$

This is exactly the same form as it was derived in Eq. (B.63) in mean field approximation.

C.4.2 Self-energy term

The self-energy term of the thermodynamic potential per volume Ω_1 contains the dressed quark propagator S_1 and the self-energy Σ_1,

$$\mathcal{T}r(\Sigma_1 iS_1) = -T\sum_{i\omega_p}\int \frac{\mathrm{d}^3p}{(2\pi)^3}\mathrm{Tr}(\Sigma_1(i\omega_p+\mu,\mathbf{p})iS_1(i\omega_p+\mu,\mathbf{p})). \quad \text{(C.52)}$$

Both quantities depend on the 4-momentum p, thus we use the abbreviation

$$p = (i\omega_p + \mu, \mathbf{p}). \quad \text{(C.53)}$$

With the decomposition of the propagator and the self-energy in different components in Dirac space,

$$\mathcal{T}r(\Sigma_1 iS_1) = T\sum_{i\omega_p}\int \frac{\mathrm{d}^3p}{(2\pi)^3}\mathrm{Tr}\left[\left(S_0(p)\gamma^0 - S_3(p)\mathbf{p}\boldsymbol{\gamma} + S_s(p)\right)\left(\Sigma_0(p)\gamma^0 - \Sigma_3(p)\mathbf{p}\boldsymbol{\gamma} + \Sigma_s(p)\right)\right], \quad \text{(C.54)}$$

the trace can be evaluated and the intermediate result

$$\mathcal{T}r(\Sigma_1 iS_1) = -4N_cN_fT\sum_{i\omega_p}\int \frac{\mathrm{d}^3p}{(2\pi)^3}\left[S_0(p)\Sigma_0(p) - S_3(p)\Sigma_3(p)\mathbf{p}^2 + S_s(p)\Sigma_s(p)\right] \quad \text{(C.55)}$$

is obtained. For the evaluation in Euclidean space-time, this is the final expression where all further steps have to be done for explicit forms of S_1 and Ω_1. The numerical effort that is required comes from the summation of fermionic Matsubara frequencies and a 1-dimensional integral,

$$T\sum_{i\omega_p}\int\frac{\mathrm{d}^3p}{(2\pi)^3} \quad \rightarrow \quad \frac{4\pi}{(2\pi)^3}\int_0^\infty \mathrm{d}|\mathbf{p}|\,\mathbf{p}^2 T\sum_{i\omega_p}. \quad \text{(C.56)}$$

In this expression, the Matsubara propagator and the Matsubara self-energy are present. In the next lines, it will be shown that the contribution to Ω_1 can also be evaluated by use of the retarded and advanced expressions, which has certain advantages and disadvantages.
For this transformations, it is useful to introduce the quantity

$$P(p_0,\mathbf{p}) = \left[\Sigma_0 S_0 - \Sigma_3 S_3 \mathbf{p}^2 + \Sigma_s S_s\right]_{p=(p_0,\mathbf{p})}, \quad \text{(C.57)}$$

because all functions in the integrand of Eq. (C.55) depend on the same argument,

$$\mathcal{T}r(\Sigma_1 iS_1) = -4N_cN_fT\sum_{i\omega_p}\int\frac{\mathrm{d}^3p}{(2\pi)^3}P(i\omega_p+\mu,\mathbf{p}). \quad \text{(C.58)}$$

We write the Matsubara sum as a contour integral in the complex plane with the usual integration path,

$$\mathcal{T}r(\Sigma_1 iS_1) = 4N_cN_f\int\frac{\mathrm{d}^3p}{(2\pi)^3}\oint_C\frac{\mathrm{d}z}{2\pi i}n_F(z)P(z+\mu,\mathbf{p}). \quad \text{(C.59)}$$

We now analyze the structure of the integrand in the complex plane. Both S_1 and Σ_1 have a branch cut for real arguments, hence beside the poles of n_F on the imaginary z-axis, there is a branch cut on the real axis. A similar situation is shown in Fig. C.2, and we can perform the same contour deformation steps as in this figure. This leads to two integral paths along the real axis, as it is shown in Fig. C.2(c). We write

$$\mathcal{T}r(\Sigma_1 iS_1) = 4N_cN_f \int \frac{\mathrm{d}^3p}{(2\pi)^3} \int_{-\infty}^{+\infty} \frac{\mathrm{d}p_0}{2\pi i} \Big[+ n_F(p_0 + i\epsilon)P(p_0 + \mu + i\epsilon, \mathbf{p}) \\ - n_F(p_0 - i\epsilon)P(p_0 + \mu - i\epsilon, \mathbf{p})\Big], \tag{C.60}$$

and can use the fact that n_F is continuous for real arguments. This leads to

$$\mathcal{T}r(\Sigma_1 iS_1) = 4N_cN_f \int \frac{\mathrm{d}^3p}{(2\pi)^3} \int_{-\infty}^{+\infty} \frac{\mathrm{d}p_0}{2\pi i} n_F(p_0 - \mu)\Big[P(p_0 + i\epsilon, \mathbf{p}) - P(p_0 - i\epsilon, \mathbf{p})\Big], \tag{C.61}$$

where the integration variable p_0 was shifted by $-\mu$. The integral over all real values p_0 is now split into the positive and and the negative part, which can be written as

$$\mathcal{T}r(\Sigma_1 iS_1) = 4N_cN_f \int \frac{\mathrm{d}^3p}{(2\pi)^3} \int_0^{\infty} \frac{\mathrm{d}p_0}{2\pi i} \Bigg\{ n_F(p_0 - \mu)\Big[P(p_0 + i\epsilon, \mathbf{p}) - P(p_0 - i\epsilon, \mathbf{p})\Big] \\ + [1 - n_F(p_0 + \mu)]\Big[P(-p_0 + i\epsilon, \mathbf{p}) - P(-p_0 - i\epsilon, \mathbf{p})\Big]\Bigg\}. \tag{C.62}$$

The vacuum term and the medium contribution can be identified immediately from the last equation. Thus, we can write the self-energy contribution

$$\mathcal{T}r(\Sigma_1 iS_1) = 4N_cN_f \int \frac{\mathrm{d}^3p}{(2\pi)^3} \int_0^{\infty} \frac{\mathrm{d}p_0}{2\pi i} \Bigg\{ P^{vac} + P^q + P^{\bar{q}} \Bigg\}, \tag{C.63}$$

where the integrand P^{vac} is the vacuum contribution,

$$P^{vac} = \left[\Sigma_0^R S_0^R - \Sigma_0^A S_0^A - (\Sigma_3^R S_3^R - \Sigma_3^A S_3^A)\mathbf{p}^2 + \Sigma_s^R S_s^R - \Sigma_s^A S_s^A\right]_{p=(-p_0,\mathbf{p})}, \tag{C.64}$$

and the other two terms can be interpreted as contributions to the partial pressure from quarks

$$P^q = n_F(p_0 - \mu)\left[\Sigma_0^A S_0^A - \Sigma_0^R S_0^R - (\Sigma_3^A S_3^A - \Sigma_3^R S_3^R)\mathbf{p}^2 + \Sigma_s^A S_s^A - \Sigma_s^R S_s^R\right]_{p=(p_0,\mathbf{p})}, \tag{C.65}$$

and from antiquarks

$$P^{\bar{q}} = n_F(p_0 + \mu)\left[\Sigma_0^R S_0^R - \Sigma_0^A S_0^A - (\Sigma_3^R S_3^R - \Sigma_3^A S_3^A)\mathbf{p}^2 + \Sigma_s^R S_s^R - \Sigma_s^A S_s^A\right]_{p=(-p_0,\mathbf{p})}, \tag{C.66}$$

respectively.

C.4.3 Glasses diagram

The glasses-diagram with dressed propagators S_1 reads

$$\Omega_H = -\frac{1}{2}\sum_M 2g \left\{ -T \sum_{i\omega_p} \int \frac{\mathrm{d}^3p}{(2\pi)^3} \mathrm{Tr}[\Gamma_M iS_1(i\omega_p + \mu, \mathbf{p})] \right\}^2, \tag{C.67}$$

where the Hartree self-energy calculated in Sec. C.2 is appearing. In order to use the previous result for Σ_H, we rewrite the contribution to the thermodynamic potential per volume in terms of this self-energy,

$$\Omega_H = -\frac{\Sigma_H^2}{4g}, \tag{C.68}$$

which has the same form as the expression in mean field approximation, but the special propagator dressing is entering in the calculation of Σ_H, of course.

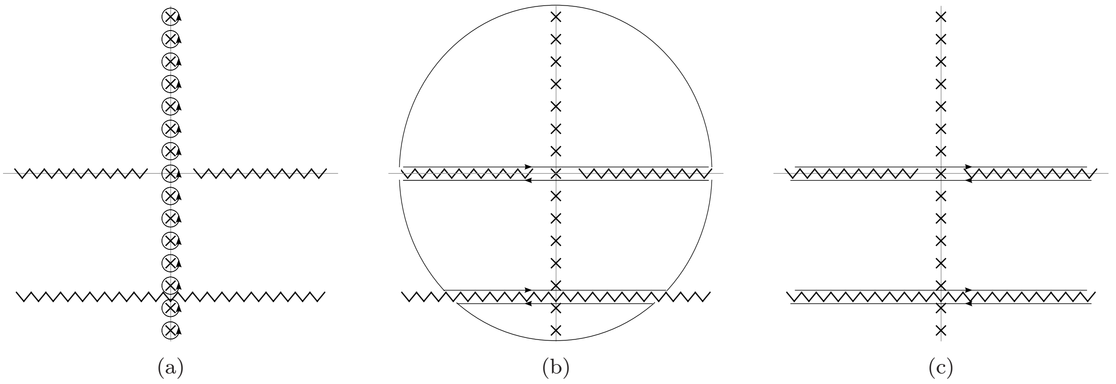
(a) (b) (c)

Figure C.4: Integration contours for the calculation of $\varSigma_M$, the next-to-leading order contribution to the quark self-energy. Eq. (C.69) was expressed in Eq. (C.70) as integral along the contour C shown in (a). Without crossing a branch cut, the contour is deformed as it is shown in (b) and (c), which leads to Eq. (C.71).

C.4.4 Ring sum

The last term in the thermodynamic potential per volume $\varOmega_1$ is the ring sum. It is the term that was already calculated in the perturbative expansion scheme, but here, the polarization loop with dressed quark propagators enter. The polarization loop was calculated in Sec. C.3, which can be put into the ring sum expression. Fortunately, we treated the ring sum contribution in the perturbative case in Sec. C.1 in the general case, so no assumptions were made concerning the dressing functions of the quarks before Eq. (C.17). Thus, we can use the same expressions as before, with the modified polarization loop $\varPi_M$.

C.5 Meson back-coupling self-energy

The next-to-leading order contribution to the quark self-energy has the form

$$\varSigma_M(i\omega_p, \mathbf{p}) = -T \sum_{i\omega_q} \int \frac{\mathrm{d}^3 q}{(2\pi)^3} D_M(i\omega_q, \mathbf{q}) \varGamma_M S_1(i\omega_q + i\omega_p + \mu, \mathbf{q}+\mathbf{p}) \varGamma_M, \tag{C.69}$$

where the sum over bosonic Matsubara frequencies can be written as a contour integral,

$$\varSigma_M(i\omega_p, \mathbf{p}) = -\int \frac{\mathrm{d}^3 q}{(2\pi)^3} \oint_C \frac{\mathrm{d}z}{2\pi i} n_B(z) D_M(z, \mathbf{q}) \varGamma_M S_1(z + i\omega_p + \mu, \mathbf{q}+\mathbf{p}) \varGamma_M. \tag{C.70}$$

The integrand has two branch cuts due to the propagators D_M and S_1, which both have cuts for real arguments. Thus, we find that the integrand in non-analytic for real z and for real $z + i\omega_p$. This situation is shown in Fig. C.4(a). We deform the contour as it is shown in Figs. C.4(b) and C.4(b), and obtain four integrals terms,

$$\begin{aligned}\varSigma_M(i\omega_p, \mathbf{p}) = -\int \frac{\mathrm{d}^3 q}{(2\pi)^3} \int_{-\infty}^{+\infty} \frac{\mathrm{d}q_0}{2\pi i} \Big\{ & n_B(q_0 + i\epsilon) D_M(q_0 + i\epsilon, \mathbf{q}) \times \\ & \times \varGamma_M S_1(q_0 + i\omega_p + \mu + i\epsilon, \mathbf{q}+\mathbf{p}) \varGamma_M \\ & - n_B(q_0 - i\epsilon) D_M(q_0 - i\epsilon, \mathbf{q}) \varGamma_M S_1(q_0 + i\omega_p + \mu - i\epsilon, \mathbf{q}+\mathbf{p}) \varGamma_M \\ & + n_B(q_0 - i\omega_p + i\epsilon) D_M(q_0 - i\omega_p + i\epsilon, \mathbf{q}) \varGamma_M S_1(q_0 + \mu + i\epsilon, \mathbf{q}+\mathbf{p}) \varGamma_M \\ & + n_B(q_0 - i\omega_p - i\epsilon) D_M(q_0 - i\omega_p - i\epsilon, \mathbf{q}) \varGamma_M S_1(q_0 + \mu - i\epsilon, \mathbf{q}+\mathbf{p}) \varGamma_M \Big\}. \end{aligned} \tag{C.71}$$

First, one can neglect all infinitesimal imaginary parts $i\epsilon$ if a finite fermionic Matsubara frequency $i\omega_p$ is added or subtracted. Furthermore, the Bose distribution functions n_B with different arguments can be simplified. We use the identity (B.6) in the third and fourth term and write

$$\begin{aligned}\mathit{\Sigma}_M(i\omega_p,\mathbf{p}) = -\int\frac{\mathrm{d}^3q}{(2\pi)^3}\int_{-\infty}^{+\infty}\frac{\mathrm{d}q_0}{2\pi i}\Big\{ &+ n_B(q_0)D_M(q_0+i\epsilon,\mathbf{q})\mathit{\Gamma}_M S_1(q_0+i\omega_p+\mu,\mathbf{q}+\mathbf{p})\mathit{\Gamma}_M \\ &- n_B(q_0)D_M(q_0-i\epsilon,\mathbf{q})\mathit{\Gamma}_M S_1(q_0+i\omega_p+\mu,\mathbf{q}+\mathbf{p})\mathit{\Gamma}_M \\ &- n_F(q_0)D_M(q_0-i\omega_p,\mathbf{q})\mathit{\Gamma}_M S_1(q_0+\mu+i\epsilon,\mathbf{q}+\mathbf{p})\mathit{\Gamma}_M \\ &+ n_F(q_0)D_M(q_0-i\omega_p,\mathbf{q})\mathit{\Gamma}_M S_1(q_0+\mu-i\epsilon,\mathbf{q}+\mathbf{p})\mathit{\Gamma}_M\Big\}.\end{aligned} \tag{C.72}$$

We can identify the spectral function of mesons ρ_M in the term proportional to n_B, and the spectral function of quarks in the term proportional to n_F,

$$\begin{aligned}\mathit{\Sigma}_M(i\omega_p,\mathbf{p}) = -\int\frac{\mathrm{d}^3q}{(2\pi)^3}\int_{-\infty}^{+\infty}\frac{\mathrm{d}q_0}{2\pi}\Big\{&2n_B(q_0)\rho_M(q_0,\mathbf{q})\mathit{\Gamma}_M S_1(q_0+i\omega_p+\mu,\mathbf{q}+\mathbf{p})\mathit{\Gamma}_M \\ &+ n_F(q_0)D_M(q_0-i\omega_p,\mathbf{q})\mathit{\Gamma}_M \rho_1(q_0+\mu,\mathbf{q}+\mathbf{p})\mathit{\Gamma}_M\Big\}.\end{aligned} \tag{C.73}$$

Now we can calculate the retarded self-energy $\mathit{\Sigma}_M^R$ by the prescription $i\omega_p \to p_0 + i\epsilon$. This analytical continuation yields

$$\begin{aligned}\mathit{\Sigma}_M(p_0+i\epsilon,\mathbf{p}) = -\int\frac{\mathrm{d}^3q}{(2\pi)^3}\int_{-\infty}^{+\infty}\frac{\mathrm{d}q_0}{\pi}\Big\{&n_B(q_0)\rho_M(q_0,\mathbf{q})\mathit{\Gamma}_M S_1(q_0+p_0+\mu+i\epsilon,\mathbf{q}+\mathbf{p})\mathit{\Gamma}_M \\ &+ \frac{1}{2}n_F(q_0)D_M(q_0-p_0-i\epsilon,\mathbf{q})\mathit{\Gamma}_M \rho_1(q_0+\mu,\mathbf{q}+\mathbf{p})\mathit{\Gamma}_M\Big\}.\end{aligned} \tag{C.74}$$

In order to prepare the separation in vacuum part and medium part, we shift the integration variable q_0 in the term proportional to n_F by μ, which yields a form more resembling the integrations before,

$$\begin{aligned}\mathit{\Sigma}_M(p_0+i\epsilon,\mathbf{p}) = &-\int\frac{\mathrm{d}^3q}{(2\pi)^3}\int_{-\infty}^{+\infty}\frac{\mathrm{d}q_0}{\pi}\Big\{n_B(q_0)\rho_M(q_0,\mathbf{q})\mathit{\Gamma}_M S_1(q_0+p_0+\mu+i\epsilon,\mathbf{q}+\mathbf{p})\mathit{\Gamma}_M \\ &+ \frac{1}{2}n_F(q_0-\mu)D_M(q_0-p_0-\mu-i\epsilon,\mathbf{q})\mathit{\Gamma}_M \rho_1(q_0,\mathbf{q}+\mathbf{p})\mathit{\Gamma}_M\Big\}.\end{aligned} \tag{C.75}$$

In this expressions, we split the integral over q_0 into two parts, according to the sign of q_0. The resulting equation

$$\begin{aligned}\mathit{\Sigma}_M(p_0+i\epsilon,\mathbf{p}) = &-\int\frac{\mathrm{d}^3q}{(2\pi)^3}\int_{0}^{+\infty}\frac{\mathrm{d}q_0}{\pi}\Big\{n_B(q_0)\rho_M(q_0,\mathbf{q})\mathit{\Gamma}_M S_1(q_0+p_0+\mu+i\epsilon,\mathbf{q}+\mathbf{p})\mathit{\Gamma}_M \\ &+ n_B(-q_0)\rho_M(-q_0,\mathbf{q})\mathit{\Gamma}_M S_1(-q_0+p_0+\mu+i\epsilon,\mathbf{q}+\mathbf{p})\mathit{\Gamma}_M \\ &+ \frac{1}{2}n_F(q_0-\mu)D_M(q_0-p_0-\mu-i\epsilon,\mathbf{q})\mathit{\Gamma}_M \rho_1(q_0,\mathbf{q}+\mathbf{p})\mathit{\Gamma}_M \\ &+ \frac{1}{2}n_F(-q_0-\mu)D_M(-q_0-p_0-\mu-i\epsilon,\mathbf{q})\mathit{\Gamma}_M \rho_1(-q_0,\mathbf{q}+\mathbf{p})\mathit{\Gamma}_M\Big\},\end{aligned} \tag{C.76}$$

with the relations (B.4), can be written in such a way that the separation is clear,

$$\begin{aligned}\mathit{\Sigma}_M(p_0+i\epsilon,\mathbf{p}) = &-\int\frac{\mathrm{d}^3q}{(2\pi)^3}\int_{0}^{+\infty}\frac{\mathrm{d}q_0}{\pi}\Big\{n_B(q_0)\rho_M(q_0,\mathbf{q})\mathit{\Gamma}_M S_1(q_0+p_0+\mu+i\epsilon,\mathbf{q}+\mathbf{p})\mathit{\Gamma}_M \\ &- [1+n_B(q_0)]\rho_M(-q_0,\mathbf{q})\mathit{\Gamma}_M S_1(-q_0+p_0+\mu+i\epsilon,\mathbf{q}+\mathbf{p})\mathit{\Gamma}_M \\ &+ \frac{1}{2}n_F(q_0-\mu)D_M(q_0-p_0-\mu-i\epsilon,\mathbf{q})\mathit{\Gamma}_M \rho_1(q_0,\mathbf{q}+\mathbf{p})\mathit{\Gamma}_M \\ &+ \frac{1}{2}[1-n_F(q_0\mu)]D_M(-q_0-p_0-\mu-i\epsilon,\mathbf{q})\mathit{\Gamma}_M \rho_1(-q_0,\mathbf{q}+\mathbf{p})\mathit{\Gamma}_M\Big\}.\end{aligned} \tag{C.77}$$

Thus, we find the vacuum term

$$\varSigma_M^R\Big|_{vac} = -\int \frac{\mathrm{d}^3 q}{(2\pi)^3} \int_0^\infty \frac{\mathrm{d}q_0}{\pi} \Bigg\{ \rho_M(q_0, \mathbf{q}) \varGamma_M S_1^R(-q_0 + p_0 + \mu, \mathbf{p} + \mathbf{q}) \varGamma_M \\ \frac{1}{2} D_M^A(-q_0 - p_0 - \mu, \mathbf{q}) \varGamma_M \rho_1(-q_0) \varGamma_M \Bigg\}, \tag{C.78}$$

and the medium term

$$\varSigma_M^R\Big|_{med} = -\int \frac{\mathrm{d}^3 q}{(2\pi)^3} \int_0^\infty \frac{\mathrm{d}q_0}{\pi} \Bigg\{ + \frac{1}{2} n_F(q_0 + \mu) D_M^A(-q_0 - p_0 - \mu) \varGamma_M \rho_1(-q_0) \varGamma_M \\ + \frac{1}{2} n_F(q_0 - \mu) D_M^A(q_0 - p_0 - \mu) \varGamma_M \rho_1(q_0) \varGamma_M \\ + n_B(q_0) \rho_M(q_0, \mathbf{q}) \varGamma_M \left(S_1^R(-q_0 + p_0 + \mu, \mathbf{p} + \mathbf{q}) - S_1^R(q_0 + p_0 + \mu, \mathbf{p} + \mathbf{q}) \right) \varGamma_M \Bigg\}. \tag{C.79}$$

In summary, one can say that the formulation for the retarded self-energy in Eqs. (C.78) and (C.79) makes use of the retarded and advanced meson and quark propagators. The regularization can be applied solely to the 4-momentum integral in Eq. (C.78), since the medium part is finite.

Appendix D

Evaluation of transport integrals

D.1 Evaluation of the Green-Kubo formula

The diagram that appears in the evaluation of transport properties is shown in Fig. 3.1, which can be expressed as

$$\mathit{\Pi}(i\omega_e) = -T\sum_{i\omega_k}\int\frac{\mathrm{d}^3k}{(2\pi)^3}\mathrm{Tr}\left[\mathit{\Gamma}(i\omega_e+i\omega_k+\mu,\mathbf{k};i\omega_k+\mu,\mathbf{k})S(i\omega_k+\mu,\mathbf{k})\gamma S(i\omega_e+i\omega_k+\mu,\mathbf{k})\right] \tag{D.1}$$

for fermions with a dressed propagator S, a dressed vertex $\mathit{\Gamma}$, and a bare vertex γ. We concentrate on the static shear viscosity η in the NJL model

$$\lim_{p_0\to 0}\eta(p_0) = -\lim_{p_0\to 0}\lim_{\mathbf{p}\to 0}\frac{1}{\omega}\mathrm{Im}\mathit{\Pi}^R(p_0,\mathbf{p}), \tag{D.2}$$

where the bare vertex $p^i\gamma^j$ can be chosen in one special direction because of isotropy, for example

$$\mathit{\Pi}(i\omega_e) = -T\sum_{i\omega_k}\int\frac{\mathrm{d}^3k}{(2\pi)^3}\mathrm{Tr}\left[\mathit{\Gamma}^{xy}_{full}(i\omega_e+i\omega_k+\mu;i\omega_k+\mu,)S(i\omega_k+\mu)p_x\gamma^2 S(i\omega_e+i\omega_k+\mu)\right]. \tag{D.3}$$

We omit the 3-momentum arguments because they are all equal to $\mathbf{k}$. In order to derive the retarded expression that is needed in the Kubo formula for shear viscosity, we first rewrite the Matsubara sum as a contour integral,

$$\mathit{\Pi}(i\omega_e) = \int\frac{\mathrm{d}^3k}{(2\pi)^3}\oint_C\frac{\mathrm{d}z}{2\pi i}n_F(z)\mathrm{Tr}\left[\mathit{\Gamma}^{xy}_{full}(i\omega_e+z+\mu;z+\mu,)S(z+\mu)p_x\gamma^2 S(i\omega_e+z+\mu)\right]. \tag{D.4}$$

If we assume that the fully dressed vertex has poles and branch cuts only at places where the dressed propagator S has branch cuts, too, we encounter a situation similar to the one in the calculation of the meson propagator. We perform the same contour deformations as they are shown in Fig. C.3 and apply the same simplifications as Sec. C.3, and obtain

$$\begin{aligned}\mathit{\Pi}(i\omega_e) = \int\frac{\mathrm{d}^3k}{(2\pi)^3}\int_{-\infty}^{+\infty}\frac{\mathrm{d}k_0}{2\pi i}n_F(k_0-\mu)\times&\\ \times\Big\{\mathrm{Tr}\left[\mathit{\Gamma}^{xy}_{full}(i\omega_e+k_0;k_0+i\epsilon)S(k_0+i\epsilon)p_x\gamma^2 S(i\omega_e+k_0)\right]&\\ -\mathrm{Tr}\left[\mathit{\Gamma}^{xy}_{full}(i\omega_e+k_0;k_0-i\epsilon)S(k_0-i\epsilon)p_x\gamma^2 S(i\omega_e+k_0)\right]&\\ +\mathrm{Tr}\left[\mathit{\Gamma}^{xy}_{full}(k_0+i\epsilon;k_0-i\omega_e)S(k_0-i\omega_e)p_x\gamma^2 S(k_0+i\epsilon)\right]&\\ -\mathrm{Tr}\left[\mathit{\Gamma}^{xy}_{full}(k_0-i\epsilon;k_0-i\omega_e)S(k_0-i\omega_e)p_x\gamma^2 S(k_0-i\epsilon)\right]\Big\}.&\end{aligned} \tag{D.5}$$

The retarded function $\mathit{\Pi}$ is obtained by the analytical continuation $i\omega_e \to p_0 + i\epsilon$,

$$\begin{aligned}\mathit{\Pi}(p_0+i\epsilon) = \int \frac{\mathrm{d}^3k}{(2\pi)^3}\int_{-\infty}^{+\infty}\frac{\mathrm{d}k_0}{2\pi i} n_F(k_0-\mu)\times \\ \times\Big\{\mathrm{Tr}\left[\mathit{\Gamma}^{xy}_{full}(p_0+k_0+i\epsilon;k_0+i\epsilon)S(k_0+i\epsilon)p_x\gamma^2 S(p_0+k_0+i\epsilon)\right] \\ -\mathrm{Tr}\left[\mathit{\Gamma}^{xy}_{full}(p_0+k_0+i\epsilon;k_0-i\epsilon)S(k_0-i\epsilon)p_x\gamma^2 S(p_0+k_0+i\epsilon)\right] \\ +\mathrm{Tr}\left[\mathit{\Gamma}^{xy}_{full}(k_0+i\epsilon;k_0-p_0-i\epsilon)S(k_0-p_0-i\epsilon)p_x\gamma^2 S(k_0+i\epsilon)\right] \\ -\mathrm{Tr}\left[\mathit{\Gamma}^{xy}_{full}(k_0-i\epsilon;k_0-p_0-i\epsilon)S(k_0-p_0-i\epsilon)p_x\gamma^2 S(k_0-i\epsilon)\right]\Big\}. \quad \text{(D.6)}\end{aligned}$$

For further simplifications, more assumptions about the symmetries of the fully dressed vertex such as

$$\mathit{\Gamma}^{xy}_{full}(p_0^1,p_0^2) \leftrightarrow \mathit{\Gamma}^{xy}_{full}(p_0^2,p_0^1)\,, \qquad \mathit{\Gamma}^{xy}_{full}(p_0^1\pm i\epsilon,p_0^2) \leftrightarrow \mathit{\Gamma}^{xy}_{full}(p_0^1\mp i\epsilon,p_0^2)\,, \qquad \ldots \quad \text{(D.7)}$$

have to be taken into account. We stop the most general derivation here and specialize in a certain class of vertices. We chose real vertices $\mathit{\Gamma}^{xy}$ which do not depend on the 0-component of the argument, like it is the case for the bare vertex. For this choice, we can write

$$\begin{aligned}\mathit{\Pi}^R(p_0) = -\int \frac{\mathrm{d}^3k}{(2\pi)^3}\int_{-\infty}^{+\infty}\frac{\mathrm{d}k_0}{2\pi} n_F(k_0-\mu)\Big\{\mathrm{Tr}\left[\mathit{\Gamma}^{xy}\rho(k_0)p_x\gamma^2 S(p_0+k_0+i\epsilon)\right] \\ +\mathrm{Tr}\left[\mathit{\Gamma}^{xy}S(k_0-p_0-i\epsilon)p_x\gamma^2\rho(k_0)\right]\Big\}, \quad \text{(D.8)}\end{aligned}$$

where ρ is the fermion spectral function. We shift the integration variable k_0 and obtain

$$\begin{aligned}\mathit{\Pi}^R(p_0) = -\int \frac{\mathrm{d}^3k}{(2\pi)^3}\int_{-\infty}^{+\infty}\frac{\mathrm{d}k_0}{2\pi}\Big\{n_F(k_0-\mu)\mathrm{Tr}\left[\mathit{\Gamma}^{xy}\rho(k_0)p_x\gamma^2 S^R(p_0+k_0)\right] \\ +n_F(k_0+q_0-\mu)\mathrm{Tr}\left[\mathit{\Gamma}^{xy}\rho(k_0)p_x\gamma^2 S^A(p_0+k_0)\right]\Big\}, \quad \text{(D.9)}\end{aligned}$$

where we wrote the expression in terms of retarded and advanced propagators. If one takes the imaginary part of Eq. (D.9), the term with the retarded propagator has the inverse sign of the term with the advanced one, thus

$$\mathrm{Im}\mathit{\Pi}^R(p_0) = \frac{1}{2}\int \frac{\mathrm{d}^3k}{(2\pi)^3}\int_{-\infty}^{+\infty}\frac{\mathrm{d}k_0}{2\pi}\left[n_F(k_0+q_0-\mu)-n_F(k_0-\mu)\right]\mathrm{Tr}\left[\mathit{\Gamma}^{xy}\rho(k_0)p_x\gamma^2\rho(p_0+k_0)\right]. \quad \text{(D.10)}$$

This expression enters in the Green-Kubo formula for the static shear viscosity,

$$\eta = -\lim_{p_0\to 0+i\epsilon}\frac{\mathrm{d}}{\mathrm{d}p_0}\mathrm{Im}\mathit{\Pi}^R(p_0). \quad \text{(D.11)}$$

If we take $\mathit{\Gamma}^{xy} = p_x\gamma^2$ and $\mu = 0$, we obtain

$$\eta = -\lim_{p_0\to 0}\frac{\mathrm{d}}{\mathrm{d}q_0}\int \frac{\mathrm{d}^3k}{(2\pi)^3}\frac{1}{2}\int_{-\infty}^{+\infty}\frac{\mathrm{d}k_0}{2\pi}\left[n_F(k_0+p_0)-n_F(k_0)\right]\mathrm{Tr}\left[\rho(k_0+p_0)k_x\gamma^2\rho(k_0)k_x\gamma^2\right], \quad \text{(D.12)}$$

and the derivative with respect to p_0 yields

$$\eta = -\lim_{p_0\to 0}\frac{\mathrm{d}}{\mathrm{d}q_0}\int \frac{\mathrm{d}^3k}{(2\pi)^3}\frac{1}{2}\int_{-\infty}^{+\infty}\frac{\mathrm{d}k_0}{2\pi}n_F'(k_0)\mathrm{Tr}\left[\rho(k_0+p_0)k_x\gamma^2\rho(k_0)k_x\gamma^2\right], \quad \text{(D.13)}$$

where the primed Bose distribution function denotes its derivative with respect to the argument k_0. Now, we evaluate the trace, which results in

$$\eta = -2N_cN_f\int \frac{\mathrm{d}^3k}{(2\pi)^3}\int_{-\infty}^{+\infty}\frac{\mathrm{d}k_0}{2\pi}n_F'(k_0)k_x^2\left[\rho_0^2-\rho_3^2(\mathbf{k}^2-2k_y^2)-\rho_s^2\right], \quad \text{(D.14)}$$

which is a 4-dimensional integral over the different components of the fermion spectral function ρ. The angular integrations can be done analytically,

$$\eta = -2N_cN_f \int_0^\infty \mathrm{d}|\mathbf{k}| \int_{-\infty}^{+\infty} \frac{\mathrm{d}k_0}{2\pi} n'_F(k_0)\mathbf{k}^4 \left\{ \frac{4\pi}{3(2\pi)^3} \left[\rho_0^2 - \rho_3^2\mathbf{k}^2 - \rho_s^2\right] + \frac{8\pi}{15(2\pi)^3}\rho_3^2\mathbf{k}^2 \right\}, \quad \text{(D.15)}$$

thus we end up with a 2-dimensional integral for the static shear viscosity at $\mu = 0$ when the vertex is truncated to the bare one.

D.2 Practical calculation of transport coefficients in kinetic theory

D.2.1 Analytical simplification

The Sonine expansion coefficients b_b^s or a multicomponent quantum gas in second order Chapman-Enskog approximations are determined by the linear equation

$$A_{ab}^{rs} b_b^s = C_a^r. \quad \text{(D.16)}$$

For N_p particles and a Sonine expansion up to order N_s, this tensor equation correspond to a system of $N_p \times N_s$ coupled linear equations. The coefficient C_a^r can be written in a short way;

$$C_a^r = -g_a \int \frac{\mathrm{d}^3p}{(2\pi)^3} \frac{1}{E_pT} f_a^{(0)}(1 + \theta_a f_a^{(0)}) P_a^r(|\mathbf{p}|) \left(\hat{p}^i\hat{p}^j - \frac{1}{3}\delta^{ij}\right) p^ip^j \quad \text{(D.17)}$$

This equation can be simplified by performing the sum over i and j, and by using the symmetries of the integrand. The final form reads

$$C_a^r = -\frac{8\pi g_a}{3(2\pi)^3T} \int \mathrm{d}p \frac{p^4}{E_p} f_a^{(0)}(1 + \theta_a f_a^{(0)}) P_a^r(|\mathbf{p}|). \quad \text{(D.18)}$$

With our choice for the integral measure in the Sonine orthogonality relation (3.74), the coefficients C_a^r have the property

$$r > 0 \Rightarrow C_a^r = 0 \quad \text{(D.19)}$$

The formula for A_{ab}^{rs} is quite extensive. The tensor A_{ab}^{rs} has the components

$$A_{ab}^{rs} = A_{ab}^{rs[1]} + \delta_{ab} \sum_b A_{aa}^{rs[b]} \quad \text{(D.20)}$$

where

$$\begin{aligned} A_{ab}^{rs[1]} \quad = \quad & \int \frac{\mathrm{d}^3p}{(2\pi)^3} \frac{\mathrm{d}^3p_1}{(2\pi)^3} \frac{\mathrm{d}^3p'}{(2\pi)^3} \frac{\mathrm{d}^3p'_1}{(2\pi)^3} \Bigg\{ \frac{(2\pi)^4\delta^4(p + p_1 - p' - p'_1)}{16EE_1E'E'_1} |\mathcal{M}_{ab}|^2 \times \\ & \times f_a^{(0)} f_{1b}^{(0)} (1 + \theta_a f_a^{(0)\prime})(1 + \theta_b f_{1b}^{(0)\prime}) P_a^r(|\mathbf{p}|) \left(\hat{p}^i\hat{p}^j - \frac{1}{3}\delta^{ij}\right) \times \\ & \times \left[P_b^s(|\mathbf{p}'_1|) \left(\hat{p}_1'^i\hat{p}_1'^j - \frac{1}{3}\delta^{ij}\right) - P_b^s(|\mathbf{p}_1|) \left(\hat{p}_1^i\hat{p}_1^j - \frac{1}{3}\delta^{ij}\right) \right] \Bigg\}, \end{aligned} \quad \text{(D.21)}$$

and

$$\begin{aligned} A_{aa}^{rs[b]} \quad = \quad & \int \frac{\mathrm{d}^3p}{(2\pi)^3} \frac{\mathrm{d}^3p_1}{(2\pi)^3} \frac{\mathrm{d}^3p'}{(2\pi)^3} \frac{\mathrm{d}^3p'_1}{(2\pi)^3} \Bigg\{ \frac{(2\pi)^4\delta^4(p + p_1 - p' - p'_1)}{16EE_1E'E'_1} |\mathcal{M}_{ab}|^2 \times \\ & \times f_a^{(0)} f_{1b}^{(0)} (1 + \theta_a f_a^{(0)\prime})(1 + \theta_b f_{1b}^{(0)\prime}) P_a^r(|\mathbf{p}|) \left(\hat{p}^i\hat{p}^j - \frac{1}{3}\delta^{ij}\right) \times \\ & \times \left[P_a^s(|\mathbf{p}'|) \left(\hat{p}'^i\hat{p}'^j - \frac{1}{3}\delta^{ij}\right) - P_a^s(|\mathbf{p}|) \left(\hat{p}^i\hat{p}^j - \frac{1}{3}\delta^{ij}\right) \right] \Bigg\}. \end{aligned} \quad \text{(D.22)}$$

The coefficients C_a^r can be identified as one dimensional integrals and are easily solved in a numerical way. However, the treatment of the 12 dimensional integral in A_{ab}^{rs} is more involved and is discussed in the following lines.
First, the δ-function from energy-momentum conservation eliminates four integrations. We choose to eliminate the $\mathbf{p}_1'$-integration by setting

$$\mathbf{p}_1' = \mathbf{p} + \mathbf{p}_1 - \mathbf{p}'. \tag{D.23}$$

With the fourth Dirac function, we can perform the integration of $|\mathbf{p}'|$ analytically. Because the number of zeros of $|\mathbf{p}| + |\mathbf{p}_1| - |\mathbf{p}'| - |\mathbf{p} + \mathbf{p}_1 - \mathbf{p}'|$ varies, one has to check all possible solutions of the equation. They read

$$|\mathbf{p}'| = \frac{Y \pm \sqrt{Y P^2 \cos^2\beta - 4\left(1 - \frac{P^2\cos^2\beta}{(E+E_1)^2}\right)\left(m^2 - \frac{((E+E_1)^2 - P^2 + m^2 - m_1^2)^2}{4(E+E_1)^2}\right)}}{2\left(1 - \frac{P^2\cos^2\beta}{(E+E_1)^2}\right)} \tag{D.24}$$

with

$$\begin{aligned} Y &= \left(1 - \frac{P^2 - m^2 + m_1^2}{(E+E_1)^2}\right) && \text{(D.25)}\\ P &= \mathbf{p} + \mathbf{p}_1 && \text{(D.26)}\\ \cos\beta &= \sphericalangle(P, p') \\ &= \frac{|\mathbf{p}|\cos\vartheta' + |\mathbf{p}_1|\left[\sin\vartheta_1 \sin\vartheta' \cos\varphi' + \cos\vartheta_1 \cos\vartheta'\right]}{\sqrt{|\mathbf{p}|^2 + |\mathbf{p}_1|^2 + 2|\mathbf{p}||\mathbf{p}_1|\cos\vartheta_1}}. && \text{(D.27)} \end{aligned}$$

The remaining eight integrals can be reduced by a appropriate choice of the coordinate systems. We choose the z-axis of the coordinate systems of p_1, p' and p_1' to be parallel to $\mathbf{p}$. With this choice, the angular integration $\mathrm{d}\Omega$ becomes trivial and leads to a factor of 4π. A shift in the integration variables φ' and φ_1' by φ_1 lead to the elimination of the φ_1 dependency.
So, seven integrals could be solved analytically:

$$\int \frac{\mathrm{d}^3p}{(2\pi)^3}\frac{\mathrm{d}^3p_1}{(2\pi)^3}\frac{\mathrm{d}^3p'}{(2\pi)^3}\frac{\mathrm{d}^3p_1'}{(2\pi)^3}(2\pi)^4\delta^4(p + p_1 - p' - p_1') \to \frac{8\pi^2}{(2\pi)^8}\int \mathrm{d}p\mathrm{d}p_1\mathrm{d}\Omega'\mathrm{d}\vartheta_1 \sum_{p_1'} \tag{D.28}$$

A set of 5-dimensional integrals remains which have to be solved in a numerical way.

D.2.2 Numerical evaluation of the collision integral

The collision integrals that have to be calculated in a numerical way for the determination of A_{ab}^{rs} are 5-dimensional, two 3-momentum integrals and three angular integrals are remaining. The integrand is lengthy, but does not contain singularities. Moreover, the main contributions come from a compact subset of the integration range since the distribution functions damp the integrand exponentially for large 3-momenta.
We used a Vegas-like algorithm [219], which is a type of Monte Carlo integration method especially common in particle physics. The integration range

$$(p, p_1, \theta', \varphi', \theta_1) \in [0, \infty[\times [0, \infty[\times [0, \pi] \times [0, 2\pi] \times [0, \pi] \tag{D.29}$$

has to be mapped a 5-dimensional unit hypercube. We first introduce an additional transformation of the momentum variables,

$$p = q\cos\psi \qquad\qquad p_1 = q\sin\psi, \tag{D.30}$$

such that $q \in [0, \infty[$ and $\psi \in [0, \pi/2]$. As the integrand is decreasing exponentially for large q and well-behaved close to zero, we introduce for simplicity a cutoff Λ_{UV} for large momenta, and a cut-off Λ_{IR} for low momenta. This yields in summary

$$\int_0^\infty \mathrm{d}p \int_0^\infty \mathrm{d}p_1 f(p, p_1) \to \int_{\Lambda_{IR}}^{\Lambda_{UV}} \mathrm{d}q \int_0^{\pi/2} \mathrm{d}\psi\, q f(q, \psi), \tag{D.31}$$

where we can improve the integration by choosing a logarithmic scaling of q. With these tricks, it is found that a accuracy of 0.1–1 % is reached with a reasonable number of evaluations of the integrand. This is possible because all systems where we applied the Chapman-Enskog expansion to calculate transport coefficients had scattering amplitudes $\mathcal{M}_{ab}$ that were known analytically, thus no additional time-consuming numerical method has to be applied at each invocation of the integrand.

Appendix E

Propagator parametrizations

E.1 Polarization loop with Breit-Wigner type propagator

The polarization loop for a Breit-Wigner type propagator will be analyzed in this section. We write the parametrized fermion propagator S in the form

$$S_F^R(p) = \frac{\not{p} + \not{m}_p^R}{p^2 - \not{m}_p^{R2}}, \tag{E.1}$$

where $\not{m}_p$ takes the form that is discussed in Eqs. (4.30), (4.31), and (4.32).
The first idea is to decompose the quark loop

$$\Pi_M(q) = T \sum_{i\omega_k} \int \frac{\mathrm{d}^3 k}{(2\pi)^3} \mathrm{Tr} \frac{\Gamma_M [\not{q} + \not{k} + \not{m}_{qk}] \Gamma_M [\not{k} + \not{m}_k]}{[(q+k)^2 - \not{m}_{qk}^2][k^2 - \not{m}_k^2]} \tag{E.2}$$

in the same way as in the Hartree approximation, where one can identify the elementary integrals iI_1 and iI. After the evaluation of the trace for Γ_σ (upper sign) and Γ_{π^a} (lower sign),

$$\mathrm{Tr}[\not{q} + \not{k} + \not{m}_{qk}][\not{k} - \not{m}_k] = 4 N_c N_f \left(k^2 + kq \pm \not{m}_{qk} \not{m}_k \right), \tag{E.3}$$

one can bring the function Π_M to the form

$$\Pi_M(q) = 4 N_c N_f T \sum_{i\omega_k} \int \frac{\mathrm{d}^3 k}{(2\pi)^3} \frac{1}{[k^2 - \not{m}_k^2]} - 2 N_c N_f T \sum_{i\omega_k} \int \frac{\mathrm{d}^3 k}{(2\pi)^3} \frac{q^2 - (\not{m}_{qk} \pm \not{m}_k)^2}{[(q+k)^2 - \not{m}_{qk}^2][k^2 - \not{m}_k^2]}. \tag{E.4}$$

This formula resembles strongly the expression of Π_M for Hartree quark propagators, the main difference is the fact that in mean field approximation, the nominator of the second integral is constant and can be separated from the integration. This second part is the origin of the imaginary part of the polarization loop and the meson propagator, so we concentrate on this part.
We call the second integral in Eq. (E.4)

$$i\mathcal{I}(i\omega_q, \mathbf{q}) = T \sum_{i\omega_k} \int \frac{\mathrm{d}^3 k}{(2\pi)^3} \frac{q^2 - (\not{m}_{qk} \pm \not{m}_k)^2}{[(i\omega_k + i\omega_q + \mu)^2 - \mathcal{E}_{qk}^2][(i\omega_k + \mu)^2 - \mathcal{E}_k^2]}, \tag{E.5}$$

where

$$\mathcal{E}_p^2 = \not{m}_p^2 + \mathbf{p}^2 \tag{E.6}$$

is a complex generalization of the energy. The aim is to calculate an expression for the retarded function $i\mathcal{I}$. We first write this form as a contour integral in the complex plane in the same way as in the general calculation of Π_M in Sec. C.3,

$$i\mathcal{I}(i\omega_q, \mathbf{q}) = -\int \frac{\mathrm{d}^3 k}{(2\pi)^3} \oint_C \frac{\mathrm{d}z}{2\pi i} n_F(z) \frac{q^2 - (\not{m}_{qk} \pm \not{m}_k)^2}{[(z + i\omega_q + \mu)^2 - \mathcal{E}_{qk}^2][(z+\mu)^2 - \mathcal{E}_k^2]}. \tag{E.7}$$

The structure in the complex plane should be the same as from the full function $\varPi_M$, but there are severe differences. The Lehmann-representation of the self-energy

$$\varSigma(z, \mathbf{k}) = \int_{-\infty}^{+\infty} \frac{\mathrm{d}\omega}{2\pi} i \frac{\varSigma^R(\omega, \mathbf{k}) - \varSigma^A(\omega, \mathbf{k})}{\omega - z} \tag{E.8}$$

for an arbitrary $z \in \mathbb{C}$ causes problems, since the self-energy in the given parametrization is

$$\varSigma(k_0 \pm i\epsilon, \mathbf{k}) = M \mp i\mathrm{sgn}(k_0)\varGamma_{\mathbf{k}}, \tag{E.9}$$

and hence the dispersion integral for the self-energy

$$\varSigma(z, \mathbf{k}) = \int_{-\infty}^{+\infty} \frac{\mathrm{d}\omega}{2\pi} \frac{-2\varGamma_{\mathbf{k}}}{\omega - z} \mathrm{sgn}(\omega) \tag{E.10}$$

is not well-defined. Moreover, the propagator in this parametrization is not continuous on the imaginary axis, due to the sign-function. The calculation of $i\mathcal{I}$ can not be done without inconsistencies due to the wrong analytic structures of the propagator parametrization.

E.2 Thermodynamic potential with naive parametrization

In this section, we show that the propagator parametrization

$$S_F^{R-1}(p_0, \mathbf{p}) = (p_0 + i\varGamma)\gamma^0 - \mathbf{p}\boldsymbol{\gamma} - M \tag{E.11}$$

leads to problems when the thermodynamic potential per volume is calculated. It is sufficient to concentrate on the free part,

$$\varOmega^{free} = i\mathcal{T}r \ln(iS_1^{-1}), \tag{E.12}$$

which has been treated in Sec. C.4. This result with the specific choice of the propagator,

$$\begin{aligned}\varOmega^{free} = 2N_cN_f \int \frac{\mathrm{d}^3k}{(2\pi)^3} \int_0^{+\infty} \frac{\mathrm{d}k_0}{2\pi i} \Bigg\{ & [1 - n_F(k_0 + \mu)] \ln \left(\frac{[(-k_0 - i\varGamma)^2 - \mathbf{k}^2 - M^2]}{[(-k_0 + i\varGamma)^2 - \mathbf{k}^2 - M^2]} \right) \\ & + n_F(k_0 - \mu) \ln \left(\frac{[(k_0 + i\varGamma)^2 - \mathbf{k}^2 - M^2]}{[(k_0 - i\varGamma)^2 - \mathbf{k}^2 - M^2]} \right) \Bigg\},\end{aligned} \tag{E.13}$$

can be used to write the free part of the thermodynamic potential per volume in a compact form,

$$\begin{aligned}\varOmega^{free} = -2N_cN_f \int \frac{\mathrm{d}^3k}{(2\pi)^3} \int_0^{\infty} \frac{\mathrm{d}k_0}{\pi} \Bigg\{ & [1 - n_F(k_0 - \mu) - n_F(k_0 + \mu)] \times \\ & \times \arg\left[(k_0 + i\varGamma)^2 - \mathbf{p}^2 - M^2\right] \Bigg\}.\end{aligned} \tag{E.14}$$

The UV-behavior of the complex angle in the integrand is especially important for the further calculation,

$$\lim_{k_0 \to \infty} \arg\left[(k_0 + i\varGamma)^2 - \mathbf{p}^2 - M^2\right] = \lim_{k_0 \to \infty} \frac{2i\varGamma}{k_0}. \tag{E.15}$$

This dependency on k_0 leads to an integral that is not well-defined, and as the asymptotic behavior is sensitive to the propagator parameter $\varGamma$, there is no unique subtraction scheme that brings $\varOmega^{free}$ to a finite value. The origin of this behavior is the self-energy: for large values of k_0 and $\mathbf{k}$, the retarded self-energy $\varSigma^R(k_0, \mathbf{k})$ is constant. In contrast to the other propagator parametrization discussed in Sec. E.1, we have no wrong analytic structures in the complex plane, but a self-energy with an unphysical UV-behavior. This is so severe that it is impossible to calculate a thermodynamic potential from this parametrization.

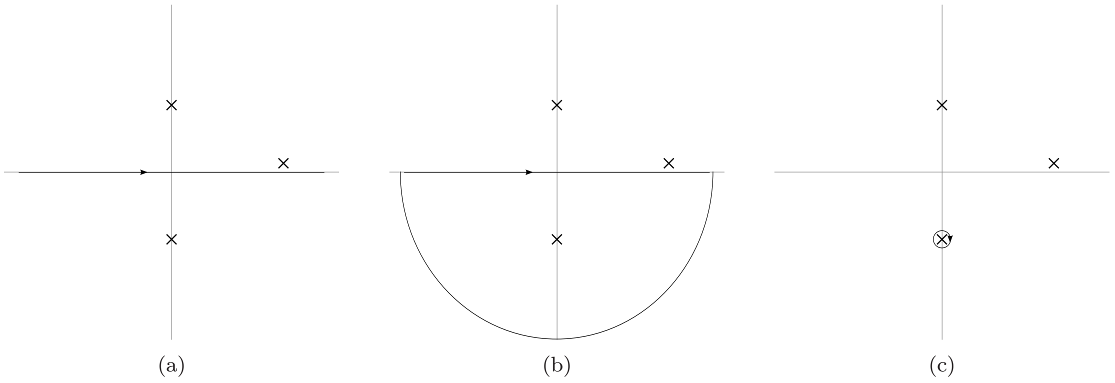

Figure E.1: Integration contours for the dispersion integral of the retarded self-energy in the parametrization SEP1. The poles lie at $\omega_{1,2} = \pm i/\lambda$ and $\omega_3 = p_0 + i\epsilon$. The integral in Eq. (E.18) can be interpreted as an integration in the complex plane along the real axis, as it is shown in (a). As the integrand goes fast enough to zero for large $|z|$, we can add a half circle as it is shown in (b). Thus, the integral is equal to the residuum of the pole that is in the closed contour (c).

E.3 SEP1: Simplest version

The imaginary part of the retarded self-energy in the simplest parametrization SEP1 is defined as

$$\mathrm{Im}\Sigma_s^{R,\,SEP1}(p_0,\mathbf{p}) = -\Gamma\frac{\lambda p_0}{1+\lambda^2 p_0^2}, \quad \mathrm{Im}\Sigma_0^{R,\,SEP1}(p_0,\mathbf{p}) = \mathrm{Im}\Sigma_3^{R,\,SEP1}(p_0,\mathbf{p}) = 0. \tag{E.16}$$

We chose the constant λ to be positive. The full SEP1 formula contains also a constant self-energy M, which is related to the mass.

E.3.1 Retarded self-energy

The retarded self-energy in this parametrization is obtained by the dispersion integral

$$\Sigma^{R,\,SEP1}(p_0,\mathbf{p}) = M - m_0 + \int_{-\infty}^{+\infty}\frac{\mathrm{d}\omega}{2\pi}\frac{-2\Gamma\lambda\omega}{[1+\lambda^2\omega^2][p_0+i\epsilon-\omega]}, \tag{E.17}$$

where the constant M has to be added to the integral. The integral over ω can be solved analytically by considering the integrand for complex values of the integration variable. From the form

$$\Sigma^{R,\,SEP1}(p_0,\mathbf{p}) = M - m_0 + \frac{2\lambda\Gamma}{2\pi\lambda^2}\int_{-\infty}^{+\infty}\mathrm{d}\omega\frac{\omega}{(\omega+\frac{i}{\lambda})(\omega-\frac{i}{\lambda})(\omega-p_0-i\epsilon)}, \tag{E.18}$$

one can see that the integrand has three poles in the complex plane. The integral contour is shown in Fig. E.1(a). As the absolute value of the integrand is proportional to $|\omega|^{-2}$ for large $|\omega|$, we can close the contour in the lower half plane as it is shown in Fig. E.1(b). After the deformation of the integration path (see Fig. E.1(c)), we can write the integral as

$$\Sigma^{R,\,SEP1}(p_0,\mathbf{p}) = M - m_0 - \frac{2\pi i 2\lambda\Gamma}{2\pi\lambda^2}\mathrm{Res}\big|_{\omega=-i/\lambda}\frac{\omega}{(\omega+\frac{i}{\lambda})(\omega-\frac{i}{\lambda})(\omega-p_0-i\epsilon)}. \tag{E.19}$$

The residuum is calculated easily,

$$\Sigma^{R,\,SEP1}(p_0,\mathbf{p}) = M - m_0 + \frac{i\Gamma}{\lambda p_0 + i}, \tag{E.20}$$

and after the separation of the real and the imaginary part, we obtain

$$\Sigma^{R,\,SEP1}(p_0,\mathbf{p}) = M - m_0 - \Gamma\frac{1}{1+\lambda^2 p_0^2} - i\Gamma\frac{\lambda p_0}{1+\lambda^2 p_0^2}. \tag{E.21}$$

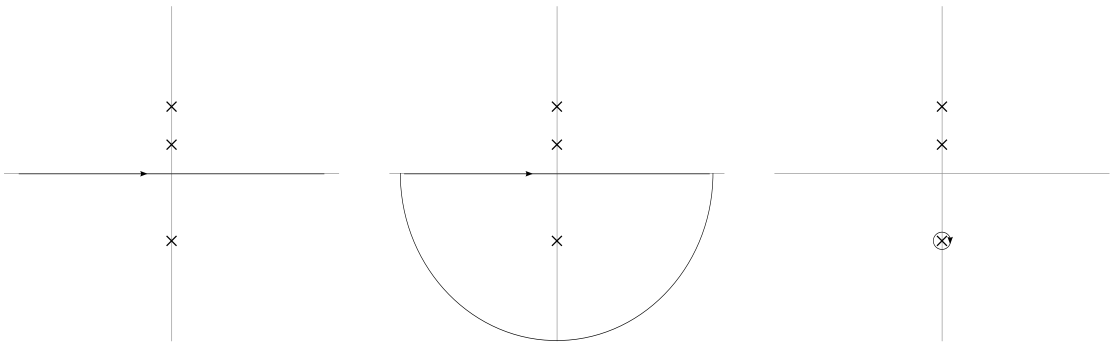

(a) (b) (c)

Figure E.2: Integration contours for the dispersion integral for the Matsubara self-energy in the parametrization SEP1. The poles lie at $\omega_{1,2} = \pm i/\lambda$ and $\omega_3 = i\omega_p$, where we assumed that $\mathrm{Im} i\omega_p > 0$.

We find that the imaginary part is again the same as before, but there is a momentum-dependent real part of the scalar self-energy additional to M, which results from the dispersion relation.

E.3.2 Matsubara self-energy

The Matsubara self-energy is obtained by a similar dispersion integral as the retarded self-energy,

$$\Sigma^{R,\,SEP1}(p_0, \mathbf{p}) = M - m_0 + \int_{-\infty}^{+\infty} \frac{\mathrm{d}\omega}{2\pi} \frac{-2\Gamma\lambda\omega}{[1+\lambda^2\omega^2][i\omega_p - \omega]}, \tag{E.22}$$

where $i\omega_p$ is a fermionic Matsubara frequency. As before, we can solve the integral in an analytical way when we use complex analysis. We identify the three poles and the integration path from the equation

$$\Sigma^{R,\,SEP1}(p_0, \mathbf{p}) = M - m_0 - \frac{2\lambda\Gamma}{2\pi\lambda^2} \int_{-\infty}^{+\infty} \mathrm{d}\omega \frac{\omega}{(\omega + \frac{i}{\lambda})(\omega - \frac{i}{\lambda})(\omega - i\omega_p)}, \tag{E.23}$$

the situation is drawn in Fig. E.2(a). A distinction has to me made according to the sign of the imaginary part of $i\omega_p$. If the sign is positive, we close the contour in the lower half plane, as it is shown in Fig. E.2(b). If the imaginary part is negative, we close it in the upper half plane. The resulting integration path is a circle which contains only one first-order pole: It is $\omega = -i/\lambda$ for the first case (see Fig. E.2(c)), and the complex conjugate value for the latter. The integration can be calculated by the evaluation of the residuum,

$$\Sigma^{R,\,SEP1}(p_0, \mathbf{p}) = M - m_0 - \frac{2\lambda\Gamma}{2\pi\lambda^2} \mathrm{Res}\big|_{z=\mp i/\lambda} \frac{\omega}{(\omega + \frac{i}{\lambda})(\omega - \frac{i}{\lambda})(\omega - i\omega_p)}, \tag{E.24}$$

which leads to the form

$$\Sigma^{R,\,SEP1}(p_0, \mathbf{p}) = \begin{cases} M - m_0 - \frac{2\Gamma}{2\pi\lambda} \frac{2\pi i \frac{i}{\lambda}}{-2\frac{i}{\lambda}[-\frac{i}{\lambda} - i\omega_p]} & \text{for}\, \omega_p > 0 \\ M - m_0 - \frac{2\Gamma}{2\pi\lambda} \frac{2\pi i \frac{i}{\lambda}}{2\frac{i}{\lambda}[\frac{i}{\lambda} - i\omega_p]} & \text{for}\, \omega_p < 0 \end{cases}.$$

This can be written in short

$$\Sigma^{R,\,SEP1}(i\omega_p, \mathbf{p}) = M - m_0 + \Gamma \frac{1}{1 + \lambda|\omega_p|}, \tag{E.25}$$

where both sign of ω_p were taken into account. We see that the Matsubara self-energy is real and momentum dependent due to the contribution from the dispersion integral.

E.4 SEP2: Grid interpolation

The imaginary part of the retarded self-energy in the SEP2 version is defined on a $N_0 \times N_3$-grid,

$$\mathrm{Im}\Sigma^{R,SEP2}_{0,3,s}((p_0)_i, (|\mathbf{p}|)_j) = \Gamma_{0,3,s}((p_0)_i, (\mathbf{p})_j), \quad i, j \in \{1, \dots, N_0\} \times \{1, \dots, N_3\}. \tag{E.26}$$

We skip the indices for the different Dirac-components of Σ in the following because all are treated in the same way. Between the discrete values $((p_0)_i, (\mathbf{p})_j)$, a linear interpolation is performed. For such a type of interpolated self-energy, the imaginary part reads

$$\mathrm{Im}\Sigma^{R,SEP2}(p_0, \mathbf{p}) = (a^0_i(|\mathbf{p}|)p_0 + b^0_i(|\mathbf{p}|)) \tag{E.27}$$

for $p_0 \in [(p_0)_i, (p_0)_{i+1}]$, where the new constants a and b can be derived from $\Gamma(p_0)_i, (\mathbf{p})_j)$,

$$a^0_i(|\mathbf{p}|) = \frac{\Gamma((p_0)_{i+1}, |\mathbf{p}|) - \Gamma((p_0)_i, |\mathbf{p}|)}{(p_0)_{i+1} - (p_0)_i} \tag{E.28}$$

$$b^0_i(|\mathbf{p}|) = \Gamma((p_0)_i, |\mathbf{p}|) - (p_0)_i a^0_i(|\mathbf{p}|). \tag{E.29}$$

The functions $\Gamma((p_0)_i, |\mathbf{p}|)$ are obtained by a interpolation of the $\mathbf{p}$-grid, that does not have to be specified for the further calculation. Values of p_0 and $\mathbf{p}$ outside the grid have to be extrapolated in suitable way. While the extrapolation of 3-momentum is done constantly, we set the imaginary part of the retarded self-energy for large $|p_0|$ to

$$\mathrm{Im}\Sigma^{R,SEP2}(|p_0| > |(p_0)_{N_0}|, \mathbf{p}) = c(|\mathbf{p}|)\frac{1}{p_0}, \tag{E.30}$$

where the constant $c(|\mathbf{p}|)$ is determined by the condition of continuity at $p_0 = (p_0)_{N_0}$,

$$c(|\mathbf{p}|) = \Gamma((p_0)_{N_0}, |\mathbf{p}|)(p_0)_{N_0}. \tag{E.31}$$

We write the imaginary part of the retarded self-energy component in the compact form

$$\mathrm{Im}\Sigma^{R,SEP2}(p_0, \mathbf{p}) = \sum_{i=1}^{N_0} \chi_{[(p_0)_i, (p_0)_{i+1}]}(p_0)(a^0_i(|\mathbf{p}|)p_0 + b^0_i(|\mathbf{p}|)) \quad + \quad \theta(p_0^2 - (p_0)^2_{N_0})\frac{c(|\mathbf{p}|)}{p_0}, \tag{E.32}$$

which can be used in a dispersion integral. For simplicity, we restrict the grid to positive frequencies p_0 and use the symmetries of the propagator components in order to obtain the negative grid points. The dispersion integral

$$f(z) = \int_{-\infty}^{+\infty} \frac{\mathrm{d}\omega}{2\pi} \frac{-2\mathrm{Im}f(\omega)}{\omega - z} \tag{E.33}$$

for such a function can be expressed with the integral over half of the interval,

$$\tilde{f}(z) = \int_0^{\infty} \frac{\mathrm{d}\omega}{2\pi} \frac{-2\mathrm{Im}f(\omega)}{\omega - z}, \tag{E.34}$$

and we get

$$f(z) = \begin{cases} \tilde{f}(z) - \tilde{f}(-z) & \text{if} \quad \mathrm{Im}f(\omega) = \mathrm{Im}f(-\omega) \\ \tilde{f}(z) + \tilde{f}(-z) & \text{if} \quad \mathrm{Im}f(\omega) = -\mathrm{Im}f(-\omega) \end{cases}. \tag{E.35}$$

Thus, it is sufficient to calculate the dispersion integral for $\omega > 0$ to obtain the retarded self-energy and the Matsubara self-energy.

E.4.1 Retarded self-energy

The retarded self-energy can be calculated with the dispersion relation

$$\begin{aligned}\Sigma^{R,SEP2}(p_0, \mathbf{p}) =& M - 2\sum_{i=1}^{N_0} \int_{(p_0)_i}^{(p_0)_{i+1}} \frac{\mathrm{d}\omega}{2\pi} \frac{a^0_i(|\mathbf{p}|)\omega + b^0_i(|\mathbf{p}|)}{\omega - p_0 - i\epsilon} - 2\int_{(p_0)_{N_0}}^{\infty} \frac{\mathrm{d}\omega}{2\pi} \frac{c(|\mathbf{p}|)}{\omega} \frac{1}{\omega - p_0 - i\epsilon} \\ & \pm \Big(p_0 + i\epsilon \to -p_0 - i\epsilon\Big),\end{aligned} \tag{E.36}$$

where the last term compensates the fact that only positive values of ω enter in the integral, as it was formulated in Eq. (E.35). We can restrict ourselves to the calculation of the real part of the retarded self-energy, since the imaginary part is known analytically. One can solve the integrals

$$\begin{aligned}\mathrm{Re}\int_{(p_0)_i}^{(p_0)_{i+1}} \frac{\mathrm{d}\omega}{2\pi}\frac{a_i^0(|\mathbf{p}|)\omega+b_i^0(|\mathbf{p}|)}{\omega-p_0-i\epsilon} =&\frac{a_i^0(|\mathbf{p}|)}{2\pi}((p_0)_i-(p_0)_{i+1})+\frac{a_i^0(|\mathbf{p}|)p_0}{2\pi}\ln\left(\frac{(p_0)_{i+1}-p_0}{(p_0)_i-p_0}\right)\\ &+\frac{b_i^0(|\mathbf{p}|)}{2\pi}\ln\left(\frac{(p_0)_{i+1}-p_0}{(p_0)_i-p_0}\right)\end{aligned} \tag{E.37}$$

and

$$\mathrm{Re}\int_{(p_0)_{N_0}}^{\infty}\frac{\mathrm{d}\omega}{2\pi}\frac{c(|\mathbf{p}|)}{\omega}\frac{1}{\omega-p_0-i\epsilon} =\frac{c(|\mathbf{p}|)}{2\pi p_0}\ln\left(1-\frac{p_0}{(p_0)_{N_0}}\right) \tag{E.38}$$

analytically, and finally the real part of the retarded self-energy is obtained:

$$\begin{aligned}\mathrm{Re}\varSigma^{R,\,SEP2}(p_0,\mathbf{p}) =&M-2\sum_{i=1}^{N_0}\left[\frac{a_i^0(|\mathbf{p}|)}{2\pi}((p_0)_i-(p_0)_{i+1})+\frac{a_i^0(|\mathbf{p}|)p_0}{2\pi}\ln\left(\frac{(p_0)_{i+1}-p_0}{(p_0)_i-p_0}\right)\right.\\ &\left.+\frac{b_i^0(|\mathbf{p}|)}{2\pi}\ln\left(\frac{(p_0)_{i+1}-p_0}{(p_0)_i-p_0}\right)\right]-2\frac{c(|\mathbf{p}|)}{2\pi p_0}\ln\left(1-\frac{p_0}{(p_0)_{N_0}}\right)\pm\Big(p_0\to -p_0\Big).\end{aligned} \tag{E.39}$$

E.4.2 Matsubara self-energy

The Matsubara self-energy is obtained from the dispersion integral

$$\begin{aligned}\varSigma^{SEP2}(i\omega_p,\mathbf{p}) =&M-2\sum_{i=1}^{N_0}\int_{(p_0)_i}^{(p_0)_{i+1}}\frac{\mathrm{d}\omega}{2\pi}\frac{a_i^0(|\mathbf{p}|)\omega+b_i^0(|\mathbf{p}|)}{\omega-i\omega_p}-2\int_{(p_0)_{N_0}}^{\infty}\frac{\mathrm{d}\omega}{2\pi}\frac{c(|\mathbf{p}|)}{\omega}\frac{1}{\omega-i\omega_p}\\ &\pm\Big(i\omega_p\to -i\omega_p\Big),\end{aligned} \tag{E.40}$$

in the same way as the retarded self-energy. The real and the imaginary part of the integrals can be calculated analytically,

$$\begin{aligned}\int_{(p_0)_i}^{(p_0)_{i+1}}\frac{\mathrm{d}\omega}{2\pi}\frac{a_i^0(|\mathbf{p}|)\omega+b_i^0(|\mathbf{p}|)}{\omega-i\omega_p} =&+\frac{a_i^0(|\mathbf{p}|)((p_0)_{i+1}-(p_0)_i)}{2\pi}\\ &-\frac{a_i^0(|\mathbf{p}|)|\omega_p|}{2\pi}\left[\arctan\left(\frac{(p_0)_{i+1}}{|\omega_p|}\right)-\arctan\left(\frac{(p_0)_i}{|\omega_p|}\right)\right]\\ &+\frac{b_i^0(|\mathbf{p}|)+i\omega_p a_i^0(|\mathbf{p}|)}{4\pi}\ln\left(\frac{(p_0)_{i+1}^2-|\omega_p|^2}{(p_0)_i^2-|\omega_p|^2}\right)\\ &+\frac{i\omega_p b_i^0(|\mathbf{p}|)}{2\pi|\omega_p|}\left[\arctan\left(\frac{(p_0)_{i+1}}{|\omega_p|}\right)-\arctan\left(\frac{(p_0)_i}{|\omega_p|}\right)\right]\end{aligned} \tag{E.41}$$

is the interpolation part and the extrapolation part reads

$$\int_{(p_0)_{N_0}}^{\infty}\frac{\mathrm{d}\omega}{2\pi}\frac{c(|\mathbf{p}|)}{\omega}\frac{1}{\omega-i\omega_p} =\frac{c(|\mathbf{p}|)(p_0)_{N_0}}{2\pi|\omega_p|}\left[\frac{\pi}{2}-\arctan(\frac{(p_0)_{N_0}}{|\omega_p|}\right]+i\frac{c(|\mathbf{p}|)(p_0)_{N_0}}{4\pi\omega_p}\ln\left(1+\frac{|\omega_p|^2}{(p_0)_{N_0}^2}\right). \tag{E.42}$$

The full Matsubara self-energy is obtained by summing the result from Eq. (E.41) over all grid-points, adding extrapolation part from Eq. (E.41) and the constant M. Furthermore, the compensation due to Eq. (E.35) has to be added.

E.5 SEP3: Intuitive parametrization

The imaginary part of the scalar self-energy in the intuitive parametrization consists of three terms,

$$\begin{aligned}\mathrm{Im}\varSigma_s^{R,\,SEP3}(p_0,\mathbf{p}) =&\mathrm{Im}\varSigma_s^{R,\,SEP1}(p_0)+\\ &+\mathrm{Im}\varSigma_s^{R,\,SEP3,\,\mathrm{cont}}(p_0,\mathbf{p})+\mathrm{Im}\varSigma_s^{R,\,SEP3,\,\mathrm{space}}(p_0,\mathbf{p}).\end{aligned} \tag{E.43}$$

The first term was analyzed in Sec. E.3. Here, we concentrate on the continuum part

$$\begin{aligned}\mathrm{Im}\varSigma_s^{R,\,SEP3,\,\mathrm{cont}}(p_0,\mathbf{p}) =&-\varGamma_{\mathrm{cont}}(\mathbf{p})\mathrm{sgn}(p_0)\chi_{[E_{\tau_1},E_{\tau_2}]}(|p_0|)\times\\ &\times(p_0^2-(E_{\tau_1}+E_{\tau_2})|p_0|+E_{\tau_1}E_{\tau_2}),\end{aligned} \tag{E.44}$$

and the spacelike part

$$\mathrm{Im}\varSigma_s^{R,\,SEP3,\,\mathrm{space}}(p_0,\mathbf{p}) = -\varGamma_{\mathrm{space}}(\mathbf{p})\theta(\mathbf{p}^2-p_0^2)\left(\mathbf{p}^2p_0-p_0^3\right). \tag{E.45}$$

These two parts are piecewise a polynomial, hence we can write the dispersion integral as

$$\int_{-\infty}^{+\infty}\frac{\mathrm{d}\omega}{2\pi}\frac{-2\mathrm{Im}\varSigma(\omega)}{\omega-z} = \sum_{j=0}^{n}a_j\int_{-\infty}^{+\infty}\frac{\mathrm{d}\omega}{2\pi}\frac{\omega^j}{\omega-z}. \tag{E.46}$$

This type of integral can be solved analytically.

E.5.1 Retarded self-energy

We obtain the retarded expressions of the self-energy components by the usual integration,

$$\begin{aligned}\varSigma_s^{R,\,SEP3,\,\mathrm{cont}}(p_0,\mathbf{p}) = 2\varGamma_{\mathrm{cont}}(\mathbf{p})\int_{E_{\tau_1}}^{E_{\tau_2}}\frac{\mathrm{d}\omega}{2\pi}\Bigg\{&\left(\frac{1}{\omega-p_0-i\epsilon}+\frac{1}{\omega+p_0+i\epsilon}\right)\times\\ &\times(\omega^2-(E_{\tau_1}+E_{\tau_2})\omega+E_{\tau_1}E_{\tau_2})\Bigg\},\end{aligned} \tag{E.47}$$

is the form for the continuum term and

$$\varSigma_s^{R,\,SEP3,\,\mathrm{space}}(p_0,\mathbf{p}) = 2\varGamma_{\mathrm{space}}(\mathbf{p})\int_{-|\mathbf{p}|}^{|\mathbf{p}|}\frac{\mathrm{d}\omega}{2\pi}\frac{\mathbf{p}^2\omega-\omega^3}{\omega-p_0-i\epsilon} \tag{E.48}$$

for the spacelike contribution. In the dispersion integral for the real part of the retarded self-energy, the integrals

$$\int\mathrm{d}\omega\frac{1}{\omega-p_0} =\ln(\omega-p_0) \tag{E.49}$$

$$\int\mathrm{d}\omega\frac{\omega}{\omega-p_0} =\omega+p_0\ln(\omega-p_0) \tag{E.50}$$

$$\int\mathrm{d}\omega\frac{\omega^2}{\omega-p_0} =\frac{1}{2}\omega^2+p_0\omega+p_0^2\ln(\omega-p_0) \tag{E.51}$$

$$\int\mathrm{d}\omega\frac{\omega^3}{\omega-p_0} =\frac{1}{3}\omega^3+\frac{1}{2}p_0\omega^2+p_0^2\omega+p_0^3\ln(\omega-p_0) \tag{E.52}$$

appear. Thus, it is possible to derive an analytic expression for the retarded and advanced self-energies $\mathrm{Re}\varSigma_s^{R,\,SEP3,\,\mathrm{cont}}$ and $\mathrm{Re}\varSigma_s^{R,\,SEP3,\,\mathrm{space}}$.

E.5.2 Matsubara self-energy

The continuation of the self-energy to the imaginary axis can be done with the dispersion integrals

$$\varSigma_s^{SEP3,\,\mathrm{cont}}(i\omega_p,\mathbf{p}) = 4\varGamma_{\mathrm{cont}}(\mathbf{p})\int_{E_{\tau_1}}^{E_{\tau_2}}\frac{\mathrm{d}\omega}{2\pi}\frac{\omega}{\omega^2+|\omega_p|^2}(\omega^2-(E_{\tau_1}+E_{\tau_2})\omega+E_{\tau_1}E_{\tau_2}) \tag{E.53}$$

and

$$\varSigma_s^{SEP3,\,\mathrm{space}}(i\omega_p,\mathbf{p}) = 2\varGamma_{\mathrm{space}}(\mathbf{p})\int_{-|\mathbf{p}|}^{+|\mathbf{p}|}\frac{\mathrm{d}\omega}{2\pi}\frac{\omega}{\omega^2+|\omega_p|^2}\left(\mathbf{p}^2\omega-\omega^3\right) \tag{E.54}$$

for the continuum part and the spacelike part, respectively. As the integrands are odd for the imaginary part of the Matsubara self-energy, one can see that $\varSigma_s^{SEP3,\,\mathrm{cont}}$ and $\varSigma_s^{SEP3,\,\mathrm{space}}$ are purely real on the imaginary axis. The integrals that enter in this calculation are

$$\int\mathrm{d}\omega\frac{\omega}{\omega^2+|\omega_p|^2} = \ln(\omega^2+|\omega_p|^2) \tag{E.55}$$

$$\int\mathrm{d}\omega\frac{\omega^2}{\omega^2+|\omega_p|^2} = \omega-|\omega_p|\arctan(\frac{\omega}{|\omega_p|}) \tag{E.56}$$

$$\int\mathrm{d}\omega\frac{\omega^3}{\omega^2+|\omega_p|^2} = \frac{1}{2}\omega^2-\frac{1}{2}|\omega_p|^2\ln(\omega^2+|\omega_p|^2) \tag{E.57}$$

$$\int\mathrm{d}\omega\frac{\omega^4}{\omega^2+|\omega_p|^2} = \frac{\omega^3}{3}+|\omega_p|^2\omega-|\omega_p|^3\arctan(\frac{\omega}{|\omega_p|}). \tag{E.58}$$

Thus, one can give explicit forms of the self-energy in the form of SEP3 on the real axis as well as on the imaginary axis.

Appendix F

Calculation of NJL scattering amplitudes

F.1 Useful formulas

We use the usual momentum labeling

$$p + p_1 \quad \longrightarrow \quad p' + p_1' \tag{F.1}$$

in the following, which is also applied to masses, spin, isospin, color of the scattering particles. We chose a coordinate system where the z-component of $\mathbf{p}_1$, $\mathbf{p'}$, and $\mathbf{p}_1'$ are parallel to the p-direction. The Mandelstam variables

$$s = (p+p_1)^2 = (E+E_1)^2 - \mathbf{p}^2 + \mathbf{p}_1^2 + 2\mathbf{p}\mathbf{p}_1 \cos\theta_1 \tag{F.2}$$

$$t = (p-p')^2 = (E-E')^2 - \mathbf{p}^2 + \mathbf{p}'^2 - 2\mathbf{p}\mathbf{p}' \cos\theta' \tag{F.3}$$

$$u = (p-p_1')^2 = (E+E_1')^2 - \mathbf{p}^2 + \mathbf{p}_1'^{\,2} + 2\mathbf{p}\mathbf{p}_1' \cos\theta_1' \tag{F.4}$$

in such a coordinate frame enter usually in the expressions for the scattering amplitudes. Sometimes, the 3-momentum in center-of-mass frame

$$\mathbf{q}_{CM}^2 = \frac{1}{s}\left[s^2 + m^4 + m_1^4 - 2m^2 m_1^2 - 2(m^2+m_1^2)s\right] \tag{F.5}$$

enters as well as the scattering angle in the same frame,

$$\cos\theta_{CM} = 1 + \frac{2t}{s\mathbf{q}_{CM}^2}. \tag{F.6}$$

The invariant matrix element $\mathcal{M}$ enters in the differential cross section, the expression for $m = m_1$ reads

$$\left(\frac{\mathrm{d}\sigma}{\mathrm{d}\Omega}\right)_{CM} = \frac{|\mathcal{M}|^2}{64\pi^2 E_{CM}^2}. \tag{F.7}$$

We now turn to the calculation of the different scattering amplitudes used in this work.

F.2 Quark-antiquark scattering

It turns out that the scattering processes in Figs. 5.5 and 5.1 can be calculated together, just by setting the mass to

$$m = \left\{ \begin{array}{ll} m_0 & \text{perturbative scattering} \\ m_H & \text{single meson exchange} \end{array} \right. .$$

Additionally, the intermediate amplitude that is D_M for single meson exchange has to be replaced by $-2g$ when only the perturbative matrix element is required.

We write the invariant matrix element for $q\bar{q}$-scattering as

$$i\mathcal{M}_{q\bar{q}} = \sum_M (\bar{v}_1 \mathit{\Gamma}_M u) D_M(s) (\bar{u}' \mathit{\Gamma}_M v_1') + (\bar{v}_1 \mathit{\Gamma}_M v_1') D_M(t) (\bar{u}' \mathit{\Gamma}_M u), \tag{F.8}$$

according to the diagrams shown in Figs. 5.5(a) and 5.5(b). We want to calculate the spin-averaged $|\mathcal{M}|^2$, thus we start with

$$\begin{aligned}|\mathcal{M}_{q\bar{q}}|^2 = \sum_{M_1,M_2} \Big\{ & (\bar{v}_1 \mathit{\Gamma}_{M_1} u \bar{u} \mathit{\Gamma}_{M_1} v_1) D_{M_1}(s) D^*_{M_2}(s) (\bar{u}' \mathit{\Gamma}_{M_1} v_1' \bar{v}_1' \mathit{\Gamma}_{M_2} u') \\ & + (\bar{v}_1 \mathit{\Gamma}_{M_1} v_1' \bar{v}_1' \mathit{\Gamma}_{M_2} v_1) D_{M_1}(t) D^*_{M_2}(t) (\bar{u}' \mathit{\Gamma}_M u \bar{u} \mathit{\Gamma}_M u') \\ & + D_{M_1}(s) D^*_{M_2}(t) (\bar{v}_1 \mathit{\Gamma}_{M_1} u \bar{u} \mathit{\Gamma}_M u' \bar{u}' \mathit{\Gamma}_{M_1} v_1' \bar{v}_1' \mathit{\Gamma}_{M_2} v_1) \\ & + D^*_{M_1}(s) D_{M_2}(t) (\bar{v}_1 \mathit{\Gamma}_{M_1} v_1' \bar{v}_1' \mathit{\Gamma}_{M_2} u' \bar{u}' \mathit{\Gamma}_{M_1} u \bar{u} \mathit{\Gamma}_{M_2} v_1) \Big\}\end{aligned} \tag{F.9}$$

and can exclude each contribution where different meson channels M_1 and M_2 mix. Thus, we see that the square of M can be written as a sum

$$\begin{aligned}|\mathcal{M}_{q\bar{q}}|^2 = 4 \sum_M \; & \left(|\mathcal{M}^s_{q\bar{q}}|^2\right)_M + \left(|\mathcal{M}^t_{q\bar{q}}|^2\right)_M \\ & + \left(\mathcal{M}^s_{q\bar{q}} \mathcal{M}^{t\,*}_{q\bar{q}}\right)_M + \left(\mathcal{M}^t_{q\bar{q}} \mathcal{M}^{s\,*}_{q\bar{q}}\right)_M,\end{aligned} \tag{F.10}$$

because of the different products. As all quarks carry spin-, isospin-, and color-quantum numbers, the matrix element squared depends on all spins s, all isospins i, and all color c. Due to the structure of the vertices in the NJL model, we can decompose $|\mathcal{M}|^2$ in a way

$$|\mathcal{M}_{q\bar{q}}|^2 = |\mathcal{M}^{ss_1s's_1'}_{q\bar{q}}|^2 \times |\mathcal{M}^{ii_1i'i_1'}_{q\bar{q}}|^2 \times |\mathcal{M}^{cc_1c'c_1'}_{q\bar{q}}|^2 \tag{F.11}$$

The spin-averaging results in a trace over the Dirac indices,

$$\begin{aligned}|\mathcal{M}_{q\bar{q}}|^2 = \sum_M \text{color} \times \text{isospin} \times \Big\{ & \mathrm{tr}_{\text{Dirac}}\Big[(\not{p}_1 - m_1)(\not{p} \pm m)\Big] \mathrm{tr}_{\text{Dirac}}\Big[(\not{p}' + m)(\not{p}_1' \mp m1)\Big] |D_M(s)|^2 \\ & + \mathrm{tr}_{\text{Dirac}}\Big[(\not{p}_1 - m_1)(\not{p}_1 \mp m_1)\Big] \mathrm{tr}_{\text{Dirac}}\left[(\not{p}' + m)(\not{p} \pm m)\right] |D_M(t)|^2 \\ & + \mathrm{tr}_{\text{Dirac}}\Big[(\not{p}_1 - m_1)(\not{p} \pm m)(\not{p}' + m)(\not{p}_1' \mp m_1)\Big] D_M(s) D^*_M(t) \\ & + \mathrm{tr}_{\text{Dirac}}\Big[(\not{p}_1 - m_1)(\not{p}_1' \mp m_1)(\not{p}' + m)(\not{p} \pm m)\Big] D_M(t) D^*_M(s) \Big\},\end{aligned} \tag{F.12}$$

where the upper sign is for $M = \sigma$, and the other sign for $M = \pi$. The isospin-averaging is done by

$$|\mathcal{M}^{\langle i\rangle}_{q\bar{q}}|^2 = \frac{1}{2} \sum_i \frac{1}{2} \sum_{i_1} \sum_{i'} \sum_{i_1'} |\mathcal{M}^{ii_1i'i_1'}_{q\bar{q}}|^2, \tag{F.13}$$

and the color-averaging by

$$|\mathcal{M}^{\langle i\rangle}_{q\bar{q}}|^2 = \frac{1}{3} \sum_i \frac{1}{3} \sum_{i_1} \sum_{i'} \sum_{i_1'} |\mathcal{M}^{ii_1i'i_1'}_{q\bar{q}}|^2. \tag{F.14}$$

The analysis of the expressions for the different channels M lead to a factor of 1 for $M = \sigma$, and a factor of 1/3 for $M = \pi$. In summary, the invariant matrix element squared for $q\bar{q}$-scattering reads

$$\begin{aligned}|\mathcal{M}_{q\bar{q}}|^2 = \sum_{M \in \{\sigma,\pi\}} \; & + 16(p_1 \cdot p \mp m^2)(p' \cdot p_1' \mp m^2)|D_M(s)|^2 \\ & + 16(p_1 \cdot p_1' \pm m^2)(p \cdot p' \pm m^2)|D_M(t)|^2 \\ & + 4\Big[p_1 \cdot p p' \cdot p_1' - p_1 \cdot p' p \cdot p_1' + p_1 \cdot p_1' p \cdot p' \\ & \quad + m^2(\mp p_1 \cdot p - p_1 \cdot p' \pm p_1 \cdot p_1' \pm p \cdot p' - p \cdot p_1' \mp p' \cdot p_1') \\ & \quad + m^4\Big]\Big[D_M(s) D^*_M(t) + D_M(s)^* D_M(t)\Big],\end{aligned} \tag{F.15}$$

where the forms of D_M and m have to be adapted to the different diagrams.

F.3 Quark-quark scattering

We calculate the quark-quark scattering amplitude for the perturbative NJL case and for the one meson exchange at the same time, as it was discussed in the previous section. With the same notation used there, we write the summed quark-quark scattering amplitude of the t- and u-channel

$$i\mathcal{M}_{qq} = \sum_M (\bar{u}'\mathit{\Gamma}_M u) D_M(t) (\bar{u}_1'\mathit{\Gamma}_M u_1) + (\bar{u}_1'\mathit{\Gamma}_M u) D_M(u) (\bar{u}'\mathit{\Gamma}_M u_1), \tag{F.16}$$

which results from the diagrams shown in Figs. 5.5(c) and 5.5(d). The squared matrix element for the qq-process has no contributions where the different channels M mix, hence

$$\begin{aligned}|\mathcal{M}_{qq}|^2 = \sum_M \Big\{ &(\bar{u}'\mathit{\Gamma}_M u \bar{u}\mathit{\Gamma}_M u')|D_M(t)|^2(\bar{u}_1'\mathit{\Gamma}_M u_1\bar{u}_1\mathit{\Gamma}_M u_1') \\ &+ (\bar{u}_1'\mathit{\Gamma}_M u\bar{u}\mathit{\Gamma}_M i_1')|D_M^*(u)|^2(\bar{u}'\mathit{\Gamma}_M u_1\bar{u}_1\mathit{\Gamma}_M u') \\ &+ [D_M(t)D_M^*(u) + D_M^*(t)D_M(u)](\bar{u}'\mathit{\Gamma}_M u\bar{u}\mathit{\Gamma}_M u_1'\bar{u}'\mathit{\Gamma}_M u_1\bar{u}_1\mathit{\Gamma}_M u')\Big\}.\end{aligned} \tag{F.17}$$

The averaging of the spin leads to

$$\begin{aligned}|\mathcal{M}_{qq}|^2 = \sum_M \text{color} \times \text{isospin} \times \Big\{ &\mathrm{tr}_{\text{Dirac}}\left[(\not{p}' + m)(\not{p} \pm m)\right] \mathrm{tr}_{\text{Dirac}}\left[(\not{p}_1' + m_1)(\not{p}_1 \pm m_1)\right] |D_M(t)|^2 \\ &+ \mathrm{tr}_{\text{Dirac}}\left[(\not{p}_1' + m_1)(\not{p} \pm m)\right] \mathrm{tr}_{\text{Dirac}}\left[(\not{p}' + m)(\not{p}_1 \pm m_1)\right] |D_M(u)|^2 \\ &+ \mathrm{tr}_{\text{Dirac}}\left[(\not{p}' + m)(\not{p} \pm m)(\not{p}_1' + m_1)(\not{p}_1 \pm m_1)\right]\left[D_M(t)D_M^*(u) + D_M(t)^*D_M(u)\right]\Big\},\end{aligned} \tag{F.18}$$

while the considerations of isospin- and color-averaging are the same as in Sec. F.2. The final result after the evaluation of the traces is

$$\begin{aligned}|\mathcal{M}_{qq}|^2 = \sum_{M\in\{\sigma,\pi\}} &16(p'\cdot p \mp m^2)(p_1'\cdot p_1 \mp m^2)|D_M(t)|^2 \\ &+ 16(p_1'\cdot p \pm m^2)(p'\cdot p_1 \pm m^2)|D_M(u)|^2 \\ &+ 4\Big[p'\cdot pp_1'\cdot p_1' - p'\cdot p_1'p\cdot p_1 + p'\cdot p_1 p\cdot p_1' \\ &\quad + m_H^2(\pm p'\cdot p + p'\cdot p_1' \pm p'\cdot p_1 \pm p\cdot p_1' + p\cdot p_1 \pm p_1'\cdot p_1) \\ &\quad + m_H^4\Big]\Big[D_M(t)D_M^*(u) + D_M(t)^*D_M(u)\Big],\end{aligned} \tag{F.19}$$

which similar to the result for $q\bar{q}$-scattering.

Appendix G

Expanded quark loop in static limit

All quark loop contributions can be written in the form

$$\varPi^{(a,b,c,d)}(i\omega_e, \mathbf{0}) = \sum_M T \sum_{i\omega_q} \int \frac{\mathrm{d}^3 q}{(2\pi)^3} P_M^{(a,b,c,d)}(i\omega_e, i\omega_q), \tag{G.1}$$

where we discussed already that the function $\varPi^{(d)}$ has no contribution to the shear viscosity.

G.1 Meson loop $\varPi^{(a)}$

We calculate the meson loop diagram shown in Fig. 5.26(a) in static limit. The diagram is

$$\begin{aligned}\varPi^{(a)}(i\omega_e, \mathbf{0}) =& \sum_M T \sum_{i\omega_q} \int \frac{\mathrm{d}^3 q}{(2\pi)^3} \frac{1}{2} \varGamma^{SL}_{\gamma^2 MM}(i\omega_e + i\omega_q, \mathbf{q}; -i\omega_q, -\mathbf{q}) D_M(i\omega_q, \mathbf{q}) \times \\ & \times \varGamma^{SL}_{\gamma^2 MM}(-i\omega_e - i\omega_q, -\mathbf{q}; i\omega_q, \mathbf{q}) D_M(i\omega_e + i\omega_q, \mathbf{q}),\end{aligned} \tag{G.2}$$

where we can write the Matsubara sum as a contour integral. We first want to analyze the quark triangles in static limit that enter in this expression. The full quark triangle diagram $\varGamma_{\gamma^2 MM}(p_1; p_2)$ is given by

$$\begin{aligned}\varGamma_{\gamma^2 MM}(p_1; p_2) = -T \sum_{i\omega_k} \int \frac{\mathrm{d}^3 k}{(2\pi)^3} \mathrm{Tr}\Big[& k_x \gamma^2 S_H(i\omega_k + i\omega_{p_1} + i\omega_{p_2} + \mu, \mathbf{k} + \mathbf{p}_1 + \mathbf{p}_2) \times \\ & \times \varGamma_M S_H(i\omega_k + i\omega_{p_1} + \mu, \mathbf{k} + \mathbf{p}_1) \varGamma_M S_H(i\omega_k + \mu, \mathbf{k})\Big] + ex.,\end{aligned} \tag{G.3}$$

and its static limit is obtained in the limit of all external momenta going to zero. For simplicity, we calculate this quantity in vacuum. After the evaluation of the trace, we obtain

$$\begin{aligned}-i\varGamma_{\gamma^2 \pi\pi} = \int \frac{\mathrm{d}^4 k}{(2\pi)^4} 4 N_c N_f \Big[& \frac{k_x k_y}{[k^2 - m_H^2]^2} - \frac{k_x p_y}{[k^2 - m_H^2][(k+p)^2 - m_H^2]} \\ & - p^2 \frac{k_x k_y}{[k^2 - m_H^2]^2 [(k+p)^2 - m_H^2]}\Big] + ex.,\end{aligned} \tag{G.4}$$

$$\begin{aligned}-i\varGamma_{\gamma^2 \sigma\sigma} = \int \frac{\mathrm{d}^4 k}{(2\pi)^4} 4 N_c N_f \Big[& \frac{k_x k_y}{[k^2 - m_H^2]^2} - \frac{k_x p_y}{[k^2 - m_H^2][(k+p)^2 - m_H^2]} \\ & - (p^2 - 4m_H^2) \frac{k_x k_y}{[k^2 - m_H^2]^2 [(k+p)^2 - m_H^2]}\Big] + ex.,\end{aligned} \tag{G.5}$$

The factors of k_x and k_y lead to many terms that are odd and vanish when integrating over all 3-components of k. We can find the remaining terms with a Feynman parameter trick. The integrals in the previous equation are expressed as

$$\frac{k_x p_y}{[k^2 - m_H^2][(k+p)^2 - m_H^2]} = -\frac{1}{2} p_x p_y \int \frac{\mathrm{d}^4 k}{(2\pi)^4} \frac{1}{[(k - \frac{p}{2})^2 - m_H^2][(k + \frac{p}{2})^2 - m_H^2]} \tag{G.6}$$

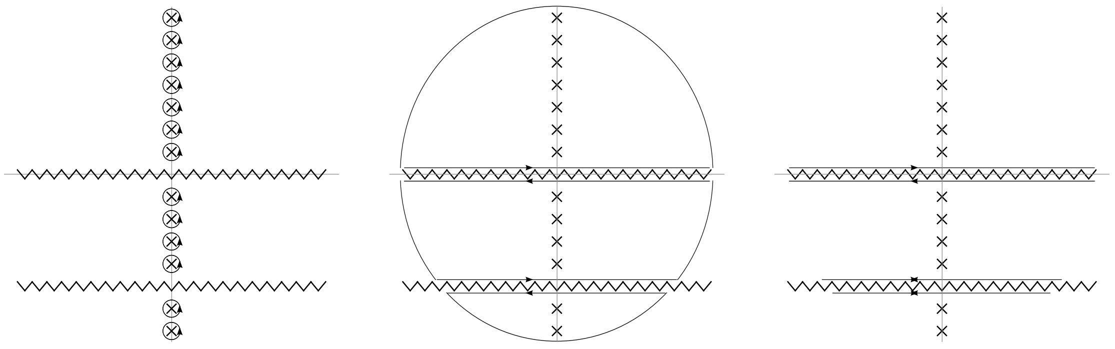

(a) (b) (c)

Figure G.1: Integration contours for the meson loop contribution to the shear viscosity. The contour C shown in (a) is deformed as it is shown in (b) and (c).

and

$$\frac{k_x k_y}{[k^2 - m_H^2][(k+p)^2 - m_H^2]} = p_x p_y \int_0^1 2(1-x)\mathrm{d}x \int \frac{\mathrm{d}^4 k}{(2\pi)^4} \frac{1}{[l^2 - m^2 + p^2 x(1-x)]}^{3}, \tag{G.7}$$

where the leading-order dependency on external 3-momentum becomes manifest. For the static limit, we just have to set all external momentum to zero in the integrand, and we get a result that is quadratic in p due to the prefactors of the integrands,

$$\varGamma^{SL}_{\gamma^2 MM} = \varLambda^{SL}_{\gamma^2 MM} p_x p_y. \tag{G.8}$$

The explicit form of the constants $\varLambda^{SL}_{\gamma^2 MM}$ is given by

$$\varLambda^{SL}_{\gamma^2 \pi\pi} = -4N_c N_f \int \frac{\mathrm{d}^4 k}{(2\pi)^4} \frac{1}{[k^2 - m_H^2]^2} \tag{G.9}$$

$$\varLambda^{SL}_{\gamma^2 \sigma\sigma} = -4N_c N_f \int \frac{\mathrm{d}^4 k}{(2\pi)^4} \Big\{ \frac{1}{[k^2 - m_H^2]^2} - \frac{4}{3} \frac{m_H^2}{[k^2 - m_H^2]^3} \Big\}. \tag{G.10}$$

This forms can now be used in order to compute the shear viscosity contribution from $\varPi^{(a)}$ in the static limit,

$$\varPi^{(a)}(i\omega_e, \mathbf{0}) = \sum_M \varLambda^2_{\gamma^2 MM} T \sum_{i\omega_q} \int \frac{\mathrm{d}^3 q}{(2\pi)^3} \frac{1}{2} q_x^2 q_y^2 D_M(i\omega_q, \mathbf{q}) D_M(i\omega_e + i\omega_q, \mathbf{q}). \tag{G.11}$$

We rewrite the Matsubara sum as a contour integral, and according to [115], we chose a special contour where the Matsubara frequency $i\omega_q = 0$ is treated separately,

$$\begin{aligned} \varPi^{(a)}(i\omega_e, \mathbf{0}) = \sum_M \frac{\varLambda^2_{\gamma^2 MM}}{2} \int \frac{\mathrm{d}^3 q}{(2\pi)^3} q_x^2 q_y^2 \Big\{ & T D_M(0, \mathbf{q}) D_M(i\omega_e, \mathbf{q}) + T D_M(-i\omega_e, \mathbf{q}) D_M(0, \mathbf{q}) \\ & + \oint_C \frac{\mathrm{d}z}{2\pi i} n_B(z) D_M(z, \mathbf{q}) D_M(i\omega_e + z, \mathbf{q}) \Big\}. \end{aligned} \tag{G.12}$$

The integral contour C is shown in Fig. G.1(a). When the integral contour is deformed according to Figs. G.1(b) and G.1(c), we obtain integrations along the branch cuts of the two meson propagators in the integrand,

$$\begin{aligned} \oint_C \frac{\mathrm{d}z}{2\pi i} n_B(z) D_M(z, \mathbf{q}) D_M(i\omega_e + z, \mathbf{q}) = \int_{-\infty}^{+\infty} \frac{\mathrm{d}q_0}{\pi i} n_B(q_0) \Big\{ & \mathrm{Im} D_M(q_0, \mathbf{q}) D_M(i\omega_e + q_0, \mathbf{q}) \\ & + D_M(q_0 - i\omega_e, \mathbf{q}) \mathrm{Im} D_M(q_0, \mathbf{q}) \Big\}. \end{aligned} \tag{G.13}$$

We perform the analytical continuation to retarded external momentum $i\omega_q \to p_0 + i\epsilon$, which leads to

$$\begin{aligned}\Pi^{(a)}(p_0+i\epsilon,\mathbf{0}) =& \sum_M \frac{\Lambda^2_{\gamma^2 MM}}{2}\int \frac{\mathrm{d}^3q}{(2\pi)^3} q_x^2 q_y^2 \Bigg\{ TD_M(0,\mathbf{q})D_M(p_0+i\epsilon,\mathbf{q}) \\ & + TD_M(-p_0-i\epsilon,\mathbf{q})D_M(0,\mathbf{q}) \\ & + \int_{-\infty}^{+\infty}\frac{\mathrm{d}q_0}{\pi i} n_B(q_0)\Big\{\mathrm{Im}D_M(q_0,\mathbf{q})D_M(p_0+q_0+i\epsilon,\mathbf{q}) \\ & + D_M(q_0-p_0-i\epsilon,\mathbf{q})\mathrm{Im}D_M(q_0,\mathbf{q})\Big\}\Bigg\}. \end{aligned} \tag{G.14}$$

A more compact form is obtained by considering the symmetries of the bosonic Green's functions D_M, thus the imaginary part reads

$$\begin{aligned}\mathrm{Im}\Pi^{(a)}(p_0+i\epsilon,\mathbf{0}) =& \sum_M \frac{\Lambda^2_{\gamma^2 MM}}{2}\int \frac{\mathrm{d}^3q}{(2\pi)^3} q_x^2 q_y^2 \Bigg\{ 2TD_M(0,\mathbf{q})\mathrm{Im}D_M(p_0+i\epsilon,\mathbf{q}) \\ & + \int_{-\infty}^{+\infty}\frac{\mathrm{d}q_0}{\pi i} n_B(q_0)\Big\{\mathrm{Im}D_M(q_0,\mathbf{q})\mathrm{Im}D_M(p_0+q_0+i\epsilon,\mathbf{q}) \\ & + \mathrm{Im}D_M(q_0-p_0-i\epsilon,\mathbf{q})\mathrm{Im}D_M(q_0,\mathbf{q})\Big\}\Bigg\}. \end{aligned} \tag{G.15}$$

After shifting the momenta and using the meson spectral function in the expression, we obtain

$$\begin{aligned}\mathrm{Im}\Pi^{(a)}(p_0+i\epsilon,\mathbf{0}) =& \sum_M \frac{\Lambda^2_{\gamma^2 MM}}{4}\int \frac{\mathrm{d}^3q}{(2\pi)^3} q_x^2 q_y^2 \Big\{ TD_M(0,\mathbf{q})\rho_M(p_0,\mathbf{q}) \\ & + \int_{-\infty}^{+\infty}\frac{\mathrm{d}q_0}{2\pi i}\left[n_B(q_0)-n_B(q_0+p_0)\right]\left[\rho_M(q_0,\mathbf{q})\rho_M(p_0+q_0,\mathbf{q})\right]\Big\}, \end{aligned} \tag{G.16}$$

from where the static shear viscosity can be extracted from the derivative with respect to p_0,

$$\eta^{(a)} = -\sum_M \frac{\Lambda^2_{\gamma^2 MM}}{4}\int \frac{\mathrm{d}^3q}{(2\pi)^3} q_x^2 q_y^2 \Big\{ TD_M(0,\mathbf{q})\rho'_M(0,\mathbf{q}) + \int_{-\infty}^{+\infty}\frac{\mathrm{d}q_0}{2\pi i} n'_B(q_0)\rho^2_M(q_0,\mathbf{q})\Big\}. \tag{G.17}$$

The primes denote the derivatives with respect to the 0-momentum component of the function arguments.

G.2 The contributions $\Pi^{(b)}$ and $\Pi^{(c)}$

The contributions to the shear viscosity η from the diagrams shown in Figs. 5.26(b) and 5.26(c) involve the integrands

$$P_M^{(b)}(i\omega_1,i\omega_2) = \Gamma^{SL}_{\gamma^2 MM\gamma^2}(-i\omega_q,-\mathbf{q};i\omega_q,\mathbf{q};-i\omega_e,\mathbf{0})D_M(i\omega_q.\mathbf{q}) \tag{G.18}$$

and

$$P_M^{(c)}(i\omega_1,i\omega_2) = \Gamma^{SL}_{\gamma^2 M\gamma^2 M}(-i\omega_q,-\mathbf{q};-i\omega_e,\mathbf{0};i\omega_q,\mathbf{q})D_M(i\omega_q.\mathbf{q}). \tag{G.19}$$

We can treat both diagrams together, since in static limit, both effective meson vertices can be written as

$$\Gamma^{SL}_{\gamma^2 MM\gamma^2} = \Lambda_M^{(b)} q_x^2 q_y^2 \qquad\qquad \Gamma^{SL}_{\gamma^2 M\gamma^2 M} = \Lambda_M^{(c)} q_x^2 q_y^2 \tag{G.20}$$

in the same way as in Sec. G.1. The quantities $\Lambda_M^{(b,c)}$ are real, constant numbers as in the case of the calculation of $\Pi^{(a)}$. We write the viscosity contributions as contour integrals,

$$\Pi^{(b,c)}(i\omega_e,0) = \sum_M \int \frac{\mathrm{d}^3q}{(2\pi)^3}\Lambda_M^{(b)} q_x^2 q_y^2 \oint_C \frac{\mathrm{d}z}{2\pi i} n_B(z)D_M(z,\mathbf{q}), \tag{G.21}$$

where the contour C is around the bosonic Matsubara frequencies. The integrand has a branch cut at the real axis, so we find a situation that was already discussed in Fig. C.1. When we perform the same deformations of C as it was discussed in the figure, we end up with the equation

$$\Pi^{(b,c)}(i\omega_e, 0) = \sum_M \int \frac{\mathrm{d}^3 q}{(2\pi)^3} \Lambda_M^{(b)} q_x^2 q_y^2 \int_{-\infty}^{+\infty} \frac{\mathrm{d}q_0}{2\pi} n_B(q_0) \rho_M(z, \mathbf{q}). \tag{G.22}$$

This expression is real and independent of the external momentum, hence the derivative of the imaginary part is zero. We see that $\eta^{(1)}$ is the only contribution to shear viscosity in the given approximation.

Appendix H

Calculation of the vertex dressing

H.1 Quark loop part

The quark loop part of the vertex in the Kubo formula for shear viscosity reads

$$\varGamma^{ij}_{\eta\,\mathrm{loop}\,M} = \sum_M -T \sum_{i\omega_l} \int \frac{\mathrm{d}^3 l}{(2\pi)^3} 2g K^{ij}_{\mathrm{loop}\,M}\big((i\omega_l + \mu, \mathbf{l}), (i\omega_l + i\omega_e + \mu, \mathbf{l})\big) \varGamma_M, \tag{H.1}$$

where the integrand $K^{ij}_{\mathrm{loop}\,M}$ is

$$K^{ij}_{\mathrm{loop}\,M}(k_1, k_2) = \mathrm{Tr}\left[\varGamma^{ij}_{\eta}(k_1, k_2) S(k_2) \varGamma_M S(k_1)\right]. \tag{H.2}$$

In the further calculations, we suppress the 3-momentum argument since it is always equal to $\mathbf{l}$ in all functions. The Matsubara sum over all frequencies $i\omega_l$ can be written as a contour integral

$$\varGamma^{ij}_{\eta\,\mathrm{loop}\,M} = \sum_M 2g\varGamma_M \int \frac{\mathrm{d}^3 l}{(2\pi)^3} \oint_C \frac{\mathrm{d}z}{2\pi i} n_F(z) K^{ij}_{\mathrm{loop}\,M}(z + \mu, z + i\omega_e + \mu), \tag{H.3}$$

where the contour is around the fermionic Matsubara frequencies. For a deformation of the contour, the singularities and nonanalyticities of the kernel in the complex plane have to be specified. The two quark propagators and the fully dressed vertex (see Eq. (H.2)) are assumed to have branch cuts for real arguments, thus there are branch cuts for

$$z = l_0 \qquad \text{and} \qquad z = l_0 - i\omega_e, \qquad l_0 \in \mathbb{R}. \tag{H.4}$$

A similar contour integral with the same structures in the complex z-plane was found in the calculation of the polarization loop $\varPi_M$. We perform the same steps as they are shown in Fig. C.3. This leads to the integral

$$\begin{aligned}\varGamma^{ij}_{\eta\,\mathrm{loop}\,M} = \sum_M 2g\varGamma_M \int \frac{\mathrm{d}^3 l}{(2\pi)^3} \int_{-\infty}^{+\infty} \frac{\mathrm{d}l_0}{2\pi i} \Big\{ &+ n_F(l_0 + i\epsilon) K^{ij}_{\mathrm{loop}\,M}(l_0 + \mu + i\epsilon, l_0 + i\omega_e + \mu + i\epsilon) \\ &- n_F(l_0 - i\epsilon) K^{ij}_{\mathrm{loop}\,M}(l_0 + \mu - i\epsilon, l_0 + i\omega_e + \mu - i\epsilon) \\ &+ n_F(l_0 - i\omega_e + i\epsilon) K^{ij}_{\mathrm{loop}\,M}(l_0 + \mu - i\omega_e + i\epsilon, l_0 + \mu + i\epsilon) \\ &- n_F(l_0 - i\omega_e - i\epsilon) K^{ij}_{\mathrm{loop}\,M}(l_0 + \mu - i\omega_e - i\epsilon, l_0 + \mu - i\epsilon)\Big\}.\end{aligned} \tag{H.5}$$

The periodicity of n_F for imaginary arguments lead to the expression

$$\begin{aligned}\varGamma^{ij}_{\eta\,\mathrm{loop}\,M} = \sum_M 2g\varGamma_M \int \frac{\mathrm{d}^3 l}{(2\pi)^3} \int_{-\infty}^{+\infty} \frac{\mathrm{d}l_0}{2\pi i} n_F(l_0) \Big\{ &+ K^{ij}_{\mathrm{loop}\,M}(l_0 + \mu + i\epsilon, l_0 + i\omega_e + \mu) \\ &- K^{ij}_{\mathrm{loop}\,M}(l_0 + \mu - i\epsilon, l_0 + i\omega_e + \mu) + K^{ij}_{\mathrm{loop}\,M}(l_0 + \mu - i\omega_e, l_0 + \mu + i\epsilon) \\ &- K^{ij}_{\mathrm{loop}\,M}(l_0 + \mu - i\omega_e, l_0 + \mu - i\epsilon)\Big\},\end{aligned} \tag{H.6}$$

where we could eliminate all infinitesimal imaginary parts $i\epsilon$ where the limit $\epsilon \to 0$ was continuous. The integration variable l_0 can be shifted by μ,

$$\begin{aligned} \Gamma^{ij}_{\eta\,\mathrm{loop}\,M} =& \sum_M 2g\Gamma_M \int \frac{\mathrm{d}^3 l}{(2\pi)^3} \int_{-\infty}^{+\infty} \frac{\mathrm{d}l_0}{2\pi i} n_F(l_0-\mu) \Big\{ + K^{ij}_{\mathrm{loop}\,M}(l_0+i\epsilon, l_0+i\omega_e) \\ & - K^{ij}_{\mathrm{loop}\,M}(l_0-i\epsilon, l_0+i\omega_e) + K^{ij}_{\mathrm{loop}\,M}(l_0-i\omega_e, l_0+i\epsilon) \\ & - K^{ij}_{\mathrm{loop}\,M}(l_0-i\omega_e, l_0-i\epsilon)\Big\}, \end{aligned} \tag{H.7}$$

and now the analytical continuation $i\omega_e \to q_0 + i\epsilon$ can be performed to get the retarded vertex contribution

$$\begin{aligned} {\Gamma^{ij}_{\eta\,\mathrm{loop}\,M}}^R =& \sum_M 2g\Gamma_M \int \frac{\mathrm{d}^3 l}{(2\pi)^3} \int_{-\infty}^{+\infty} \frac{\mathrm{d}l_0}{2\pi i} n_F(l_0-\mu) \Big\{ + K^{ij}_{\mathrm{loop}\,M}(l_0+i\epsilon, l_0+q_0+i\epsilon) \\ & - K^{ij}_{\mathrm{loop}\,M}(l_0-i\epsilon, l_0+q_0+i\epsilon) + K^{ij}_{\mathrm{loop}\,M}(l_0-q_0-i\epsilon, l_0+i\epsilon) \\ & - K^{ij}_{\mathrm{loop}\,M}(l_0-q_0-i\epsilon, l_0-i\epsilon)\Big\}. \end{aligned} \tag{H.8}$$

In the end, we split the vertex into a vacuum and a medium part with the usual trick (see appendix C for details) and obtain

$$\begin{aligned} {\Gamma^{ij}_{\eta\,\mathrm{loop}\,M}}^R =& \sum_M 2g\Gamma_M \int \frac{\mathrm{d}^3 l}{(2\pi)^3} \int_0^{\infty} \frac{\mathrm{d}l_0}{2\pi i} \Bigg\{ \Big[1-n_F(l_0+\mu)\Big] \Big[K^{ij}_{\mathrm{loop}\,M}(-l_0+i\epsilon, -l_0+q_0+i\epsilon) \\ & - K^{ij}_{\mathrm{loop}\,M}(-l_0-i\epsilon, -l_0+q_0+i\epsilon) + K^{ij}_{\mathrm{loop}\,M}(-l_0-q_0-i\epsilon, -l_0+i\epsilon) \\ & - K^{ij}_{\mathrm{loop}\,M}(-l_0-q_0-i\epsilon, -l_0-i\epsilon)\Big] \\ & + n_F(l_0-\mu)\Big[K^{ij}_{\mathrm{loop}\,M}(l_0+i\epsilon, l_0+q_0+i\epsilon) \\ & - K^{ij}_{\mathrm{loop}\,M}(l_0-i\epsilon, l_0+q_0+i\epsilon) + K^{ij}_{\mathrm{loop}\,M}(l_0-q_0-i\epsilon, l_0+i\epsilon) \\ & - K^{ij}_{\mathrm{loop}\,M}(l_0-q_0-i\epsilon, l_0-i\epsilon)\Big]\Bigg\}. \end{aligned} \tag{H.9}$$

This is the final result, the retarded vertex contribution as a function of the external real momentum q_0.

Summation of the bare vertex

An important issue is the special case of the RPA-like summation of fermion loops in the Green-Kubo relation. This correspond to a series of polarization loops, where all possible chains have the functions

$$\Pi\big|_{end} = \sum_M -T \sum_{i\omega_l} \int \frac{\mathrm{d}^3 l}{(2\pi)^3} 2g\mathrm{Tr}\left[l^i\gamma^j S(i\omega_l+\mu, \mathbf{1})\Gamma_M S(i\omega_l+i\omega_e+\mu, \mathbf{1})\right] \tag{H.10}$$

at their ends. This is exactly the quark loop part of the vertex iteration formula, with the difference that the bare vertex from the Green-Kubo relation enters in the expression and not the fully dressed one. It is easy to show that this Feynman diagram element is equal to zero. For $M = \pi^a$, the Pauli matrices in isospin space lead to a vanishing trace in the integrand. The scalar channel is also equal to zero since the integrand is odd in l^i due to the factor from the energy-momentum tensor. That means that only the single quark loop contributes to the viscosity if the vertex equation is truncated to the first two diagrams.

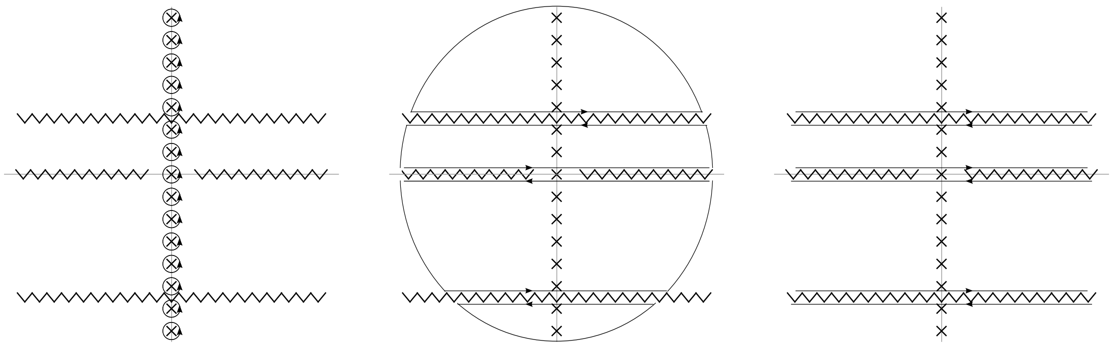

(a) (b) (c)

Figure H.1: Integration contours for the one-meson part of the viscosity vertex. (a) is the rewritten Matsubara sum involving the contour C, which is deformed in (b) in order to arrive at the final form (c).

H.2 One-meson part

The one-meson part of the vertex iteration equation reads

$$\varGamma^{ij}_{\eta\,1\text{ meson}\,M} = \sum_M -T\sum_{i\omega_l}\int\frac{\mathrm{d}^3l}{(2\pi)^3}K^{ij}_{1\text{ meson}\,M}((i\omega_l+i\omega_{p_2}+\mu,\mathbf{p}+\mathbf{l}),(i\omega_l,\mathbf{l}),(i\omega_l+i\omega_{p_1}+\mu,\mathbf{p}+\mathbf{l})), \tag{H.11}$$

where the integrand is defined by the equation

$$K^{ij}_{1\text{ meson}\,M}(k_1,k_2,k_3) = \varGamma^{ij}_{\eta}(k_1,k_3)S(k_1)\varGamma_M D_M(k_2)\varGamma_M S(k_3). \tag{H.12}$$

As usual, we rewrite the summation over the bosonic Matsubara frequencies as a contour integral, with a contour C around the poles of the Bose distribution function n_B,

$$\begin{aligned} K^{ij}_{1\text{ meson}\,M} =& \sum_M -\int\frac{\mathrm{d}^3l}{(2\pi)^3}\oint_C\frac{\mathrm{d}z}{2\pi i}\Big\{n_B(z)\times \\ &\times K^{ij}_{1\text{ meson}\,M}((z+i\omega_{p_2}+\mu,\mathbf{p}+\mathbf{l}),(z,\mathbf{l}),(z+i\omega_{p_1}+\mu,\mathbf{p}+\mathbf{l}))\Big\}. \end{aligned} \tag{H.13}$$

The 3-momentum arguments of the kernel will not change in the whole calculation, thus we suppress them for simplicity in the rest of the section. The integration path of the variable z can be deformed depending on the structure of the kernel. There are three propagators with different arguments in the integrand, each of them has a branch cut on the real axis. The condition can be written as

$$z+i\omega_{p_2}\in\mathbb{R} \quad\text{or}\quad z\in\mathbb{R} \quad\text{or}\quad z+i\omega_{p_1}\in\mathbb{R}, \tag{H.14}$$

thus we have a situation as it is shown in Fig. H.1. We deform the integration contour as it is indicated in Figs. H.1(b) and H.1(c), which leads to the expression

$$\begin{aligned} \varGamma^{ij}_{\eta\,1\text{ meson}\,M} =& \sum_M -\int\frac{\mathrm{d}^3l}{(2\pi)^3}\int_{-\infty}^{+\infty}\frac{\mathrm{d}l_0}{2\pi i}\Big\{n_B(l_0)\big[K^{ij}_{1\text{ meson}\,M}(l_0+i\omega_{p_2}+\mu,l_0+i\epsilon,l_0+i\omega_{p_1}+\mu) \\ &\qquad - K^{ij}_{1\text{ meson}\,M}(l_0+i\omega_{p_2}+\mu,l_0-i\epsilon,l_0+i\omega_{p_1}+\mu)\big] \\ &+ n_B(l_0-i\omega_{p_1})\big[K^{ij}_{1\text{ meson}\,M}(l_0+i\omega_{p_2}-i\omega_{p_1}+\mu,l_0-i\omega_{p_1},l_0+\mu+i\epsilon) \\ &\qquad - K^{ij}_{1\text{ meson}\,M}(l_0+i\omega_{p_2}-i\omega_{p_1}+\mu,l_0-i\omega_{p_1},l_0+\mu-i\epsilon)\big] \\ &+ n_B(l_0-i\omega_{p_2})\big[K^{ij}_{1\text{ meson}\,M}(l_0+\mu+i\epsilon,l_0-i\omega_{p_2},l_0+i\omega_{p_1}-i\omega_{p_2}+\mu) \\ &\qquad - K^{ij}_{1\text{ meson}\,M}(l_0+\mu-i\epsilon,l_0-i\omega_{p_2},l_0+i\omega_{p_1}-i\omega_{p_2}+\mu)\big]\Big\}. \end{aligned} \tag{H.15}$$

The continuity of the Bose distribution functions and the propagators for complex arguments have already been implemented (see Sec. H.1 for details). We use the relation (B.6) to eliminate the fermionic Matsubara frequencies in the arguments of the Bose distribution functions and arrive at

$$\begin{aligned}\mathit{\Gamma}^{ij}_{\eta\,1\ \mathrm{meson}\ M} =& \sum_M - \int \frac{\mathrm{d}^3 l}{(2\pi)^3} \int_{-\infty}^{+\infty} \frac{\mathrm{d}l_0}{2\pi i} \Big\{ n_B(l_0) \big[K^{ij}_{1\ \mathrm{meson}\ M}(l_0 + i\omega_{p_2} + \mu, l_0 + i\epsilon, l_0 + i\omega_{p_1} + \mu) \\ &\qquad - K^{ij}_{1\ \mathrm{meson}\ M}(l_0 + i\omega_{p_2} + \mu, l_0 - i\epsilon, l_0 + i\omega_{p_1} + \mu) \big] \\ & - n_F(l_0) \big[K^{ij}_{1\ \mathrm{meson}\ M}(l_0 + i\omega_{p_2} - i\omega_{p_1} + \mu, l_0 - i\omega_{p_1}, l_0 + \mu + i\epsilon) \\ &\qquad - K^{ij}_{1\ \mathrm{meson}\ M}(l_0 + i\omega_{p_2} - i\omega_{p_1} + \mu, l_0 - i\omega_{p_1}, l_0 + \mu - i\epsilon) \big] \\ & - n_F(l_0) \big[K^{ij}_{1\ \mathrm{meson}\ M}(l_0 + \mu + i\epsilon, l_0 - i\omega_{p_2}, l_0 + i\omega_{p_1} - i\omega_{p_2} + \mu) \\ &\qquad - K^{ij}_{1\ \mathrm{meson}\ M}(l_0 + \mu - i\epsilon, l_0 - i\omega_{p_2}, l_0 + i\omega_{p_1} - i\omega_{p_2} + \mu) \big] \Big\}. \end{aligned} \tag{H.16}$$

We first perform the analytic continuation for the external momentum p_1, and then the continuation p_2. This leads to the retarded vertex contribution

$$\begin{aligned}{\mathit{\Gamma}^{ij}_{\eta\,1\ \mathrm{meson}\ M}}^R =& \sum_M - \int \frac{\mathrm{d}^3 l}{(2\pi)^3} \int_{-\infty}^{+\infty} \frac{\mathrm{d}l_0}{2\pi i} \Big\{ n_B(l_0) \big[K^{ij}_{1\ \mathrm{meson}\ M}(l_0 + i\omega_{p_2} + \mu, l_0 + i\epsilon, l_0 + i\omega_{p_1} + \mu) \\ &\qquad - K^{ij}_{1\ \mathrm{meson}\ M}(l_0 + p_2^0 + \mu + i\epsilon, l_0 - i\epsilon, l_0 + p_1^0 + \mu + i\epsilon) \big] \\ & - n_F(l_0) \big[K^{ij}_{1\ \mathrm{meson}\ M}(l_0 + p_2^0 - p_1^0 + \mu + i\epsilon, l_0 - p_1^0 - i\epsilon, l_0 + \mu + i\epsilon) \\ &\quad - K^{ij}_{1\ \mathrm{meson}\ M}(l_0 + p_2^0 - p_1^0 + \mu + i\epsilon, l_0 - p_1^0 - i\epsilon, l_0 + \mu - i\epsilon) \\ &\quad + K^{ij}_{1\ \mathrm{meson}\ M}(l_0 + \mu + i\epsilon, l_0 - p_2^0 - i\epsilon, l_0 + p_1^0 - p_2^0 + \mu - i\epsilon) \\ &\quad - K^{ij}_{1\ \mathrm{meson}\ M}(l_0 + \mu - i\epsilon, l_0 - p_2^0 - i\epsilon, l_0 + p_1^0 - p_2^0 + \mu - i\epsilon) \big] \Big\}. \end{aligned} \tag{H.17}$$

The splitting of the l_0-integral yields the identification of the vacuum part and the medium part. This procedure, which is analog to the calculation in Sec. H.1, leads to the final equation

$$\begin{aligned}{\mathit{\Gamma}^{ij}_{\eta\,1\ \mathrm{meson}\ M}}^R =& - \sum_M \int \frac{\mathrm{d}^3 l}{(2\pi)^3} \int_0^{\infty} \frac{\mathrm{d}l_0}{2\pi i} \Bigg\{ [1 - n_B(l_0)] \times \\ & \times \Big[K^{ij}_{1\ \mathrm{meson}\ M}(-l_0 + \mu + i\epsilon, -l_0 + i\epsilon, -l_0 + q_0 + \mu + i\epsilon) \\ & - K^{ij}_{1\ \mathrm{meson}\ M}(-l_0 + \mu + i\epsilon, -l_0 - i\epsilon, -l_0 + q_0 + \mu + i\epsilon) \\ & - n_B(l_0) \Big[K^{ij}_{1\ \mathrm{meson}\ M}(l_0 + \mu + i\epsilon, l_0 + i\epsilon, l_0 + q_0 + \mu + i\epsilon) \\ & - K^{ij}_{1\ \mathrm{meson}\ M}(l_0 + \mu + i\epsilon, l_0 - i\epsilon, l_0 + q_0 + \mu + i\epsilon) \Big] \\ & - [1 - n_F(l_0)] \Big[K^{ij}_{1\ \mathrm{meson}\ M}(-l_0 - q_0 + \mu + i\epsilon, -l_0 - q_0 - i\epsilon, -l_0 + \mu + i\epsilon) \\ & - K^{ij}_{1\ \mathrm{meson}\ M}(-l_0 - q_0 + \mu + i\epsilon, -l_0 - q_0 - i\epsilon, -l_0 + \mu - i\epsilon) \\ & + K^{ij}_{1\ \mathrm{meson}\ M}(-l_0 + \mu + i\epsilon, -l_0 - i\epsilon, -l_0 + q_0 + \mu - i\epsilon) \\ & - K^{ij}_{1\ \mathrm{meson}\ M}(-l_0 + \mu - i\epsilon, -l_0 - i\epsilon, -l_0 + q_0 + \mu - i\epsilon) \Big] \\ & - n_F(l_0) \Big[K^{ij}_{1\ \mathrm{meson}\ M}(l_0 - q_0 + \mu + i\epsilon, l_0 - q_0 - i\epsilon, l_0 + \mu + i\epsilon) \\ & - K^{ij}_{1\ \mathrm{meson}\ M}(l_0 - q_0 + \mu + i\epsilon, l_0 - q_0 - i\epsilon, l_0 + \mu - i\epsilon) \\ & + K^{ij}_{1\ \mathrm{meson}\ M}(l_0 + \mu + i\epsilon, l_0 - i\epsilon, l_0 + q_0 + \mu - i\epsilon) \\ & - K^{ij}_{1\ \mathrm{meson}\ M}(l_0 + \mu - i\epsilon, l_0 - i\epsilon, l_0 + q_0 + \mu - i\epsilon) \Big] \Bigg\}. \end{aligned} \tag{H.18}$$

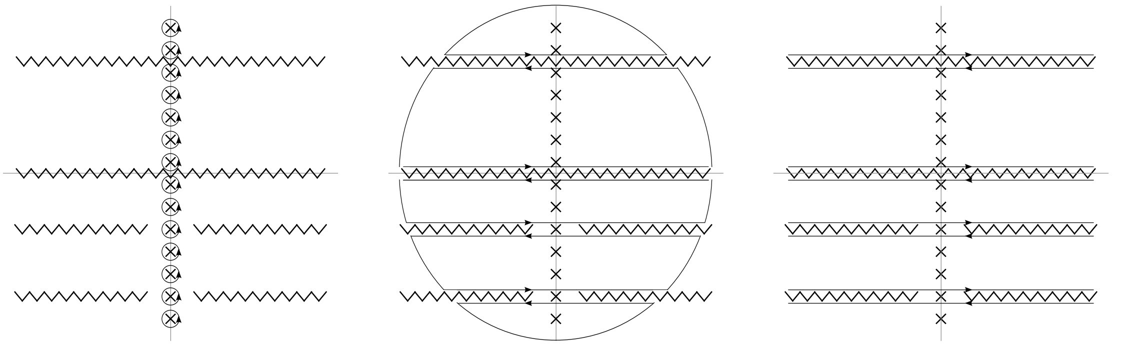
(a) (b) (c)

Figure H.2: Integration contours for the two-meson contribution to the viscosity vertex. The Matsubara sum over $i\omega_k$ in Eq. H.19 is written as the integration along the contour C in (a). The contour is deformed as it is shown in (b) and (c).

The medium part consists of the terms proportional to the distribution functions n_B and n_F.

H.3 Two-meson part

The last diagram in the vertex equation involves two mesons,

$$\begin{aligned}\mathit{\Gamma}^{ij}_{\eta\,2\text{ mesons }M_1M_2} = & \sum_{M_1,\,M_2} -T\sum_{i\omega_l}\int\frac{\mathrm{d}^3l}{(2\pi)^3} - T\sum_{i\omega_k}\int\frac{\mathrm{d}^3k}{(2\pi)^3}\times \\ & \times\Big\{\mathit{\Lambda}^{ij}_{2\text{ mesons }M_1M_2}(i\omega_l+i\omega_{p_1}+\mu, i\omega_l-i\omega_k+\mu, i-\omega_l+i\omega_{p_2}+\mu)\times \\ & \times K_{2\text{ mesons }M_1M_2}(i\omega_k+i\omega_{p_1}, i\omega_k+\mu, i\omega_k+i\omega_{p_2})\Big\}. \end{aligned} \tag{H.19}$$

The two functions in the integrand $\mathit{\Lambda}^{ij}_{2\text{ mesons }M_1M_2}$ and $K_{2\text{ mesons }M_1M_2}$ are

$$\mathit{\Lambda}^{ij}_{2\text{ mesons }M_1M_2}(k_1,k_2,k_3) = \mathrm{Tr}\left[\mathit{\Gamma}^{ij}_{\eta}(k_1,k_3), S(k_1)\mathit{\Gamma}_{M_2}S(k_2)\mathit{\Gamma}_{M_1}S(k_3)\right] \tag{H.20}$$

and

$$K_{2\text{ mesons }M_1M_2}(k_1,k_2,k_3) = D_{M_1}(k_1)\mathit{\Gamma}_{M_1}S(k_2)\mathit{\Gamma}_{M_2}D_{M_2}(k_3). \tag{H.21}$$

We want to proceed in the same way as we did for the other vertex contributions: we start with the formulation of one of the Matsubara sums as a contour integral. If we do this with the summation over the fermionic Matsubara frequencies $i\omega_k$, the result is

$$\begin{aligned}\mathit{\Gamma}^{ij}_{\eta\,2\text{ mesons }M_1M_2} = & \sum_{M_1,\,M_2} -T\sum_{i\omega_l}\int\frac{\mathrm{d}^3l}{(2\pi)^3}\int\frac{\mathrm{d}^3k}{(2\pi)^3}\oint_C\frac{\mathrm{d}z_k}{2\pi i}n_F(z_k)\times \\ & \times\Big\{\mathit{\Lambda}^{ij}_{2\text{ mesons }M_1M_2}(i\omega_l+i\omega_{p_1}+\mu, i\omega_l-z_k+\mu, i\omega_l+i\omega_{p_2}+\mu)\times \\ & \times K_{2\text{ mesons }M_1M_2}(z_k+i\omega_{p_1}, z_k+\mu, z_k+i\omega_{p_2})\Big\}. \end{aligned} \tag{H.22}$$

The integration contour can be deformed in the complex z_k-plane. The integrand has four different branch cuts due to the different propagators S_1 and D_M. The situation is sketched in Fig. H.2(a), including the poles of $n_F(z_k)$ and the integration contour C. If the contour C is deformed in a way that is shown in Figs. H.2(b) and H.2(c), we obtain an integral along the lines parametrized by the formulas

$$C_{1,2}(k_0) = k_0 + i\omega_l \pm i\epsilon \qquad C_{3,4}(k_0) = k_0 \pm i\epsilon$$
$$C_{5,6}(k_0) = k_0 - i\omega_{p_1} \pm i\epsilon \qquad C_{7,8}(k_0) = k_0 - i\omega_{p_2} \pm i\epsilon$$

for $k_0 \in \mathbb{R}$. This leads to the sum

$$
\begin{aligned}
\varGamma^{ij}_{\eta\,2\ \mathrm{mesons}\,M_1 M_2} = \sum_{M_1,\,M_2} -T \sum_{i\omega_l} \int \frac{\mathrm{d}^3 l}{(2\pi)^3} \int \frac{\mathrm{d}^3 k}{(2\pi)^3} \int_{-\infty}^{+\infty} \frac{\mathrm{d}k_0}{2\pi i} \Big\{& \\
n_F(k_0 + i\omega_l) \Big[K_{2\ \mathrm{mesons}\,M_1 M_2}(k_0 + i\omega_l + i\omega_{p_1}, k_0 + i\omega_l + \mu, k_0 + i\omega_l + i\omega_{p_2}) \times & \\
\times \varLambda^{ij}_{2\ \mathrm{mesons}\,M_1 M_2}(i\omega_l + i\omega_{p_1} + \mu, -k_0 + \mu - i\epsilon, i\omega_l + i\omega_{p_2} + \mu) & \\
- K_{2\ \mathrm{mesons}\,M_1 M_2}(k_0 + i\omega_l + i\omega_{p_1}, k_0 + i\omega_l + \mu, k_0 + i\omega_l + i\omega_{p_2}) \times & \\
\times \varLambda^{ij}_{2\ \mathrm{mesons}\,M_1 M_2}(i\omega_l + i\omega_{p_1} + \mu, -k_0 + \mu + i\epsilon, i\omega_l + i\omega_{p_2} + \mu) \Big] & \\
+ n_F(k_0) \Big[K_{2\ \mathrm{mesons}\,M_1 M_2}(k_0 + i\omega_{p_1}, k_0 + \mu + i\epsilon, k_0 + i\omega_{p_2}) \times & \\
\times \varLambda^{ij}_{2\ \mathrm{mesons}\,M_1 M_2}(i\omega_l + i\omega_{p_1} + \mu, i\omega_l - k_0 + \mu, i\omega_l + i\omega_{p_2} + \mu) & \\
- K_{2\ \mathrm{mesons}\,M_1 M_2}(k_0 + i\omega_{p_1}, k_0 + \mu - i\epsilon, k_0 + i\omega_{p_2}) \times & \\
\times \varLambda^{ij}_{2\ \mathrm{mesons}\,M_1 M_2}(i\omega_l + i\omega_{p_1} + \mu, i\omega_l - k_0 + \mu, i\omega_l + i\omega_{p_2} + \mu) \Big] & \\
+ n_F(k_0 - i\omega_{p_1}) \Big[K_{2\ \mathrm{mesons}\,M_1 M_2}(k_0 + i\epsilon, k_0 - i\omega_{p_1} + \mu, k_0 - i\omega_{p_1} + i\omega_{p_2}) \times & \\
\times \varLambda^{ij}_{2\ \mathrm{mesons}\,M_1 M_2}(i\omega_l + i\omega_{p_1} + \mu, i\omega_l - k_0 - i\omega_{p_1} + \mu, i\omega_l + i\omega_{p_2} + \mu) & \\
- K_{2\ \mathrm{mesons}\,M_1 M_2}(k_0 - i\epsilon, k_0 - i\omega_{p_1} + \mu, k_0 - i\omega_{p_1} + i\omega_{p_2}) \times & \\
\times \varLambda^{ij}_{2\ \mathrm{mesons}\,M_1 M_2}(i\omega_l + i\omega_{p_1} + \mu, i\omega_l - k_0 - i\omega_{p_1} + \mu, i\omega_l + i\omega_{p_2} + \mu) \Big] & \\
+ n_F(k_0 - i\omega_{p_2}) \Big[K_{2\ \mathrm{mesons}\,M_1 M_2}(k_0 - i\omega_{p_2} + i\omega_{p_1}, k_0 - i\omega_{p_2} + \mu, k_0 + i\epsilon) \times & \\
\times \varLambda^{ij}_{2\ \mathrm{mesons}\,M_1 M_2}(i\omega_l + i\omega_{p_1} + \mu, i\omega_l - k_0 - i\omega_{p_2} + \mu, i\omega_l + i\omega_{p_2} + \mu) \Big] \Big\}. &
\end{aligned}
\tag{H.23}
$$

This is the result for the first Matsubara sum, where one can simplify the distribution functions

$$
n_F(k_0 + i\omega_l) = n_F(k_0), \quad n_F(k_0 - i\omega_{p_1}) = -n_B(k_0), \quad n_F(k_0 - i\omega_{p_2}) = -n_B(k_0). \tag{H.24}
$$

Now, the next Matsubara sum can be expressed as a contour integral,

$$
-T \sum_{i\omega_l} \Big(\ldots \Big) \to \oint_C \frac{\mathrm{d}z_l}{2\pi i} n_B(z_l) \Big(\ldots \Big). \tag{H.25}
$$

One can estimate that the number of branch cuts in the complex plane of z_l is more complex than for z_k, which was shown in Fig. H.2. Indeed, there are five branch cuts in the whole integrand, which results in a sum of integrals along the curves

$$
\begin{aligned}
C_{1,2} &= l_0 - i\omega_{p_1} \pm i\epsilon & \qquad C_{3,4} &= l_0 + i\omega_{p_1} \pm i\epsilon \\
C_{5,6} &= l_0 - i\omega_{p_2} \pm i\epsilon & \qquad C_{7,8} &= l_0 + i\omega_{p_2} \pm i\epsilon \\
C_{9,10} &= l_0 \pm i\epsilon. & &
\end{aligned}
\tag{H.26}
$$

for real l_0. If one wrote down this sum explicitly, one would end up with a sum of 80 terms, a formula that is ten times longer than Eq. (H.23). We stop the calculation at this point. The complete derivation of the retarded two-meson contribution to the shear viscosity vertex would additionally require the analytical continuation of the two external momenta p_1 and p_2.

Bibliography

[1] M. Gell-Mann, "A schematic model of baryons and mesons," *Physics Letters* **8** no. 3, (1964) 214–215.

[2] G. Zweig, "An SU_3 model for strong interaction symmetry and its breaking; Part I," *CERN-TH-401* (1964) 1–25.

[3] G. Zweig, "An SU_3 model for strong interaction symmetry and its breaking; Part II," *CERN-TH-412* (1964) 1–80.

[4] S. Weinberg, "Non-Abelian Gauge Theories of the Strong Interactions," *Phys. Rev. Lett.* **31** no. 7, (1973) 494–497.

[5] H. Fritzsch, M. Gell-Mann, and H. Leutwyler, "Advantages of the color octet gluon picture," *Physics Letters B* **47** no. 4, (1973) 365 – 368.

[6] D. J. Gross and F. Wilczek, "Asymptotically Free Gauge Theories. I," *Phys. Rev. D* **8** no. 10, (1973) 3633–3652.

[7] D. J. Gross and F. Wilczek, "Ultraviolet Behavior of Non-Abelian Gauge Theories," *Phys. Rev. Lett.* **30** no. 26, (1973) 1343–1346.

[8] H. D. Politzer, "Reliable Perturbative Results for Strong Interactions?," *Phys. Rev. Lett.* **30** no. 26, (1973) 1346–1349.

[9] R. Hagedorn, "Statistical thermodynamics of strong interactions at high- energies," *Nuovo Cim. Suppl.* **3** (1965) 147–186.

[10] S. Frautschi, "Statistical Bootstrap Model of Hadrons," *Phys. Rev. D* **3** no. 11, (1971) 2821–2834.

[11] N. Cabibbo and G. Parisi, "Exponential hadronic spectrum and quark liberation," *Physics Letters B* **59** no. 1, (1975) 67 – 69.

[12] J. C. Collins and M. J. Perry, "Superdense Matter: Neutrons or Asymptotically Free Quarks?," *Phys. Rev. Lett.* **34** no. 21, (1975) 1353–1356.

[13] E. V. Shuryak, "Quark-gluon plasma and hadronic production of leptons, photons and psions," *Physics Letters B* **78** no. 1, (1978) 150–153.

[14] Y. Aoki, G. Endrodi, Z. Fodor, S. D. Katz, and K. K. Szabo, "The order of the quantum chromodynamics transition predicted by the standard model of particle physics," *Nature* **443** (2006) 675–678, `arXiv:hep-lat/0611014`.

[15] Y. Aoki, Z. Fodor, S. Katz, and K. Szabó, "The QCD transition temperature: Results with physical masses in the continuum limit," *Physics Letters B* **643** no. 1, (2006) 46 – 54, `arXiv:hep-lat/0609068`.

[16] M. Cheng *et al.*, "Transition temperature in QCD," *Phys. Rev. D* **74** no. 5, (2006) 054507, `arXiv:hep-lat/0608013`.

[17] Y. Nambu and G. Jona-Lasinio, "Dynamical Model of Elementary Particles Based on an Analogy with Superconductivity. I," *Phys. Rev.* **122** no. 1, (1961) 345–358.

[18] Y. Nambu and G. Jona-Lasinio, "Dynamical model of elementary particles based on an analogy with superconductivity. II," *Phys. Rev.* **124** (1961) 246–254.

[19] B. C. Barrois, "Superconducting quark matter," *Nuclear Physics B* **129** no. 3, (1977) 390–396.

[20] D. Bailin and A. Love, "Superfluidity and superconductivity in relativistic fermion systems," *Physics Reports* **107** no. 6, (1984) 325–385.

[21] P. Braun-Munzinger and J. Wambach, "Colloquium: Phase diagram of strongly interacting matter," *Rev. Mod. Phys.* **81** no. 3, (2009) 1031–1050.

[22] M. G. Alford, A. Schmitt, K. Rajagopal, and T. Schäfer, "Color superconductivity in dense quark matter," *Rev. Mod. Phys.* **80** no. 4, (2008) 1455–1515, `arXiv:0709.4635 [hep-ph]`.

[23] M. Gyulassy and L. McLerran, "New forms of QCD matter discovered at RHIC," *Nuclear Physics A* **750** no. 1, (2005) 30–63, `arXiv:nucl-th/0405013`. Quark-Gluon Plasma. New Discoveries at RHIC: Case for the Strongly Interacting Quark-Gluon Plasma. Contributions from the RBRC Workshop held May 14-15, 2004.

[24] P. Braun-Munzinger and J. Stachel, "The quest for the quark-gluon plasma," *Nature* **448** (2007) 302–309.

[25] CERN, "New state of matter created at CERN." Press release, 2000. PR01.00.

[26] U. W. Heinz and M. Jacob, "Evidence for a new state of matter: An assessment of the results from the CERN lead beam programme," `arXiv:nucl-th/0002042`.

[27] L. D. Landau, "On the multiparticle production in high-energy collisions," *Izv. Akad. Nauk SSSR Ser. Fiz.* **17** (1953) 51–64.

[28] A. Andronic, P. Braun-Munzinger, and J. Stachel, "Hadron production in central nucleus-nucleus collisions at chemical freeze-out," *Nuclear Physics A* **772** no. 3–4, (2006) 167–199, `arXiv:nucl-th/0511071`.

[29] T. Matsui and H. Satz, "J/psi Suppression by Quark-Gluon Plasma Formation," *Phys. Lett.* **B178** (1986) 416.

[30] X.-N. Wang and M. Gyulassy, "Gluon shadowing and jet quenching in A+A collisions at $\sqrt{s}$ =200A GeV," *Phys. Rev. Lett.* **68** no. 10, (1992) 1480–1483.

[31] I. Arsene *et al.*, "Quark-gluon plasma and color glass condensate at RHIC? The perspective from the BRAHMS experiment," *Nuclear Physics A* **757** no. 1–2, (2005) 1–27, `arXiv:nucl-ex/0410020`. First Three Years of Operation of RHIC.

[32] B. Back *et al.*, "The PHOBOS perspective on discoveries at RHIC," *Nuclear Physics A* **757** no. 1–2, (2005) 28–101, `arXiv:nucl-ex/0410022`. First Three Years of Operation of RHIC.

[33] J. Adams *et al.*, "Experimental and theoretical challenges in the search for the quark-gluon plasma: The STAR Collaboration's critical assessment of the evidence from RHIC collisions," *Nuclear Physics A* **757** no. 1–2, (2005) 102–183, `arXiv:nucl-ex/0501009`. First Three Years of Operation of RHIC.

[34] K. Adcox *et al.*, "Formation of dense partonic matter in relativistic nucleus-nucleus collisions at RHIC: Experimental evaluation by the PHENIX Collaboration," *Nuclear Physics A* **757** no. 1-2, (2005) 184 – 283. First Three Years of Operation of RHIC.

[35] J.-Y. Ollitrault, "Anisotropy as a signature of transverse collective flow," *Phys. Rev. D* **46** no. 1, (1992) 229–245.

[36] **(E877 Collaboration)** Collaboration, J. Barrette *et al.*, "Observation of Anisotropic Event Shapes and Transverse Flow in Ultrarelativistic Au + Au Collisions," *Phys. Rev. Lett.* **73** no. 19, (1994) 2532–2535.

[37] S. Voloshin and Y. Zhang, "Flow study in relativistic nuclear collisions by Fourier expansion of azimuthal particle distributions," *Zeitschrift für Physik C Particles and Fields* **70** (1996) 665–671, `arXiv:hep-ph/9407282`.

[38] A. M. Poskanzer and S. A. Voloshin, "Methods for analyzing anisotropic flow in relativistic nuclear collisions," *Phys. Rev.* **C58** (1998) 1671–1678, `arXiv:nucl-ex/9805001`.

[39] **(STAR Collaboration)** Collaboration, K. H. Ackermann *et al.*, "Elliptic Flow in $Au + Au$ Collisions at $\sqrt{s_{NN}} = 130GeV$," *Phys. Rev. Lett.* **86** no. 3, (2001) 402–407, `arXiv:nucl-ex/0009011`.

[40] E. V. Shuryak, "Quantum Chromodynamics and the Theory of Superdense Matter," *Phys. Rept.* **61** (1980) 71–158.

[41] J. D. Bjorken, "Highly relativistic nucleus-nucleus collisions: The central rapidity region," *Phys. Rev. D* **27** no. 1, (1983) 140–151.

[42] P. Huovinen, P. F. Kolb, U. W. Heinz, P. V. Ruuskanen, and S. A. Voloshin, "Radial and elliptic flow at RHIC: further predictions," *Phys. Lett.* **B503** (2001) 58–64, `arXiv:hep-ph/0101136`.

[43] D. Teaney, J. Lauret, and E. V. Shuryak, "Hydro + Cascade, flow, the equation of state, predictions and data," *Nucl. Phys.* **A698** (2002) 479–482, `arXiv:nucl-th/0104041`.

[44] **PHENIX Collaboration** Collaboration, A. Adare *et al.*, "Scaling Properties of Azimuthal Anisotropy in $Au + Au$ and $Cu + Cu$ Collisions at $\sqrt{s_{NN}} = 200\ GeV$," *Phys. Rev. Lett.* **98** no. 16, (2007) 162301, `arXiv:nucl-ex/0608033`.

[45] **STAR** Collaboration, J. Adams *et al.*, "Azimuthal anisotropy in Au + Au collisions at s(NN)**(1/2) = 200-GeV," *Phys. Rev.* **C72** (2005) 014904, `arXiv:nucl-ex/0409033`.

[46] R. Baier, P. Romatschke, and U. A. Wiedemann, "Dissipative hydrodynamics and heavy-ion collisions," *Phys. Rev. C* **73** no. 6, (2006) 064903, `arXiv:hep-ph/0602249`.

[47] M. Luzum and P. Romatschke, "Conformal relativistic viscous hydrodynamics: Applications to RHIC results at $\sqrt{s_{NN}} = 200$ GeV," *Phys. Rev. C* **78** no. 3, (2008) 034915, `arXiv:0804.4015 [nucl-th]`.

[48] M. Luzum and P. Romatschke, "Erratum: Conformal relativistic viscous hydrodynamics: Applications to RHIC results at $\sqrt{s_{NN}} = 200$ GeV [Phys. Rev. C 78, 034915 (2008)]," *Phys. Rev. C* **79** no. 3, (2009) 039903.

[49] H. Song and U. Heinz, "Extracting the QGP viscosity from RHIC data — a status report from viscous hydrodynamics," *Journal of Physics G: Nuclear and Particle Physics* **36** no. 6, (2009) 064033, `arXiv:0812.4274 [nucl-th]`.

[50] P. K. Kovtun, D. T. Son, and A. O. Starinets, "Viscosity in Strongly Interacting Quantum Field Theories from Black Hole Physics," *Phys. Rev. Lett.* **94** no. 11, (2005) 111601, `arXiv:hep-th/0405231`.

[51] A. Peshier and W. Cassing, "The Hot Nonperturbative Gluon Plasma Is an Almost Ideal Colored Liquid," *Phys. Rev. Lett.* **94** no. 17, (2005) 172301, `arXiv:hep-ph/0502138`.

[52] K. M. O'Hara, S. L. Hemmer, M. E. Gehm, S. R. Granade, and J. E. Thomas, "Observation of a Strongly Interacting Degenerate Fermi Gas of Atoms," *Science* **298** no. 5601, (2002) 2179–2182.

[53] J. Kinast, S. L. Hemmer, M. E. Gehm, A. Turlapov, and J. E. Thomas, "Evidence for Superfluidity in a Resonantly Interacting Fermi Gas," *Phys. Rev. Lett.* **92** no. 15, (2004) 150402.

[54] M. Bartenstein, A. Altmeyer, S. Riedl, S. Jochim, C. Chin, J. H. Denschlag, and R. Grimm, "Collective Excitations of a Degenerate Gas at the BEC-BCS Crossover," *Phys. Rev. Lett.* **92** no. 20, (2004) 203201.

[55] J. Kinast, A. Turlapov, and J. E. Thomas, "Breakdown of Hydrodynamics in the Radial Breathing Mode of a Strongly-Interacting Fermi Gas," *Phys. Rev.* **A70** (2004) 051401, `arXiv:cond-mat/0408634`.

[56] P. Massignan, G. M. Bruun, and H. Smith, "Viscous relaxation and collective oscillations in a trapped Fermi gas near the unitarity limit," *Phys. Rev.* **A71** (2005) 033607, `arXiv:cond-mat/0409660`.

[57] G. M. Bruun and H. Smith, "Viscosity and Thermal Relaxation for a resonantly interacting Fermi gas," *Phys. Rev.* **A72** (2005) 043605, `arXiv:cond-mat/0504734`.

[58] G. M. Bruun and H. Smith, "Shear viscosity and damping for a Fermi gas in the unitarity limit," *Phys. Rev.* **A75** (2007) 043612, `arXiv:cond-mat/0612460`.

[59] T. Schafer, "The Shear Viscosity to Entropy Density Ratio of Trapped Fermions in the Unitarity Limit," *Phys. Rev.* **A76** (2007) 063618, `arXiv:cond-mat/0701251`.

[60] J. Bardeen, L. N. Cooper, and J. R. Schrieffer, "Microscopic Theory of Superconductivity," *Phys. Rev.* **106** no. 1, (1957) 162–164.

[61] S. P. Klevansky, "The Nambu-Jona-Lasinio model of quantum chromodynamics," *Rev. Mod. Phys.* **64** (1992) 649–708.

[62] T. Hatsuda and T. Kunihiro, "QCD phenomenology based on a chiral effective Lagrangian," *Phys. Rept.* **247** (1994) 221–367, `arXiv:hep-ph/9401310`.

[63] M. Buballa, "NJL-model analysis of dense quark matter," *Physics Reports* **407** no. 4–6, (2005) 205–376, `arXiv:hep-ph/0402234`.

[64] M. E. Peskin and D. V. Schroeder, *An Introduction to Quantum Field Theory.* Westview Press, 1995.

[65] J. M. Luttinger and J. C. Ward, "Ground-State Energy of a Many-Fermion System. II," *Phys. Rev.* **118** no. 5, (1960) 1417–1427.

[66] G. Baym and L. P. Kadanoff, "Conservation Laws and Correlation Functions," *Phys. Rev.* **124** no. 2, (1961) 287–299.

[67] J. M. Cornwall, R. Jackiw, and E. Tomboulis, "Effective action for composite operators," *Phys. Rev. D* **10** no. 8, (Oct, 1974) 2428–2445.

[68] W. Pauli and F. Villars, "On the Invariant regularization in relativistic quantum theory," *Rev. Mod. Phys.* **21** (1949) 434–444.

[69] M. Oertel, *Investigation of meson loop effects in the Nambu-Jona-Lasinio model.* PhD thesis, Technische Universität Darmstadt, 2000. `arXiv:hep-ph/0012224`.

[70] A. Bazavov *et al.*, "Equation of state and QCD transition at finite temperature," *Phys. Rev. D* **80** no. 1, (2009) 014504, `arXiv:0903.4379 [hep-lat]`.

[71] S. Borsanyi *et al.*, "QCD transition temperature: full staggered result," `arXiv:1011.4230 [hep-lat]`.

[72] **Wuppertal-Budapest** Collaboration, S. Borsanyi *et al.*, "Recent results on QCD thermodynamics: lattice QCD versus Hadron Resonance Gas model," `arXiv:1012.5215 [hep-lat]`.

[73] F. Karsch *et al.*, "Where is the chiral critical point in 3-flavor QCD?," *Nucl. Phys. Proc. Suppl.* **129** (2004) 614–616, `arXiv:hep-lat/0309116`.

[74] P. de Forcrand and O. Philipsen, "Towards the QCD phase diagram," *PoS* **LAT2006** (2006) 130, `arXiv:hep-lat/0611027`.

[75] F. Karsch, B.-J. Schaefer, M. Wagner, and J. Wambach, "Towards finite density QCD with Taylor expansions," `arXiv:1009.5211 [hep-ph]`.

[76] R. D. Pisarski, "Quark-gluon plasma as a condensate of SU(3) Wilson lines," *Phys. Rev.* **D62** (2000) 111501, `arXiv:hep-ph/0006205`.

[77] K. Fukushima, "Chiral effective model with the Polyakov loop," *Phys. Lett.* **B591** (2004) 277–284, `arXiv:hep-ph/0310121`.

[78] C. Ratti, M. A. Thaler, and W. Weise, "Phases of QCD: Lattice thermodynamics and a field theoretical model," *Phys. Rev.* **D73** (2006) 014019, `arXiv:hep-ph/0506234`.

[79] C. Ratti, S. Roessner, M. A. Thaler, and W. Weise, "Thermodynamics of the PNJL model," *Eur. Phys. J.* **C49** (2007) 213–217, `arXiv:hep-ph/0609218`.

[80] E. Quack and S. P. Klevansky, "Effective $1/N_c$ expansion in the Nambu–Jona-Lasinio model," *Phys. Rev. C* **49** no. 6, (1994) 3283–3288.

[81] J. Hüfner, S. P. Klevansky, P. Zhuang, and H. Voss, "Thermodynamics of a quark plasma beyond the mean field: A generalized Beth-Uhlenbeck approach," *Annals Phys.* **234** (1994) 225–244.

[82] V. Dmitrašinović, H. J. Schulze, R. Tegen, and R. H. Lemmer, "Chirally Symmetric (1/NC) Corrections to the Nambu-Jona-Lasinio Model," *Annals of Physics* **238** no. 2, (1995) 332–369.

[83] H. Abuki, "BCS / BEC crossover in quark matter and evolution of its static and dynamic properties: From the atomic unitary gas to color superconductivity," *Nucl. Phys.* **A791** (2007) 117–164, `arXiv:hep-ph/0605081`.

[84] P. Nozières and S. Schmitt-Rink, "Bose condensation in an attractive fermion gas: From weak to strong coupling superconductivity," *Journal of Low Temperature Physics* **59** (1985) 195–211.

[85] R. B. Diener, R. Sensarma, and M. Randeria, "Quantum fluctuations in the superfluid state of the BCS-BEC crossover," *Phys. Rev. A* **77** no. 2, (2008) 023626.

[86] F. Karsch and M. Kitazawa, "Quark propagator at finite temperature and finite momentum in quenched lattice QCD," *Phys. Rev. D* **80** no. 5, (2009) 056001, `arXiv:0906.3941 [hep-lat]`.

[87] C. S. Fischer, "Infrared properties of QCD from Dyson-Schwinger equations," *Journal of Physics G: Nuclear and Particle Physics* **32** no. 8, (2006) R253–R291, `arXiv:hep-ph/0605173`.

[88] C. Fischer and R. Alkofer, "Infrared exponents and running coupling of SU(N) Yang-Mills theories," *Physics Letters B* **536** no. 1-2, (2002) 177–184, `arXiv:hep-ph/0202202`.

[89] J. C. R. Bloch, "Two-Loop Improved Truncation of the Ghost-Gluon Dyson-Schwinger Equations: Multiplicatively Renormalizable Propagators and Nonperturbative Running Coupling," *Few-Body Systems* **33** (2003) 111–152. 10.1007/s00601-003-0013-3.

[90] D. Müller, M. Buballa, and J. Wambach, "The Quark Propagator in the NJL Model in a self-consistent 1/Nc Expansion," *Phys. Rev.* **D81** (2010) 094022, `arXiv:1002.4252 [hep-ph]`.

[91] D. Müller, "Der Quarkpropagator in selbstkonsistenter $1/N_c$ Entwicklung im NJL Modell," Master's thesis, Technische Universität Darmstadt, 2009.

[92] M. Oertel, M. Buballa, and J. Wambach, "Meson loop effects in the NJL model at zero and non-zero temperature," *Phys. Atom. Nucl.* **64** (2001) 698–726, `arXiv:hep-ph/0008131`.

[93] L. D. Landau and E. Lifshitz, *Fluid Mechanics, Second Edition: Volume 6 (Course of Theoretical Physics).* Butterworth-Heinemann, 1987.

[94] S. R. de Groot, W. A. van Leeuwn, and C. G. van Weert, *Relativistic Kinetic Theory.* North-Holland publishing company, 1980.

[95] W. Israel and J. M. Stewart, "Transient relativistic thermodynamics and kinetic theory," *Annals of Physics* **118** no. 2, (1979) 341–372.

[96] R. Baier, P. Romatschke, D. T. Son, A. O. Starinets, and M. A. Stephanov, "Relativistic viscous hydrodynamics, conformal invariance, and holography," *JHEP* **04** (2008) 100, `arXiv:0712.2451 [hep-th]`.

[97] B. Betz, D. Henkel, and D. H. Rischke, "From kinetic theory to dissipative fluid dynamics," *Prog. Part. Nucl. Phys.* **62** (2009) 556–561, `arXiv:0812.1440 [nucl-th]`.

[98] M. A. York and G. D. Moore, "Second order hydrodynamic coefficients from kinetic theory," *Phys. Rev. D* **79** no. 5, (2009) 054011, `arXiv:0811.0729 [hep-ph]`.

[99] R. Zwanzig, "Time-Correlation Functions and Transport Coefficients in Statistical Mechanics," *Annual Review of Physical Chemistry* **16** no. 1, (1965) 67–102.

[100] S. Jeon and L. G. Yaffe, "From Quantum Field Theory to Hydrodynamics: Transport Coefficients and Effective Kinetic Theory," *Phys. Rev.* **D53** (1996) 5799–5809, `arXiv:hep-ph/9512263`.

[101] M. S. Green, "Markoff Random Processes and the Statistical Mechanics of Time-Dependent Phenomena," *J. Chem. Phys.* **20** no. 8, (1952) 1281–1296.

[102] M. S. Green, "Markoff Random Processes and the Statistical Mechanics of Time-Dependent Phenomena. II. Irreversible Processes in Fluids," *J. Chem. Phys.* **22** no. 3, (1954) 398–414.

[103] H. Mori, "A Quantum-statistical Theory of Transport Processes," *Journal of the Physical Society of Japan* **11** no. 10, (1956) 1029–1044.

[104] R. Kubo, "Statistical-Mechanical Theory of Irreversible Processes. I. General Theory and Simple Applications to Magnetic and Conduction Problems," *Journal of the Physical Society of Japan* **12** no. 6, (1957) 570–586.

[105] A. Hosoya, M. aki Sakagami, and M. Takao, "Nonequilibrium thermodynamics in field theory: Transport coefficients," *Annals of Physics* **154** no. 1, (1984) 229–252.

[106] G. D. Mahan, *Many Particle Physics (Physics of Solids and Liquids).* Springer, 2010.

[107] D. Fernández-Fraile and A. Gómez Nicola, "Transport coefficients and resonances for a meson gas in chiral perturbation theory," *The European Physical Journal C - Particles and Fields* **62** (2009) 37–54, `arXiv:0902.4829 [hep-ph]`.

[108] J. M. Luttinger, "Theory of Thermal Transport Coefficients," *Phys. Rev.* **135** no. 6A, (1964) A1505–A1514.

[109] J. I. Kapusta, "Strongly interacting low viscosity matter created in heavy-ion collisions," *Journal of Physics G: Nuclear and Particle Physics* **34** no. 8, (2007) S295–304, `arXiv:0705.1277 [nucl-th]`.

[110] R. Horsley and W. Schoenmaker, "Quantum field theories out of thermal equilibrium : (I). General considerations," *Nuclear Physics B* **280** (1987) 716–734.

[111] P. Arnold and L. G. Yaffe, "Effective theories for real-time correlations in hot plasmas," *Phys. Rev. D* **57** no. 2, (1998) 1178–1192, `arXiv:hep-ph/9709449`.

[112] M. Iwasaki, H. Ohnishi, and T. Fukutome, "Shear viscosity and spectral function of the quark matter," `arXiv:hep-ph/0606192`.

[113] W. Alberico, S. Chiacchiera, H. Hansen, A. Molinari, and M. Nardi, "Shear viscosity and entropy of quark matter," *The European Physical Journal A - Hadrons and Nuclei* **38** (2008) 97–103, `arXiv:0707.4442 [hep-ph]`.

[114] M. Iwasaki, H. Ohnishi, and T. Fukutome, "Shear viscosity of the quark matter," *Journal of Physics G: Nuclear and Particle Physics* **35** no. 3, (2008) 035003.

[115] K. Heckmann, "Die Scherviskosität im Nambu-Jona-Lasinio-Modell," 2007. Diplomarbeit.

[116] D. Enskog, *Kinetische Theorie der Vorgänge in mäßig verdünnten Gasen*. PhD thesis, Uppsala, 1917.

[117] S. Chapman, "On the Law of Distribution of Molecular Velocities, and on the Theory of Viscosity and Thermal Conduction, in a Non-Uniform Simple Monatomic Gas," *Phil. Trans. R. Soc. Lond. A* **216** (1916) 279–348.

[118] S. Chapman and T. G. Cowling, *The Mathematical Theory of Non-Uniform Gases*. Cambridge University Press, 1970.

[119] L. Landau and E. Lifschitz, *Lehrbuch der Theoretischen Physik, Bd 10:Physikalische Kinetik*. Akademie Verlag GmbH, 1990.

[120] C. Cercignani, *Mathematical Methods in Kinetic Theory*. Plenum Press, 1969.

[121] R. L. Liboff, *Kinetic theory: classical, quantum, and relativistic descriptions*. Springer, 2003.

[122] P. B. Arnold, G. D. Moore, and L. G. Yaffe, "Transport coefficients in high temperature gauge theories: (I) Leading-log results," *JHEP* **11** (2000) 001, `arXiv:hep-ph/0010177`.

[123] P. B. Arnold, G. D. Moore, and L. G. Yaffe, "Transport coefficients in high temperature gauge theories. II: Beyond leading log," *JHEP* **05** (2003) 051, `arXiv:hep-ph/0302165`.

[124] A. Dobado and F. J. Llanes-Estrada, "Viscosity of meson matter," *Phys. Rev. D* **69** no. 11, (2004) 116004, `arXiv:hep-ph/0309324`.

[125] K. Itakura, O. Morimatsu, and H. Otomo, "Shear viscosity of a hadronic gas mixture," *Phys. Rev. D* **77** no. 1, (2008) 014014.

[126] N. Sonine, "Recherche sur les functions cylindiques et le développement des fonctions continues en séries," *Mathematische Annalen* **8** (1880) 1–80.

[127] A. Dobado and S. N. Santalla, "Pion gas viscosity at low temperature and density," *Phys. Rev.* **D65** (2002) 096011, `arXiv:hep-ph/0112299`.

[128] P. Drude, "Zur Elektronentheorie der Metalle," *Annalen der Physik* **306** no. 3, (1900) 566–613.

[129] P. Drude, "Zur Elektronentheorie der Metalle; II. Teil. Galvanomagnetische und thermomagnetische Effecte," *Annalen der Physik* **308** no. 11, (1900) 369–402.

[130] N. W. Ashcroft and N. D. Mermin, *Festkörperphysik*. Oldenbourg, 2001.

[131] C. Gerthsen, *Gerthsen Physik (Springer-Lehrbuch) (German Edition)*. Springer, 2001.

[132] W. Israel and J. Vardalas, "Transport coefficients of a relativistic quantum gas," *Lettere Al Nuovo Cimento (1969 - 1970)* **4** (1970) 887–892.

[133] P. Danielewicz and M. Gyulassy, "Dissipative phenomena in quark-gluon plasmas," *Phys. Rev. D* **31** no. 1, (1985) 53–62.

[134] R. Franz and G. Wiedemann, “Ueber die Wärme-Leitungsfähigkeit der Metalle,” *Annalen der Physik* **165** no. 8, (1853) 497–531.

[135] J. C. Maxwell, “Illustrations of the dynamical theory of gases. — Part I. On the motions and collisions of perfectly elastic spheres,” *Philosophical Magazine Series 4* no. 19, (1860) 19–32.

[136] J. C. Maxwell, “II. Illustrations of the dynamical theory of gases,” *Philosophical Magazine Series 4* no. 20, (1860) 21–37.

[137] H. Mori, “Time-Correlation Functions in the Statistical Mechanics of Transport Processes,” *Phys. Rev.* **111** no. 3, (1958) 694–706.

[138] S. Fujita, “Theory of Transport Coefficients. II Viscosity Coefficients of Quantum Gases Obeying the Boltzmann Statistics,” *Journal of Mathematical Physics* **3** no. 2, (1962) 359–367.

[139] J. James A. McLennan and R. J. Swenson, “Theory of Transport Coefficients in Low-Density Gases,” *Journal of Mathematical Physics* **4** no. 12, (1963) 1527–1536.

[140] S. Jeon, “Hydrodynamic transport coefficients in relativistic scalar field theory,” *Phys. Rev. D* **52** no. 6, (1995) 3591–3642, `arXiv:hep-ph/9409250v3`.

[141] G. Aarts and J. M. Martinez Resco, “Transport coefficients from the 2PI effective action,” *Phys. Rev.* **D68** (2003) 085009, `arXiv:hep-ph/0303216`.

[142] G. Aarts and J. M. Martinez Resco, “Shear viscosity in the O(N) model,” *JHEP* **02** (2004) 061, `arXiv:hep-ph/0402192`.

[143] M. A. Valle Basagoiti, “Transport coefficients and ladder summation in hot gauge theories,” *Phys. Rev. D* **66** no. 4, (2002) 045005, `arXiv:hep-ph/0204334`.

[144] J. L. Goity and H. Leutwyler, “On the mean free path of pions in hot matter,” *Physics Letters B* **228** no. 4, (1989) 517–522.

[145] D. Fernández-Fraile and A. Gómez Nicola, “Transport coefficients in Chiral Perturbation Theory,” *The European Physical Journal A - Hadrons and Nuclei* **31** (2007) 848–850, `arXiv:hep-ph/0610197`.

[146] A. Dobado, F. J. Llanes-Estrada, and J. M. Torres-Rincon, “Minimum of η/s and the phase transition of the linear sigma model in the large-N limit,” *Phys. Rev. D* **80** no. 11, (2009) 114015, `arXiv:0907.5483 [hep-ph]`.

[147] L. Bergmann and C. Schaefer, *Lehrbuch Der Experimentalphysik: Mechanik, Relativität, Wärme (German Edition)*. Walter De Gruyter Inc, 1998.

[148] J. Liao and V. Koch, “Fluidity and supercriticality of the QCD matter created in relativistic heavy ion collisions,” *Phys. Rev. C* **81** no. 1, (2010) 014902, `arXiv:0909.3105 [hep-ph]`.

[149] C. Schaefer and L. Bergmann, *Lehrbuch Der Experimentalphysik: Gase, Nanosysteme, Flüssigkeiten (Bergmann-Schaefer Lehrbuch Der Experimentalphysik) (German Edition) (v. 5)*. Walter De Gruyter Inc, 2005.

[150] C. C. Agosta, S. Wang, L. H. Cohen, and H. Meyer, “Transport properties of helium near the liquid-vapor critical point. IV. The shear viscosity of ^{3}He and ^{4}He,” *Journal of Low Temperature Physics* **67** (1987) 237–289.

[151] T. Hirano and M. Gyulassy, “Perfect fluidity of the quark-gluon plasma core as seen through its dissipative hadronic corona,” *Nuclear Physics A* **769** (2006) 71 – 94, `arXiv:nucl-th/0506049`.

[152] T. Schäfer, “Nearly perfect fluidity,” *Physics* **2** (2009) 88.

[153] J. Maldacena, "The Large-N Limit of Superconformal Field Theories and Supergravity," *International Journal of Theoretical Physics* **38** (1999) 1113–1133, `arXiv:hep-th/9711200`.

[154] E. Witten, "Anti-de Sitter space, thermal phase transition, and confinement in gauge theories," *Adv. Theor. Math. Phys.* **2** (1998) 505–532, `arXiv:hep-th/9803131`.

[155] O. Aharony, S. S. Gubser, J. M. Maldacena, H. Ooguri, and Y. Oz, "Large N field theories, string theory and gravity," *Phys. Rept.* **323** (2000) 183–386, `arXiv:hep-th/9905111`.

[156] G. Policastro, D. T. Son, and A. O. Starinets, "Shear Viscosity of Strongly Coupled $N = 4$ Supersymmetric Yang-Mills Plasma," *Phys. Rev. Lett.* **87** no. 8, (2001) 081601, `arXiv:hep-th/0104066`.

[157] S. S. Gubser, I. R. Klebanov, and A. M. Polyakov, "A semi-classical limit of the gauge/string correspondence," *Nucl. Phys.* **B636** (2002) 99–114, `arXiv:hep-th/0204051`.

[158] P. Kovtun, D. T. Son, and A. O. Starinets, "Holography and hydrodynamics: Diffusion on stretched horizons," *JHEP* **10** (2003) 064, `arXiv:hep-th/0309213`.

[159] A. Einstein, "Zur Theorie des statischen Gravitationsfeldes," *Ann. Physik* **343** no. 7, (1912) 443–458.

[160] A. Buchel and J. T. Liu, "Universality of the Shear Viscosity from Supergravity Duals," *Phys. Rev. Lett.* **93** no. 9, (2004) 090602, `arXiv:hep-th/0311175`.

[161] L. P. Csernai, J. I. Kapusta, and L. D. McLerran, "Strongly Interacting Low-Viscosity Matter Created in Relativistic Nuclear Collisions," *Phys. Rev. Lett.* **97** no. 15, (2006) 152303, `arXiv:nucl-th/0604032`.

[162] R. A. Lacey, N. N. Ajitanand, J. M. Alexander, P. Chung, W. G. Holzmann, M. Issah, A. Taranenko, P. Danielewicz, and H. Stöcker, "Has the QCD Critical Point Been Signaled by Observations at the BNL Relativistic Heavy Ion Collider?," *Phys. Rev. Lett.* **98** no. 9, (2007) 092301, `arXiv:nucl-ex/0609025`.

[163] J.-W. Chen, M. Huang, Y.-H. Li, E. Nakano, and D.-L. Yang, "Phase transitions and perfectness of fluids in weakly coupled real scalar field theories," *Physics Letters B* **670** no. 1, (2008) 18–21, `arXiv:0709.3434 [hep-ph]`.

[164] A. Dobado, F. J. Llanes-Estrada, and J. M. Torres-Rincon, "η/s and phase transitions," *Phys. Rev. D* **79** no. 1, (2009) 014002, `arXiv:0803.3275 [hep-ph]`.

[165] J.-W. Chen, C.-T. Hsieh, and H.-H. Lin, "Minimum Shear Viscosity over Entropy Density at Phase Transition? — A Counterexample," `arXiv:1010.3119 [hep-ph]`.

[166] I. Fouxon, G. Betschart, and J. D. Bekenstein, "Bound on viscosity and the generalized second law of thermodynamics," *Phys. Rev. D* **77** no. 2, (2008) 024016, `arXiv:0710.1429 [gr-qc]`.

[167] T. D. Cohen, "Is There a "Most Perfect Fluid" Consistent with Quantum Field Theory?," *Phys. Rev. Lett.* **99** no. 2, (2007) 021602, `arXiv:hep-th/0702136`.

[168] M. Brigante, H. Liu, R. C. Myers, S. Shenker, and S. Yaida, "Viscosity Bound Violation in Higher Derivative Gravity," *Phys. Rev.* **D77** (2008) 126006, `arXiv:0712.0805 [hep-th]`.

[169] A. Cherman, T. D. Cohen, and P. M. Hohler, "A sticky business: the status of the conjectured viscosity/entropy density bound," *Journal of High Energy Physics* **2008** no. 02, (2008) 026.

[170] A. Jakovac, "Nonuniversal lower bound for the shear viscosity to entropy density ratio," *Phys. Rev. D* **81** no. 4, (2010) 045020, `arXiv:0911.3248 [hep-th]`.

[171] H. A. Weldon, "Structure of the quark propagator at high temperatures," *Phys. Rev. D* **61** no. 3, (2000) 036003, `arXiv:hep-ph/9908204`.

[172] M. L. Bellac, *Thermal Field Theory.* Cambridge University Press, 2000.

[173] F. J. Dyson, "The S Matrix in Quantum Electrodynamics," *Phys. Rev.* **75** no. 11, (1949) 1736–1755.

[174] J. Schwinger, "Euclidean Quantum Electrodynamics," *Phys. Rev.* **115** no. 3, (1959) 721–731.

[175] P. Maris, "Confinement and complex singularities in QED in three- dimensions," *Phys. Rev.* **D52** (1995) 6087–6097, `arXiv:hep-ph/9508323`.

[176] K. Osterwalder and R. Schrader, "Axioms for Euclidean Green's functions," *Communications in Mathematical Physics* **31** (1973) 83–112.

[177] K. Osterwalder and R. Schrader, "Axioms for Euclidean Green's functions II," *Communications in Mathematical Physics* **42** (1975) 281–305.

[178] J. A. Müller, *Dyson-Schwinger Approach to Finite Temperature QCD.* PhD thesis, Technische Universität Darmstadt, 2010.

[179] H. Fujii, "Scalar density fluctuation at the critical end point in the Nambu–Jona-Lasinio model," *Phys. Rev. D* **67** no. 9, (2003) 094018, `arXiv:hep-ph/0302167`.

[180] A. Schäfer and M. H. Thoma, "Quark propagation in a quark-gluon plasma with gluon condensate," *Physics Letters B* **451** no. 1–2, (1999) 195–200, `arXiv:hep-ph/9811364`.

[181] M. Kitazawa, T. Kunihiro, K. Mitsutani, and Y. Nemoto, "Spectral properties of massless and massive quarks coupled with massive boson at finite temperature," *Phys. Rev. D* **77** no. 4, (Feb, 2008) 045034, `arXiv:0710.5809 [hep-ph]`.

[182] F. Frömel, S. Leupold, and U. Mosel, "Spectral function of quarks in quark matter," *Phys. Rev. C* **67** no. 1, (2003) 015206, `arXiv:nucl-th/0111004`.

[183] M. Kitazawa, T. Kunihiro, and Y. Nemoto, "Quark spectrum above but near critical temperature of chiral transition," *Physics Letters B* **633** no. 2–3, (2006) 269–274, `arXiv:hep-ph/0510167`.

[184] V. Sauli and J. Adam, "Solving the Schwinger-Dyson equation for a scalar propagator in Minkowski space," *Nucl. Phys.* **A689** (2001) 467–470, `arXiv:hep-ph/0110298`.

[185] V. Sauli, "Implications of analyticity to solution of Schwinger-Dyson equations in Minkowski space," *Few Body Syst.* **39** (2006) 45, `arXiv:hep-ph/0412188`.

[186] V. Sauli and Z. Batiz, "General method of solution of Schwinger-Dyson equations in Minkowski space," *PoS* **QCD-TNT09** (2009) 040, `arXiv:0911.0275 [hep-ph]`.

[187] J. A. Mueller, C. S. Fischer, and D. Nickel, "Quark spectral properties above Tc from Dyson-Schwinger equations," `arXiv:1009.3762 [hep-ph]`.

[188] H. A. Weldon, "Dynamical holes in the quark-gluon plasma," *Phys. Rev. D* **40** no. 7, (1989) 2410–2420.

[189] M. Asakawa, Y. Nakahara, and T. Hatsuda, "Maximum entropy analysis of the spectral functions in lattice QCD," *Progress in Particle and Nuclear Physics* **46** no. 2, (2001) 459 – 508, `arXiv:hep-lat/0011040`.

[190] D. Nickel, "Extraction of spectral functions from Dyson-Schwinger studies via the maximum entropy method," *Annals of Physics* **322** no. 8, (2007) 1949–1960, `arXiv:hep-ph/0607224`.

[191] M. Iwasaki, H. Ohnishi, and T. Fukutome, "Shear viscosity of the quark matter," `arXiv:hep-ph/0703271`.

[192] V. M. Galitskii and A. B. Migdal, "Application of quantum field theory methods to the many body problem," *Soviet Phys. JETP* **7** no. 3, (1958) 96–104.

[193] K. Nakamura and P. D. Group, "Review of Particle Physics," *Journal of Physics G: Nuclear and Particle Physics* **37** no. 7A, (2010) 075021.

[194] M. Kataja and P. V. Ruuskanen, "Non-zero chemical potential and the shape of the pT-distribution of hadrons in heavy-ion collisions," *Physics Letters B* **243** no. 3, (1990) 181–184.

[195] D. Davesne, "Transport coefficients of a hot pion gas," *Phys. Rev.* **C53** (1996) 3069–3084.

[196] C. Song and V. Koch, "Chemical relaxation time of pions in hot hadronic matter," *Phys. Rev. C* **55** no. 6, (1997) 3026–3037, `arXiv:nucl-th/9611034`.

[197] D. Fernández-Fraile and A. Gómez Nicola, "Chemical nonequilibrium for interacting bosons: Applications to the pion gas," *Phys. Rev. D* **80** no. 5, (2009) 056003, `arXiv:0903.0982 [hep-ph]`.

[198] A. Dobado and J. R. Peláez, "Chiral symmetry and the pion gas virial expansion," *Phys. Rev. D* **59** no. 3, (1998) 034004, `arXiv:hep-ph/9806416`.

[199] S. Weinberg, "Pion Scattering Lengths," *Phys. Rev. Lett.* **17** no. 11, (1966) 616–621.

[200] H. Lehmann, "Chiral invariance and effective range expansion for pion-pion scattering," *Physics Letters B* **41** no. 4, (1972) 529–532.

[201] H. Pagels, "Departures from chiral symmetry," *Physics Reports* **16** no. 5, (1975) 219–311.

[202] S. Weinberg, "Phenomenological Lagrangians," *Physica A: Statistical and Theoretical Physics* **96** no. 1–2, (1979) 327–340.

[203] J. Gasser and H. Leutwyler, "Chiral perturbation theory to one loop," *Annals of Physics* **158** no. 1, (1984) 142–210.

[204] M. Prakash, M. Prakash, R. Venugopalan, and G. Welke, "Nonequilibrium properties of hadronic mixtures," *Phys. Rept.* **227** (1993) 321–366.

[205] A. Dobado and J. R. Peláez, "Global fit of $\pi\pi$ and πK elastic scattering in chiral perturbation theory with dispersion relations," *Phys. Rev. D* **47** no. 11, (1993) 4883–4888, `arXiv:hep-ph/9301276`.

[206] R. Venugopalan and M. Prakash, "Thermal properties of interacting hadrons," *Nuclear Physics A* **546** no. 4, (1992) 718–760.

[207] H. J. Schulze, "Pion-pion scattering lengths in the SU(2) Nambu-Jona-Lasinio model," *Journal of Physics G: Nuclear and Particle Physics* **21** no. 2, (1995) 185–191.

[208] E. Quack, P. Zhuang, Y. Kalinovsky, S. P. Klevansky, and J. Hüfner, "$\pi - \pi$ scattering lengths at finite temperature," *Physics Letters B* **348** no. 1–2, (1995) 1–6, `arXiv:hep-ph/9410243`.

[209] M. Loewe, J. R. A., and J. C. Rojas, "Thermal behavior of $\pi - \pi$ scattering lengths in the Nambu–Jona-Lasinio model," *Phys. Rev. D* **78** no. 9, (2008) 096007, `arXiv:0805.3719 [hep-ph]`.

[210] A. A. Osipov, A. E. Radzhabov, and M. K. Volkov, "pi pi scattering in a nonlocal Nambu - Jona-Lasinio model," `arXiv:hep-ph/0603130`.

[211] T. Hatsuda and T. Kunihiro, "Character changes of pion and σ-meson at finite temperatures," *Physics Letters B* **185** no. 3-4, (1987) 304 – 309.

[212] Y. B. He, J. Hüfner, S. P. Klevansky, and P. Rehberg, "$\pi\pi$ scattering in the ρ-meson channel at finite temperature,".

[213] P. Piwnicki, S. P. Klevansky, and P. Rehberg, "$\pi - K$ scattering lengths at finite temperature in the Nambu-Jona-Lasinio model," *Phys. Rev.* **C58** (1998) 502–516, `arXiv:hep-ph/9804286`.

[214] M. Oertel, M. Buballa, and J. Wambach, "Pion properties in the 1/Nc-corrected NJL model," *Physics Letters B* **477** no. 1–3, (2000) 77–82, `arXiv:hep-ph/9908475`.

[215] M. Oertel, M. Buballa, and J. Wambach, "Meson properties in the 1/Nc-corrected NJL model," *Nuclear Physics A* **676** no. 1–4, (2000) 247–272, `arXiv:hep-ph/0001239`.

[216] M. Cheng *et al.*, "Baryon number, strangeness, and electric charge fluctuations in QCD at high temperature," *Phys. Rev. D* **79** no. 7, (2009) 074505, `arXiv:0811.1006 [hep-lat]`.

[217] H. B. Meyer, "Density, short-range order, and the quark-gluon plasma," *Phys. Rev. D* **79** no. 1, (2009) 011502, `arXiv:0808.1950 [hep-lat]`.

[218] J. I. Kapusta, *Finite-Temperature Field Theory (Cambridge Monographs on Mathematical Physics).* Cambridge University Press, 1989.

[219] G. P. Lepage, "A new algorithm for adaptive multidimensional integration," *Journal of Computational Physics* **27** no. 2, (1978) 192–203.

Acknowledgements

An erster Stelle möchte ich mich bei Prof. Dr. J. Wambach für das Angebot danken, diese Arbeit über ein spannendes Thema in einer spannenden Zeit anzufertigen, wie auch für die fortlaufende Unterstützung und Diskussion. Für die intensive Betreuung dieser Arbeit möchte ich Dr. Michael Buballa danken, von dem ich auch sehr viel über das NJL-Modell lernen konnte.
Bei den anderen Mitgliedern der Arbeitsgruppe möchte ich mich ebenfalls für die angenehme Atmosphäre in den vergangenen Jahren bedanken. Neben Dr. Haris Djapo, Dr. Verena Kleinhaus und Dr. Dominik Nickel möchte ich hier vor allem Dr. Hannes Basler für viele Diskussionen über verschiedene Aspekte des NJL-Modells und numerische Verfahren danken, wie auch Daniel Müller für die erfolgreiche gemeinsame Untersuchung der selbstkonsistenten $1/N_c$-Näherung.
Materiell wurde meine Arbeit auch von der Helmholtz Graduate School for Hadron and Ion Research gefördert. Dieser möchte ich für diese Unterstützung ebenso danken wie Prof. Dr. D. Rischke, der sich bereit erklärt hat, in meinem "PhD-Commitee" im Rahmen der Graduate School mitzuwirken.
Die fruchtbare wissenschaftliche Atmosphäre in den Theoriegruppen des Institus für Kernphysik haben sicherlich viel zu meinem Verständnis der modernen Physik im Allgemeinen und der der starken Wechselwirkung im Besonderen beigetragen. Für viele fachliche und auch nichtfachliche Diskussionen möchte ich mich bei Tobias Göcke, Christian Kellermann, Sabine Reinhardt und Thorsten Zöller bedanken.
Zuletzt möchte ich noch Prof. Dr. C. Fischer, Jan Lücker und Dr. Richard Williams für ihre Erläuterungen und Diskussionen bezüglich der Methode der Dyson-Schwinger-Gleichungen und ihrer numerischen Realisierung in Euklidischer Metrik danken.

Übersicht des Lebens- und Bildungsganges

gemäß §8 Abs. 1a der Promotionsordnung

Name	Klaus Heckmann
Geburtsdatum	1. September 1982
Geburtsort	Groß-Gerau
Staatsangehörigkeit	deutsch

08/1993–06/2002	Besuch der Justus-Liebig-Schule in Darmstadt
06/2002	Abitur (Leistungsfächer: Chemie, Mathematik; Note: 1,1)
10/2002–11/2007	Studium der Physik an der TU Darmstadt
08/2005–04/2006	Studium am ENSPG / INP Grenoble (Frankreich)
11/2007	Diplom (Thema: Die Scherviskosität im Nambu-Jona-Lasinio-Modell)
seit 12/2007	Promotionsstudium an der TU Darmstadt, Anfertigung der Dissertation

Erklärung

gemäß §9 Abs. 1 der Promotionsordnung.

Ich erkläre hiermit, dass ich diese Arbeit — abgesehen von den in ihr ausdrücklich genannten Hilfen und Quellen — selbständig verfasst habe.